UNIVERSITA' DEGLI STUDI DI SASSARI

FACOLTA' DI CHIMICA E FARMACIA

Scuola di Dottorato di Ricerca in Scienze e Tecnologie Chimiche

Indirizzo: Nanochimica, Nanomateriali e Materiali funzionali

XXVIII Ciclo

Ceria nanoparticles as smart platform for biomedical applications

Relatore:

Dr. Luca Malfatti

Correlatore:

Prof. Plinio Innocenzi

Dottoranda:

Alessandra Pinna

Anno accademico 2014-2015

Abstract

The present doctoral thesis focuses on the antioxidant activity of cerium oxide nanostructured materials (nanoceria) in biological systems. This goal is obtained through an interdisciplinary approaches spanning from chemistry and physics to biology and medicine. Nanoceria is studied in form of nanoparticles both naked and integrated nanocomposites films. The physicochemical properties are studied by a complete set of characterization techniques such as XRD, FTIR and Raman spectroscopies, DLS, AFM, μ-XRF, SEM and TEM. A specific emphasis is placed on the interactions with cells (PC12, PBMC, oocyte and spermatozoa) as a function of the nanoceria concentration. Different techniques for cell analysis, such as flow cytometry and confocal microscopy, allow monitoring the fate and viability of nanoparticles into the cells. Our results show that nanoceria can be successfully used as antioxidant agent in biomedical field to improve the cells viability both in physiological condition (IVM) and in Parkinson-like diseases. Moreover, the antioxidant activity of nanoceria is also verified in composite materials for prospected applications as ophthalmic medical devices and smart Petri dishes. These results pave the way to the development of an innovative smart "platform" based on the antioxidant properties of functional nanoceria.

Note

Much of the work presented in this thesis has been published in scientific journals as shown in appendix.

Dott.ssa Alessandra Pinna
Ceria nanoparticles as smart platform for biomedical applications
Tesi di Dottorato in Scienze e Tecnologie Chimiche
Indirizzo: *Nanochimica, Nanomateriali e Materiali funzionali* -XXVIII Ciclo
Università degli Studi di Sassari- Facoltà di Chimica e Farmacia

Index

List of Symbols and Abbreviations

A549	adenocarcinomic human alveolar basal epithelial cells
Ac	acrosome
AD	Alzheimer disease
AFM	atomic force microscopy
AI	artificial insemination
ALH	lateral head displacement
APTES	aminopropyltriethoxysilane
BBB	blood–brain barrier
BCF	beat cross frequency
CAT	catalase
CCD	charge coupled device
CLs	contact lenses
cM	cytoplasmic membrane
CMC	critical micelle concentration
CMNC	ceramic matrix nanocomposites
COC	oocytes-cumulus complex
CTAB	1-hexadecyl trimethylammonium bromide
CVD	chemical vapour deposition

DA	dopamine
DAPI	4,6-diamidino-2- phenylindole dihydrochloride
DLS	dynamic light scattering
DMEM	Dulbecco's modified Eagle's medium
DMF	dimethylformamide
DNA	desoxyribonucleic acid
DOPAC	dihydroxyphenylacetic acid
DXRL	deep X-ray lithography
EDTA	ethylenediaminetetraacetic acid
EISA	evaporation-induced self-assembly
ESEM	environmental scanning electron microscopy
EtOH	ethanol
FBS	fetal bovine serum
FDA	food and drug administration
FITC	fuorescein isothiocyanate
FSH	follicle stimulating hormone
FTIR	Fourier transform infrared
GDNF	glial cell line-derived neurotrophic factor
GISAXS	grazing-incidence small angle scattering
GPTMS	glycidopropyltrimethoxysilane

GSH	glutathione peroxidase
GV	germinal vesicle oocytes
H9c2	cardiac myocytes
HaCat	cultured human keratinocyte
HDS	highly dispersed silica
HeLa	human cervical cancer cells
HEK293	human embryonic kidney
HPLC-EC	high performance liquid chromatography electro-chemical detection
HT22	hippocampal neuronal cell line
HVA	homovanillic acid
IBM	international business machines
i.p	intraperitoneally
IR	infra red
ICM	inner cell mass
ISCOMs	immune stimulating complexes
IUPAC	international Union of Pure and Applied Chemistry
i.v.	intravenously
IVM	*in vitro* maturation
L929	murine fibrosarcoma cells

L-DOPA	levodopa
LH	lutein hormone
MII	metaphase II oocytes
MCF-7	breast cancer cell line
MFI	median fluorescence intensity
MeOH	methanol
MIMIC	micromolding in capillaries
MMNC	metal matrix nanocomposites
MOFs	metal−organic frameworks
MSE	mean square error
MT	methoxytyramine
MTT	3-(4,5-dimethylthiazol-2-yl)-2,5-diphenyltetrazolium bromide
NAC	n-acetylcysteine
NADPH	nicotinamide adenine dinucleotide phosphate
NBB	nano-building block
NIR	near infrared
NPs	nanoparticles
NSMs	nanostructured materials
Nu	nucleus
OSS	oestrus sheep serum

P19	mouse embryonal carcinoma cells
PBMC	peripheral blood mononuclear cells
PBS	phosphate buffer saline
PC12	pheochromocytoma cell line
PD	Parkinson's disease
PEG	polyethylene glycol
PGA	polyglycolic acid
pHEMA	hydroxyethyl methacrylate
PI	propidium iodide
PLD	Parkinson like disease
PM	progressive motility
PMMA	polymethylmethacrylate
PMNC	polymer matrix nanocomposites
PS	polystyrene
PSA	pisum sativum agglutinin
PSA	prostate specific antigen
PSD	position sensitive detector
PVA	polyvinyl alcohol
PVD	physical vapour deposition
RH	relative humidity

Rh6G	rhodamine 6G
ROH	alcohol group
RNS	reactive nitrogen species
ROS	reactive oxygen species
RPM	revolutions per minute
SAXS	small-angle X-ray scattering
SEM	scanning electron microscopy
SERS	surface-enhanced Raman spectroscopy
SMGT	sperm-mediated gene transfer
SOD	superoxide dismutase
SOF	synthetic oviductal fluid
SN	substantia nigra
SPIONs	super paramagnetic iron oxide nanoparticles
TB	trypan blue
TCM 199	tissue culture medium
TE	trophectoderm cell
TEM	transmission electron microscopy
TEOS	tetraethoxysilane
TM	total motility
TMOS	tetramethoxysilane

UV	ultra violet
VAP	smoothed path velocity
VCL	track velocity lateral
Vis	visible
VSL	straight line velocity
XRD	X-ray diffraction
ZP	zona pellucida

1. Introduction

1.1. Nanotechnologies, nanomaterials: key enabling technologies to the innovation

Although nanotechnology is a new area of research, nanomaterials are known to be used for centuries. For example, the color of roman glass artifacts is due to the presence of nanoparticles. Thousand years ago, Chinese used gold nanoparticles as an inorganic dye to introduce red color into their ceramic porcelains.[1]

Nowadays, the importance of nanotechnology and nanomaterials is growing rapidly and their meaning has been, recently, defined from European Commission (2011)."Nanotechnology is the study of phenomena and fine-tuning of materials at atomic, molecular and macromolecular scales, where properties differ significantly from those at a larger scale".

The nanomaterials have been defined as "a natural, incidental or manufactured material containing particles, in an unbound state or as an aggregate or as an agglomerate and where, for 50 % or more of the particles in the number size distribution, one or more external dimensions is in the size range 1 -100 nm. In specific cases and where warranted by concerns for the environment, health, safety or competitiveness the number size distribution threshold of 50 % may be replaced by a threshold between 1 and 50 %".

The global market for nanomaterials is estimated at 11 million tonnes at a market value of 20 billion €. The materials that dominate for decades are represented by carbon black (mainly used in tyres) or synthetic amorphous silica (used in a wide variety of applications including tyres, as polymer filler, but also in toothpaste or as anticoagulant in food powders). In the recent years, new nanomaterials have been developed for many applications such as UV-filters in sun creams, anti-odour textiles, medical devices for tumors therapies, lithium-ion batteries for energy storage and photovoltaic devices. These applications have the potential to create major technological breakthroughs, and therefore nanomaterials have been recently

identified as a key enabling technology by the European Community.[2] Nowadays nanomaterials are no longer a laboratory curiosity; in fact they have reached the stage of commercialization in many countries, such as in the USA, UK, Japan, Singapore, Malaysia, Taiwan, Korea, Germany and in recent years China and Australia[3], although supported by the government funding. The importance of nanomaterials is definitely due to their size; in fact when an object has a size between 1 and 100 nm, it can shows remarkable and novel properties which largely differ from those at a larger scale. This difference is due to two main reasons: firstly, nanomaterials have an extremely high surface area respect to the bulk materials. This can improve the chemical reactivity and affects the mechanical strength or electrical properties. Secondly, in some cases quantum confinement effects dramatically modify the optical, electrical and magnetic behaviour of the material.

Nanostructured materials (NSMs) can be classified depending on the shape (dimensionality) and chemical composition of their microstructural constituents (boundary regions and crystallites) (Fig.1.1), or on the dimensions (Fig.1.2).

According to the shape of the crystallite, we can distinguish three categories: *layer-shaped* crystallites, *rod-shaped* crystallites (with layer thickness or rod diameters in the order of a few nm) and *equiaxed* nm-sized crystallites.

Depending on the chemical composition of the crystallites, the three categories of nanostructured materials may be represented by four families. To the first family belong NSMs with all crystallites and interfacial regions with the same chemical composition (e.g. semicrystalline polymers which consist of stacked crystalline lamellae separated by non-crystalline regions). Nanostructured materials represented by second family consist of crystallites with different chemical compositions (quantum well (multilayer) structures are examples of this family). The third family is formed by nanostructured materials showing a compositional variation that primarily occurs between crystallites and the interfacial regions, (e.g. nanometer-sized Al_2O_3 crystals separated by a network of non-crystalline layers of Ga). The fourth family of nanostructured materials is formed by nm-sized crystallites (layers, rods, equiaxed

crystallites) dispersed in a matrix of different chemical composition (e.g. precipitation-hardened alloys).[4]

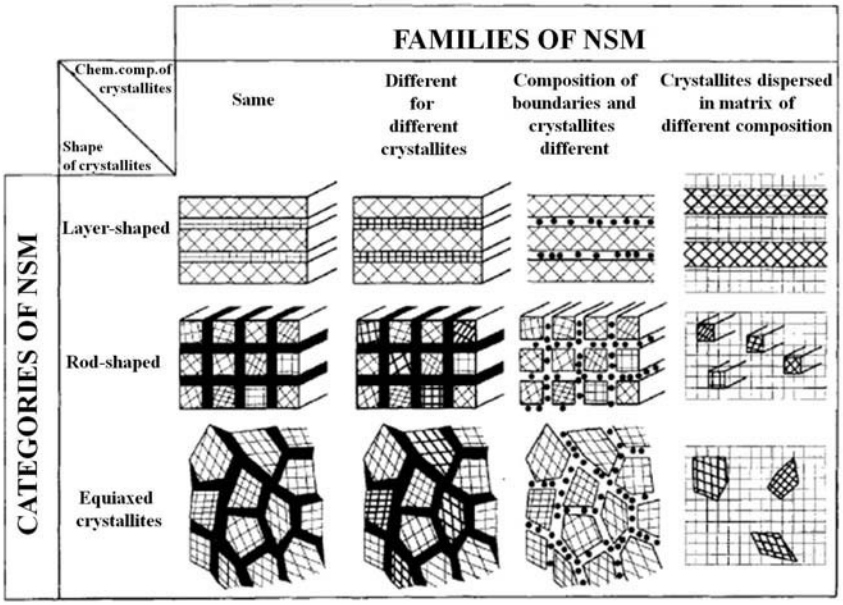

Fig.1.1 Classification of nanostructured materials based on shape and chemical composition of crystallites.[4]

The NSMs considered so far consisted mainly of crystalline components, which include the most of materials studied in this thesis (iron, cerium and titanium oxide). In fact in the fourth family we can include some of the ceria based nanocomposite, synthesized and characterized in the paragraph 4.2. However a fifth family covering NSMs in which one or all constituents are non-crystalline should be envisaged. Amorphous silica and hybrid organic-inorganic matrix ceria based nanocomposites should be considered as examples of this last class of NSMs.

Another classification of the nanostructured materials is based on the number of *dimensions* which lie within the nanometer range (Fig.1.2). According to this criterion, four classes can be distinguished:

- materials confined in three nano-dimension with zero dimension (0D) structures (nanoparticles, nanoshells, nanocrystals, nanorings, fullerenes, colloidal particles, quantum dots);

- materials confined in two nano-dimension with one dimension (1D) structures (nanorods, nanofilaments, nanotubes, quantum wires;

- materials confined in one nano-dimension with a two dimension (2D) structures (discs, platelets, ultrathin films, super lattices, quantum wells, graphene, layer-by-layer assemblies);

- materials not confined in nano-dimension with three dimension (3D) structures (bulk materials with nanoscale structural control, nanohybrids, nanocomposites and mesoporous materials).[5,6]

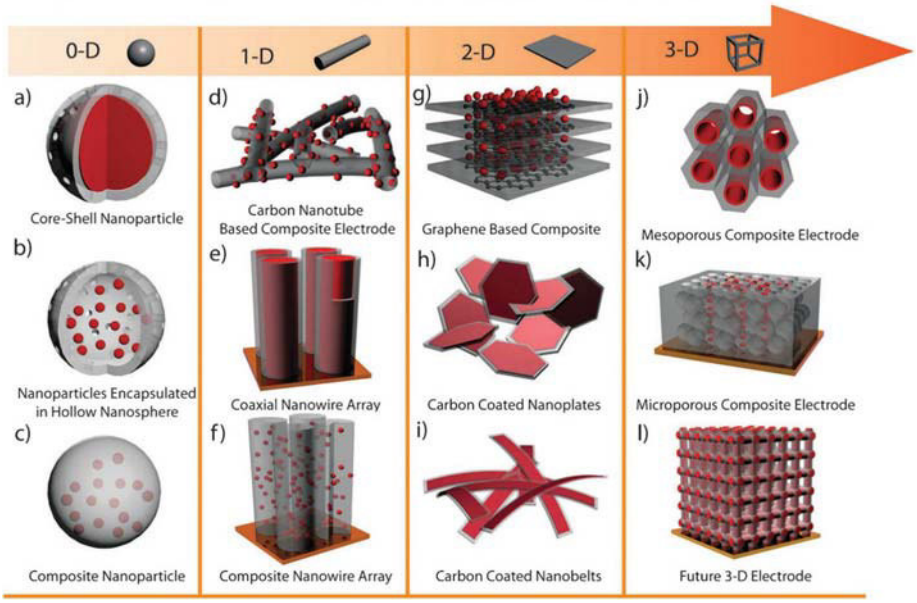

Fig.1.2 Classification of nanostructured materials based on size of their structural elements. 0D (zero-dimensional); 1D (one-dimensional); 2D (two-dimensional); 3D (three-dimensional).[7]

The most common representation of zero dimensional nanomaterial is a nanoparticle which can be:

- amorphous or crystalline
- single or polycrystalline
- composed of single or multi-chemical elements
- exhibit various shapes and forms
- exist individually or incorporated in a matrix

- metallic, ceramic, or polymeric.

The one dimensional material can be:

- amorphous or crystalline
- single or polycrystalline
- chemically pure or impure
- stand alone materials or embedded in within another medium
- metallic, ceramic, or polymeric.

The two dimensional material can be:

- amorphous or crystalline
- made up of various chemical compositions
- used as a single layer or as multilayer structures
- deposited on a substrate
- integrated in a surrounding matrix material
- metallic, ceramic, or polymeric

Finally, the three dimensional materials are bulk nanomaterials that are not confined to the nanoscale in any dimension. These materials show a nanocrystalline structure or involve the presence of features at the nanoscale. In terms of nanocrystalline structure, bulk nanomaterials can be composed of a multiple arrangement of nanosize crystals, typically in different orientations. With respect to the presence of features at the nanoscale, 3-D nanomaterials can contain dispersions of nanoparticles, bundles of nanowires, and nanotubes as well as multi-nanolayers. The materials prepared in this work can be included in the class of 0D NSMs, if we consider the nanoparticle as it is, or in the class of 3D NSMs, if we look at the combination of nanoparticles with mesoporous and hybrid nanocomposite films.

The fabrication of NSMs can be achieved by a wide variety of techniques providing different quality, speed and cost of the products. These manufacturing approaches are generally classified in two main groups defined as '*top-down*' and '*bottom-up'*. In 1959, Richard Feynman introduced first these two approaches in the famous talk "There's Plenty of Room at the Bottom" given at the Caltech during an American

Physical Society meeting.[8] The *top-down* approach is a process where each nanostructured component becomes part of a superstructure whilst the *bottom-up* approach consists in the miniaturization of the components starting from bulk structures. The *top-down* route can be done by using different technique such as plasma etching, ball milling and lithography. The latter method allows producing pattern through surface exposure to light, ions or electrons, and then leads to obtain electronic devices, chip and mask.[9] The *bottom-up* route can be achieved by chemical synthesis, self assembly and positional assembly. The first one is a method used to produce materials such as particles and molecules. Using the second approach, crystals films and tubes are produced by physical or chemical interactions between atoms or molecules which arrange themselves into ordered nanoscale structures. The third one consists in manipulation and positioning one by one of atoms, molecules and clusters into experimental atomic or molecular devices. One of the most interesting routes to *bottom-up* preparation of nanomaterials is represented by sol-gel process.

1.2. Sol-gel chemistry

The sol-gel chemistry is a well-established "wet" technology that has been performed for more than a century. The first sol-gel patent, concerning the preparation of TiO_2 and SiO_2 coatings, was published in 1939.[10] In the last 30 years it has shown a rapid growth, due to the integration of the sol-gel techniques into different areas of materials science such as nanostructured materials, soft matter, polymers and biomaterials. The resulting multidisciplinary approach of this technique has allowed producing highly complex materials and new functionalities which are used in many industrial sectors and applications from catalysis, sensors, and optics to biomedicine and energy. Sol-gel chemistry is a simple and relatively low-cost process used for the production of various materials with carefully controlled properties. This method is characterized by a set of chemical reactions which convert a homogeneous solution of molecular reactant precursors with defined size (a sol) into a three-dimensional polymer (a gel). A sol is a liquid suspension of colloidal particles (1-1000 nm) that show short-range

interactions due to van der Waals forces and surface charges. When the surface charge of the sol particles is significantly reduced, the gelation occurs and the obtained material is able to maintain its shape. The gel is composed by a solid network that encloses a liquid phase or solvent excess.

More in details, the entire sol-gel process can be divided in different steps: preparation of the precursor solution, hydrolysis, condensation, gelation, ageing, drying and densification (Fig.1.3)

The preparation of the precursor solution is the first stage in the sol-gel process and the selection of reactants plays the key role. In fact the sol may be produced starting from inorganic or organic precursor such as metallic salts (nitrates or chloride) or alkoxides and may consist of dense oxide particles or polymeric cluster. The general formula of metallic salts is M_mX_n where M is the metal, X an anionic group and m and n stoichiometric coefficients; an example is aluminium chloride ($AlCl_3$), cerium nitrate ($CeNO_3$), iron chloride ($FeCl_3$,$FeCl_2$) etc. Whilst $M(OR)_n$ is the alkoxide general formula, which indicates the combination of cation M with an alcohol groups ROH. An example is aluminum ethoxide ($Al(OC_2H_5)$), tetraethoxysilane (TEOS), titanium isopropoxide ($Ti[OCH(CH_3)_2]_4$) and so on.

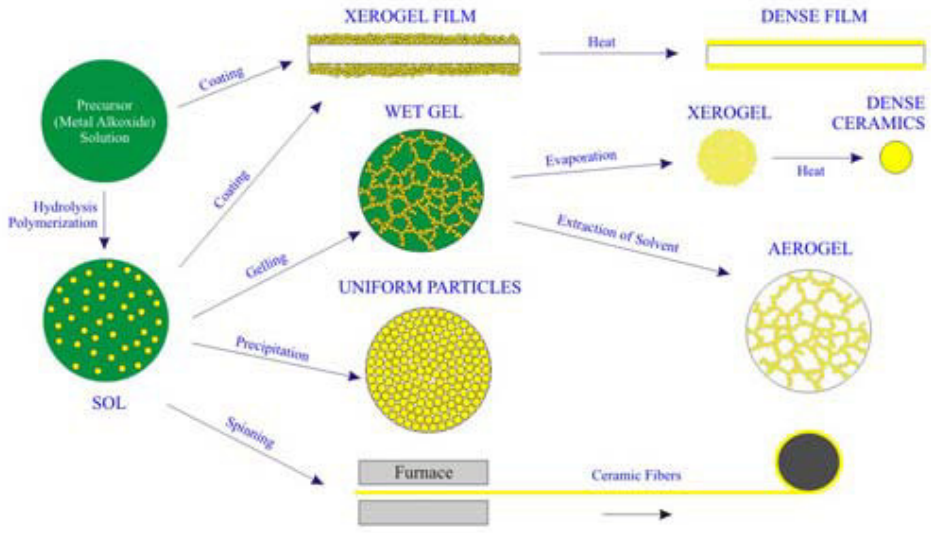

Fig.1.3 Overview of the sol-gel process.[11]

A broad library of alkoxysilanes, such as aminopropyl-triethoxysilane ($H_2N(CH_2)Si(OEt)_3$), glycidyloxypropyltrimethoxysilane ($C_9H_{20}O_5Si$) etc. is available for the synthesis of hybrid materials combining both inorganic (silica) and diverse organic functions. There is another class of precursors which is represented by organometallic compound, where a metal M is directly linked to carbon atom. The most widely used precursors in sol-gel research are the alkoxides, such as tetramethoxysilane (TMOS) and tetraethoxysilane (TEOS). In this thesis for example inorganic salts have been employed to produce on the one hand a crystalline ceria and iron nanoparticles and on the other hand titania crystalline and hafnia amorphous films, while alkoxide has been used to produce amorphous silica films. An alkoxysilane precursor in our sol-gel procedure, for example, has been used to synthesise amorphous hybrid film.

The second stage is characterized by the hydrolysis of the precursor promoted by water molecules, which leads to a transformation of sol in a liquid. The reactivity of the precursor in this step is different; in fact for example metal alkoxides of titanium, zirconium or aluminium are much more reactive towards water than alkoxysilanes due to the lower electronegativity and higher Lewis acidity. The reaction between alkoxysilanes and water is quite gentle avoiding phase separation and leading to good homogeneity.

The third stage in the sol-gel reaction is the condensation of the particles in the gel phase. In the last stages the resulting porous gel is usually chemically purified and treated by high temperatures, or by UV or IR radiation, to form oxide materials. These can be either totally inorganic in nature or both inorganic and organic.

A general reaction scheme for the chemical synthesis of sol-gel derived compounds is shown in (Fig.1.4), where the mechanism of formation of a metal oxide bond from metal alkoxide precursors takes place via hydrolysis of the alkoxide moiety followed by a condensation reaction which eliminates an H_2O or ROH group.[12]

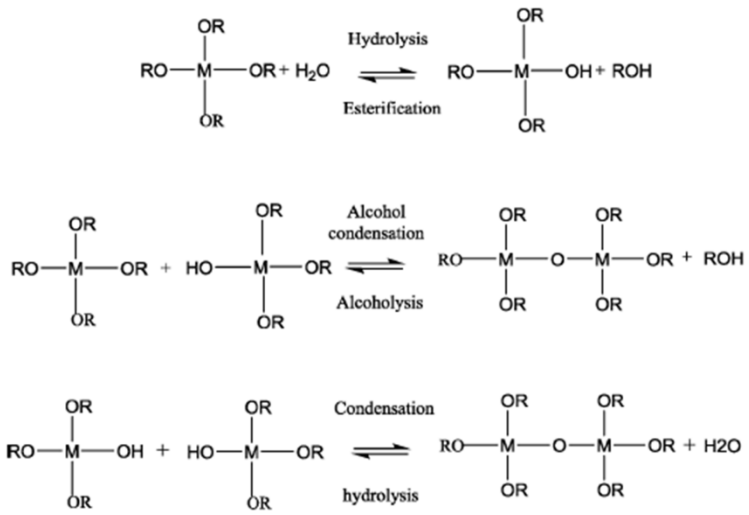

Fig.1.4 Scheme of the sol–gel process. The formation of the M–OH bond takes place via a hydrolysis reaction whereas the formation of the metal oxide bond takes place via a condensation reaction.[12]

The entire process can be influence by different parameters such as precursors, pH, and temperature, molar ratios of reactants, solvent composition and by the aging and drying conditions. The precursors have to be soluble in the reaction media and reactive enough to participate at the gel formation.[13] The pH controls the hydrolysis and condensation reactions as it is reported in Fig.1.5; in fact, when the reaction is under acid conditions, the hydrolysis kinetic is favoured instead of the condensation, which generally starts when hydrolysis is completed. [14,15] In basic conditions, on the contrary, the condensation is faster than the hydrolysis, resulting in a highly condensed species that may agglomerate into fine particles.[16] In order to stabilize the sol and avoiding the aggregation or agglomeration between the colloidal particles, the pH can be maintained in a range close to the point of zero charge. When the pH is changed or the particles distance is reduced by the solvent evaporation, the surface charge decrease and the gelation take place. On the contrary if the particles agglomerate, becoming too large, the precipitation occurs instead of gelation.

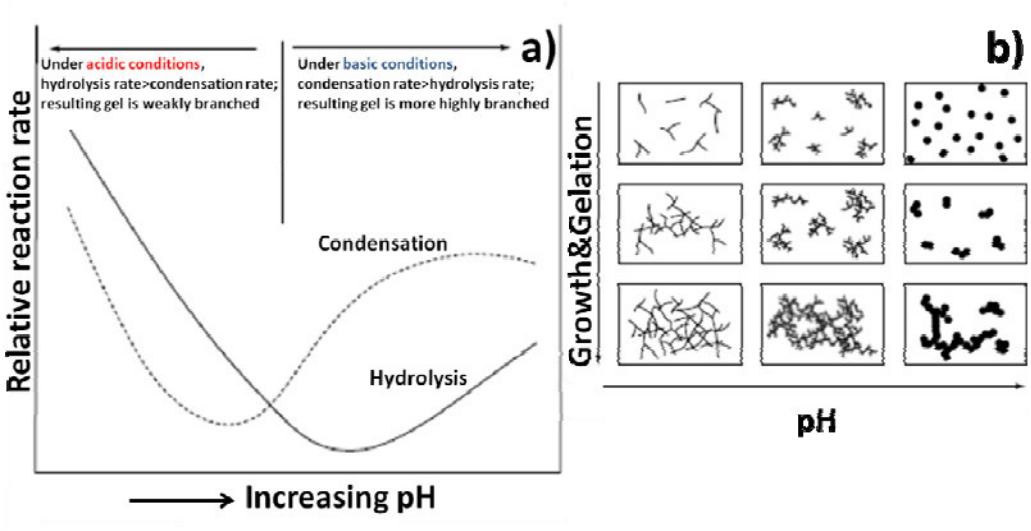

Fig.1.5 Dependence on pH of (a) hydrolysis and condensation rates of $Si(OR)_4$ and (b) the structure of the obtained gel. (a) Redrawn from Ref.[17]; (b) redrawn from Ref.[18]

The catalysts, such as HCl, H_2SO_4, NH_4OH, HI and H_2O, in some reactions show effects on gelation time, density and volume shrinkage on drying process. For example the reaction rate in silicon alkoxides sol-gel process can be slowed by adding water or speeded up by using acid or base catalysts.[19] The type of catalyst can also affect the film thickness, porosity and optical quality. The role of the temperature, aging and drying is important in term of homogeneity, purity and porosity of the obtained material. During the drying step under atmospheric conditions, occurs the loss of water, alcohol and other volatile components leading to the gel shrinkage[20] with a high strain in the structure of the material. If the strain is not stopped by relaxation, the cracks appear with the consequence of structure breaking.

The sol-gel process has many advantages. It allows obtaining not only materials with oxide composition, but also hybrid organic-inorganic materials which do not exist in nature. Moreover the sol-gel materials can show a huge variety of textures, shapes and dimensions (nanoparticles, porous structures, thin fibers, dense powders and thin films). It is possible to synthesize porous, amorphous and nanocrystalline materials and we can also control the particle and pore size, by monitoring the rate of hydrolysis and condensation. Furthermore, pore size and mechanical strength can be tuned by controlling the ageing and the drying conditions. The chemical process, especially for

the first steps, requires low temperature and no extreme pH condition. The equipment used in sol-gel route is simple and inexpensive. In this work, it is shown that the sol-gel process is a suitable method for obtain different kind of materials; in fact nanoparticles, inorganic and hybrid films and nanocomposites, have been produced through sol-gel chemistry.

1.2.1. Metal oxide nanoparticles

Nanoparticles have attracted the attention of an increasing number of researchers and the term nanoparticles came into frequent use in the early 1990s together with the related concepts, nanoscaled or nanosized particle.[21] Various chemical methods such as co-precipitation, hydrothermal, sol-gel technology, and combustion method, have been developed for nanoparticles synthesis. Among the various chemistry routes, sol-gel procedure is particularly successful in the preparation of metal oxide nanoparticles. The chemistry of sol-gel can be done in aqueous or non-aqueous environment.[22] The aqueous sol-gel process is complex since the metal precursors are very reactive in water and also because water plays a double role as a ligand and as a solvent. In many cases the three reactions, hydrolysis, condensation and aggregation occur at the same time and it is difficult to control the reaction rate. As a matter of fact small changes in experimental condition result in altered particle morphologies. For instance, the fast hydrolysis and condensation rate for most transitional metal oxide precursor (inorganic metal salts such as acetate, chloride and nitrate or metal organic species such as metal alkoxide) can result in loss of structure and morphology control with a consequence of amorphous material.

In most cases, the major limitations of the aqueous system can be overcome by using a non-aqueous chemistry in a synthesis of nanoparticles. This is related to the manifold role of the organic component in the sol-gel reaction (solvent, organic ligand of the precursor molecule, surfactants, or *in situ* formed organic condensation products). Non-aqueous chemistry pathways are reliable and allow obtaining reproducible metal oxide nanoparticles with the possibility to scale up the nanoparticles production. The

type of the precursor and the solvent are strictly related to the morphology of the nanoparticles, in fact metal nanoparticles with the same composition and crystal structure have shown different particle size and shape. The oxygen eventually contained into the organic part enables the formation of the metal oxide nanoparticles and strongly determines their surface properties, size and shape. Moreover, the oxygen-carbon bond has a moderate reactivity resulting in a reduction of reaction rate. In comparison with the aqueous chemistry the synthesis of metal oxide nanoparticles in an organic solvent allowed to better understand and control the reaction pathways on a molecular level, which is a crucial step to design a nanoparticles synthesis. Unlike the aqueous process, where obtained nanoparticles are in most cases amorphous and subsequent thermal treatment is required to induce crystallization, in non-aqueous route, crystalline nanoparticles can be directly obtained by carrying out the synthesis at high temperatures (oil bath, autoclave or microwave).

The non-aqueous processes can be divided in surfactant and solvent controlled routes.[23] The uses of surfactant consist of organic molecules with a coordinating head group and long alkyl chain which can coat the nanoparticles during the synthesis preventing their agglomeration and then improving the stability in the solvent. Throughout the growth step, by dynamic absorption e desorption on the nanoparticles surface, the role of the surfactant is to control the size, the distribution and the morphology. Despite the advantages, the surface functionalization with the surfactant affects the nanoparticles toxicity.[24] The most important parameters that determine the final oxide material are the temperature, the reaction time, the concentration of the reagents, the nature and concentration of the surfactant. In fact tuning these conditions, the surfactant controlled synthesis procedure produces metal oxide particles with remarkable monodispersity and astonishing particle morphology.[25] One typical example is represented by the Fe_3O_4 magnetic nanoparticles.[26] In this case, the particle diameter can be carefully controlled so that nanoparticles in the size range of 6-13 nm can be synthesized in one nanometer increments.[27] The use of surface capping agent allows modifying the nanomaterials surface by ligand exchange reactions as shown in the production of titania nanorods. In this last process, the oleic acid coating of titania

nanorods has been exchanged by capping with an alkylphosphonic acid with a result of the increments of the stability of titania dispersion.[28] It is important to point out the importance of surfactant in exchange reaction since it allows obtaining a wide range of chemical functionalities on the surface of the nanoparticles. In comparison to the surfactant assisted synthesis, the other non-aqueous process is considerably simpler. The initial reaction is characterized by a mixture of only two components, the metal oxide precursor and the organic solvent. Indeed the presence of a small number of reactant makes simpler the characterization of the final reaction solution and then the better understanding of the chemical reaction mechanisms. The main important advantage of the solvent controlled synthesis is the improvement in product purity. In the last few years the application of this process for the metal oxide nanoparticles synthesis enables the use of a large variety of precursor such as acetate, acetylacetonates, alkoxide and also a mixture of different precursors. The types of solvents that have been generally used are alcohols, ketones or aldehydes, amines, toluene. The appropriate choice of the solvent depends on its role during nanoparticles growth, the composition of the final product and the target morphology. The capping agent is represented by the organic solvent and/or the organic species formed during the reaction; its role is to limit the crystal growth and influence the particle morphology by binding the surface of the particles. The surfactant free synthesis is used in a production of metal oxide nanoparticles starting from metal halides and alcohol.[29] This synthesis, in general, occurs at low temperatures, which makes the procedure particularly useful where the nanoparticles surface needs to be functionalized with organic ligands.

Nowadays, the use of non-aqueous processes to prepare the metal oxide nanoparticles has grown immensely and ranges from simple binary metal oxides to more complex ternary, multi-metal and doped systems.

Despite the non aqueous process is defined as a chemical transformation of molecular precursor, dissolved in organic solvent, into an extended metal oxide network under exclusion of water, in some cases the used precursor salts or solvents are hydrate and the hydrolytic formation of metal oxide network cannot be excluded. This is the case

of the synthesis procedure used in this thesis, as it is reported in 3.2.1 paragraph, for ceria nanoparticles where the water derives only from the hydrate precursor. Following the definition reported by Levy et al.[30] we can include our nanoceria synthesis in non-aqueous process since that the reaction took place in organic solvent and the formation of water occurs *in situ.*

1.2.2. Films: a versatile layout for mesoporous and hybrid matrices

The sol-gel process offers the striking advantage of fabrication thin and thick coating starting from liquid-phase. This approach enables low temperature processing, easy coating of large surface, high purity and optical quality of the deposited films.[31] The coating technology is of pivotal importance in different fields such as solar cells, bio-materials, semiconductor and smart windows. Based on their functionality the coatings can be classified in several categories: optical properties (filtering, mirrors), mechanical properties (such as scratch-resistance), electrical properties (such as dielectrics and membranes) and chemical properties (such as catalysts for anti-pollution).

The dip- and spin-coatings are used to deposit the sol-gel solution on the substrate. Compared to the conventional thin films forming processes such as chemical vapour deposition (CVD), the deposition of thin films by sol-gel technology is cheaper and does not requires equipment working in vacuum conditions (for evaporation and sputtering). Moreover, the sol-gel method allows for a careful control of the deposited film in the in terms of porosity (pore volume, and size), surface area, crystal size and refractive index.

The schematic depicted in Fig.1.6 shows the five stages of the dip-coating technique (immersion, start-up, deposition, drainage and evaporation). During dip-coating, the substrate to be coated is immersed in a sol and then withdrawn with a well-defined speed under controlled temperature and atmospheric conditions. As the substrate is withdrawn upward, a layer of solution is formed on the substrate and the combination of viscous drag and gravitational forces determines the film thickness. The evaporation

of the solvent from the liquid layer promotes the condensation and the cross-linking of the inorganic precursor, thus forming a gel. The gel state can be defined as a phase constituted by a more or less condensed inorganic network within which residual solvent molecules form an interconnected liquid phase. Choosing an appropriate viscosity of the sol is possible to tune with high precision the coating thickness maintaining at the same time high optical quality of the film.[32]

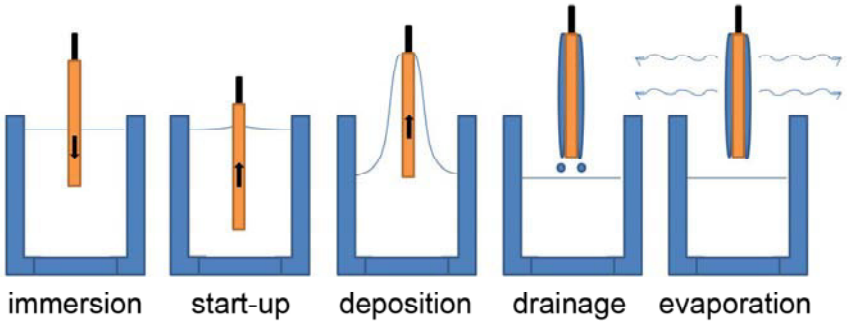

Fig.1.6 Scheme of the five stages of the dip coating process.

Although the composition of the sol cannot be affected by the evaporation, an increased concentration of the sol-gel precursors leads to the deposition of thicker films. Moreover, in the draining regime, a slower withdrawal speed produces thinner films.[33] The condensation and the evaporation rates affect the extent of further cross-linking, which occurs during the deposition and drainage stages.

Besides the depositions conditions, the sol preparation also plays a fundamental role in the chemical design of the coating. In silicate system, for example, during the solution preparation the control of ratio between water and alkoxide precursor is quite important. The different value of the molar ratio can lead to a different synthesis of products as bulk gels, films, fibers and powders. Theoretically, a molar ratio value equal to 2 is enough to complete hydrolysis and condensation, however in excess water the reaction does not go to completion. In fact, when the molar ratio H_2O: Si is $\leq$ 2, the formed gel is characterized by lower cross-linking density, which is suitable for the formation of gel fibers and coating films. On the other hand, when the molar ratio

H_2O: Si is ≥ 4, the gel shows higher cross-linking density, with tendency to remain monolithic when dried carefully.

The film deposition can be also obtained by spin-coating the solution on a rotating substrate. The spin-coating process can be divided in 4 stages (Fig.1.7): deposition, spin-up, spin-off, and gelation by solvent evaporation.[34] An excess of liquid is deposited on the surface and, during the spin-up stage, it flows radially outward, driven by centrifugal force. In the spin-off stage, excess liquid flows to the perimeter and is removed from the substrate as droplets. In the fourth stage the evaporation takes over as the primary mechanism of thinning. The coating thickness is inversely proportional to the square root of the rotation speed and also depends on the coating solution properties, like viscosity and composition. An advantage of spin coating is that a film of liquid tends to become uniform in thickness during spin-off and once uniform, tends to remain so, provided that the viscosity is not shear dependent and does not vary over the substrate.[35] This tendency arises due to the balance between the two main forces: the rotation induced centrifugal force, which drives radically outward flow, and the resisting viscous force, which acts radically inward. [36] During spin-up, the centrifugal force overwhelms the force of gravity, and the rapid thinning quickly squelches all inertial forces other than centrifugal force. Even with non flat substrate is possible to obtained very homogeneous coating thickness.[31]

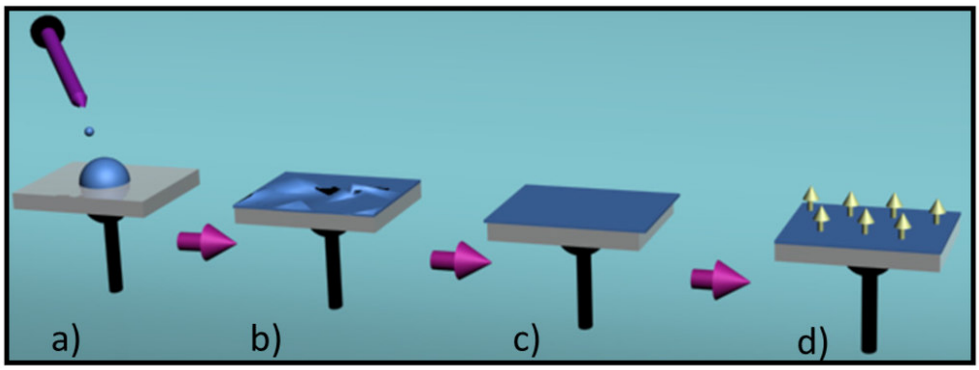

Fig.1.7 Scheme of the four stages of the dip-coating process: a) deposition b) spin-up c) spin-off d) evaporation.[37]

- Mesoporous film

The sol-gel chemistry can be combined with more sophisticated nano-synthesis techniques to get ordered and hierarchical structures.[38] The combination of sol-gel and supramolecular chemistry allows obtaining a type of nano-engineered materials known as mesoporous ordered materials. The large number of publications in different field such as microelectronics, photonics, optoelectronics, electrochemistry and biosensing testifies the importance and the potential of these materials.[39] According to IUPAC recommendations, *meso*-porous materials are characterised by the presence of ordered porosity in the 2 to 50 nm range; they can be reproducibly synthesized in a variety of shapes (thin or thick films, membranes, powders, microspheres) and compositions (silicates, transition metal oxides, etc.). The important features related to these systems is that they show a high surface area (~ 1500 $m^2 \cdot g^{-1}$) and the possibility of tuning important parameters such as pore size, shape and pore accessibility. The first self-supporting mesoporous film appeared between 1994 and 1996 and was synthesised by precipitating the precursors at the solution air interface, involving transport of the precursor in the liquid phase towards the interface.[40] The films prepared according to this procedure are inhomogeneous and have a bad optical quality, which makes them unsuitable for some applications. More recently, a new synthesis of mesoporous films from the research group at the Sandia National Laboratories (US) paved the way to the most largely employed technique for mesoporous film production. The new synthesis is based on the so called evaporation-induced self-assembly (EISA) approach. This definition was coined by Brinker and co-workers in 1999 to indicate a new synthesis process where mesophase formation is triggered by solvent evaporation rather than precipitation reactions.[41]

The so-called EISA process take place during the formation of mesoporous thin film by a spontaneous organization of chemical entities through interaction as hydrogen bonding, van der Waals forces or electrostatic forces, without any external intervention. The self-assembly process occurs when surfactant molecules with amphiphilic properties are free to organize into well-defined supramolecular

assemblies. The amphiphilic molecules are able to form, in water, a variety of supramolecular aggregates such as lamellar, spherical, cylindrical micelles and arrange in ordered structures with different symmetries such as cubic, hexagonal, gyroid etc. The symmetries and the morphology of micelles depend on the solvent to be used and the environmental conditions such as pH or electrolyte concentration. In aqueous solution, micelles formation takes place when the amount of surfactant exceeds the critical micelle concentration (CMC) leaving the hydrophilic parts of the molecule in contact with the water and segregating the hydrophobic parts within the micellar core.
In details, a typical synthesis of mesoporous thin film (Fig.1.8) is based on diluted solution containing an alkoxide or inorganic salt as a precursor and a surfactant or block-copolymer as the structure directing agent. The solvent is an alcohol (generally ethanol or methanol) and small amounts of water may be added. A delicate balance among polycondensation of the precursor, micelle formation and formation of hybrid interface is requested to achieve a self-assembly process. The solution is then deposited on a substrate by dip- or spin-coating technique and then a liquid layer is formed on the substrate, whose thickness depends on the extraction or rotational speed and the viscosity of the solution. The solvent evaporation, which occurs in the first seconds after deposition, triggers the micelle formation and their organization, leading to an organized array of templating micelles into a periodic mesophase. At the same time the formation of an interconnected network containing the organic ordered mesophase is promoted. Thermal treatments can follow the deposition step in order to promote further condensation and remove the surfactant.[42] Post treatments such as chemical grafting of functional groups or molecules on the mesopore surface can be performed in order to change the physicochemical properties or the functional properties (e.g. inclusion of metallic or semiconductor nanoparticles within the mesopores).[43]

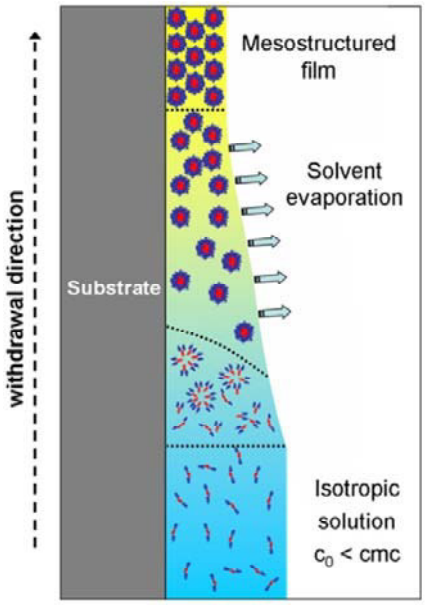

Fig.1.8 Scheme of the formation of a mesostructured film by evaporation-induced self-assembly. In the isotropic solution, the condensation is slow, the inorganic precursors only form discrete oligomers and the surfactant molecules are not yet organized in micelles. The subsequent solvent evaporation triggers the formation of surfactant-inorganic units. When the evaporation is complete, the film equilibrates its water content with the environment giving rise to an ordered mesophase. The final thermal treatment stabilizes the film.[44]

A large part of mesoporous materials is made by siliceous system because the self-assembly process can be easily controlled due to the extraordinary slow hydrolysis kinetics of the silica precursor (alkoxide, chloride). On the contrary transition metal precursors are more prone to hydrolysis, redox reactions or phase transitions involving thermal breakdown of the structure, which makes much more difficult to remove the template and create an ordered mesoporosity maintaining the optical quality of the film.[45] Despite the higher complexity of the synthesis, transition metals and transition metal oxides are of particular interest in the synthesis of mesoporous materials because often show unusual magnetic, electronic, and optical properties.[46]

The EISA process has been demonstrate to be suitable for the synthesis of the mesoporous matrix reported in paragraph 3.3, which are based on titanium, hafnium and silicon oxide. The porous structure has been used as a host for the *in situ* growth of nanoceria.

- *Hybrid films*

Most part of the traditional materials, such as metals, ceramics or organic polymers cannot fulfil the technological requirements which are necessary for the development of new applications. The possibility of combining the properties of organic and inorganic components in a unique *hybrid* material, however, opens a smart pathway to design advanced materials. A material is usually defined as *hybrid* when it is made by two constituents, one of these being organic, the other inorganic, which are both present at the molecular or nanometric scale. The organic moiety offers structural flexibility, convenient processing, tunable electronic properties, photoconductivity, efficient luminescence, and the potential for semiconducting and even metallic behaviour. Inorganic moiety provides the potential for high carrier mobilities, band gap tuning, a range of magnetic and dielectric properties, and thermal and mechanical stability. In addition, new or enhanced phenomena can also arise as a result of the interface between the organic and inorganic components.[47] Hybrid materials were developed long time ago; thousands of years ago, in fact, the mixing of organic and inorganic components was used for the production of bright and colourful paints. [48]

Nowadays, different applications are already developed in many field such as optic, electronic, ionic, mechanic, separation, protective coating, catalysis, sensing and biology.[49,50] A particular feature of hybrid materials is that their nanostructure, their degree of organization and then their properties depend not only to the chemical nature of the inorganic and organic parts, but it is also tightly correlated to their synergy. Contrary to pure solid state inorganic materials that often require a high temperature treatment for their processing, hybrid materials show a more polymer-like handling, either because of their large organic content or the formation of cross-linked inorganic networks from small molecular precursors, like in polymerization reactions.

The nature of the organic-inorganic interface has been used to classify the hybrid in two main classes. The hybrid materials belonging to the Class I show weak interactions between the two phases, such as van der Waals, hydrogen bonding or weak electrostatic interactions whilst the materials grouped in the Class II show strong

chemical interactions, like a covalent bonding, between the components.[51] The control of the nano-structure of these materials is an important issue, especially if the tailored properties are targeted. To achieve a control of the materials structure, two main approaches (or a combination of both) are usually adopted: the i*n si*tu formation of hybrid materials starting from hybrid organic-inorganic precursors (route 1) and the nano-building block assembly (NBB, route 2) as reported in Fig.1.9.

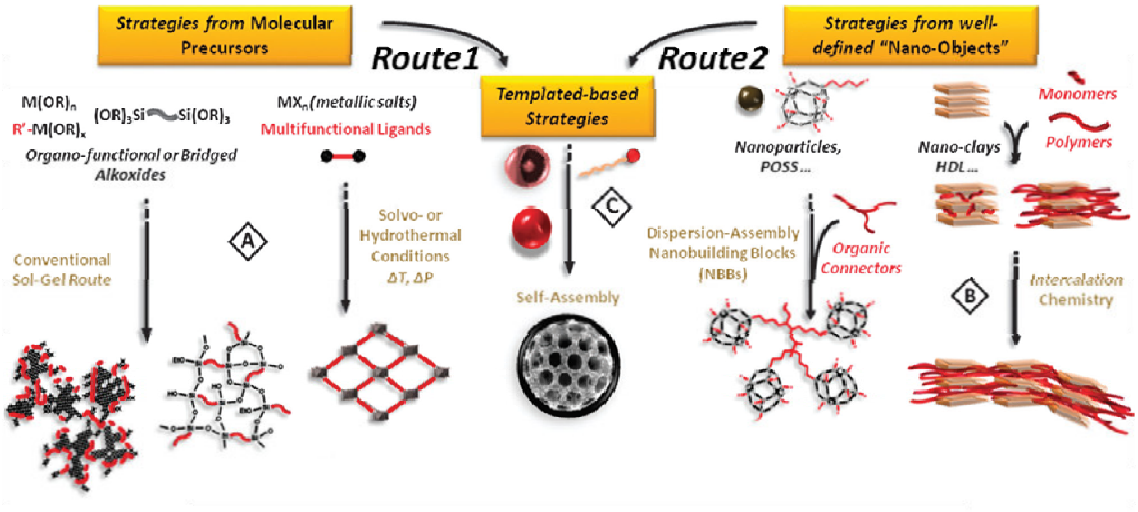

Fig.1.9 Schematic representation of the chemical routes for preparing hybrid materials. [52]

In general, the route 1 is based on an in *situ* formation of the hybrid which consists in a chemical transformation of the precursors used throughout material's preparation.[48] The sol-gel process is the most suitable route for the *in situ* hybrid materials formation, especially because the low temperature processing preserves the organic part. The conventional sol–gel pathways described in paragraph 1.2 are simple, low cost and yield amorphous hybrid materials. These materials, exhibiting infinity of microstructures, can be transparent and easily shaped as films or bulks. However, they are generally polydisperse in size and locally heterogeneous in chemical composition. The local and semi-local control of the hybrid materials structure and their degree of organization is an important issue and can be achieved by two main approaches. The first one consist in the use of bridged precursors such as silsesquioxanes, while the second one includes the use of hydrothermal synthesis performed at moderates

temperatures (20–200 °C) in polar solvents (water, formamide, toluene, alcohol, DMF).

The route 2 is characterized by the hybridization of preformed NBB such as clusters, nanoparticles or nanolayer compounds. They react with each other, *via* assembling or intercalation or intercalation and dispersion, to form the final hybrid material. In this procedure, the precursors still keep their original integrity while one or both structural units are formed from the precursors that are transformed into a new network; in fact the structural units that are used as precursor can also be found in the final material without any significant structural changes during the matrix formation. Moreover, the step-by-step preparation of these materials usually allows for a high control over their semi-local structure.[52]

In addition to the routes 1 and 2, a new way in which mesostructured hybrid network growth by organic surfactants template has been explored. One possibility is to achieve a templated surfactant growth of mesoporous hybrids by using bridged silsesquioxanes as precursors. This approach leads to a new class of periodically organised mesoporous hybrid silica with organic functionalities within the walls.[53] Another possibility is the combination of self-assembly and NBB approaches with a generation of a large variety of *hybrid* organic-inorganic interfaces via covalent bonding, complexation and electrostatic interactions.[54]

The deposition techniques of hybrid films are strictly correlated with their potential applications and they are challenging because of the different physical and chemical character of organic and inorganic components. Spin-coating is one method of depositing films of the soluble organic-inorganic hybrid on a variety of substrates including glass, quartz, sapphire, and silicon.[55,56] As the solution spreads on the substrate, it dries and leaves a deposit of the hybrid. The relevant parameters for the deposition include the choice of substrate, the concentration of the hybrid in the solvent, the substrate temperature, and the rotation speed. Other techniques for depositing the organic-inorganic *hybrids* are ink-jet printing, stamping, and spray coating, opening up the possibility of depositing these materials under a wide range of conditions and on many different types of substrates (including flexible plastic).[47]

1.2.3. Nanocomposite film

The term nanocomposite refers to a composite in which at least one of the phases shows dimensions in the nanometre range (1 nm = 10^{-9} m).[57] The unique design and the property combination of this type of nanomaterial are not founded in the conventional composites; the interactions at the interphase at the nanometer level in fact, largely improved the materials properties such as electrical conductivity, insulating behavior, elasticity, greater strength, different color, and greater reactivity.[58] There is no a clear distinction between hybrid and nanocomposite materials since the molecular building blocks and inorganic cluster in hybrid materials can be at the nanometric scale. The concept of enhancing properties and improving the materials properties through the creation of multi-phase systems is not recent. The excellent example of using synthetic nanocomposites in antiquity is represented by Mayan paintings developed in Mesoamericas. The structure of the paints consisted of a clay matrix mixed with organic colorant molecules. They also contained inclusion of metal nanoparticles, encapsulated in an amorphous silicate substrate, which were formed during heat treatment from impurities (Fe, Mn,Cr).[59] Nowadays, nanocomposites offer new technology and business opportunities for all sectors of industry, from packaging to bio-medical. According to their matrix material, the nanocomposite can be classified in three different categories:

1. Ceramic Matrix Nanocomposites (CMNC), (Al_2O_3-SiO_2, SiO_2/Ni, Al_2O_3-TiO_2, Al_2O_3/SiC, Al_2O_3/CNT.
2. Metal Matrix Nanocomposites (MMNC), (Fe-Cr/Al_2O_3, Ni/Al_2O_3, Co/Cr, Fe/MgO, Al/CNT, Mg/CNT).
3. Polymer Matrix Nanocomposites (PMNC), (Thermoplastic/thermoset polymer/layered silicates, polyester/TiO_2, polymer/CNT, polymer/layered double hydroxide).

1) Although the ceramic materials have a good wear resistance and high thermal and chemical stability, they are brittle. The CMNC are produced to overcome these limitations by increasing the mechanical properties. For example the addition of whiskers, fibres, platelets or particles in a ceramic matrix increases the fracture toughness.[60] Recently it has given more attention to the passive control of the microstructures by incorporating nanometer-size second phase dispersion into ceramic matrices. The dispersion can be characterized as intragranular or intergranular. The additive can segregates at the grain boundary with a gradient concentration or precipitates as molecular or cluster sized particles with the grains or at the grain boundaries. Niihara et al. demonstrated that the Al_2O_3 matrix has been strengthened by adding a low volume fraction (10%) of SiC particles.[61] Consequently, the incorporation of high strength nanofibres into ceramic matrices has allowed the preparation of advanced nanocomposites with high toughness and superior failure characteristics compared to the brittleness of ceramic materials. The most common method used to prepare ceramic matrix nanocomposites are conventional powder method, polymer precursor route, spray pyrolysis, vapour technique (CVD), sol-gel process, colloidal and precipitation approaches and template synthesis.

2) The MMNC are formed by ductile metal or alloy matrix (including aluminium, titanium, copper, nickel and iron) in which some nanosized reinforcement materials (including borides, carbides, nitrides, oxides and their mixture) is implanted, combining the properties of metal and ceramic such as ductility and toughness with high strength and modulus. This class of nanocomposites is suitable for production of materials with high strength in shear/compression processes and high service temperature capabilities.[62] It has attracted considerable attention as a result of availability of various type of reinforcement at competitive costs, the successful development of manufacturing process to produce MMCs with reproducible structure and properties and the availability of standard metal working method which can be used to fabricate these composites. The MMCs are of particular interest due to their easy fabrication, lower costs and isotropic properties.[63]

This type of nanocomposite is produced by different techniques such as spray pyrolysis, liquid metal infiltration, rapid solidification, vapour techniques (PVD, CVD), electrodeposition and sol-gel processes.

3) The most widely used nanocomposites are the PMNC class due to their easy production, lightweight and often ductile nature. However, they have some disadvantages such as low modulus and strength compared to metals and ceramics. Also in this case the matrix can be reinforced by adding particles, whiskers or platelets. For example to increase the heat and impact resistance, flame retardancy and mechanical strength, and decrease electrical conductivity and gas permeability with respect to oxygen and water vapour, the polymer have been filled with inorganic compounds.[64] Furthermore, the metal nanoparticles can confer unique properties, such as magnetic, electronic, optical or catalytic, which add up to other polymer properties such as processing and film forming capability.[65] Using this approach, polymers can be improved while keeping their lightweight and the ductile nature. Among the synthetic methods used to produce polymer nanocomposites the most important are intercalation of the polymer or pre-polymer from solution, *in situ* intercalative polymerization, melt intercalation, direct mixture of polymer and particulate, template synthesis, *in situ* polymerization and sol-gel process.[66]

The application of nanocomposite system includes both the generation of new material and the improvement of known devices such as sensor and coatings. The polymer based nanocomposites are in more advanced development status compared to ceramic and metal counterpart and they are in a forefront of applications. Their transition from research field to industry applications have already started and is expected to increase in the next few years.

Nanocomposites, especially belonging to the first class, have been developed in this thesis through a combination of ceramic matrix and cerium oxide nanoparticles. The prospective of this material are based on the capability of the matrix incorporating metal oxide nanoparticles to significantly improve the mechanical properties.[67,68] In fact, we would like to use thin films embedding nanoceria as a coating on plastic substrates in order to increase the surface properties.

The possibility to design nanoceria based nanocomposites has been developed by Arjun Prakash et al., incorporating ceria nanoparticles with controlled shapes and sizes into epoxy resin and testing the enhancement in impact strength of the composite; which is about four times that of the neat epoxy resin.[69]

1.2.4. Cerium oxide

Cerium belongs to the lanthanide series or rare earth elements and it is the most abundant in the earth's crust. After Europium, Cerium is the most reactive element of the rare earth metals, easily oxidizing at room temperature.[70] The electron configuration of Cerium is [Xe] $4f^1 5d^1 6s^2$ with two common valence states Ce(III) and Ce(IV). Ground state electron in a 4f orbital is responsible for its efficient reduction/oxidation (redox) behaviour. In fact, Cerium atoms can cyclically switch their oxidation state between the two ionic states, +3 (reduced) and +4 (oxidised). When Cerium is in form of oxide nanoparticles (nanoceria) there is a reduction of surface Cerium atoms to Ce^{3+} while the atoms in the core remain Ce^{4+}. Nanoceria shows high intrinsic defects and oxygen vacancies in its crystalline structure, alternating CeO_2 and CeO_{2-X} (X=0-0.5) (Fig.1.10) in the redox reaction and enabling nanoceria to show an auto-catalytic mechanism.[71] The lattice oxygen in Cerium oxide is considered to be highly mobile over a wide range of working temperatures. High oxygen mobility imparts several important properties to nanoceria such as (a) oxygen storage and release (b) promoting noble metal activity and dispersion for application in catalysis[72] (c) stabilization of chemically active Ce^{3+} oxidation state (d) reduction in band gap and solar cells.[73] Thus the creation of oxygen vacancies stabilizes the thermodynamically instable Ce^{3+} in Cerium oxide. It was shown that the oxygen vacancies could originate on the surface or subsurface and could act as catalytically active hot spots.[74]

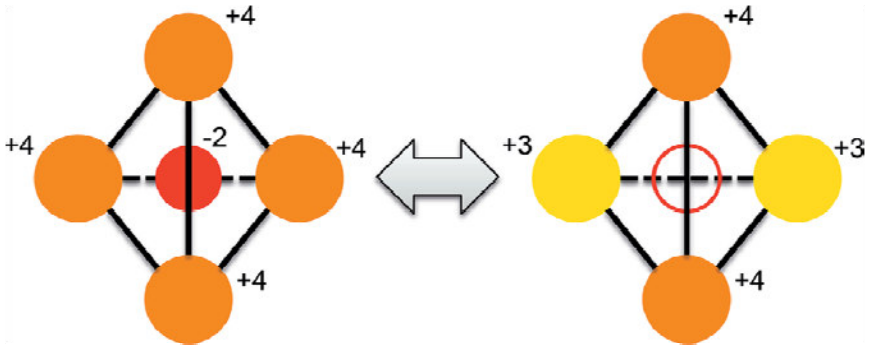

Fig.1.10 Charge redistribution in CeO_2 upon the occurrence of an oxygen vacancy.[75]

The potential catalytic activity of nanoceria depends on the surface structures, which is strongly influenced by the interaction with the environment. In this work we are interested in nanoceria as platform for biological applications where water environment plays an important role, since aqueous solution promotes the easy formation of vacancies.[76] Most of the theoretical models show that water molecules are easy adsorbed on reduced ceria surface; however the role of water in reduction or oxidation of cerium oxide at the nanoscale regime is still under debate. Watkins et al[77] and Chen et al[78], for example, hypothesized that H_2O molecules can be oxidized on the surface of ceria, while other groups disagree with this observation.[79] More detailed investigations showed that the presence of water molecules on stoichiometric ceria surface may increase the number of vacancies on ceria (111) surface.[76] Thus, the aqueous media around cerium oxide nanoparticles may favour the surface reduction and retention of Ce^{3+} oxidation state leading to the most stable structure. However, the nominal valence of Cerium atoms and the defective structure of cerium oxide are dynamic and may change spontaneously or in response to some other parameters such as temperature, presence of other ions, and oxygen partial pressure.[80]

The unique chemistry of Cerium makes ceria nanoparticles an interesting material with a dual role, either as an antioxidant or as pro-oxidant system, depending on the reaction conditions. In 2007, Korsvik et al.[81] first reported that nanoceria can also scavenge superoxide radicals efficiently. Due to the lower reduction potential (~1.52

V) of the Ce^{3+}/Ce^{4+} couple, Cerium atoms can easily switch back and forth. This interchangeable property between Ce^{3+} and Ce^{4+} makes them regenerative.[82]

Ceria nanoparticles have been tested for this unique regenerative antioxidant property in different areas of biotechnology and medicine where pathologies are associated with excessive oxidative stress. The physicochemical properties, particularly for biological applications, of cerium oxide nanoparticles are dependent on the synthetic process. In fact physical properties such as size, agglomeration status in liquid, surface charge, and coating or residual contamination of the surfactant on the surface of the nanoparticles mainly influence interactions at the nano–bio interface.[83] Moreover the Ce^{3+}/Ce^{4+} ratio on the surface also affects the surface chemistry of the nanoparticles enabling a fine control of the interactions at the interfaces with biological systems.[84]

Considering its scientific and technological interest, it is not surprising that numerous methods have been developed to synthesize nanoceria. The temperature used during the synthesis significantly affects agglomeration, crystallite size, crystal structure, surface defects, and oxidation state; so that the synthetic methods are divided into three categories[85] based on the specific ranges of temperature at which the reactions are conducted.

- **High Temperature:** nanoceria heated or calcined at >300°C (e.g., sintering, calcination, high-temperature or flame and spray pyrolysis, and thermal decomposition), no residual surfactant on nanoceria surface are expected after pyrolysis. A surfactant can be added after heat treatment to disperse the nanoparticles in solution.
- **Heated in Solvent:** nanoceria heated in solvents <100°C (e.g., thermal hydrolysis, solvothermal, and hydrothermal) with or without surfactants.
- **Room Temperature:** nanoceria synthesized at room temperature (e.g., acid or base hydrolysis or microemulsion), with or without surfactant as coordinating agent.

High-temperature methods often involve techniques such as spray pyrolysis and sol-gel synthesis followed by high temperature calcination of nanoparticles to crystallize nanoparticles and remove impurities. These processes employ ceria precursors such as cerium alkoxides or carboxylates.[70] High temperature processes produces quite large (>25 nm), crystalline and dense ceria nanoparticles which tend to form hard agglomerates during the firing. Furthermore nanoceria shows sharp facets or edges.

The nanoceria synthesized by the second method, which include hydrothermal, solvothermal, and high-temperature hydrolysis of cerium salts are smaller and show a uniform distribution in size with a spherical morphology. These nanoparticles are less agglomerated, less crystalline, and better dispersible in aqueous media.

The last categories includes wet-chemical synthetic methods for the production of nanoceria such as co-precipitation,[86,87] hydrothermal,[88] solvothermal,[84] sol–gel,[89] Pechini[90] (a modified sol–gel method using citric acid), micro emulsion[71] and reversed micelle methods.[91] These techniques are based on a source of Ce^{3+} and an oxidant: the oxidant converts the Cerium ions into the more insoluble Ce^{4+}. To obtain a well dispersed colloidal suspension of nanoparticles, one or more stabilizer can be also added before or after the nanoparticle synthesis. In the latter case, the concentration and binding strength of the stabilizer on the nanoparticle surface controls the final particle size. The most commonly stabilizers used in a nanoceria synthesis are: organic alcohols, polymers such as poly vinyl pyrrolidone, carboxylates and organic amines. The ceria nanoparticles prepared at room temperature, even in absence of surfactants or coatings, are usually weakly agglomerated and they typically show a size from 10–20 nm down to 3-6-nm. Moreover, by adjusting the pH of the nanoparticles suspension to an acidic pH, it is possible to have a stable unagglomerated (3–5 nm) or loosely agglomerated (10–12 nm) nanoparticle suspension.[92] Furthermore, the room-temperature synthesis of ceria nanoparticles produces particles that retain more surface defects with higher Ce^{3+}/Ce^{4+} ratio.[93,94]

In addition to the conventional methods described above, the treatment with microwaves is also used to synthesise nanoceria. The microwave-assisted method is characterized by rapid and homogeneous heating in contrast to the conventional one,

even thought the thermal effects are similar to those of other heating method.[95] Microwave treatment has many benefits such as rapid volumetric heating, high reaction rates, high reaction selectivity (different parts of the material can be heated creating a temperature gradients between them; for example chemo-, regio- and stereo-selectivity for organic compounds can be achieved by using this treatment), high product yield, and energy saving.[96] It is an inexpensive, facile and fast method for preparing nanocrystalline particles. Several studies on the microwave-assisted synthesis of materials, in fact, have proved that the kinetics of the organic and inorganic chemical reactions can be accelerated significantly by microwave. The irradiation under the microwave produces a better crystallinity in a shorter time. This indicates that the introduction of the microwave really can save energy and time with faster kinetics of crystallization.[97]

Regarding to the nanoceria bioactivity, the synthetic method can be selected in relationship to the biological effect, antioxidant or pro-oxidant for the cellular environment, depending on the prospected applications. In the Table 1.1 we can group the biological effects of nanoceria in three responses: pro-oxidative (red; which include inflammatory response), anti-oxidative (blue; which include beneficial effect) and neutral (green; which include no effect or ambiguous effects). Most of the nanoceria synthesized by using high temperature show pro-oxidative effects on cells, while those synthesized at low temperature in solvents or at room temperature show anti-oxidative response or ambiguous response or no effects.

Synthesis	Study	Response
High temperature	Inflammation in lungs by metal oxide nanoparticles	Pro-oxidative
	Oxidative stress of ceria nanoparticles in bronchial epithelial cells	Pro-oxidative
	Inflammatory response in mice treated with ceria nanoparticles by intratracheal instillation	Pro-oxidative
	Biodistribution and oxidative stress of commercial ceria nanomaterials	Pro-oxidative
	Toxicity of cerium oxide nanoparticles in human lung cancer cells	Pro-oxidative
	Ceria-nanoparticle-induced pulmonary inflammation in rats	Pro-oxidative
	Oxidative stress induced by ceria nanoparticles in BEAS-2B cells	Pro-oxidative
	Cerium oxide nanoparticles trigger neuronal survival	Anti-oxidative
	Cardioprotective effects of ceria nanoparticles	Anti-oxidative
	Comparison of toxicity of zinc oxide and ceria nanoparticles based on dissolution of metal ions	Anti-oxidative
	Screening nanoparticulate ceria as a diesel fuel additive	Neutral or Both
	Hazard and risk assessment of ceria nanoparticles	Neutral or Both
	Effect of ceria nanoparticles in vascular endothelial cells	Neutral or Both
Heated in Solvent	Cytotoxicity of ceria nanoparticles for *E coli*	Neutral or Both
	Nanoceria exhibits no detrimental effects on eye lens proteins	Neutral or Both
	Interaction between ceria nanoparticles and 3T3 fibroblasts	Neutral or Both
	DNA damage in human dermal fibroblasts by ceria nanoparticles	Pro-oxidative
	Brain distribution and toxicological evaluation of ceria nanoparticles	Neutral or Both
Room Temperature	Altered vascular reactivity and ischemia-reperfusion injury following ceria nanoparticle instillation	Pro-oxidative
	pH-dependent antioxidant activity of ceria nanoparticles	Anti-oxidative
	Yttria and ceria nanoparticles are neuroprotective	Anti-oxidative
	Ceria nanoparticles inhibit oxidative stress in H9c2 cardiomyocytes exposed to cigarette smoke	Anti-oxidative
	Combined cytotoxic and anti-invasive properties of redox-active nanoparticles in tumor stroma–interactions	Anti-oxidative
	Rare earth nanoparticles prevent retinal degeneration induced by intracellular peroxides	Anti-oxidative
	Protection from radiation-induced pneumonitis using cerium oxide nanoparticles	Anti-oxidative
	Auto-catalytic ceria nanoparticles offer neuroprotection to adult rat spinal cord neurons	Anti-oxidative
	Vacancy-engineered ceria nanostructures for protection from radiation-induced cellular damage	Anti-oxidative
	PEGylated Nanoceria as Radical Scavenger with Tunable Redox Chemistry	Anti-oxidative
	The role of cerium redox state in the SOD mimetic activity of nanoceria	Anti-oxidative
	Anti-inflammatory properties of cerium oxide nanoparticles	Anti-oxidative
	Rare earth oxides as nanoadditives in 3-D nanocomposite scaffolds for bone regeneration	Anti-oxidative
	Superoxide dismutase mimetic properties exhibited by vacancy-engineered ceria nanoparticles	Anti-oxidative
Synthesis	**Study**	**Response**
	Nanoceria Inhibit the Development and Promote the Regression of Pathologic Retinal Neovascularization in the *Vldlr* Knockout Mouse	Anti-oxidative

Tab.1.1 Classification of biological response of nanoceria based on the synthesis method. [85]

1.2.5. Crystallinity

In general crystal grains are the elementary building blocks of nanoparticles. Nanoparticles and nanoceria can be either mono-or polycrystalline.[70] Ceria (CeO_2) is a lanthanide oxide with the cubic fluorite crystal structure (*Fm*3*m*) (Fig.1.11a) and a cell parameter of 5.41 Å at room temperature. There are also a number of diverse oxides of cerium with composition CeO_{2-x}, where x=0-0,5. The practical reduction limit of non-stoichiometric ceria is Ce_2O_3, where all Cerium ions are found in a Ce^{3+} oxidation state. The crystal structure of Ce_2O_3 under normal conditions is the A-type sesquioxide (*P*3*m*1) (Fig.1.11b). [98]

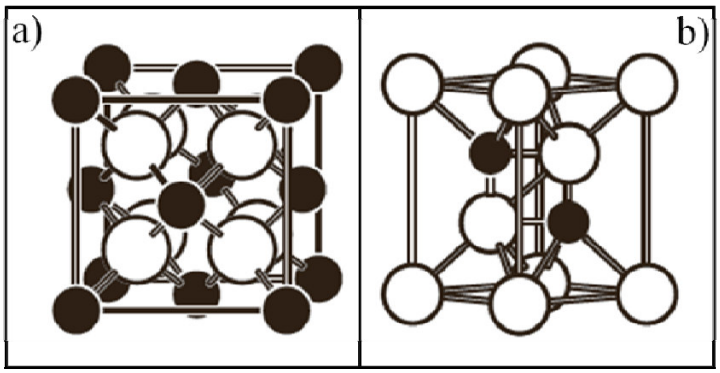

Fig.1.11 (a) The fluorite structure of CeO_2. (b) The A-type Ce_2O_3 structure. Oxygen ions are large open circles and cerium ions small filled circles.[98]

In CeO_2 fluorite crystal structure each Ce^{4+} cation is coordinated by eight nearest oxygen anions and each oxygen anion by four nearest Ce^{4+} cations (Fig.1.12). Loss of oxygen and/or its electrons forms oxygen vacancies or defects in the lattice. This defect results in lattice strain. Crystal strain is the displacement of atoms from their equilibrium lattice positions that results in a higher energy respect to the equilibrium value. The strain energy can be exploited to modulate chemical reactivity (strain-tuneable reactivity).

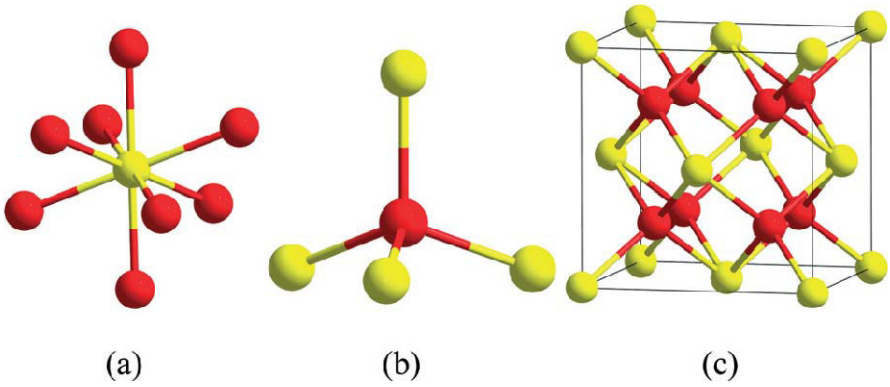

Fig.1.12 Structural analysis of ceria crystals and unit cells. Eight-fold coordinated cerium atoms (yellow) with four-fold coordinated oxygen atoms (red) in ceria crystals (a and b) and the primitive unit cell (c). [70]

The distortion may arise and change with temperature, oxygen partial pressure, doping with other ions, electrical field or surface stress. As mentioned several features of the ceria nanoparticles can be related to the presence of oxygen vacancies, whose formation involves a reversible change in the oxidation state of two Cerium ions from Ce^{4+} to Ce^{3+}.

Therefore the oxygen in form of O^{2-} leaves the lattice while $½O_2$ and the two electrons become trapped between two Cerium sites. The result is that the Ce4f band in ceria splits into two bands: an occupied Ce4f Full band and an empty Ce4f Empty band. In Ce_2O_3 structure the electronic band is similar to that of partially reduced ceria, the main difference being that the Ce4f Empty and Ce5d bands have merged together in the conduction band.[98]

Characteristic peaks of cubic nanoceria phase can be indexed in an X-ray diffractogram as (111), (200), (220) and (311) planes, from which it is possible to measure the crystallite size by using Sherrer equation. The crystallite size and the lattice strain may be affected by the thermal treatment during the annealing process, in fact Kurian et al.[99] demonstrated that nanoceria treated at low temperature (400°C) show broad peaks with low intensity and average crystallite size ranges from 4.2 to 4.9 nm. However, when the samples are annealed at high temperature (700 °C), the peaks are significantly narrower with higher intensities indicating an increase in the particle

size. Therefore the calcination at high temperature results in rapid grain growth leading to agglomeration. When nanoceria has high crystallinity, the strain and strain-induced relaxation can be reduced. However, samples with particle size below 10 nm calcined at 400 °C have characteristic strain. This may arise due to lack of crystallinity as well as the small size effect.

1.2.6. The importance of being *Nano*ceria

Nanoparticles size is a critical parameter in determining particle reactivity. Compared to the other nanostructures, nanoceria is unique in that the lattice expands as the particle becomes smaller. The lattice strain is due to the hydrolysis of Cerium ions to form hydroxides on the surface when the hydrogen atoms in the solution bind with the oxygen atoms within the lattice.[100] The hydroxyl species act as precursors to remove oxygen during a reduction process that generates Ce^{3+} cations. In small-sized particles (~3 nm), the loss of one oxygen atom creates a high lattice strain leading to an increase in the lattice parameter favouring formation of oxygen vacancies.[71] Formation of more oxygen vacancies was found to promote reducibility and reactivity of nanosized ceria, as studied by Hailstone and colleagues. By comparing different nanoceria with a size ranging from 11.8 nm to 1.1 nm,[101] it was found that the lattice expansion due to the oxygen vacancies increases with the decrease of the nanoparticle size: 1.1% for the 11.8 nm particles and 6.8% for those of 1.1 nm. A reasonable rationalization of this phenomenon is that at 1.1 nm, a large fraction of the Cerium atoms are in the fully reduced state (3+), even though the ceria nanoparticles retain a cubic lattice, and not the predicted hexagonal lattice. This explanation is in agreement with other recent findings: Seal at al.[71], in particular, showed that the concentration of Ce^{3+} increases from 17 to 44% as particle size decreases from 30 to 3 nm. To support these data, the oxygen storage capacity (OSC) of the nanoceria has been calculated and the results have proved that the size of 2-3 nm has the maximum OSC value. This suggests that nanoparticles reactivity increase monotonically with the size reduction, down to the range of 2-3 nm, while the oxygen vacancy formation energy decreases dramatically as the particle size increases. The correlation between the oxidation state and the

nanoparticles size is not linear and is strongly affected by the synthesis adopted for the preparation of nanoceria and the difficulty of producing monodisperse nanoparticles without residual surfactant or capping agent adsorbed on the surface (Table 1.2).

The particles size is a critical point in biological environment, because it controls the nanoceria uptake in the cells. It has been proved that nano-sized particles are internalised by the cells better than the micro-sized[102] and the prevalent uptake mechanism is endocytosis. Depending on the particles dimension, the cell activates different types of endocytosis: clathrin-mediated endocytosis, caveolin-mediated endocytosis and macropinocytosis.[103] As it is reported in Fig.1.13, the macropinocytosis process for particles with bigger size takes place with low rate requiring more time, while clathrin-mediated endocytosis for smaller particle occurs at higher rate requiring less time. Following the uptake, nanoceria is internalized in endosomes which then fused with lysosomes. Moreover, the acidic pH of the endo-lysosomal compartment promotes the release of nanoceria into the cytoplasm due to the inversion of the surface charge of the nanoparticles. [104]

Particle size (nm)	[Ce^{3+}]	Synthesis	Ref.
23-28	15.6	Thin Films	[105]
3	44	Microemulsion	[71]
6	29	Water based	" "
30	17	Thermal	" "
3	18	Templated on Silica aerogel	[106]
6	35.6	Wet chemical and precipitation	[107]
10	24.2	Wet chemical and precipitation	" "
5000	12.5	Wet chemical and precipitation	" "
4	6	Wet chemical and precipitation	" "
7	21	Size fractionation after emulsion synthesis	[108]
4.6	38	Size fractionation after emulsion synthesis	" "
2.6	74	Size fractionation after emulsion synthesis	" "

Tab.1.2 Size dependent changes in concentration of trivalent Cerium in nanoceria.

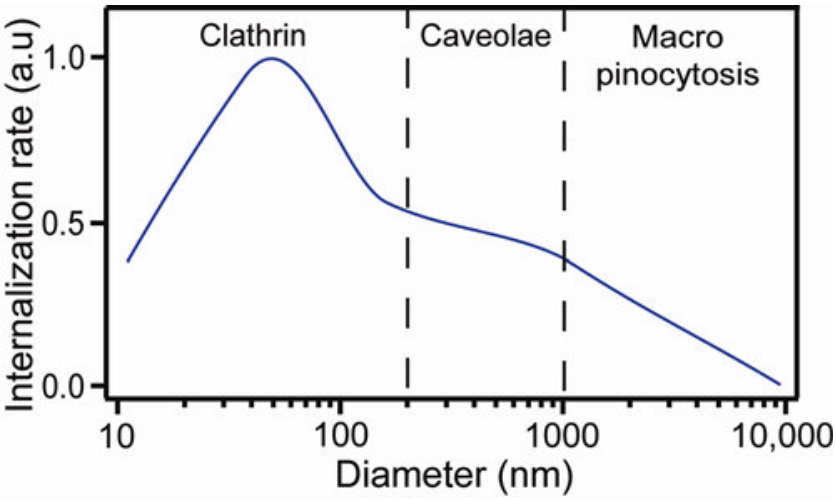

Fig.1.13 Qualitative plot of the internalization level versus the particle size.[103]

The Cerium oxide nanoparticles can also interact with a protein of biofluid, such as blood plasma, which forms a so-called protein corona shell around the nanoparticles surface. The effect of nanoparticle size on the adsorbed proteins is a complex function of protein size, shape, amino-acid composition, and 3D structure. The effect of nanoparticle size becomes significant only when it approaches the protein size that is in the sub-30 nm range.[109] For the ceria nanoparticles in the sub-10 nm range, changes in size are expected to influence the composition of the protein corona. The nanoceria size can be controlled not only by synthetic method, but also by the preparation conditions such as temperature, pH and chemical precursor. As it is shown in the section "cerium oxide" (see paragraph 1.2.4), high temperature treatments allow for the production of nanoceria with a dimension bigger than 20 nm, while low temperature syntheses often lead to smaller nanoparticles, with less toxicity and even more antioxidative properties, that may affect the interaction kinetics at the biological interface. It has been demonstrated by Nguyen et al.[110] that different size and shape nanoceria has been obtained by increasing the pH value of the reaction mixture from 7 to 14 (Fig.1.14).

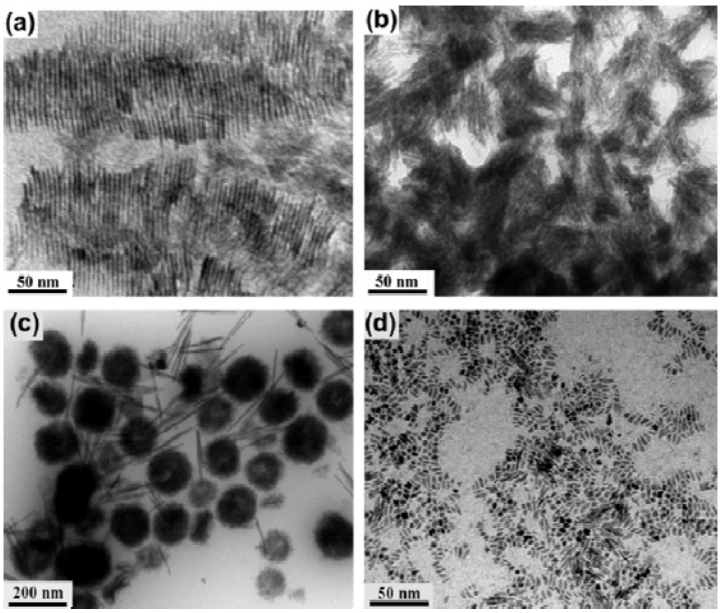

Fig.1.14 TEM images of ceria nanoparticles formed through surfactant-stabilized synthesis in controlling the shape and the size by changing the reaction parameters: (a) (b) (c) pH7 (d) pH14.[110]

Chemical composition of the nanoceria precursor can also have a strong effect on the particle size. The cerium ammonium nitrate and cerium sulphate precursors (Ce (IV) salts) give similar results while cerium nitrate leads to different results. For example, the average grain size of nanoceria prepared by Ce (III) salt is approximately 8 nm and this value becomes half when Ce (IV) salts were used. A possible explanation is that when Ce (III) salt is used as a precursor, it needs an extra step of oxidation. The reaction, therefore, is slower and the particles have enough time to grow, leading to bigger particle size.[96]

The toxicity of the nanoceria is also correlated with the nanoparticles size. In general, it is assumed that toxicity increases as the nanoparticles size gets smaller.[111] This can be explained by the fact that cellular uptake is facilitated for smaller nanoparticles and they are more likely to be distributed in the blood stream or even in the central nervous system. In addition, smaller particles have a larger surface area per mass unit in such a way that they are potentially more active.[112] However, this is not always applicable for all ceria materials; in fact, a study demonstrated that larger ceria particles can have a

higher toxicity towards eukaryotic cells and that ceria with smaller particle size can show lower toxicity which can be explained by the higher tendency of smaller nanoparticles to form agglomerates.[112] Moreover, Gaiser et al.[113] showed that nanoceria smaller than 25 nm or with a size between 1 and 5 μm does not show any significant cytotoxicity. A study by Yokel et al.[114] shows that 30 nm nanoceria did not cross the blood–brain barrier (BBB) and nanoceria remains in the body, especially in the spleen, liver, and bone marrow, for long time periods of up to 90 days. On the contrary, bigger-sized nanoceria (55 nm) tends to aggregate at the site of injection rather than being distributed in the body.[115]

1.3. Ceria-based nanocomposites

Fascinating new opportunities and challenges for materials scientists are opening due to the progresses in the synthesis of nanostructured ceria based materials. In the future, ceria based nanomaterials will play more important role in energy conversion (e.g., fuel cells and the renewable production of fuels from solar energy), energy storage (e.g., lithium-air batteries), environmental protection and remediation (e.g., treatment of toxic contaminants), as well as the new field of biomedical applications (e.g., anti-oxidant agent, free radical scavenging and immunoassays).[116] Some examples of advanced nanostructured ceria based materials are reported in this section to fully understand the potential of these systems.

The nanocomposite materials synthesized in this thesis have been prepared by using three different methods; one-pot synthesis, post grafting and a combined of top-down and bottom-up approach.

- *One pot method*

In *one pot* method several reactions are conducted in the same flask as reported in Fig.1.15. In this way it becomes possible to avoid long processes, saving not only time, but also resources (equipment, chemical compounds, solvents, etc.). In addition, the chemical yield can be increased with a reduced loss of intermediate substance.[117]

Fig.1.15 Scheme of one pot reaction.[118]

The one pot method allows producing nanocomposites with a variety of compositions. Goncalves et al.[119] reported the novel single-pot synthesis process based on sol–gel for the production of a highly transparent hybrid matrix containing CdS nanoparticles (NPs). The formation of quantum confined CdS NPs occurs simultaneously with the condensation and polymerization of the gel precursors that evolves to a macromolecular hybrid organic–inorganic network. The final material is characterized as highly transparent, homogeneous and flexible xerogel incorporating stabilized and high crystalline CdS NPs. Recently Yang et al.[120] for example developed a one pot method to prepare mesoporous CeO_2 nanoparticles. Compared to the widely used nanocasting method to prepare mesoporous metal oxides, which involves the preparation of a mesoporous template, the introduction and synthesis of metal oxides and the removal of the template, the one pot method provides a simplified way to produce mesoporous materials with large surface area and good crystallinity.

- Post synthesis grafting method

Among various surface functionalization method, the post synthesis grafting method is the most popular approach for incorporating functionalities such as chemical groups or nanoparticles on an inorganic, hybrid organic-inorganic or polymeric surfaces. The introduction of functional groups on the biomaterial surface can be, for example, achieved by a silanization of the material surface which can react with hydroxyl

groups present in a surface such as bioglass, titania or other metal oxide surface. There are many types of commercially available silane coupling agents, which are easy to react with hydroxylated surface and introduce active groups (e.g. amino group and carboxyl group) to the surface. The silanized surface can be then modified by further grafting. Although the silanization is simple and effective, the reaction conditions such as concentration of the silane and reaction time must be carefully controlled to prevent forming thick polymerized silane network on the surface. Otherwise, the bond between silane and the surface can also subject to hydrolysis in some conditions.[121] The gold -polymer nanocomposite, used for biosensing and bioimaging, is a nanosized composites that consist of gold core coated with a polymer shell (biopolymer: peptide and oligonucleotides and artificial polymer: poly-N-isopropylacrylamide) prepared by three different post grafting process: the *grafting- from*, in which a polymer chain is extended from the surface of the gold core, *grafting-to*, where a gold core is generated in polymer aggregates and *post-modification* which involves the conjugation of as-prepared gold nanoparticles with the polymer.[122] It is also reported the use of post synthetic grafting method to incorporate functional group (organometallic species, amine and thiol groups and epoxide functions) to the surface of the pore walls in order to tailor the chemical properties. However, this method quite often leads to low loadings, an inhomogeneous distribution of the functional groups and a decrease of pore volume. In fact, in order to have an effective grafting via silylation reaction, it is necessary to have a large number of surface silanols in the material. The pore walls grafted with catalytically active material have been used to investigate hydrogenation, oxidation, dehydration, hydrolysis, epoxidation and other catalytic activity.[123]

-Top down and bottom up approach

At present, a significant challenge in nanotechnology is the positioning of self-organized nano-objects onto surfaces to fabricate functional systems. In order to obtained multifunctional nanostructures with useful properties and high quality, precise control over the relative position and orientation of the nanocomponents is frequently required. Moreover, the integration and the stability of interfaces to these nanostructures is a key parameter for the success of future applications. An attractive approach for creating such a bridge between macroscopic systems and nanoscale dimensions is the texturing of macroscopic surfaces by top-down nanolithography techniques for controlling the bottom-up self-organization of preformed nano-objects. An impressive number of patterning technologies involving top-down and bottom-up approach have been developed in these last years. Several strategies rely on the formation of an ultrathin film on the surface material of interest, followed by chemical transformation/ damage on the film caused by a lithographic technique and finally the immobilization of nanoscaled components on the modified surfaces through either covalent or supramolecular interactions to form functionalized three-dimensional nanostructures.[124] Generally, the top-down and bottom-up methods are quite different concepts; the first one is an application of a writing beam, such as UV light, X-rays, electrons, to a material that responds to the radiation. The writing process can be direct or used for preparing a mold and to pattern through replica. The bottom-up approach of nanostructured films, on the contrary, is more compatible with soft-lithography techniques, such as micromolding in capillaries (MIMIC) or dip-pen nanolithography. These techniques, however, appear at the moment not well integrated with the current technologies of mass production, which are mainly top-down.[125] However, both the top-down and bottom-up methods are at the heart of such developments in nanotechnology and neither the top-down nor the bottom-up approach is superior to its competitor, as a result of the numerous fundamental breakthroughs made in the past three decades. Nowadays there are different examples showing the combination of the top-down and the bottom-up techniques. IBM, for example, developed the Airgap

technology which combines standard complementary metal–oxide–semiconductor fabrication with nanopatterning based on self organization in polymeric layers, at the industrial scale. Here, the metal wires of an electronic chip are mutually isolated by means of gaps, realized by using a nanoporous self-assembled polymer film.[126] In Fig.1.16 is reported an intimate integration of different lithographic methods used to realize chemically patterned polymer brushes and mats or even features made of nanoparticles immobilized on the brushes. The top-down approach, that is the photolithography, is performed on a photoresist deposited onto a crosslinked PS mat, and then an etching step is carried out for finely determining the feature size in polymers. Afterwards, the remaining regions of the cross-linked PS mat, with dimensions down to 10 nm, leave exposed areas of the substrate underneath, which allow endgrafted polymer brushes or PS-PMMA random copolymer to be grafted from spin-coated films. Finally, the resulting chemical pattern can be employed to site-specific immobilization of metal nanoparticles or overlying PS-b-PMMA self-assembly, completing the ultimate, bottom-up part of the method.[127] X-Rays are the most common writing tools used to pattern different types of materials such as self assembled mesoporous film and sol-gel processed materials.

In the last years a new frontier in the application of deep X-ray lithography (DXRL) has been opened. The lithographic processes, that have been applied for the fabrication of molds or structural materials in the micron-scale, have been successfully applied to functional resist, designed at the nanoscale, which are synthesized through a ‘‘soft matter’’ state by a wet-chemistry approach. This new approach represents a real opportunity to combine bottom-up and top-down technologies.

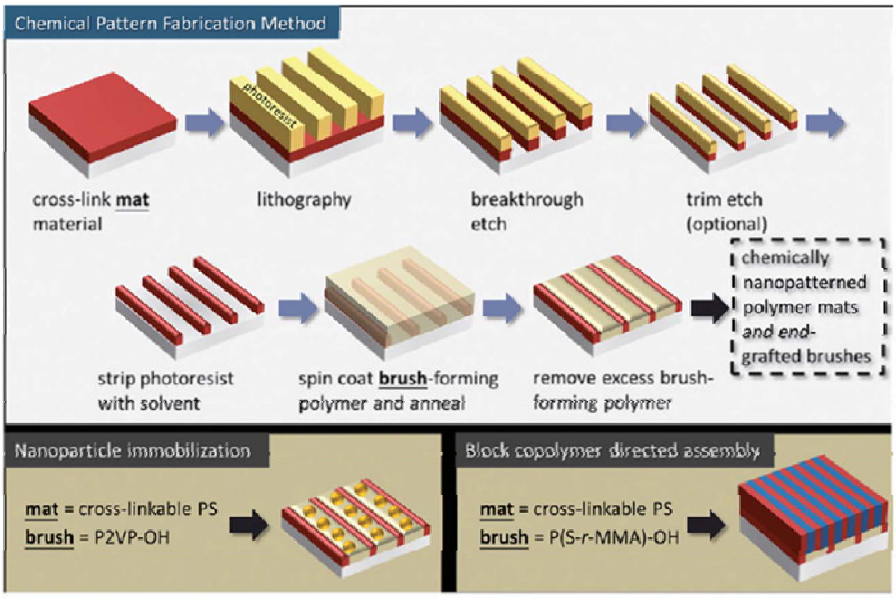

Fig.1.16 Schemes showing the formation of a chemical pattern, followed by nanoparticle immobilization or directed assembly. A film of cross-linked PS is patterned and etched, and a hydroxyl-terminated random copolymer of styrene and methyl methacrylate is grafted onto the exposed spaces of the substrate. Nanoparticle immobilization and BCP directed assembly are also enabled in this way.[127]

The combination of hard X-ray and soft-matter, in fact, offers remarkable advantages towards the improvement of the existing micro-fabrication techniques. Sol–gel materials, hybrid organic–inorganic materials, mesoporous films, and block copolymers are good candidates to be directly modified and written by hard X-rays.[128] Recently it has been reported the possibility of using X-rays to produce at the same time changes in the film porous structure, patterning its surface and promoting growth of nanoparticles in the organized mesopores or directly in the matrix. Malfatti et al.[129] reported the fabrication of pattered silica mesoporous film with gold nanoparticles (Fig.1.17) by using DXRL. X-rays, produced by highly brilliant sources of synchrotron light, induce condensation of the pore walls, remove the surfactant and partially remove the covalently bonded organic groups, at the same time gold nanoparticles are formed in a simple and controlled way. The process, which combines top-down and bottom-up technologies is direct, highly reproducible, and does not need several complicate steps for the fabrication of functional materials.

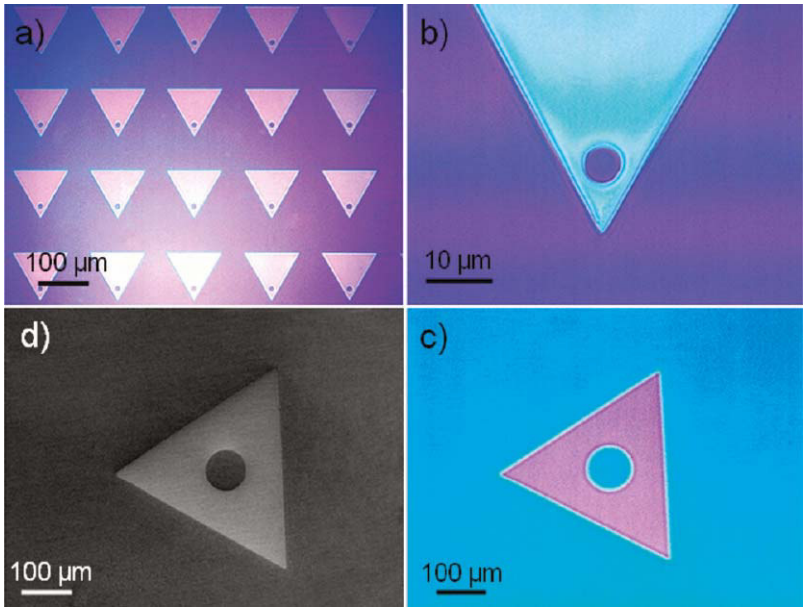

Fig.1.17 Optical images taken from as deposited films on silicon after exposition to X-rays and before etching. The pink-red color is indicative of the presence of gold nanoparticles, whereas the unexposed part of the film appears light blue. The same pattern of image c after etching is shown in the SEM image in d.[129]

A subsequent extension to bio-functionalized platforms by using DXRL would possibly open new frontiers in biomedical application. In this thesis, DXRL has been applied to fabricate a device based on antioxidant nanoparticles embedded in mesoporous matrix with a high integration of bottom-up and top-down technologies with potential application in biomedical field.

1.4. Aging and oxidative stress

One of the pilot schemes of the European Commission is to increase the average healthy lifespan of Europeans by 2 years by 2020 by improving health and quality of life with a focus on older population. Among the several theories proposed to explain aging process, has been shown that oxidative stress plays an important role in the aging which is becoming one of the challenges in the public health.[130] Denham Harman is the pioneer of the "free radical theory of aging" and he proposed the first attempts to treat or modify the rate of aging using antioxidants. Experiments, conducted in mice over the 1969– 1980 time interval, were based on the premise that

free radical reactions contribute significantly to the degradation of biological systems and they play an important role in aging. Therefore the administration of antioxidants would increase the lifespan.[131]

Oxidative stress is defined as an imbalance between the production of reactive oxygen species (ROS), reactive nitrogen species (RNS) and the cellular antioxidant defences. ROS include both free radicals (reactive chemicals with an unpaired electron in an outer orbit) and molecules containing non free radical oxygen such as hydrogen peroxide (H_2O_2), superoxide ($O_2^{\cdot -}$), singlet oxygen ($^1O_2$), and the hydroxyl radical ($^{\cdot}OH$). There are also reactive nitrogen ($NO^{\cdot}$), Iron, Copper, and Sulfur species which can increase ROS formation, impair the redox balance and then lead to oxidative stress.[132] ROS are produced in the living organism as a result of the normal metabolism. At low concentration, they contribute to the physiological cell process in a variety of cellular signaling molecules and pathways, modulating cell proliferation, apoptosis and gene expression through activation of transcription factors, like NFkappa-B. Conversely when cellular antioxidant defences are overwhelmed, there is an overproduction of ROS which can react with lipids, proteins and DNA, causing cell damage and death, aging and diseases.[133] ROS mechanism has been involved in the pathology of several diseases, such as cancer, [134] atherosclerosis, [135] rheumatoid arthritis, [136] Parkinson[137] and Alzheimer.[138] The role of free-radical reactions, not only in human disease, but also in biology, toxicology and the deterioration of food has become an area of intense interest.

The increase of ROS production is caused by endogenous and exogenous reasons. Inflammation, elevation in O_2 concentration, and increased mitochondrial leakage belong to the first one cause, instead environmental pollution, smoking, nutrition, chronic inflammation, ultraviolet light, ionizing radiation and chemotherapeutics belong to the second one.

In the body, superoxide dismutase (SOD), catalase (CAT) and glutathione peroxidase (GSH) enzymes are able, as endogenous antioxidant, to remove $O_2^{\cdot -}$ and H_2O_2 ROS. SOD has an important role in repairing cells from the damage produced by $O_2^{\cdot -}$ by accelerating its conversion to H_2O_2; meanwhile CAT is responsible for the degradation

of H_2O_2 into water and O_2. Other important H_2O_2-removing enzyme in human cells is the glutathione peroxidase. Moreover, in the human body are present low molecular mass antioxidants substances like uric acid, ascorbate (vitamin C), glutathione, tocopherol (vitamin E) and lipoic acid. [139]

When the endogenous antioxidants are not able to neutralize the ROS overproduction, the administration of exogenous antioxidant is required. An ideal antioxidant should be readily absorbed by body and should prevent or quench free radical formation or chelate redox metals at physiologically relevant levels. It should work in aqueous and/or membrane domains and effect gene expression in a positive way.

Several organic exogenous antioxidants including β-carotene, vitamins C and E, NAC, coenzyme Q10 provide protective effects in cellular and animal models. In spite of the positive effect, however, they show some limitation such as chemical instability[140], inability to cross cell membrane barriers, extensive first-pass metabolism, rapid clearance from cell and then repetitive dosing,[141] underscoring the need for alternative strategies. Treatment efficacy of diseases that respond to antioxidants should be improved by using catalytic antioxidants, which would then decrease the need for repetitive dosing.[132] Pro- and antioxidant effects of antioxidants (e.g., vitamin C) are dose dependent, and thus, more is not necessarily better.

A material that fully satisfies these requirements and has been studied in this work is represented by the nano-sized cerium oxide (nanoceria), an inorganic nanoparticle with radical scavenger property.

1.5. Enzyme activity mimicked by nanoceria

The unique chemistry of cerium oxide, which is related to the presence of the mixed valence states of Cerium (Ce^{3+} and Ce^{4+}) and the presence of oxygen vacancies, make ceria nanoparticles an interesting material with a dual role, either as an antioxidant and radical sink or as pro-oxidant system, depending on the reaction conditions. This dualism makes nanoceria suitable for a wide range of applications such as UV-blockers and filters,[142]oxidation catalysts, [143] solar cells,[73] free-radical scavengers,[82] protector of primary cells from the detrimental effects of radiation therapy, [144]

neuroprotector of spinal cord neurons[145] and blocking of retinal degeneration.[104] Recently nanoceria gained an important position in the biotechnology and therapeutics fields for its capability to mimic a multi-enzyme activity, including superoxide oxidase (SOD) and catalase (CAT) with self-regeneration properties. SOD is an enzyme that repairs cells and reduces the damage produced by superoxide, the most common free radical in the body. It catalyzes the disproportionation of superoxide to H_2O_2 and O_2. The dismutation of superoxide by nanoceria is catalyzed[146] as reported in Fig.1.18.

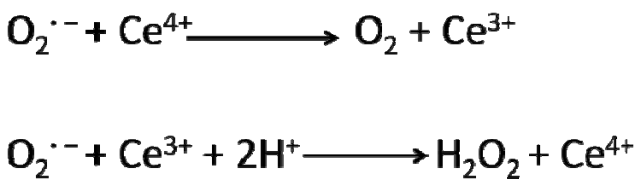

Fig.1.18 Chemical process of the dismutation of superoxide by nanoceria. [146]

Celardo et al.[147] explained in details the molecular mechanism of superoxide dismutation by nanoceria. As illustrated in Fig.1.19, using (4) as the original state, superoxide can bind to oxygen vacancy sites around two Ce^{3+} (5). Then, an electron transfers from one Ce^{3+} to an oxygen atom. Two protons from the solution can bind to the two electronegative oxygen atoms to form one molecule of H_2O_2 and be released (6). The remaining oxygen vacancy can provide a binding site for a second superoxide molecule (7). After reaction, a second H_2O_2 molecule is released and the original $2Ce^{3+}$ will be oxidized to $2Ce^{4+}$ (1). However, the reaction did not stop at this step. An oxygen vacancy sited on the surface (1) exposes a $2Ce^{4+}$ binding site for one molecule of H_2O_2 (2); hence, the H_2O_2 plays the role of a reducing agent. After the release of protons, two electrons will transfer to the two Cerium ions, to reduce them to $2Ce^{3+}$ (3). Next, oxygen is released and the fully reduced oxygen vacancy site returns to the initial state (4).

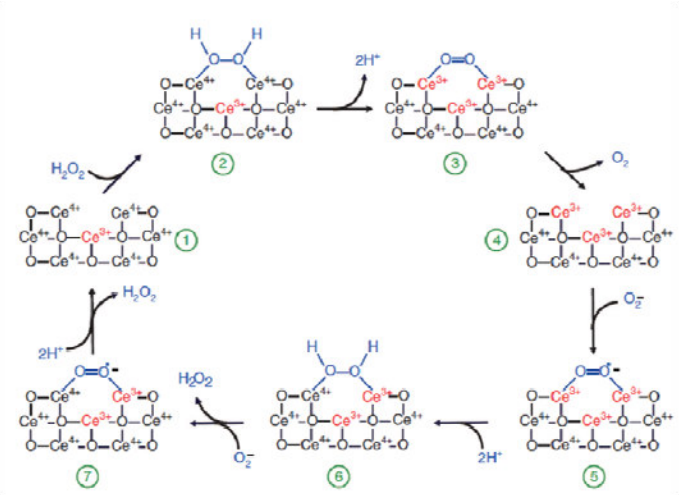

Fig.1.19 A model of the reaction mechanism for the dismutation of superoxide by nanoceria.[147]

Celardo et al. also proposed a possible molecular mechanism for the molecular mechanism of CAT (Fig.1.20). The latter is a protective enzyme found in nearly all living organisms exposed to oxygen. It is responsible for the degradation of H_2O_2, a powerful and potentially harmful oxidizing agent. The oxidative half reaction of nanoceria is shown in Fig.1.20 (1–4). One molecule of H_2O_2 reacts with Ce^{4+}, reducing it to Ce^{3+} and releasing protons and O_2. The reductive half reaction is shown in Fig.1.20 (4–6–1). A second H_2O_2 molecule can bind to the oxygen vacancy site (5), oxidize the Ce^{3+} to the initial Ce^{4+} state and release H_2O.

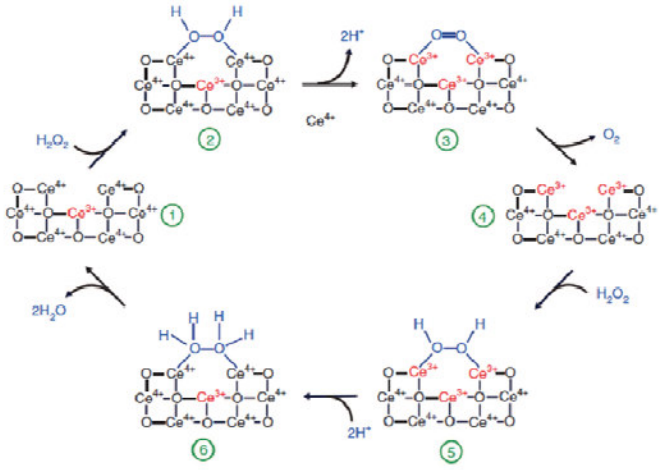

Fig.1.20 A model of the reaction mechanism for the dismutation of hydrogen peroxide by nanoceria.[147]

Thanks to both CAT and SOD like activities of nanoceria, the H_2O_2 generated in the SOD-mimetic process can enter into the catalase-mimetic dismutation cycle and produce innocuous H_2O and O_2, making nancoeria an excellent antioxidant.

The multi-enzyme mimetic activity of nanoceria could be affected by many factors such as Ce^{3+}/ Ce^{4+} ratio*, particle size, buffer species and pH conditions. In fact, ceria nanoparticles with higher ratios of Ce^{3+}/ Ce^{4+} exhibit a higher SOD-like activity, while nanoceria with lower ratios shows a CAT-like activity. Since that Ce^{3+} state increases with decreasing particle size, we can assert that nanoceria with small size dimension have more SOD than CAT -like activity.

The phosphate is a basic substance in biological systems; its impact on the activity of nanoceria should be taken into account when nanoceria is used in cell culture or animal studies. Exposure of nanoceria to phosphate buffer results in a decrease in SOD-mimetic activity and an increase in CAT-mimetic activity. However, it is not observe a change when nanoceria is exposed to other buffers such as carbonate and sulfate.[148]

The pH value can also influence the catalytic properties of nanoceria. The CAT-mimetic activity of nanoceria significantly decreases from physiological pH to an acidic pH, whereas the SOD activity of nanoceria is only slightly affected over a variety of pH changes. This suggests that at a more acidic pH, nanoceria cannot detoxify the hydrogen peroxide at the same rate as it can at neutral pH, whereas the rate for superoxide converting to peroxide is not affected. Thus, in an environment with low pH, nanoceria could be harmful. [146]

It has been shown that nanoceria is also capable to scavenge the hydroxyl radical, one of the strongest oxidants, and the nitric oxide radical.

---

* A simple visual comparison of different nanoceria samples can be used to identify what is the dominant oxidation state. A dark yellow color of the sample indicates a higher concentration of Ce^{+4} ions while a light yellow color indicates the predominance of Ce^{+3}.

1.6. Nanoceria in biomedicine: interaction nanoparticles - cellular environment

The anti-oxidant property of nanoceria has generated deep interest among researchers as a potential tool for bio-medical systems. Some pioneering studies, began in around 2006, showed that nanoceria exhibited antioxidant behaviour in cell culture models.[104,149] However, the fate of nanoparticles in the environment and their interactions with the biological systems are not fully understood yet. A change in the environment, in fact, causes a modification of the nanoparticle structures, such as size, shape and surface properties. Therefore the study of the bio-physicochemical interactions of nanoceria is of fundamental importance, since these can affect its therapeutic property.

Recently, three different nano–bio interfaces have been identified: the nanoparticle surface, the solid–liquid interface around the nanoparticle, and the solid–liquid interface's contact zone with biological substrates (Fig1.21).[150] Among these three zones, the characterization of the solid-liquid interface is a key challenge to understand the nano-bio interface. In cell culture media, specific parameters, such as pH and ionic strength, affect particle aggregation, biodegradability, zeta potential and valence of the surface layer. When nanoparticles are dispersed in a biological medium, the adsorption of bio-molecules (ions, proteins, lipids, sugars, and small molecules) is favoured, leading to the formation of bio-molecular corona.[148] The adsorption of the protein on the nanoparticles surface depends on the electrostatic, hydrophobic and specific chemical interactions between protein and the nanoparticle surface. The protein adsorption is favoured when nanoceria has a positively charged surface, whereas negatively charged surface does not significantly adsorb proteins.

The presence of functional group on the nanoparticles surface can play an important role in cell-nanoparticles interaction or cellular uptake by avoiding the protein corona formation and then the nanoparticles aggregation. Cimini et al.[151] reported that the surface functionalization with polyethylene glycol (PEG) increases nanoceria colloidal stability without affecting its catalytic activity, minimizes the attachment of opsonin

protein and suppresses uptake by macrophages, favouring the uptake of nanoceria into neuronal cells.

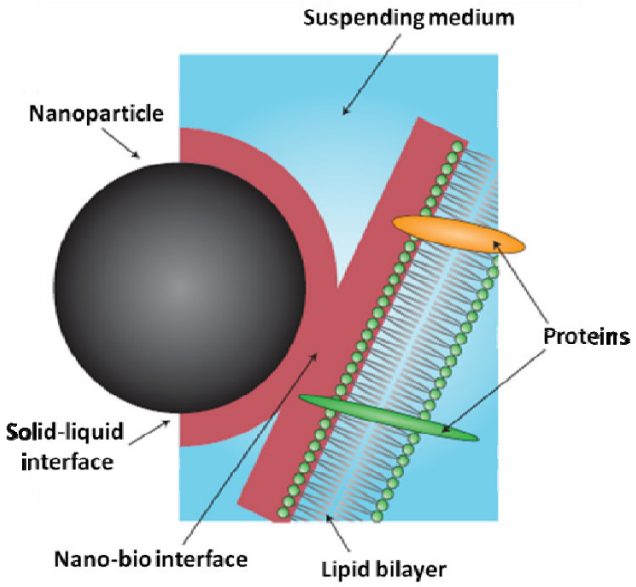

Fig.1.21 Representation of the interface between a nanoparticle and a lipid bilayer.[150]

Several types of cell have been used to explore the effects of nanoceria in cells environment. For example studying on squamous carcinoma cells and normal dermal fibroblasts, show that when nanoceria is internalized in the squamous carcinoma cells, it induces reactive oxygen species whereas it does not cause any oxidative stress in normal dermal fibroblasts. The increase in ROS generation is mainly due to the acidic environment of cancer cells because, in these conditions, nanoceria converts superoxide radical into hydrogen peroxide and does not scavenge hydrogen peroxide, therefore hydrogen peroxide is accumulated in cells.[152]

The particle size determines if the nanoceria are internalised into the cells. Smaller nanoceria (3–5 nm) are more efficiently taken up into the cells. [102] Singh et al. reported that 3-5 nm nanoceria, are internalised into keratinocyte (HaCat) cells by clathrin and caveolae mediated endocytosis pathways. The nanoceria is internalized in endosomes which then fused with lysosomes. The acidic pH of the endo-lysosomal compartment promotes release of nanoceria to the cytoplasm due to the inversion of the surface charge of the nanoparticles. Since that the diameter of nucleus pore is 9 nm

and it can also dilate to 26 nm during internalization, individual nanoceria particles of several ~3–5 nm could pass through nuclear pores if they are not aggregated in the cytosol.[153]

The changes on the nanoceria surface can also influence the cellular uptake. The surface charge has been demonstrated to play an important role in cellular uptake of nanoceria and also in its toxicity profile which is furthermore related to the cells type. Nanoceria with a positive or neutral charge enters most of the normal cell lines studied in literature, while nanoceria with a negative charge internalizes mostly in the cancer cell lines. In the study reported by Asati et al. the cellular uptake of different types of functionalized nanoceria (+, - and 0 charged) has been monitored in different cell lines. Cardiac myocytes (H9c2) and human embryonic kidney (HEK293) cells were selected as non-transformed (normal) cells, whereas lung (A549) and breast (MCF-7) carcinomas were selected as transformed (cancer) cell lines.

Results showed that positively charged nanoceria internalizes in all cell types, except for the breast carcinoma, localizing preferentially in the lysosomes and subsequently becoming toxic. In contrast, nanoceria with a negative charge is internalized only by lung carcinoma (A549) cells, but not by the breast carcinoma cells (MCF-7), thus exhibiting toxicity only to the lung carcinoma cells. Notably, the negative charged nanoceria localized into the lysosomes of the A549 cells, while they are not internalized and therefore are not toxic to the normal cells (either cardiac myocytes or human embryonic kidney cells). Surprisingly, nanoceria with neutral charge is not toxic to normal cells or cancer cells, as these nanoparticles primarily localized in the cytoplasm. These results suggest that the internalization and sub-cellular localization of nanoceria plays a critical role in the toxicity profile of this nanomaterial.[154]

In vivo studies have been done to assess the fate of nanoceria in the body and also its potential toxicity. Nanoceria (<10 nm) is well tolerated by animals without inducing overt toxicity or immune responses across a range of doses. When administered intravenously (i.v.) or intraperitoneally (i.p.), nanoceria accumulates primarily in the spleen and liver, to a lesser extent in the lungs and kidneys, but not in the heart or brain. Furthermore, nanoceria is not readily cleared, persisting in the animals for at

least 30 days without appreciable elimination through the urine or faeces, suggesting that other nanoceria destinations within the body have yet to be identified.[155]

1.6.1. Nanoceria and Parkinson' s like disease

Parkinson's disease (PD) is the second most common neurodegenerative disease after Alzheimer's disease, and affects approximately seven million individuals in the world, with an increasing occurrence as the world population ages. The clinical syndrome of PD is characterized by bradykinesia, resting tremor, rigidity, and postural instability. In addition to these motor symptoms, many patients suffer of no motor symptoms that sometimes even precede the typical movement disorder, such as hyposmia, sleep disturbances (i.e. rapid eye movement sleep behavior disorder), depression, constipation, and other dysautonomic symptoms. The motor symptoms of PD are due to the loss of dopaminergic (DA) neurons within the substantia nigra (SN).

The disease is caused by the interplay of a number of factors, such as age, genetic risk, environmental (the narcotic drug meperidine, various insecticides, solvents and agricultural chemistry), exposure to metals (iron, copper, manganese and zinc), mitochondrial dysfunction, and other conditions leading to a reactive oxygen species (ROS) overproduction.[156] Currently available pharmacological treatments based on the administration of DA biosynthesis precursors can only attenuate these symptoms; however they do not remove causes nor hinder progression of the disease. PD aetiology is complex and several nanotechnology approaches have been developed to address different aspects of this pathological condition. For example, PEGylated immunoliposomes containing tyrosine hydroxylase expression plasmids were used as gene therapy carriers able to cross the blood brain barrier and restore motor behaviour in a murine model of the disease.[157] Delivery of plasmids mediated by polyplexes for the expression of a neurotrophic factor (GDNF) was also successfully tested for biochemical, anatomical, and behavioural recovery from PD in rats.[158]

Since the relationship between PD onset and oxidative stress is increasingly recognized in medicine, antioxidants have been proposed to treat the PD and other

neurodegenerative disease. However, the use of antioxidants molecules (polyphenols, coenzyme Q10, and vitamins A, C, and E)[159] was not particularly effective. This was attributed to the limits of the antioxidants molecules: (1) they are not easily taken up directly by cells, which results in an inability to achieve satisfactory levels of antioxidants at the site of injury; (2) many antioxidants are able to scavenge only one type of reactive species, whereas neurodegenerative diseases often generate a mix of reactive species; and (3) they cannot cross the blood–brain barrier (BBB). Therefore, there is an urgent need for novel classes of antioxidants with improved properties.

Special attention has been focused on ceria nanoparticles, because they can scavenge almost all types of reactive species, with excellent regeneration ability. Moreover, they can easily cross the BBB because of their nano-size.[146] The neuroprotective effects of nanoceria to enhance the average lifespan of neuron cells were reported for the first time in 2003.[160] Nanoceria successfully protect neurons from free-radical-mediated damage initiated by UV light, H_2O_2, irradiation and excitotoxicity. [161]Schubert et al.[162] reported protection from exogenous oxidants in a neuronal cell line (HT22) in the presence of nanoceria and yttrium oxide nanoparticles. Das and colleagues[163] reported that nanoceria provides a significant neuroprotective effect on adult rat spinal cords against H_2O_2. D'Angelo et al. investigated the effects of nanoceria protection of neuronal cells against cell death induced by Alzheimer's injury on an *in vitro* human AD model.[164]

The experimental approach of this thesis is based on the paper of Ciofani et al,[165] which reported the effects of incubation of PC12 neuron-like cells with increasing concentrations of a commercial nanoceria. No evidences of toxicity related to the nanoceria PC12 treatment were found; however, an increase of differentiation in terms of neurite length was observed. Evaluation of ROS production confirmed the anti-oxidant properties of nanoceria also in these cells. Finally, the effects of nanoceria on dopamine production were studied, showing beneficial effects of nanoparticles in dopamine secretion.

1.6.2 Nanoceria in veterinary medicine

The application of nanotechnology in veterinary medicine and in animal production is gaining importance in many areas, which includes imaging, drug delivery system and tissue engineering. Several formulations of nanoparticles are already available on the market and will be more and more accessible for the application in the veterinary medicine. Nanoparticles formulation in veterinary field allows significantly reducing the dose, compared to the free drug, enabling the use of human pharmaceuticals whose application has been previously precluded because of the cost of dosing.

Nanoparticles approved for veterinary use (or in clinical trials) include emulsions, liposomes, polystyrene nanobeads, immune-stimulating complexes (ISCOMs) and inorganic particles.[166]

At present, the use of nanoceria in veterinary medicine and especially in reproductive system is limited and only few studies have been published. Chaudhury et al.[167] reported the mechanisms of interactions and the biological effects between mouse oocytes and nanoceria. The results show that nanoceria, used at low concentration and entrapped in follicular cell endocytosis and zona pellucida, protect oocytes by decreasing oxidative stress and DNA damage. However, at high concentrations, the antioxidant effect is insufficient to prevent induction of oxidative stress leading to DNA damage. Moreover nanoceria can shows its pro-oxidative activity, inducing DNA damage, when oocytes are exposed in their earlier stages of maturation, with no or immature ZP and fewer follicular cells.

Lacham-Kaplan et al.[168] performed experiments on mice with experimentally induced endometriosis followed by treatment with nanoceria. The results prove that the treatment prevents or reduces the adverse effects of endometriosis-related quality of oocytes.

Regarding to the nanoceria effects on male germs, Kobyliak et al. confirmed that the administration of citrate coated nanoceria leads to an increase of the sex hormone levels, sperm count, and quality, as well as the activation of spermatogenesis in 24-

month-old male rats. These changes are related to the improvement of serum oxidative–antioxidative balance by cerium oxide nanoparticles.

The study of the inorganic nanoparticles effects such as gold and silver in germ cells is more defused even if their potential effects have not been clearly demonstrated. Gold nanoparticles do not have any effect on porcine oocytes-cumulus complex (COC) and spermatozoa, while silver nanoparticles are detrimental for COCs but not for spermatozoa.[169] Similarly, gold and silver nanoparticles do not affect vitality and motility parameters of human spermatozoa.[170] On the contrary, bovine spermatozoa incubated with gold nanoparticles display alterations in the decondensation of chromatin[171]and exposure to silver leads to cytotoxicity and genotoxicity of testicular cells in the mouse.[172]

It is clear that the ROS play an important role in the reproductive system. The next two sub-paragraphs will briefly explain the role of ROS in the development of oocyte and spermatozoa and the importance of neutralizing their overproduction to ensure proper embryo development.

-ROS production in vitro maturation of oocytes

The oxidative stress is involved in the aetiology of defective embryo development. The contribution of the ROS sources depends on the species, the stage of the development and the culture condition.

ROS can be generated by endogenous enzymatic mechanisms involved in embryo metabolism such as oxidative phosphorylation, NADPH oxidase and xanthine oxidase and exogenous sources such as oxygen tension, presence of metallic ions, visible light, excess of glucose, amines oxidases and the freeze-thaw process, which are quite important for *in vitro* embryo maturation. The exogenous factors and culture conditions can enhance the production of oxidative stress, altering most type of cellular molecules and also inducing development of block and retardation.[173] In fact, the ROS production increases during culture at atmospheric concentration, while, when the oxygen concentration is reduced, the embryo development is enhanced.

Furthermore, the aerobic conditions may alter the defence mechanism such as GSH against oxidative stress.

The metallic cations (Fe and Cu e.g), which are often present in water or in chemical products used for culture media preparation, may have deleterious effect on oocyte development. It has been also shown that the exposure to the visible light can induce the ROS production with a consequent cellular damage such as oxidation of bases and DNA strand break.[174] Furthermore, the freeze-thaw process in IVM makes cells more sensitive to ROS, in fact after cryopreservation has been observed the DNA instability in oocyte and reduction of GSH concentration and SOD activity in spermatozoa.[175]

The proper oocyte *in vitro* maturation (IVM) depends largely on the presence of surrounding cumulus cells that rule nutritive and regulatory functions during this process. The *in vitro* culture results in higher oxygen concentrations than *in vivo* environments, leading to an increased level of reactive oxygen species (ROS) such as namely superoxide anion, hydrogen peroxide, and hydroxyl radical. The role of ROS in IVM and its influence on later embryonic development is controversial. ROS may participate in the meiotic arrest of the oocyte and they are a major cause of embryonic developmental arrest and cell death. Oxidative stress during meiotic maturation *in vitro* may induce chromosomal errors that prove undetectable in the living oocytes and whose developmental consequences may become manifest after fertilization.[176]

The importance of protecting pre-implantation embryo from oxidative damage *in vitro* is being increasingly recognized. To optimise *in vitro* embryo production, oxidative stress must be controlled during the culture, the oocyte must be protected by reducing oxygen concentration in the gaseous environment and adding supplements to the culture medium.

-ROS production in spermatozoa

Over the recent years, the generation of reactive oxygen species (ROS) in sperm preparations became a real concern because of the toxic effects that they have at high concentrations on sperm functions, and their possible involvement in male idiopathic infertility.[177] However, recent evidence strongly suggests that ROS are also needed for

the acquisition of fertilizing ability by spermatozoa and they are involved in capacitation and acrosome reaction. The balance between their production and inactivation by various scavengers is strongly controlled due to physiological conditions. Violation of this balance occurs with aging. ROS level is positively correlated with the proportion of sperm with amorphous heads, damaged acrosomes, midpiece defects, cytoplasmic droplets, and tail defects. Excessive ROS formation leads to peroxidation of phospholipids in the spermatozoa mitochondria and thus impairs their motility or can damage the sperm membrane and flagellum structure and disrupt morphology. Oxidative stress within a sperm results in protein or DNA damage that leads to a reduction in Leydig cells and synthesis of testosterone.[178]

An important source of ROS is represented by the cooling, freezing, and thawing processes, which occurs in the artificial insemination (AI). Whereby the long term storage and preservation of animal semen remains a subject of interest. Freezing and thawing, two major steps in cryopreservation of spermatozoa, have major effects on cell structure and function, in fact, the freezing/thawing cycle causes damage to the plasma membrane reduces motility and fertilizing ability of spermatozoa and induces premature capacitation and nuclear decondensation Even in the presence of cryoprotectants such as glycerol, egg yolk, and milk, significant alterations take place including those of the mitochondria and the plasma membrane.[179]

Very recently Kobyliak et al.[178] reported the effect of nanoceria on a sperm of rat. They demonstrate that after 10-day of nanoceria administration, there is a significant decrease of lipid peroxidation products in serum and increase of catalase and SOD activity, associated with increase of sperm count and improvement in quantitative sperm parameters (motility, viability, and percentage of spermatozoa). The nanoceria is also able to increase number and activation of Leydig cells, and serum testosterone.

1.7. Nanoceria in nanocomposite for biological application

Development of new nanomaterials with metal nanoparticles (Ag, Au, Cu, Rh, Pd, Ce, etc.) deposited on surfaces, embedded within pores, or encapsulated in matrices, have gained much attention in material science because of the increasing applications of such nanocomposites in medical diagnostics, in biology, chemistry, etc.

Very often, several types of inorganic nanoparticles are not suitable for medical use. To improve their biocompatibility is necessary to coat their surface and create a new nanocomposite material. The coating materials should be a natural polymer (carbohydrates, peptides), a synthetic polymer (PEG, PVA, PGA) or gold and silica, which are found to be no-toxic and relatively inert inside human body. Also, specific functionalities are normally tagged onto the surface of these coated nanoparticles in order to provide specific targeting towards certain tissues or cell types.

One common example of nanocomposite materials for biological applications is the combination of Ag and Au nanoparticles with improved bactericide properties. Since that many bacteria are antibiotics resistant, it is therefore necessary to look for new bactericidal materials. Silver nanoparticles show a broad spectrum of antibacterial activity and are no toxic for human at low concentrations.[180] When administered in large amount, the toxicity of Ag nanoparticles is increased and the biocompatibility is substantially lower than that of gold nanoparticles. To overcome this problem, the Ag nanoparticles can be deposited on the surface of highly dispersed silica (HDS) obtaining nanocomposite antimicrobial materials for medical and pharmaceutical application. Furthermore, recent advances in nanotechnologies are producing significant progress in the development of sensor systems based on nanocomposite materials. Construction of platforms for enzyme immobilization and signal detection involves progresses in nanotechnologies and nanomaterials, including the development of nanofibers, nanotubes, nanoparticles, polymeric films and membranes. Several materials can be used as a matrix of the nanocomposite systems: polymer and

carbon nanotubes, clays, surfactants, ion liquids etc. For example Hemin[†]containing Fe (III) has been inserted into a matrix made of carbon nanotubes and Nafion. The obtained nanocomposite exhibits catalytic activity towards typical hemoprotein substrates, hydrogen peroxide, nitrite ion or oxygen.[181]

In this thesis, the experimental work has been focused on the development of nanoceria-based nanocomposites whose properties has been designed for two specific applications: mesoporous nanocomposite layer for the improvement of Petri dishes performances, and nanocomposite surfaces for the controlled release of ceria nanoparticles from contact lenses. The background for these two applications is briefly described in the following paragraphs.

1.7.1. Petri dishes and ROS production

Polystyrene Petri dishes are in use in hundreds of thousands of laboratories worldwide. The glass and polystyrene version were introduced by Petri (1887)[182] and Fisk (1956),[183] respectively. Test of novel pharmaceutical and biomaterials are performed on a polystyrene Petri dishes providing fundamental information in a wide range of biomedical applications.

Very recently Sommer et al.[184] reported a critical deficiency of polystyrene Petri dishes that can affect cells culture. They quantify the performance of three types of cells, P19 (mouse embryonal carcinoma cells), L929 (murine fibrosarcoma cells) and HeLa (human cervical cancer cells) by testing their ability to climb and adhere to the vertical wall of the dishes. In order to compare the data obtained with polystyrene surface, they used different biocompatible materials, such as glass, silicon and nanocrystalline diamond. The results have been proved the lowest performance of cells on polystyrene surface. The cell's inability to climb the wall of Petri dishes has been ascribed to the superficial softening and swelling of the polymer. This should be a consequence of water incorporation into the polystyrene dishes with establishment of

[†] Hemin is a small molecule present either free or bound to hemoglobin in the bloodstream of mammals.

a stable nanoscopic interfacial layer of hydroxide ions (OH^-), which corresponds to a local raise in interfacial pH and is equivalent with an immobilized layer of Reactive Oxygen Species (ROS). The hydroxide ions are supposed to be anchored to hydronium ions (H_3O^+), which are prevalent in water due to natural dissociation, and are predominantly attracted into the polymer matrix by the negatively charged groups injected into its molecular structure for hydrophilization. The dimension of the variation in surface softening is at the nanoscale. The elasticity and the hardness of the surface dishes are very important since that they can affect the cell behaviour. Indeed cells tend to migrate towards increasing substrate stiffness showing the existence of sensing receptor of elasticity and hardness.

Another experiment was carried out by Sommer's group in order to confirm the softening and swelling of the polymer in Petri dishes. The sperm extract from human semen was cultured in standard *in vitro* fertilization (IVF) medium in four types of dishes. One of these was a standard lab dish made of hard polystyrene, while the other three were made of a purified glass (untreated, sandblasted and coated with a layer of synthetic diamond 1 micrometre thick, smooth and coated with the nanodiamond layer). After 42 hours of incubation, the percentage of sperm cells that still alive was less in polystyrene Petri dishes. The production of ROS from the polymer interaction with medium could affect the sperm viability and then explaining why IVF sometimes does not work in the way that it is expected.

In this thesis the possibility to combine a new matrix, with improved mechanical property, and nanoceria as radical scavenger has been studied. The new nanocomposites are expected to increase the performance of Petri dishes in a cell culture procedure with positive effects in cells viability.

1.7.2. Drug release by contact lenses

Most of the therapies for the treatment of ocular disease involve the use of drop to deliver the drug, which represent the 90% of ophthalmic formulation. This topical delivery system has the major advantage to minimize the side effects related to the systemic administration, since the drug can be precisely delivered, avoiding undesirable drug interactions. However, in ophthalmic formulation the drug resides for a short time in the cornea, due to its rapid clearance and the dilutive effect of tears. Moreover, the 50-100% of the applied droplets is drained through the nasolacrimal duct with a consequent absorption of the drug in the gastrointestinal tract. Consequently, the drugs have a very low bioavailability. Furthermore, non compliance and therapeutic failure of treatments with eye drops appear to be most significantly related to the geriatric population with inability to correctly instil the drops in the eye.[185]

To overcome these limitations, a drug delivery system based on contact lenses (CLs) has been proposed. The potential use of soft CLs as drug delivery platform through diffusion mechanisms has been introduced in 1965 by Wichterle.[186] In the same year Sedlacek [187]used hydrogel lenses to load and release homatrope, indicating that the drug release from CLs could potentially be more effective than topical eye drop administration. The CLs can be classified in two groups: rigid, mainly consisting of poly(methylmethacrylate) (PMMA) and soft (gelatinous), consisting mainly of polymers of hydroxyethyl methacrylate (pHEMA).[188] The FDA also classifies them as hydrophilic (adopting the suffix -filcon) or hydrophobic (adopting the suffix -focon).[189]

Therapeutic CLs consist of soft lenses formed by pHEMA polymeric matrices with or without silicone, impregnated with drugs through various techniques: soaking in a solution with the drug, molecular imprinting and loading with colloidal particles ion ligands or microemulsion gels.[190] Examples of drug-loaded CLs are: econazole (antifugal)[191], cyclosporin A (dry eye)[192], dexametasone (ocular inflammation)[193], timolol (glaucoma)[194] and ketotifen by Vistakon/Johnson&Johnson (allergic

cinjunctivitis). [195] Colloidal nanoparticles, for example, are sub-micron-sized particles dispersed into the contact lens matrix. The particles are usually made of lipid spheres (liposomes) or colloidal gold and silver[196]. Once the lenses are placed on the eye, the nanoparticles diffuse from the contact lens to the tear film.

The material used for the contact lenses has to meet specific requirements such as a balance between good wettability and permeability, and sufficient scratch resistance and flexibility. Conventional silicone materials do not meet these requirements because they are hydrophobic, but a silicon-like unit, containing a $–Si–CH_2–CH_2–$ group favor oxygen diffusion, while the presence of CH_2OH groups can be suitable for hydrophilicity.

Philipp et al.[197] prepared a new material for CLs based on Si- and Ti alkoxide by sol-gel process. $Ti(OR)_4$ has been added as a condensation catalyst to Si- source to improve the mechanical properties and to decrease shrinkage of the obtained materials. This resulted in dense, but unfortunately brittle materials, which were not machinable for lenses. Therefore, MEMO $(RO)_3–Si(CH_2)n–O–CO–CH(CH_3)QCH_2$ was introduced with hydroxy ethyl methacrylate HEMA to generate a flexible polymethacrylate based substructure via thermal polymerization. HEMA instead of MMA was selected to maintain good wettability and retain the mechanical integrity. The resulting hybrid materials exhibited balance of all the required properties.

Glycidopropyltrimethoxysilane (GPTMS) is also a good candidate for CLs, since its pre-hydrolyzation allows obtaining hydrophilic diol units, generated by a controlled epoxide ring opening. In this doctoral work, nanoceria-loaded GPTMS films have been studied as a nanocomposite device to treat degenerative ocular disease.

1.8. References

[1] Pokropivny V., Lohmus R., Hussainova I., Pokropivny A., Vlassov S. Tartu University Press.**(2007).**

[2] Savolainen K., Backman U., Brouwer D., Fadeel B., Fernandes T., Kuhlbusch T., Landsiedel R., Lynch I., Pylkkänen L. Nanosafety in Europe 2015-2025: Towards Safe and Sustainable Nanomaterials and Nanotechnology Innovations. www.ttl.fi/en/publications/electronic_publications/pages/default.aspx

[3] Lines M.G. J. Alloys Compd. **(2008)**, 449, 242-245.

[4] Gleiter H. Nanostructured Materials. **(1995)**, 6, 3-14.

[5] Ariga K., Li M., Richards G.J., Hill J.P. J. Nanosci. Nanotechnol. **(2011)**, 11, 1-13.

[6] Gusev A. I., Rempel A. A. Cambridge Int. Science. Publ. **(2004)**. 351p.

[7] Liu R., Duaya W.J., Lee S.B. Chem. Commun. **(2011)**, 47, 1384-1404.

[8] R. P. Feynman. *Eng. Sci.* **(1960)**, 23, 22-36.

[9] The Royal Society & The Royal Academy of Engineering. Nanoscience and nanotechnologies. **(2004).**

[10] Musa S. M. Computational Finite Element Methods in Nanotechnology. CRC press.**(2013)**.

[11] www.chemat.com

[12] Liao Y., Xu Y., Chan Y. Phys.Chem. Chem. Phys. **(2013)**, 15, 13694.

[13] Schmidt, H.K., Geiter, E., Mennig M., Krug H., Becker C., Winkler R.P. J. Sol-Gel Sci. and Tech. **(1998)**, **13,** 397.

[14] Vives, S., Meunier, C. In: Ceramics International. **(2008)**, 34, 37-44.

[15] Milea C.A., Bogatu C., Duta A. Bulletin of the *Transilvania* University of Braşov **(2011)**, 4, 59-66.

[16] Chiang, C., Ma, C.M., Wu D.L., Kuan H.C. J. Polym. Sci. A Polym. Chem. **(2003)**, 41, 905-913.

[17] Ko E. I. Preparation of Solid Catalysts, Ertl G., Knözinger H., Weitkamp J. (Eds.), Wiley-VCH, Weinheim. **(1999)**, p. 85.

[18] Cushing B. L., Kolesnichenko V. L., O'Connor C. J., Chem. Rev. *(***2004)**, 104, 3893.

[19] Fardad, M.A. J. Mater. Sci. **(2000)**, 35, 1835-1841.

[20] Estella, J., Echeverría, J.C., Laguna M., Garrido J.J. Microporous and Mesoporous Mater. **(2007)**, 102, 274-282.

[21] Kruis F. E., Fissan H., Peled A. J. Aerosol Sci. **(1998)**, 29, 511-535.

[22] Niederberger M., Pinna N. Metal Oxide Nanoparticles In Organic Solvents. Springer. **(2009)**.

[23] Niederberger M. Acc. Chem. Res. **(2007)**, 40, 793–800.

[24] Nel A., Xia T., Madler L., Li N. Science. **(2006)**, 311, 622 -627.

[25] Rao C.N.R., Muller A., Cheetam A.K. Nanomaterials Chemistry: Recent Developments and New Directions. **(2007)**, Wiley-VCH.

[26] Hyeon, T. Chem.Commun. (**2003)**, 927–934.

[27] Park, J.; Lee, E.; Hwang, N.-M.; Kang, M.; Kim, S. C.; Hwang, Y.; Park, J.-G.; Noh, H.-J.; Kim, J.-Y.; Park, J.-H.; Hyeon, T. Angew. Chem. **(2005)**, *44*,2872–2877.

[28] Li, X.-L.; Peng, Q.; Yi, J.-X.; Wang, X.; Li, Y.. Chem. Eur. J. **(2006),** 12, 2383–2391.

[29] Niederberger, M.; Bartl, M. H.; Stucky, G. D. J. Am. Chem. Soc. **(2002)**, 124, 13642–13643.

[30] Levy D., Zayat M. The sol-gel handbook: synthesis, characterization and applications. Wiley VCH. **(2015)**.

[31] Attia S.M., Wang J., Guangming W.U., Shen Jun., Ma J. J Mater. Sci. Technol. **(2002)**, 18,211-218.

[32] Scriven L.E. In Better Ceramics Through Chemistry III eds. C.J. Brinker, D.E. Clark, D.R. Ulrich Materials Research Society in Pittsburgh, PA, **(1988)**, 717-729.

[33] Faustini M., Louis B., Albouy P.A., Kuemmel M., Grosso D. J. Phys. Chem. C. **(2010),** 114, 7637–7645.

[34] Bomside D. E., Macosko C.W., Scriven L.E.J. Imaging Tech. **(1987)**, 13, 122.

[35] Brinker C.J., Scherer G.W. Sol-gel Science: The Physics and Chemistry of Sol-gel Processing. Academic Press.Inc. **(1990)**.

[36] Higgins B., Phys. Fluids. **(1986)**, 29, 3522.

[37] Llorens E., Armelin E., del Mar Pérez-Madrigal M., del Valle L.J., Alemán C., Puiggalí J. Polymers. **(2013)**, 5, 1115-1157.

[38] Soler-Illia G., Sanchez C., Lebeau B., Patarin J. Chem. Rev. **(2002)**, 102, 4093-4138.

[39] Innocenzi P., Malfatti L. Chem. Soc. Rev. **(2013)**, 42, 4198--4216.

[40] Brown A.S., Holt S.A., Dam T., Trau M., White J.W. Langmuir. **(1997)**, 13, 6363–6365.

[41] Brinker C.J., Sellinger Y. Lu, A., Fan H. Adv. Mater. **(1999)**, 11, 579–585.

[42] Innocenzi P., Zub L.Y., Kessler V.G. Sol-gel method for material processing. Springer. **(2008)**.

[43] Buso D, Falcaro P., Costacurta S., Guglielmi M., Martucci A., Innocenzi P., Malfatti L., Bello V., Mattei G., Sada C., Amenitsch H., Gerdova I., Hache. A. Chem. Mater. **(2005)**, 17, 4965-4970.

[44] Innocenzi P., Malfatti M., Falcaro P. Water Droplets to Nanotechnology. RSC. **(2013)**.

[45] Schüth F. Chem. Mater. **(2001)**, 13, 3184–3195.

[46] He X., Antonelli D. Angew. Chem. Int. Ed. **(2002)**, 41, 214 - 229.

[47] Mitzi D.B., Chem. Mater. **(2001)**, 13, 3283-3298.

[48] Kickelbick G. Introduction to Hybrid Materials, in Hybrid Materials: Synthesis, Characterization, and Applications (ed G. Kickelbick), Wiley-VCH Verlag GmbH & Co. KGaA, Weinheim, Germany, **(2006)**.

[49] Ruiz Hitzky E., Ariga K., Lvov Y.M., in Bio-inorganic Hybrid Nanomaterials: Strategies, Syntheses, Characterization and Applications, Weinheim. **(2007)**.

[50] Gòmez-Romero P. Sanchez C., in Functional Hybrid Materials, **(2004)**.

[51] Grosso D., Ribot F., Boissiere C., Sanchez C. Chem. Soc. Rev. **(2011)**, 40, 829–848.

[52] Sanchez C., Belleville P., Popall M., Nicolea L. Chem. Soc. Rev. **(2011)**, 40, 696–753.

[53] Corriu R.J.P., Mehdi A., Reye C., Thieuleux C., New J. Chem. **(2003)**, 27, 905 908.

[54] Steunou N., Forster S., Florian P., Sanchez C., Antonietti M. J. Mater. Chem. **(2002)**, 12, 3426–3430.

[55] Mitzi, D. B. Prog. Inorg. Chem. **(1999)**, 48, 1, 121.

[56] Mitzi, D. B.; Chondroudis, K.; Kagan, C. R. IBM J. Res. Dev. **(2001)**, 45, 29.

[57] Roy R., Roy R.A., Roy D.M. Materials Letters. **(1986)**, 4, 323-328.

[58] Cuppoletti J., Nanocomposites and Polymers with Analytical Methods. In Tech. **(2011)**.

[59] Ajayan P.M., Schadler L.S., Braun P.V. Nanocomposite Science and Technology. **(2003)**, Wiley & Sons, Incorporated, John.

[60] Becher P.F. J. Am. Ceram. Soc. **(1991)**, 74, 255-269.

[61] Nakahira A., Niihara K. J. Ceramic Society of Japan. **(1992)**, 100, 448-453.

[62] Tjong S.C., Wang G,S., Materials Science and Engineering: A. **(2004)**, 386, 48-53.

[63] Alexandre M., Dubois P. Mater. Sci. Eng. **(2000)**, 28, 1-63.

[64] Fischer H. Mat. Sci Eng. C. **(2003)**, 23, 763-772.

[65] Zavyalov S.A., Pivkina A.N. Solid State Ionics. **(2002)**, 147, 415-419.

[66] Cury Camargo P.H., Satyanarayana K.G., Wypych F. Materials Research. **(2009)**, 12, 1-39.

[67] Chatterjee A., Islam M.S. Mater. Sci. Eng. **(2008)**, 487,574-585.

[68] Yagci Y., Sangermano M., Rizza G. Macromolecules. **(2008)**, 41, 7268-7270.

[69] Arjun Prakash M., Kumar G.S., Sandeep N., Ravikumar K. IOSR-JMCE. **(2015)**, 12, 1-3.

[70] Reed K., Cormack A., Kulkarni A., Mayton M., Sayle D., Klaessig F., Stadlera B. Environ. Sci.Nano, **(2014)**, 1, 390-405.

[71] Deshpande S., Patil S., Kuchibhatla K. V. N. T., Seal S. Appl. Phys. Lett. **(2005)**, 87, 133113–133113-3.

[72] Fu Q., Saltsburg H., Flytzani-Stephanopoulos M., Science. **(2003)**, 301, 935.

[73] Corma A., Atienzar P., Garcia H., Chane-Ching J. Y. Nature Materials. **(2004)**, 3, 394.

[74] Campbell C. T., Peden C.H.F. Science. **(2005)**, 309, 713.

[75] Shoko E., Smith M.F., McKenzie R.H., J. Phys. Condens. Matter **(2010)**, 22, 223201.

[76] Fronzi M., Piccinin S., Delley B., Traversa E., Stampfl C. Phys. Chem. Chem. Phys. **(2009)**, 11, 9188.

[77] Watkins M. B., Foster A.S., Shluger A.L. J. Phys. Chem. C. **(2007)**, 111, 15337.

[78] Chen H.T., Choi Y.M., Liu M.L., Lin M.C. Chem.Phys.Chem. **(2007)**, *8*, 849.

[79] Henderson M. A., Perkins C. L.,. Engelhard M. H, Thevuthasan S., Peden C. H. F. Surf. Sci. **(2003)**, 526, 1.

[80] Mamontov E., Egami T., Brezny R., Koranne M., Tyagi S. J. Phys. Chem. B. **(2000)**, 104, 11110-11116.

[81] Korsvik C. Patil S., Seal S., Self W.T. Chem. Commun. **(2007)**, 10, 1056–1058.

[82] Karakoti A., Singh S., Dowding J.M., Seal S., Self W.T. Chem Soc Rev. **(2010)**, 39, 4422 -32.

[83] Karakoti A.S., Munusamy P., Hostetler K. Kodali V., Kuchibhatla S., Orr G., Pounds J.G., Teeguarden J.G., Thrall B.D., Baer D.R .Surf. Interface Anal. **(2012)**, 44, 882–889.

[84] Dowding JM, Das S, Kumar A., Dosani T., McCormack R., Gupta A., Sayle T.X.T, Sayle D.C., von Kalm L., Seal S., Self W.T. ACS Nano. **(2013)**, 7, 4855–4868.

[85] Karakoti A.S., Munusamy P., Hostetler K., Kodali V., Kuchibhatla S., Orr G., Pounds J.G., Teeguarden J.G., Thrall B.D., Baer D.R. Surf. Interface. Anal. **(2012)**, 44, 882-889.

[86] Chen H.I., Chang, H.Y. Ceram. Int. **(2005)**, 31, 795–802.

[87] Zhang F., Jin Q., Chan S.W. J. Appl. Phys. **(2004)**, 95, 4319–4326.

[88] Matsui K., Kyotani T., Tomita A., Adv. Mater. **(2002)**, 14, 1216–1219.

[89] Niederberger M. Acc. Chem. Res. **(2007)**, 40, 793–800.

[90] Abanades S., Legal A., Cordier A., Peraudeau G., Flamant G., Julbe A. J. Mater. Sci. **(2010)**, 45, 4163–4173.

[91] Patil S., Seal S., Yu G., Schulte A., Norwood J. Appl. Phys. Lett. **(2006)**, 88, 243110.

[92] Das S., Singh S., Dowding J.M., Oommen S., Kumar A., Sayle T.X.T., Saraf S., Patra C.R., Vlahakis Dean C., Sayle N.E., Self W.T., Seal S. Biomaterials. **(2012)**, 33, 7746–7755.

[93] Patil S., Kuiry S.C., Seal S., Vanfleet R. J. Nanopart. Res. **(2002)**, 4, 433–438.

[94] Zhang Y.W., Si R., Liao C.S., Yan C.H., Xiao C.X., Kou Y. J. Phys. Chem. B. **(2003)**, 107, 10159–10167.

[95] Horikoshi S., Serpone N. Microwaves in Nanoparticle Synthesis: Fundamentals and Applications. John Wiley & Sons. **(2013)**.

[96] Samiee S., Goharshadi E.K. Mater. Res. Bull. **(2012)**, 47, 1089–1095.

[97] Komarneni S., Roy R., Li Q.H., Mater. Res. Bull. **(1992)**, 27, 1393.

[98] Castleton C.W.M., Kullgren J., Hermansson K.J. Chem. Phys. **(2007),** 127, 244704.

[99] Kurian M., Kunjachan C. Int. Nano Lett. **(2014),** 4, 73–80.

[100] Zou H., Lin Y.S., Rane N., He T., Ind. Eng. Chem. Res. **(2004)**, 43, 3019–3025.

[101] Hailstone R.K., DiFrancesco A.G., Leong J. G., Allston T. D., Reed K.J., J. Phys. Chem. C. **(2009)**, 113, 15155–15159.

[102] Panyama J., Labhasetwara V. Adv. Drug Deliv. Rev. **(2003)**, 55, 329–347.

[103] Kelf T.A., Sreenivasan V.K.A., Sun .J, Kim E.J., Goldys E.M., Zvyagin A.V. Nanotechnology. **(2010)**, 21, 285105.

[104] Chen J., Patil S., Seal S., McGinnis J.F. Nat. Nano. **(2006)**, 1, 142–50.

[105] Patsalas P., Logothetidis S., Sygellou L., Kennou S. Phys. Rev. B. **(2003)**, 68, 035104.

[106] Dutta P., Pal S., Seehra M.S., Shi Y., Eyring E.M, Ernst R.D. Chem. Mater. **(2006)**, 18, 5144.

[107] Kohler N., Fryxell G.E., Zhang M.Q.J. Am. Chem. Soc. **(2004)**, 126, 7206.

[108] Tsunekawa S., Sivamohan R., Ito S., Kasuya A., Fukuda T., Nanostruct Mater. **(1999)**, 11, 141.

[109] Walkey C., Das S., Seal S., Erlichman J, Heckman K, Ghibelli L., Traversa E., McGinnis J.F., Self W.T. Environ. Sci.: Nano. **(2015)**, 2, 33.

[110] Nguyen T.D., Dinh C.T., Mrabet D., Tran-Thi M.N., Do T.O. J. Colloid Interface Sci. **(2013)**, 394, 100–107.

[111] Nemmar A., Holme J.A., Rosas I., Schwarze P.E., Alfaro- Moreno E., Biomed. Res. Int. **(2013)**, ID 279371, 22.

[112] Gagnon J., Fromm K. M. Eur. J. Inorg. Chem. **(2015)**, 4510–4517.

[113] Gaiser B.K., Fernandes T.F., Jepson M.A., Lead J.R., Tyler C.R., Baalousha M., Biswas A., Britton G.J., Cole P.A., Johnston B.D., Ju-Nam Y., Rosenkranz P., Scown T.M., Stone V., Environ. Toxicol. Chem. **(2012)**, 31, 144–154.

[114] Yokel R.A., Au T.C., MacPhail R., Hardas S.S., Butterfield D.A., Sultana R., Goodman M., Tseng M.T., Dan M., Haghnazar H., Unrine J.M., Graham U.M., Wu P., Grulke E.A., Toxicol. Sci. **(2012)**, 127, 256–268.

[115] Yokel R.A., Tseng M.T., Dan M., Unrine J.M., Graham U.M., Wu P., Grulke E. A., Nanomed.Nanotechnol. **(2013)**, 9, 398–407.

[116] Sun C., Li H., Chen L. Energy Environ. Sci. **(2012)**, 5, 8475–8505.

[117] Tan, Y.H., Li, J.X., Xue, F.L., Qi, J., Wang, Z.Y. Tetrahedron. **(2012)**, 68, 2827-2843.

[118] Sydnes M.G. Current Green Chem. **(2014)**, 1, 216-226.

[119] Gonçalves L.F.F.F., Kanodarwala F.K., Stride J.A., Silva C.J.R., Gomes M.J.M. Optical Mater. **(2013)**, 36, 186–190.

[120] Yang N., Pang F., Ge J. J. Mater. Chem. A. **(2015)**, 3, 1133.

[121] Qiu Z.Y., Chen C., Wang X.M., Lee S. Regenerative Biomaterials. **(2014)**, 67–79.

[122] Kumar C.S.S.R. Nanocomposites.Wiley. **(2010)**.

[123] Merhari L. Hybrid Nanocomposites for Nanotechnology. Springer. **(2009)**.

[124] Iqbal P., Preece J.A., Mendes P.M. Supramolecular Chemistry: From Molecules to Nanomaterial. John Wiley & Sons, Ltd **(2012)**.

[125] Malfatti L., Marongiu D., Costacurta S., Falcaro P., Amenitsch H., Marmiroli B., Grenci G., Casula M.F., Innocenzi P. Chem. Mater. **(2010)**, 22, 2132–2137.

[126] http://www-03.ibm.com/press/us/en/pressrelease/21473.wss.

[127]Liu C.C., Han E., Onses M.S., Thode C.J., Ji S., Gopalan P., Nealey P.F., Macromolecules. **(2011)**, 44, 1876.

[128] Innocenzi P., Malfattia L., Falcaro P. Soft Matter. **(2012)**, 8, 3722.

[129] Malfatti L., Marongiu D., Costacurta S., Falcaro P., Amenitsch H., Marmiroli B., Grenci G., Casula M.F., Innocenzi P. Chem. Mater. **(2010)**, 22, 2132–2137.

[130] Sanchez M.A., Favier I.H., Meunier N., Venneria E., O'Connor J.M., Maiani G., Coudra C., Roussel A.M. Eur. J. Clin. Nutr. **(2005)**, 59, S58–S62.

[131] Floyd R.A., Towner R.A., He T., Hensley K., Maples K.R. Free Radic. Biol. Med. **(2011)**, 51, 931–941.

[132] Poljsak B., Šuput D., Milisav I. Oxid. Med. Cell. Longev. **(2013)**, Article ID 956792, 1-11.

[133] Giordano F.J. Clin Invest. **(2005)**, 115, 500-508.

[134] Sabharwal S.S., Schumacker P.T. Nat.Rev.Cancer . **(2014)**, 14, 709–721.

[135] Victor M.V. Syst. Biol. Free Rad. and Antiox. **(2014)**, 53, 1305-1323.

[136] Hitchon C. A., El-Gabalawy H.S. Arthritis Res. Ther. **(2004)**, 6, 265-278.

[137] Zuo L., Motherwell M.S. Gene. **(2013)**, 532, 18-23.

[138] Dumont M., Beal M.F. Free Radic Biol Med. **(2011)**, 51, 1014-26.

[139] Aruoma O.I. JAOCS, **(1998)**, 75, 199-212.

[140] Stevanovìc M., Savìc J., Jordovìc Br., Uskokovìc D., Colloids Surf. B. **(2007)**, 59, 215–223.

[141] Suntres Z.E. J. Toxicology. **(2011)**, Article ID 152474, 1-16.

[142] Anupriya K., Vivek E., Subramanian B.J. Alloys Compd. **(2014)**, 590, 406-410.

[143] Tschope A., Liu W., Stephanopoulos M.F., Ying J.Y. J. Catal. **(1995)**, 157, 42-50.

[144] Tarnuzzer R.W., Colon J., Patil S., Seal S. Nano Lett. **(2005)**, 5, 2573–7.

[145] Das M., Patil S., Bhargava N., Kang J.F., Riedel L.M., Seal S. et al. Biomaterials. **(2007)**, 28, 1918–25.

[146] Xu C., Qu X. NPG Asia Materials. **(2014)**, 6, 1-16.

[147] Celardo I., Pedersen J. Z., Traversa E., Ghibelli L. Nanoscale. **(2011)**, 3, 1411–1420.

[148] Kumar A., Das S., Munusamy P., Self W., Baer D.R., Saylee D.C., Seal S. Environ. Sci. Nano. **(2014)**, 1, 516.

[149] Rzigalinski B.A., Meehan K., Davis R. M., Xu Y., Miles W.C., Cohen C.A. Nanomedicine. **(2006)**, 1, 399–412.

[150] Nel A.E., Madler L., Velegol D., Xia T., Hoek E.M.V., Somasundaran P., Klaessig F., Castranova V., Thompson M. Nat. Mater. **(2009)**, 8, 543–557.

[151] Cimini A., D'Angelo B., Das S., Gentile R., Benedetti E., Singh V., Monaco A. M., Santucci S., Seal S. Acta Biomater. **(2012)**, 8, 2056–2067.

[152] Alili L., Sack M., Karakoti A.S., Teuber S., Puschmann K., Hirst S. M., Reilly C.M., Zanger K., Stahl W., Das S. Biomaterials. **(2011)**, 32, 2918–2929.

[153] Singha S., Kumarb A., Karakoti A., Seal S., Selfa W.T. Mol Biosyst. **(2010)**, 6, 1813–1820.

[154] Asati A., SantraS., Kaittanis C., Perez J.M. ACS Nano. **(2010)**, 4, 5321–5331.

[155] Wason M.S., Zhao J. Am. J. Transl. Res. **(2013)**, 5, 126-131.

[156] Antony P.M.A., Diederich N.J., Kruger R., Balling R., FEBS J. **(2013)**, 280, 5981–5993.

[157] Zhang Y., Schlachetzki F., Zhang Y.F., Boado R.J., Pardridge W.M. Hum. Gene. Ther. **(2004)**, 15, 339-350.

[158] Gonzalez-Barrios J.A., Lindahl M., Bannon M.J., Martínez, Gonzalo Flores V.A., Navarro- Quiroga I. , Trudeau L.E. , Aceves J., Martinez-Arguelles D.B., Ismael Jiménez R.G.V., Martinez-Fong S.J.D., Mol. Ther. **(2006)**, 14, 857-865.

[159] Sutachan J.J., Casas Z., Albarracin S.L., Stab B.R.2nd., Samudio I., Gonzalez J., Morales L., Barreto G.E. Nutr. Neurosci. **(2012)**, 15, 120-6.

[160] Ellison A, Fry R, Merchant S., Kuiry S.C., Patil S., Seal S., Rzigalinski B. J. Neurotrauma **(2003)**, 10, 1105.

[161] Rzigalinski B.A., Meehan K., Davis R.M., Xu Y., Miles W.C., Cohen, C.A. Nanomedicine. **(2006)**, 1, 399–412.

[162] Schubert D., Dargusch R., Raitano J., Chan S.W. Biochem. Biophys. Res. Commun. **(2006)**, 342, 86–91.

[163] Hickman J.J., Das M., Patil S., Bhargava N., Kang J. F., Riedel L., Seal, S.Tissue Eng. **(2007)**, 13, 873–874.

[164] D'Angelo B., Santucci S., Benedetti E., Di Loreto S., Phani R. A., Falone S., Amicarelli F., Ceru M. P., Cimini A. Curr. Nanosci. **(2009)**, 5, 167–176.

[165] Ciofani G., Genchi G.G., Liakos I., Cappello V., Gemmi M., Athanassiou A., Mazzolai B., Mattoli V. Phar. Res. **(2013)**, 30, 2133–2145.

[166] Underwood C., van Eps A.W. The Veterinary J. **(2012)**, 193, 12–23.

[167] Chaudhury, K., Babu, N.K., Singh, A.K., Das, S., Kumar, A., Seal, S. Nanomed. Nanotechnol. **(2013)**, 9**,** 439-48.

[168] Lacham-Kaplan O., Trounson A. Reprod. Biol. Endocrinology. **(2008)**, 6, 58.

[169] Tiedemann D., Taylor U., Rehbock C., Jakobi J., Klein S., Kues W.A., Barcikowski S., Rath D. Analyst. **(2014)**, 139, 931-42.

[170] Moretti E., Terzuoli G., Renieri T., Iacoponi F., Castellini C., Giordano C., Collodel G. Andrologia. **(2013)**, 45, 392-6.

[171] Zakhidov S.T., Pavlyuchenkova S.M., Samoylov A.V., Mudzhiri N.M., Marshak T.L., Rudoy V.M.,. Dement'eva O.V, Zelenina I. A., Skuridin S. G., Yevdokimov Yu. M. Biology Bulletin. **(2013)**, 40, 493-9.

[172] Asare N., Instanes C., Sandberg W.J., Refsnes M., Schwarze P., Kruszewski M., Brunborg G. Toxicology. **(2012)**, 291, 65-72.

[173] Guerin P. El Mouatassim S. Menezo Y. Hum. Reprod. update. **(2001)**, 7, 175-189.

[174] Beehler B.C., Przybyszewski J., Box H.B., Kulesz-Martin M.F. Carcinogenesis. **(1992)**, 13, 2003- 2007.

[175] Bilodeau J.F., Chatterjee S., Sirard M.A., Gagnon C. Biol.Reprod. **(1999)**, 60, 102.

[176] Cetica P. D., Pintos L. N., Dalvit G. C., Beconi M. T. IUBMB Life. **(2001)**, 51, 57–64.

[177] de Lamirande E., Gagnon C. Hum. Reprod. **(1995)**, 10, 15-21.

[178] Kobyliak N.M., Falalyeyeva T.M., Kury O.G., Beregova T.V., Bodnar P.M., Zholobak N.M., Shcherbakov O.B., Bubnov R.V., Spivak M.Y. The EPMA Journal. **(2015)**, 6, 2-22.

[179] Chatterjee S. Gagnon C. Mol. Reprod. Dev. **(2001),** 59, 451- 458.

[180] Jin Y., Zhao X. Springer, edited by Tomas J. Webster, ISBN978-0-387- 78607-0, New York, USA. **(2009)**, 19-31.

[181] Shumyantseva V.V., Suprun E.V., Bulko T.V., Dobrynina O.V., Archakov A.I. Biomed. Chem. **(2010)**, 4, 25–36.

[182] Petri RJ. Centralblatt für Bacteriologie und Parasitenkunde. **(1887)**, 1, 279-280.

[183] Fisk RT. Disposable culturing device. U.S. Patent 2,874,091, **(1956)**.

[184] Sommer A.P., Haddad M.K., Fecht H.J. J. Bionic Eng. **(2012)**, 9, 353-357.

[185] Carvalho I.M., Marques C.S., Oliveira R.S., Coelho P.B., Costa P.C., Ferreira D.C. J. Control. Release. **(2015)**, doi: 10.1016/j.jconrel.2015.01.023.

[186] Wichterle O., Lim D. Nature. **(1960)**, 185, 117-118.

[187] Sedlacek J. Cesk. Slov. Oftalmol. **(1965)**, 21, 509-512.

[188] Nicolson PC, Vogt J. Biomaterials.**(2001)**, 22, 3273-83.

[189] FDA U. No Title. 2014. Available http://www.fda.gov/downloads/MedicalDevices/.../ucm080960.pdf.

[190] White C.J., Tieppo A., Byrne M.E. J. Drug Del. Sci. Tech., **(2011)**, 21, 369-384.

[191] Ciolino J.B., Hudson S.P., Mobbs A.N., Hoare T.R., Iwata N.G., Fink G.R., Kohane D.S. **(2011)**, 52, 6286-91.

[192] Peng C.C., Chauhan A. J. Control. Release. **(2011)**,154, 267-74.

[193] Kim J., Peng C.C., Chauhan A. J. Control. Release. **(2010)**, 148, 110-6.

[194] Jung H.J., Abou-Jaoude M., Carbia B.E., Plummer C., Chauhan A. J. Control. Release **(2013)**, 165, 82-9.

[195] Soluri A., Hui A., Jones L. Optom. Vis. Sci. **(2012)**, 89, 1140-9.

[196] Sung A.Y, Kim T.H. J. Nanosci. Nanotechnol. **(2012)**, 12, 5210-5.

[197] Philipp G., Schmidt H., J. Non-Cryst. Solids. **(1984)**, 63, 283–292.

2 Characterization techniques

The antioxidant property of nanoceria is strictly correlated to the nanoparticles size, crystalline structure and the environment which is in contact. The different interactions of nanoceria with cells and inorganic matrix, developed in this thesis, need a detailed investigation with several characterizations, ranging from spectroscopic to microscopic techniques. This chapter, which is divided in three main parts (spectroscopic, microscopic and other techniques), provides the fundamentals of the characterization techniques used in the experimental part. Using a multi-technique approach, different features of the materials such as morphology, composition, presence of specific bonding, fate of nanoparticles into the cells and cells viability have been detected.

Fourier-transform infrared spectroscopy (FTIR) is always utilized in order to provide information on the presence of specific chemical species and bindings within the film and the nanoparticles. A powerful technique for investigating the structure of nanoparticles and the mesoporous materials is the X-ray diffraction spectroscopy (XRD), which provides information related to the crystalline or amorphous structure and also the dimension of the crystallite which in our cases correspond to the nanoparticles dimension. In association with XRD, transmission electron microscopy (TEM), gives direct images of the mesostructure of the films and the nanoparticles distribution in the matrix with nanometric resolution. This last technique, together with Raman and confocal microscopy has been also employed to study the fate and the distribution of nanoceria inside the cells in order to understand its localization in a different cellular compartment and its antioxidant effect. Other techniques, such as dynamic light scattering (DLS) and atomic force microscopy (AFM) have been used to the investigation of nanoparticles aggregation in solution and in matrix respectively.

Dott.ssa Alessandra Pinna
Ceria nanoparticles as smart platform for biomedical applications
Tesi di Dottorato in Scienze e Tecnologie Chimiche
Indirizzo: *Nanochimica, Nanomateriali e Materiali funzionali* -XXVIII Ciclo
Università degli Studi di Sassari- Facoltà di Chimica e Farmacia

2.1 Spectroscopic techniques

The spectroscopy studies the absorption and the emission of the light and the other radiation by the matter covering a sizable fraction of the electromagnetic spectrum. Its processes are dependent by wavelength of the radiation. Spectroscopic techniques are extremely sensitive and non destructive and widely used to detect molecules, to measure the concentration of a species in solution, and to determine molecular structure. In the following paragraph FTIR, UV-*vis*, XRD, SAX, Raman and Ellipsometry spectroscopy have been described.

2.1.1 Fourier transform infrared (FTIR)

Infrared spectroscopy allows studying of any sample in any physical state. The main goal of IR spectroscopic analysis is to determine the chemical functional groups in the compounds by exploiting the IR radiation interaction with the matter. The infrared portion of the electromagnetic spectrum ranges from 12800 to 10 $cm^{-1}$and it is divided into three regions: the near-, mid- and far- infrared, named for their relation to the visible spectrum. The far-infrared, (400–10 cm^{-1}) lying adjacent to the microwave region, has low energy and may be used for rotational spectroscopy. The mid-IR region (4000–400 cm^{-1}) may be used to study the fundamental vibrations and associated rotational-vibrational structure. The higher energy near-IR (14000–4000 cm^{-1}) can excite overtone or harmonic vibrations.

This technique is based on the vibrations of the atoms of a molecule. The essential component of optical hardware in a FTIR spectrometer is the interferometer. This component simultaneously allows source radiation of all wavelengths to reach the detector. In Fig. 2.1 is reported how the interferometer works: radiation from the source is focused on a beam splitter that transmits half of the radiation to a fixed mirror, while reflecting the other half to a movable mirror. The radiation recombines at the beam splitter, where constructive and destructive interference determines, for each wavelength, the intensity of light reaching the detector. As the moving mirror

changes position, the wavelengths experiencing maximum constructive interference and maximum destructive interference also change. The signal at the detector, called *interferogram*, shows intensity as a function of the moving mirror position, expressed in units of distance or time. The *interferogram* is mathematically converted, by a process called a Fourier transform, to the normal spectrum (also called a frequency domain spectrum) of intensity as a function of the radiation energy.

Each band in an infrared spectrum can be assigned to a particular deformation of the molecule, the movement of a group of atoms, or the bending or stretching of a particular bond, however many vibrations may vary by hundreds of wavenumbers even for similar molecules. The mid-infrared spectrum is the range taken into account to characterize the materials engineered in this thesis. It shows the bands related to X-H stretching like O-H, C-H and N-H stretching; the triple-bond, the double-bond and the fingerprint.

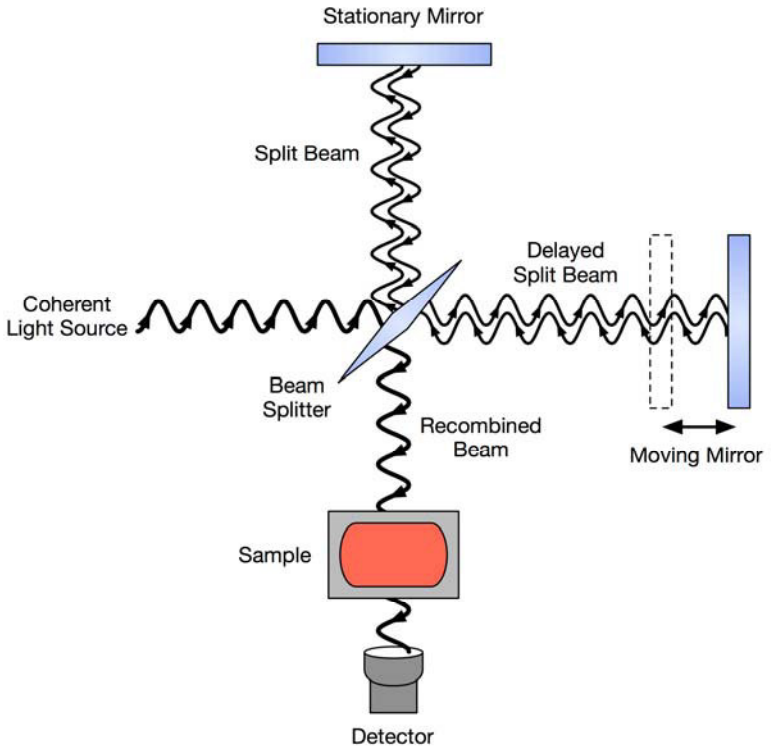

Fig.2.1Block diagram of an interferometer.

The instrument used for the experimental part of this thesis is a Bruker infrared microscope Hyperion 2000 coupled with Vertex 70 interferometer and optimized for mid-ir (4000-400 cm^{-1}) measurements.

2.1.2 Uv-visible (Uv-*vis*)

Ultraviolet-Visible (UV-Vis) spectroscopy is a standard and cheap technique to characterize the absorption properties of solid and liquid samples. In typical UV-Vis absorption spectra, the absorbance is reported as a function of the wavelength transmitted through the sample as it is shown in the equation (Equ. 2.1).

$$A = -\log_{10} T = \log_{10}(I_0/I)$$

Equ.2.1

A block scheme of a double beam spectrometer is shown in Fig.2.2.[1] Double-beam instruments are more versatile than single-beam instruments, being useful for both quantitative and qualitative analyses. A chopper, similar to that shown in the figure, controls the radiation path, alternating it between the sample, the blank, and a shutter. The signal processor uses the chopper's known speed of rotation to resolve whether the signal reaching the detector is coming to the transmission of the blank (P_0) or the sample (P_T). By including an opaque surface as a shutter it is also possible to continuously adjust the 0% transmittance response of the detector. The effective bandwidth of a double-beam spectrophotometer is controlled by means of adjustable slits at the entrance and exit of the monochromator. Effective bandwidths of between 0.2 nm and 3.0 nm are common. In this doctoral work, UV-grade fused silica slides have been used as the substrate to perform UV-Vis spectroscopy (Nicolet Evolution 300 UV−vis spectrophotometer working in intelliscan mode) on hybrid organic-inorganic films and quartz cuvettes as sample holder for nanoparticles solution.

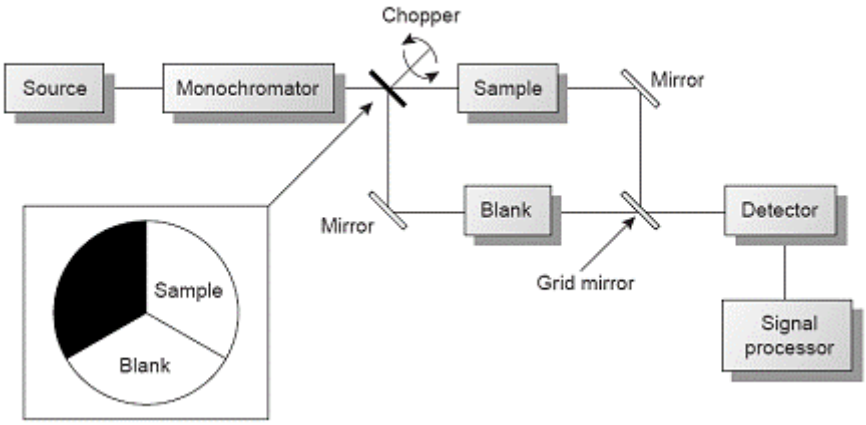

Fig.2.2 Block diagram of a double-beam scanning spectrophotometer.

2.1.3 X-ray based techniques (XRD and SAXS)

X-ray diffraction (XRD) is a wide used techniques to perform structural characterisation of solid materials. When a beam of X-rays interacts with an arbitrary material its atoms may scatter the rays into all possible directions. In a crystalline solid, however, the atoms are arranged in a periodic array, the scattered waves add up and give constructive and destructive interference, and their intensity is recorded by a detector as a function of the exit angle which results in a characteristic diffraction pattern.

A visual way to rationalise X-ray diffraction by an ordered crystal lattice is provided by the so called Bragg's interpretation (Fig.2.3). In the Bragg description, X-ray diffraction (XRD) is yield by the constructive interference of waves scattered from successive lattice planes in the crystal. When an incident beam of wave vector k hits on a set of lattice planes to form an angle θ with respect to the planes, the angle of deviation between the outgoing and incident rays is $\phi = 2\theta$. The separation between neighboring planes is denoted by d. The Bragg condition is given by $2d \sin\theta = n\lambda$. Constructive interference between successive paths occurs when the path difference equals an integer number of wavelengths.

The instrument used for the experimental part of this thesis is a Bruker D8-Discover diffractometer equipped with a Goebel mirror giving a parallel beam. The XRD patterns can be acquired by a scintillator counter or a PSD detector. This technique has been used in this thesis to characterize the crystalline structure of films and nanoparticles.

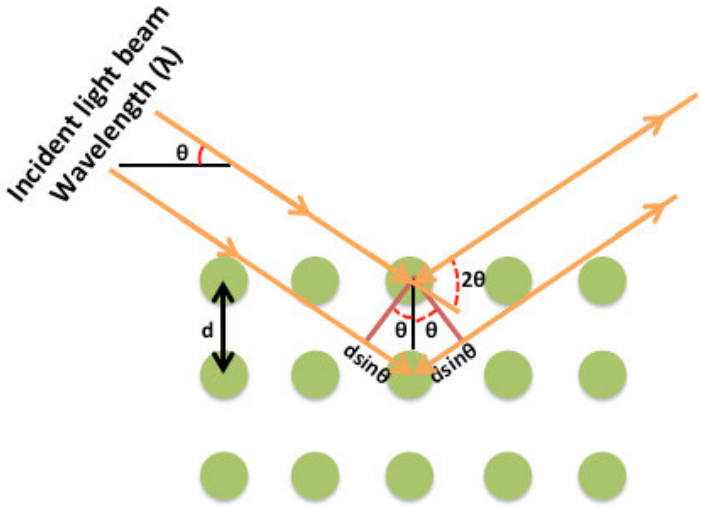

Fig.2.3 Schematic representation of the Bragg's diffraction.

In a Small Angle X-ray Scattering (SAXS) technique, incident X-rays of wavelength ~1 Å give diffraction at 2θ angles in the range 0.1– 1°, which is suitable to study the mesostructure size of the materials synthesized in this work. The interaction of X-ray radiation with mesostructured and mesoporous materials provides diffraction and information on the symmetry of the ordered mesophase. The "small-angle" refers to the angular range of the scattered beams, containing information on the structure in the reciprocal space in the nanometre range. SAXS on mesostructured materials is often performed at synchrotron facilities.

A few aspects of synchrotron radiation, such as very small beam divergence, high beam flux, and in some cases energy tuning, have made small angle scattering very effective for the studies of mesostructure film. It is crucial to have small beam

divergence in order to isolate weak scattering at very small angles from the direct beam which is orders of magnitude stronger. The flux of a synchrotron source is usually several orders of magnitude higher than those from conventional X-ray sources; therefore a diffraction pattern can be acquired in short times, typically on the order of 500 ms.

The SAXS experiments on mesoporous films presented in this doctoral work were conducted at the Austrian beamline at the ELETTRA synchrotron in Trieste.[2] The beamline has the 57-pole NdFeB hybrid wiggler as the photon source. The wiggler delivers a very intense radiation between 4 and 25 keV, of which three discrete energies (5.4, 8 and 16 keV) can be selected by a flat double crystal (111 Si) monochromator in optics hutch 1 and focused by a double focusing toroidal mirror in optics hutch 2 (Fig.2.4). The entire beamline is controlled via a software interface developed with LabView programme. The optical table in the experimental hutch allows optimisation of the sample-to-detector distance with respect to SAXS resolution and sample size setup. A two-dimensional CCD detector (Photonic Science, UK) is used for data acquisition. Before starting a measurement session, the sample-to-detector distance is adjusted in order to ensure that the diffracted beams were well separated from the direct beam, and a sufficiently large area of the reciprocal space be sampled by the CCD detector. The beam stopper has to be correctly positioned for preventing the direct beam from hitting the detector, as this may cause irreversible damage to the CCD array.

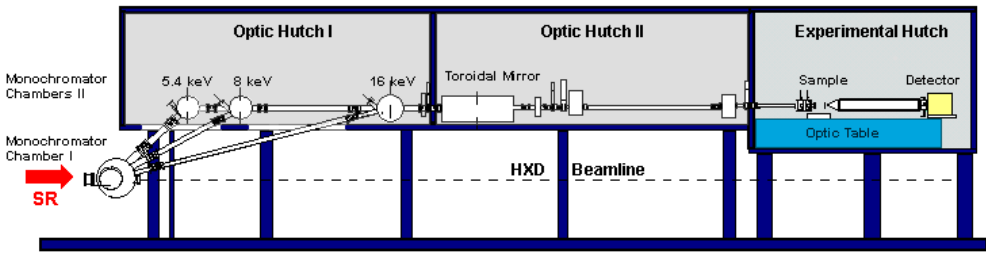

Fig.2.4 Scheme of the Austrian SAXS beamline at ELETTRA.

In a typical SAXS analysis, the sample is placed on the sample holder, which can be rotated via a servo motor from the control room, so that the angle of incidence can be varied. Silver behenate powder standard ($CH_3(CH_2)20COOAg$, d-spacing = 58.38 Å) has been used as diffraction standards, which provide a tool to determine accurately the beam centre position and the sample-to-detector distance. Diffraction patterns are acquired using the CCD detector provided with a software-triggered fast shutter positioned upstream. The incidence angle of radiation can influence the diffraction pattern of a mesostructured film. In fact there are essentially two configurations used in the acquisition of SAXS patterns of mesostructured films: the angle of incidence of the X-ray beam impinging on the sample may be set to either small angle (slightly above the critical angle, i.e. 0.2–0.3°) or perpendicular to the film surface (90°). These two configurations are referred to as grazing and transmission incidence, respectively, and yield information on the out-of-plane and in-plane mesostructure order. When the sample is in grazing incidence (grazing incidence SAXS, or GISAXS) the detector acquires out-of-plane reflections that are not accessible by transmission mode, whereas in transmission mode in-plane reflections are sampled which cannot be recorded in grazing incidence. Due to the lack of global in-plane order, the reciprocal lattice is a collection of concentric rings, centred on the axis perpendicular to the substrate. These rings can be thought as the infinite replication of the spots around the axis perpendicular to the substrate and intersecting the origin. Diffraction patterns can be stored in 12-bit TIFF files which can readily manipulated with proper software. During this doctoral work Fit2d7 programme, which includes important image analysis tools such as intensity scaling, one-click d-spacing calculation, 1-d integration, calibration and correction for detector distortions, has been used for both interactive and batch data processing.

2.1.4 Raman

The photons of monochromatic light interact with molecules producing two types of scattering, elastic (Rayleigh scattering) and inelastic (Raman effect). In the Rayleigh scattering the frequency of emitted photon has the same wavelength as the absorbing photon, while in Raman scattering the energies of the incident and scattered photons are different. Raman spectroscopy in fact is based on inelastic scattering of monochromatic light, usually from a laser source. Photons of the laser light are absorbed by the sample and then reemitted. Frequency of the reemitted photons is shifted up or down in comparison with original monochromatic frequency, which is called the Raman effect. This shift provides information about vibrational, rotational and other low frequency transitions in molecules. The Raman effect comprises a very small fraction, about 1 in 10^7, of the incident photons. It is based on molecular deformations in electric field E determined by molecular polarizability α. The laser beam can be considered as an oscillating electromagnetic wave with electrical vector E. Upon interaction with the sample it induces electric dipole moment $P = \alpha E$ which deforms molecules. Because of periodical deformation, molecules start vibrating with characteristic frequency ν_m. Amplitude of vibration is called a nuclear displacement. In other words, monochromatic laser light with frequency ν_0 excites molecules and transforms them into oscillating dipoles. Such oscillating dipoles emit light of three different frequencies (Fig.2.5) when:

1. A molecule with no Raman-active modes absorbs a photon with the frequency ν_0. The excited molecule returns back to the same basic vibrational state and emits light with the same frequency ν_0 as an excitation source. This type if interaction is called an elastic **Rayleigh scattering**.

2. A photon with frequency ν_0 is absorbed by Raman-active molecule which at the time of interaction is in the basic vibrational state. Part of the photon's energy is transferred to the Raman-active mode with frequency υm and the resulting frequency

of scattered light is reduced to $\nu_0 - \nu_m$. This Raman frequency is called Stokes frequency, or just "**Stokes**".

3. A photon with frequency ν_0 is absorbed by a Raman-active molecule, which, at the time of interaction, is already in the excited vibrational state. Excessive energy of excited Raman-active mode is released, molecule returns to the basic vibrational state and the resulting frequency of scattered light goes up to $\nu_0 + \nu_m$. This Raman frequency is called Anti- Stokes frequency, or just "**Anti-Stokes**".[3]

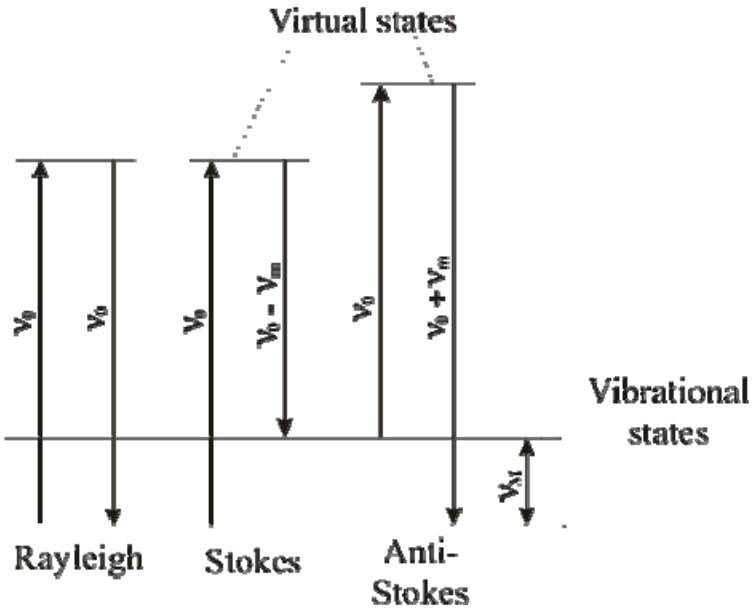

Fig.2.5 Raman transitional scheme[3]

Raman spectroscopy can be used to study solid, liquid and gaseous samples. In this thesis a Bruker Senterra confocal Raman microscope working with a three lasers excitation wavelength of 532, 633 and 785 nm has been employed to confirm the presence of nanoparticles in the films matrix and monitor the uptake into the cells.

A Raman system typically consists of four major components: excitation source (Laser), sample illumination system and light collection optics, wavelength selector (Filter or Spectrophotometer) and detector (Photodiode array, CCD or PMT).

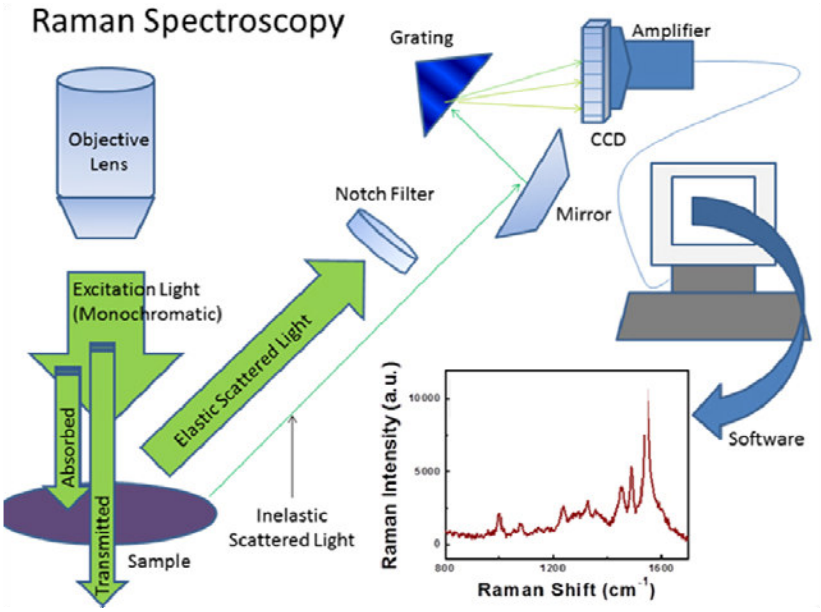

Fig.2.6 Scheme of the process involved in collecting Raman spectra.[4]

In a Raman spectrometer (Fig.2.6) the sample is illuminated with a laser beam in the ultraviolet (UV), visible (Vis) or near infrared (NIR) range. Scattered light is collected with a lens and is sent through interference filter or spectrophotometer to obtain Raman spectrum of a sample.

2.1.5 Ellipsometry

Ellipsometry is a non-invasive optical technique based on analysis of elliptical polarization. It is used to determine the properties of thin films (particularly the thickness and refractive index) on dielectric or metal surfaces. This technique uses the change in polarization of light upon reflection from a material to determine the real part (refractive index), n(λ) and the imaginary part (extinction coefficient), k(λ) of the complex refractive index, of a material, $N(\lambda) = (n(\lambda)+ik(\lambda))$ where λ is the wavelength of the electromagnetic radiation. Linearly polarized light is generally elliptical polarized upon reflection with asymmetric intensity difference (tan ψ) and phase difference (Δ). The ellipticity, or ratio of minor to major axis of the ellipse, and the

orientation of the reflected beam is determined by the relative phase difference Δ and azimuth ψ (Fig. 2.7).

These values are measured using ellipsometry. The ellipticity of the reflected light depends on the optical constants of the thin film and its thickness. Physical informations about the sample such as film refractive index and thickness are extracted by fitting the spectra to a physical model. The model is built up based on the available information and knowledge of the porous film structure and components of the sample to predict the optical response of the sample to the incident polarized light. For porous thin films usually refractive index, film thickness, porosity and other fit parameters are to be determined. For the sol-gel films studied in this work, the optical model used in the fitting of ellipsometric data consists of one or two layers on substrate. Native SiO_2 layer on Si substrate and porous film layer on top or just porous film layers on substrate. The instrument used for the characterizations of this thesis is an R-SEWollam spectroscopic ellipsometer. The ellipsometric spectra analysis is done using CompleteEASE 4.06 software assuming a Cauchy film as fitting model which calculates the refractive index as a function of the wavelength: $n(\lambda) = A + B/\lambda^2 + C/\lambda^4$.

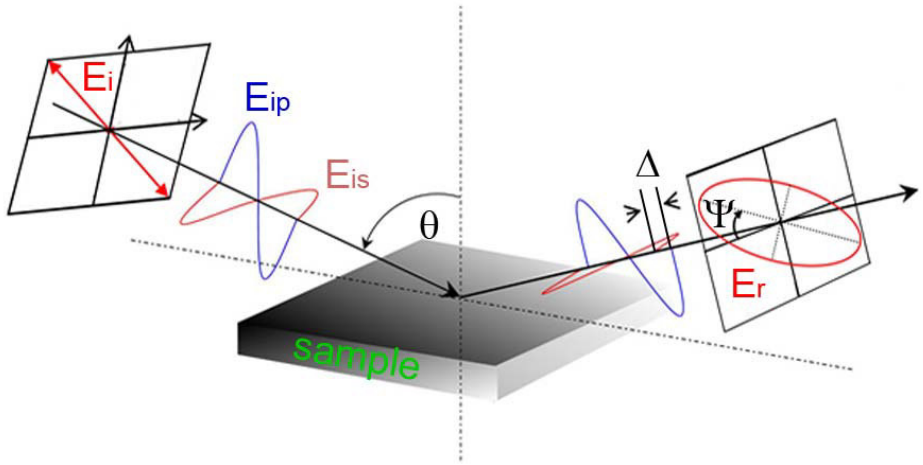

Fig.2.7 Scheme of ellipsometry principle.

2.2 Microscopic techniques

Microscopic techniques are based on a use of an apparatus which is designed to produce magnified visual or photographic images of small objects. The microscope should reproduce a magnified image of the specimen, separate the details in the image, and make the details visible to the human eye or camera. Here we will describe the details for of optical, electronic and atomic microscopy.

2.2.1 Scanning electron microscopy (SEM)

Scanning electron microscopy (SEM) allows characterizing the morphology and composition of materials ranging from inorganic or organic-inorganic films until biological materials such as cells. It is a non-destructive and one of the most versatile techniques. The main advantages of SEM are the high lateral resolution (1–10 nm), large depth of focus (typically 100 mm at x1000 magnification), and the numerous types of electron– specimen interaction that can be used for imaging or chemical analysis purposes. In contrast to transmission electron microscopy sample preparation is not elaborate. All of these advantages, as well as the actual strikingly clear images, make the scanning electron microscope one of the most useful instruments in research today.

The scanning electron microscope (Fig.2.8) consists of an electron–optical column mounted on a vacuum chamber where a beam of electrons is produced by an electron gun; electron gun is placed on top of this column. The pressure in the specimen chamber is 10^{-3}- 10^{-5} Pa. The electron beam follows a vertical path through the microscope, which is held within a vacuum. The beam travels through electromagnetic fields and lenses, which focus the beam down toward the sample. Once the beam hits the sample, electrons and X-rays are ejected from the sample. Detectors collect these X-rays, backscattered electrons, and secondary electrons and convert them into a signal that is sent to a screen producing the final image.

During this doctoral work the SEM images have been obtained in collaboration with Salvatore Marceddu (Institute of Sciences of Food Production (ISPA), CNR, Sassari, Italy) by using a Zeiss EVOLS10 environmental scanning electron microscopy (ESEM), in high vacuum modality with secondary electron detector. The analyses were performed on samples previously coated with gold in an Edwards S150A Sputter unit.

Because the SEM utilizes vacuum conditions, the pressure inside specimen chamber is much lower than the saturation vapour pressure of water and it uses electrons to form an image, special preparations must be done to the sample. All water must be removed from the samples because the water would vaporize in the vacuum. All metals are conductive and require no preparation before being used. All non-metals need to be made conductive by covering the sample with a thin layer of conductive material. This is done by using a device called a "sputter coater."

The sputter coater uses an electric field and argon gas. The sample is placed in a small chamber that is at a vacuum. Argon gas and an electric field cause an electron to be removed from the argon, making the atoms positively charged. The argon ions then become attracted to a negatively charged gold foil. The argon ions knock gold atoms from the surface of the gold foil. These gold atoms fall and settle onto the surface of the sample producing a thin gold coating.

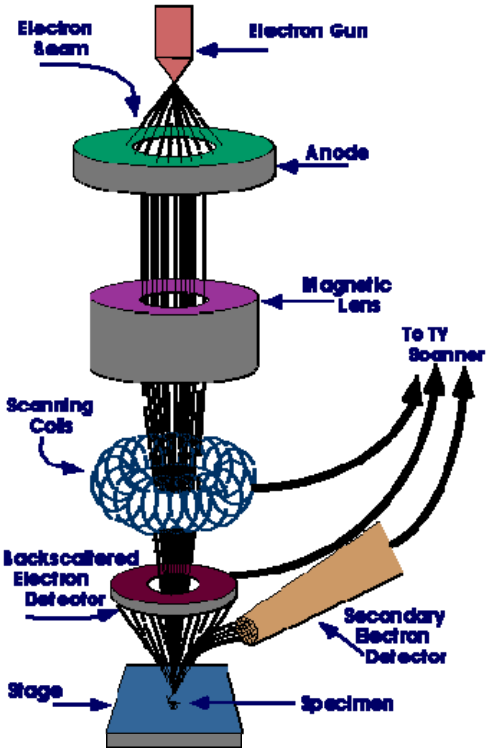

Fig.2.8 Scheme of a typical SEM microscope.[5]

The topographic contrast observed in most SE micrographs gives these images a clear 3D appearance Fig.2.9. The observed contrast is mainly due to three effects:[6]

1) *tilt contrast*: the SE yield, δ, depends on the local tilt angle of the surface θ. For voltages 45 kV the dependence of δ on local tilt angle, θ, is given approximately by: $\boldsymbol{\delta(\theta) = \delta_0 / \cos(\theta)}$ where δ_0 is the SE coefficient at 0° tilt. At low voltages, when the distance travelled by the beam electrons within the solid becomes comparable with the mean escape depth, λ of the SEs, this surface tilt contrast is greatly reduced;

2) *shadow contrast*: this is the shadowing of the SE signal due to holes or protrusions. The amount of shadowing depends on the presence of electrostatic and magnetic extraction fields on the surface;

3) *edge effect contrast*: this is due to SEs that penetrate through the edges of structures. This contrast is observed in most micrographs as white edges extending distance of the order of the electron range. Therefore, the width and magnitude of the observed edge

contrast depend on the beam energy and are greatly reduced at low voltages. This effect is most disturbing when the spatial variation of the background due to the edge effect is comparable with the size of the surface structures to be examined. At high voltages this situation occurs at medium magnifications. Low voltages are therefore preferred when observing cross-sections or details on small topographic structures, such as patterns on integrated circuits.

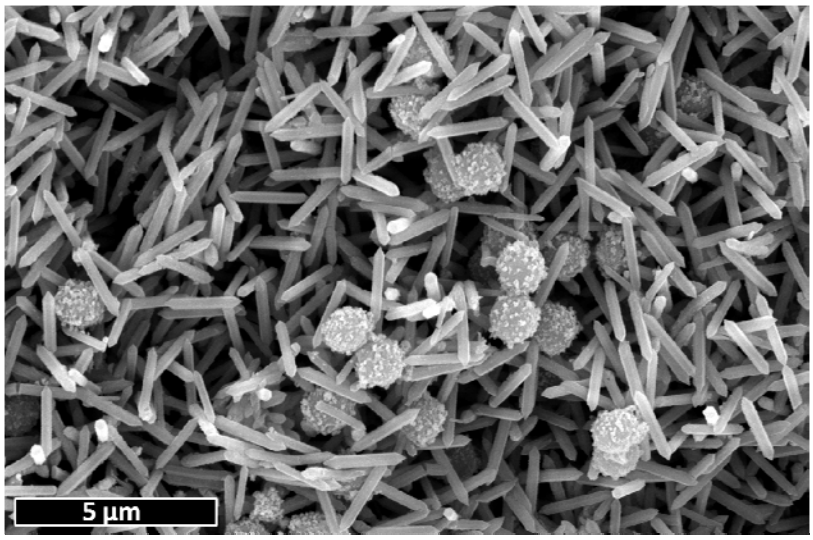

Fig.2.9 SEM picture of Iron nanoparticles dispersed in a MILL88A metal-organic-framework cristals.

2.2.2 Transmission electron microscopy (TEM)

TEM is a versatile technique used to characterize the details of the internal structure of micro- and nanostructure materials. The electron microscope configuration is shown in Fig.2.10; Electrons are accelerated by a tungsten filament or a LaB_6 crystal through an evacuated column (vacuum 10^{-7} Torr) containing an assembly of condenser, objective and projector lenses.[7] The interaction of the electron beam with the sample the incident electromagnetic wave impinges on the grating object and is diffracted. The diffraction pattern is then reconverted into a real image in the image plane by the objective lens through an inverse Fourier transform. The intermediate lens then

produces a second intermediate image which is magnified at the viewing screen by the final projector lens. Because electrons are used, electrostatic lenses are employed to deflect the electron trajectory. The resolution of the image depends on the number of grating orders that are transmitted through the optical system.

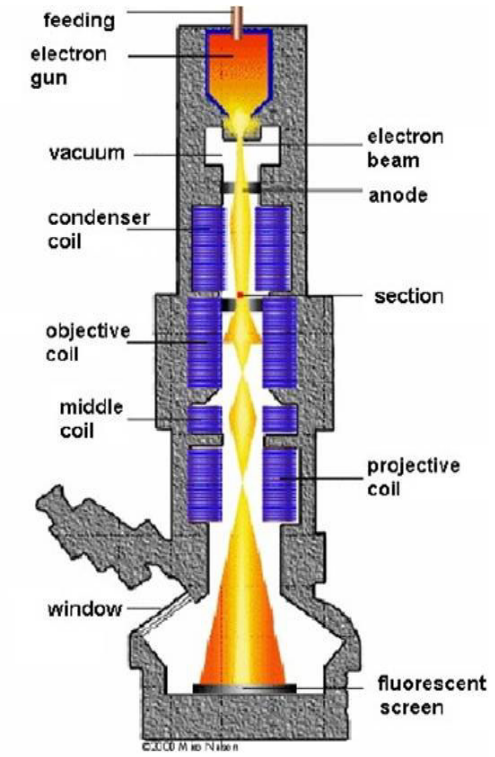

Fig.2.10Scheme of a typical TEM microscope.

If an objective aperture intercepts all the diffracted beams and allows only the direct beam to pass, deficiency contrast occurs and a bright field image is formed. Alternatively, the objective aperture can be used to select a single diffracted beam to produce a dark field image.

TEM measurements of the samples produced in this thesis have been obtained through collaboration with Dr. Maria Francesca Casula at Chemical Department in University of Cagliari. A Transmission Electron Microscope Jeol 200CX equipped with a

tungsten cathode operating at 200 kV has been used. Sample preparations have been done by scratching a film from its silicon substrate and disperse the fragments in an organic solvent.

2.2.3 Atomic force microscopy (AFM)

Scanning probe atomic techniques represent a class of microscopy techniques which uses the interaction between a sharp tip and a surface to obtain a high-resolution and high-magnification images. The sharp tip is scanned back-and-forth over a specimen to be examined. In particular, atomic force microscopy (AFM) uses a force sensing probe to track sample topography. The working principle is the measurement of the interactive force between a tip and the sample surface using special probes made by an elastic cantilever with a sharp tip on the end. The force applied to the tip by the surface, results in bending of the cantilever.[8]

There are three modes used to perform AFM imaging: contact mode, tapping mode and force modulation mode. In contact mode, the tip touches the sample but it can lead to sample damage from the dragging tip on soft materials. Tapping (or semi-contact) mode avoids this drawback: the tip is oscillated and only touches intermittently, so that dragging during scanning is minimized. Non-contact mode is where the tip feels only the attractive forces with the surface, and causes no damage. It is technically more difficult to implement since these forces are weak compared with contact forces. In non-contact mode at larger tip-surface separation, the imaging resolution is poor, and the technique not often used. However, at small separation, true atomic resolution can be achieved in non-contact mode AFM.

Acquisition of an AFM surface topography may be done by recording the small deflections of the elastic cantilever. For this purpose optical methods are widely used in atomic force microscopy. The optical system is aligned so that the beam emitted by a diode-laser is focused on the cantilever, and the reflected beam hits the center of a

photodetector. Four-section split photodiodes are used as position-sensitive photodetectors.

Atomic force microscopy measurements have been performed by a NT-MDT Ntegra AFM in semi-contact mode on a nanocomposite film.

2.2.4 Confocal microscopy

Confocal microscopy was invented in 1955 by Marvin Minsky during his postdoctoral at Harvard, who was trying to see the interconnections between neuronal cells. Compared to the conventional optical microscopy, the confocal microscopy is able to control depth of field, eliminate or reduce background information away from the focal plane (that leads to image degradation), and capable to collect serial optical sections from thick specimens.[9] The basic key to the confocal approach is the use of spatial filtering techniques to eliminate out-of-focus light or glare in specimens whose thickness exceeds the immediate plane of focus. In the Fig.2.11 are reported a series of images that compare the traditional (a,b,c) with the confocal (d,e,f) microscopy. Is it is clear that the images of stained human medulla captured by confocal microscopy show significant degree of structural detail.

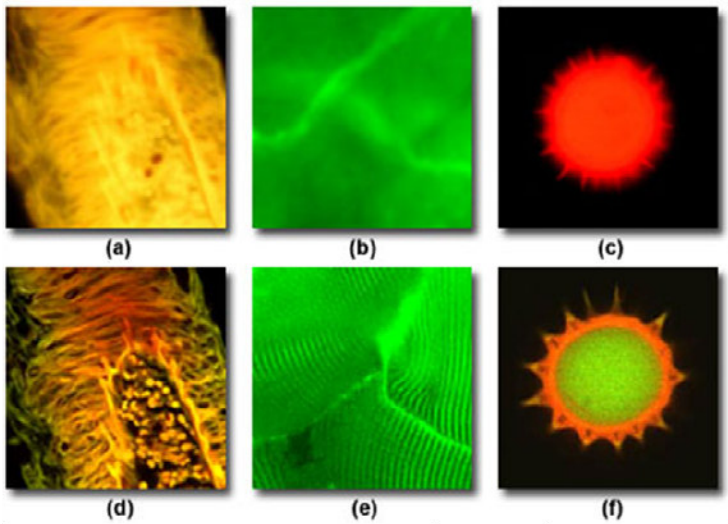

Fig.2.11 Stained human medulla images comparison of a)b)c) traditional and d)e)f)laser scanning confocal fluorescence microscopy.[10]

A major application is in optical sectioning, a process similar to using a microtome to obtain slices except that it is done optically. The procedure is to start at the top of the cell, take an image, move the microscope stage (cell) up one step, take another image, and so on, until the entire cell has been imaged. The resulting "stack" of images can be computer processed to reconstruct the object in three dimensions.

In Fig.2.12 is shown the confocal configuration and principle in epi-fluorescence laser scanning microscopy. Confocal microscopy is made of multiple laser excitation sources, a scan head with optical and electronic components, electronic detectors (usually photomultipliers), and a computer for acquisition, processing, analysis, and display of images.

Coherent light emitted by the excitation source passes through a pinhole aperture that is situated in a conjugate plane (confocal) with a scanning point on the specimen and a second pinhole aperture positioned in front of the detector. As the laser is reflected by a dichromatic mirror and scanned across the specimen in a defined focal plane, secondary fluorescence emitted from points on the specimen (in the same focal plane)

passes back through the dichromatic mirror and is focused as a confocal point at the detector pinhole aperture.

The significant amount of fluorescence emission that occurs at points above and below the objective focal plane is not confocal with the pinhole (termed Out-of-Focus Light Rays in Figure 2.12) and forms extended Airy disks in the aperture plane. Because only a small fraction of the out-of-focus fluorescence emission is delivered through the pinhole aperture, most of this extraneous light is not detected by the photomultiplier and does not contribute to the resulting image. Refocusing the objective in a confocal microscope shifts the excitation and emission points on a specimen to a new plane that becomes confocal with the pinhole apertures of the light source and detector.[10]

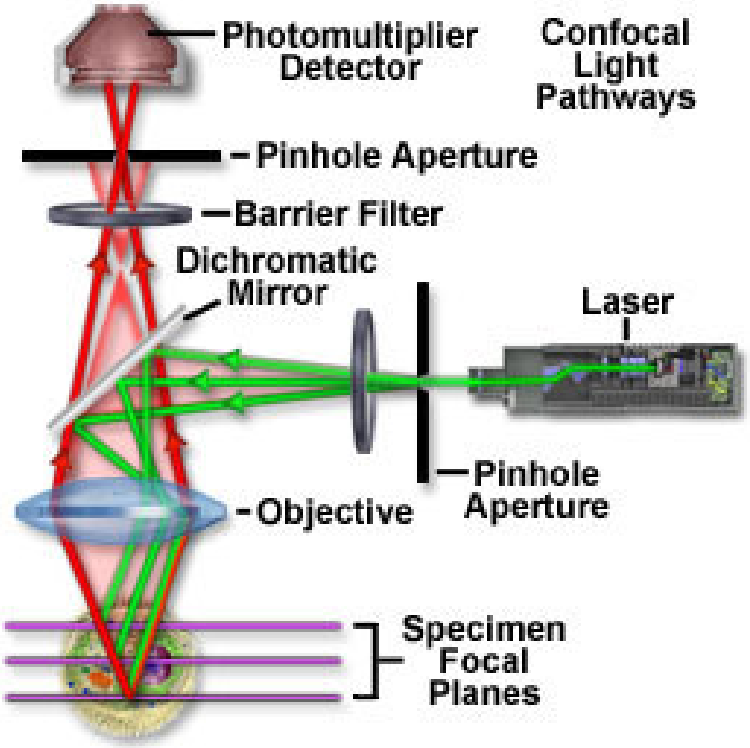

Fig.2.12 Configuration of confocal microscope.[10]

In this thesis, the confocal characterization have been performed to study the fate of nanoceria into the cells in collaboration with Dr.ssa Grazia Galleri at Department of Clinical and Experimental Medicine, University of Sassari. The samples have been observed with a Leica Microscope, equipped with a Leica Confocal Laser System C2s.

2.3 Other techniques

2.3.1 Flow Cytometry

Flow cytometry is based on fluorescence measurement of multiple physical characteristics (optical and fluorescence) of a single cell (size and internal complexity), as the cell flows in suspension through a measuring device. In addition, it is also possible to measure extrinsic features such as specific protein expression and nucleic acid content using added reagents, such as fluorescent stains and antibodies.

When labeled cells are passed by a light source, usually laser light, the fluorescent molecules are excited to a higher energy state. Upon returning to their resting states, the fluorochromes emit light energy at higher wavelengths. The use of multiple fluorochromes, each with similar excitation wavelengths and different emission wavelengths (or "colors"), allows several cell properties to be measured simultaneously.

Commonly used dyes include propidium iodide, phycoerythrin, and fluorescein.

A schematic diagram of the fluidic and optical components of a flow cytometer is shown in Fig.2.13. Inside a flow cytometer, cells in suspension are drawn into a stream created by a surrounding sheath of isotonic fluid that creates laminar flow, allowing the cells to pass individually through an interrogation point. At the interrogation point, a beam of monochromatic light intersects the cells. Emitted light is given off in all directions and is collected via optics that direct the light to a series of filters and dichroic mirrors that isolate particular wavelength bands. The light signals are detected by photomultiplier tubes and digitized for computer analysis. The resulting information usually is displayed in histogram or two dimensional dot-plot formats.[11]

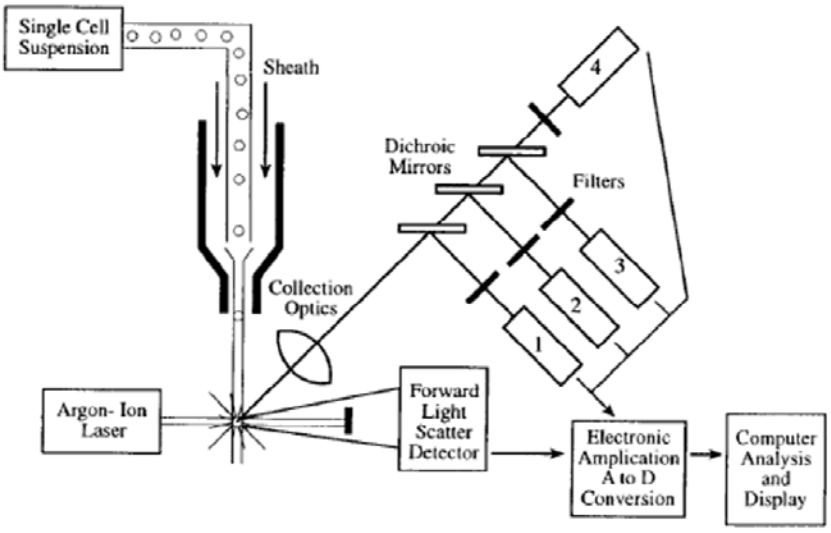

Fig.2.13 Schema of a flow cytometer. A single cell suspension is hydrodynamically focused with sheath fluid to intersect an argon-ion laser. Signals are collected by a forward angle light scatter detector, a sidescatter detector (1), and multiple fluorescence emission detectors (2–4). The signals are amplified and converted to digital form for analysis and display on a computer screen.[11]

The sample preparation requires to suspend the samples in a liquid. After a single-cell suspension is obtained, the cells are stained with dyes that bind to the specific features that are to be measured.[12]

In this doctoral work the cells containing nanoceria have been analyzed in collaboration with Dr.ssa Grazia Galleri at Department of Clinical and Experimental Medicine, University of Sassari by using FACS Calibur flow Cytometer (Becton Dickinson, FACScalibur™, USA).

2.3.2 Dynamic light scattering (DLS)

Dynamic light scattering also known as Photon Correlation Spectroscopy or Quasi-Elastic Light Scattering is a technique used in Chemistry, Biochemistry, and Physics primarily to characterize the hydrodynamic radius of polymers, proteins, and colloids in solution. It allows determining particle size down to 1 nm, shape and flexibility by measuring the random changes in the intensity of light scattered from a suspension or solution. Moreover it offers the possibility to study the nature of the interactions between particles and their environments. This technique can provide such information in relatively quickly and inexpensively, compared with other methods.

Considerable emphasis is placed on the Brownian motion of particles diffusing in a background fluid such as water, because an understanding of Brownian motion opens the door to understanding a broad range of subjects, including the dynamical behavior of fluids and fluid mixtures, and magnetic materials near their respective critical points. [13]

In general, when a sample of particles with diameter much smaller than the wavelength of light is irradiated with light, each particle will diffract the incident light in all directions. This is called Rayleigh Scattering.

In a typical DLS experiment, a suspension of analyte such as nanoparticles or polymer molecules is irradiated with monochromatic light from a laser while intensity of the diffracted light is measured as function of time. The detector is typically a photomultiplier positioned at 90° to the light source and it is used to collect light diffracted from the sample. Collimating lenses are used to focus laser light to the center of the sample holder.[14] A scheme of typical dynamic light scattering is reported in Fig.2.14.

Ideally, the sample itself should be free of unwanted particles that could contribute to light scattering. For this reason dispersions are often filtered or purified before being measured. Samples are also diluted to low concentrations in order to prevent the particles from interacting with each other and disrupting Brownian motion.

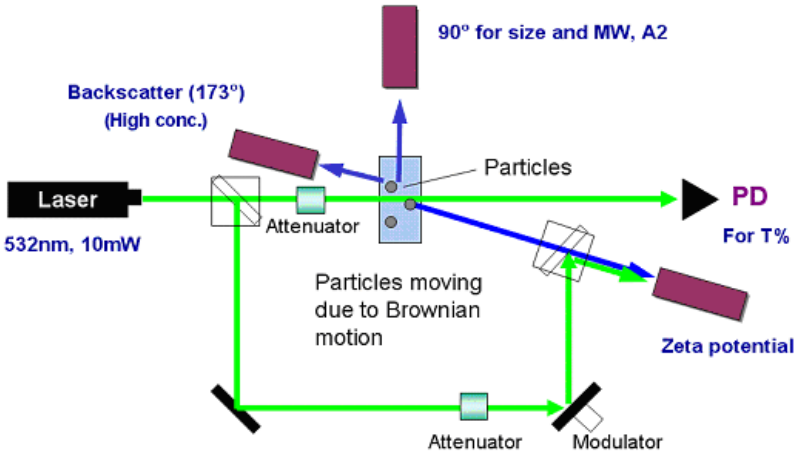

Fig.2.14 Scheme of a typical Dynamic light scattering[15]

The Dynamic light scattering (DLS; Malvern Instruments Zetasizer Nano S90 with a He-Ne laser 633 119 nm) has been used to evaluate the nanoceria aggregation. The analyses have been performed in collaboration with Dr. Sebastiano Garroni at Department of Chemistry University of Sassari.

2.4 References

[1] Skoog D.A. Fundamentals of analytical chemistry. (**1995)** (7th edition), Philadelphia, Harcourt Brace College Publishers.

[2] Amenitsch H., Rappolt M., Kriechbaum M., Mio H., Laggner P., Bernstoff S. J.Synchrotron Rad. **(1998)**, 5, 506–508.

[3] Princeton Instrument http://www.princetoninstruments.com.

[4] Halvorson R.A., Vikesland P. J. Environ. Sci. Technol. **(2010)**, 44, 7749-7755.

[5] https://www.purdue.edu

[6] Amelinckx S., van Dyck D., van Landuyt J., van Tendeloo G. Handbook of Microscopy. **(1997)**, Weinheim, VCH.

[7] Williams D.B., Carter C.B. Transmission Electron Microscopy. A Text book for Materials Science. **(1996),** New York, Plenum.

[8] Mironov V.L. Fundamentals of Scanning Probe Microscopy. The Russian Academy of sciences institute for physics of microstructures. **(2004)**.

[9] Dean P.N. Confocal Microscopy: Principles and Practices in Current Protocols in Cytometry. 2.8.1-2.8.12. **(1998)** by John Wiley & Sons, Inc.

[10] http://www.olympusfluoview.com

[11] Brown M., Wittwer C. Clinical Chem. **(2000)**, 46, 8(B), 1221–1229.

[12] Dean P.N., Hoffman R.A. Current Protocols in Cytometry. 1.1.1-1.1.8. John Wiley & Sons, Inc. **(2007)**.

[13] Goldburg W.I. Am. J. Phys. **(1999)**, 67**,** 1152-1160.

[14] http://chemwiki.ucdavis.edu

[15] http://www.horiba.com

3. Materials and method

3.1. Materials

Chemicals for nanoparticles synthesis

Cerium(III) nitrate hexahydrate ($Ce(NO_3)_3.6H_2O$, ABCR 99.9%), 1-hexadecyl trimethylammonium bromide (CTAB 98%, ABCR), urea (CH_4N_2O, Aldrich 99%), Pluronic F127 (PEO_{106}-PPO_{70}-PEO_{106}, Aldrich), iron chloride (III) hexahydrate ($FeCl_3.6H_2O$, ABCR GmbH&Co), iron chloride (II) tetrahydrate ($FeCl_2.4H_2O$, ABCR GmbH&Co), sodium hydroxide (NaOH pellets 98 %, Carlo Erba), 3-aminopropyltriethoxysilane (APTES, $NH_2(CH_2)_3Si(OC_2H_5)_3$, 99%, Aldrich), fluorescein isothiocyanate isomer I (FITC, $C_{21}H_{11}NO_5S$, 90%, Aldrich), ethanol (EtOH, Fluka 99.8%), acetone (Aldrich 99.5%), N,N-dimethylformamide (DMF, C_3H_7NO, Aldrich), 2-propanol (99.7%, Carlo Erba), 1 M hydrochloric acid (HCl, Aldrich) and 5 M aqueous ammonia (NH_4OH, Aldrich) were used as received without further purification. Bidistilled water (H_2O) was employed in the synthesis.

Chemicals for films synthesis

3-glycidoxypropyltrimethoxysilane (GPTMS, Aldrich 98 %), sodium hydroxide (NaOH pellets 98%, Carlo Erba), titanium tetrachloride ($TiCl_4$, Aldrich), Pluronic F127 (PEO_{106}-PPO_{70}-PEO_{106}, Aldrich), rhodamine 6G (Rh6G, Aldrich), ethanol (EtOH, Aldrich 99.8%) and acetone (Aldrich 99.5%) were used as received without further purification; bidistilled water (H_2O) was employed in the synthesis and p-type boron-doped silicon wafers, silica and soda-lime glass slides were employed as substrates for film deposition.

Chemicals for biological assay

Phosphate buffered saline 10X concentrate (Sigma Aldrich), Dulbecco's modified Eagle's medium (DMEM/F-12, HEPES, no phenol red), horse and fetal bovine (FBS) serum were purchased from Life Technologies, L-3,4,dihydroxyphenylalanine (L-DOPA, 98%) from Sigma-Aldrich (Milan, Italy) and manganese chloride ($MnCl_2$) from Merck (Darmstadt, Germany). 3-(4,5-Dimethyl-thiazol-2-yl)-2,5,diphenyltetrazoliumbromide for MTT assay (97.5%), phosphate buffer saline

solution (PBS, 0.2 mm filtered), trypan blue (0.4%), gelatin, 4,6-diamidino-2-phenylindole dihydrochloride (DAPI, 98%), 0.5 M citric acid (99.5%), 1.0 M sodium acetate (NaAc, 99%), 12.5 mM ethylenediaminetetraacetic acid (EDTA, 98.5%), methanol 10% (MeOH, 99.93%), sodium octylsulphate ($CH_3(CH_2)_7OSO_3Na$, pH 3.0, 95%), annexin V-fluorescein isothiocyanate (FITC) propidium iodide (PI), annexine V-FITC kit (MACS Mylteny Biotec), and trypan blue 0.4% were purchased from Sigma Aldrich.

OVIXcell (IMV Technologies), 4% glutaraldehyde, 1% OsO_4, PI (Propidium Iodide, 1mg/ml; Sigma-Aldrich, USA), FITC-*PSA* (*Pisum Sativum* agglutinin conjugated with fluorescein isothiocyanate; 1mg/ml; Sigma-Aldrich, USA), Acridine Orange, TNE buffer (0.15M NaCl, 1mM EDTA, 10mM Tris, pH 7.2), Acid Detergent Solution (0.08 M HCl, 0.15 M NaCl, 0.1% Triton X-100, pH 1.4), staining solution (0.15 M NaCl, 1 mM EDTA, 10 mM Tris, 0.2 M Na_2HPO_4, 0.1 M citric acid, pH 6), paraformaldehyde, Mitotracker Orange (Molecular Probes, Oregon, USA).

20 mM Hepes buffered TCM 199, polyvinyl alcohol (PVA), 10% heat-treated oestrus sheep serum (OSS), 0.1 IU/ml FSH, 0.1 IU/ml LSH, mineral oil, cacodylate buffer (0.1 M, pH = 7.4), 2.5% glutaraldehyde, osmium tetroxide 2%, uranyl acetate, lead citrate, microtubule stabilizing buffer (100 mM PIPES, 5 mM $MgCl_2$, 2.5 mM EGTA, 2% formaldehyde, 0.1% Triton- X-100, 1 mM taxol, 10 U/ml of aprotinin, and 50% deuterium oxide), 2% bovine serum albumin, 2% skim milk powder, 2% normal goat serum, 100 mM glycine, 0.01% Triton-X-100, and 0.2% sodium azide, Hoechst 33258 (1μg/ml in blocking solutions, 50% glycerol, sodium azide , 2,7-dichlorodihydrofluorescein diacetate (H_2DCFDA), 2% paraformaldehyde, SOF medium, 1% Triton X-100 in 20mM Hepes buffered, propidium iodide (PI), 10 mg/ml Hoechst 33342, glycerol were purchased from Sigma Chemical CO. (St. Louis, MO, USA). Monoclonal anti–αβ-tubulin, blocking solution, donkey anti-mouse Alexa Fluor 488 secondary antibody (Invitrogen) and rhodamine phalloidin (1:150, Invitrogen).

3.2. Synthesis of nanoparticles

3.2.1. Nanoceria

The synthesis of ceria nanoparticles uses as coordinating agent 1-hexadecyl-trimethylammonium bromide (CTAB) or Urea $Ce(NO_3)_3$ and NH_4OH as inorganic precursors; 7 g of $Ce(NO_3)_3 \cdot 6H_2O$ was dissolved and 0.5 ml hydrochloric acid was added in 20 ml of 2-propanol and left under stirring until a homogeneous solution has been obtained. In a separate vial, 2 g of CTAB or Urea and 0.5 ml of HCl were dissolved in 20 ml of 2-propanol and left under stirring for 5 min. The CTAB or urea solution was then added, dropwise, to the $Ce(NO_3)_3$ solution under stirring, immediately after 14 ml of NH_4OH(aq) were added to the mixture to form a precipitate that was exposed to microwaves (4 times at 600 W for 10 s), washed with water and centrifuged at 10.000 rpm. A light yellow milky dispersion was obtained and diluted with water to reach a concentration of 0.08 g CeO_2 per ml (ceria stock suspension).The yield of the cerium oxide nanoparticles was estimated in 58 % by assuming CeO_2 as the average formula for the calculations.

- *Functionalization of nanoceria with FITC*

Nanoceria was firstly functionalized with 3-aminopropyltriethoxysilane by mixing 200 mg of nanoceria with 3 ml of APTES and 50 ml of EtOH at room temperature under stirring. The amino-functionalized nanoceria (NH_2-nanoceria) was washed with EtOH and centrifuged at 10 000 rpm. 4mg of nanoceria were then re-suspended in 0.5 ml of DMF, mixed with 0.5 ml of 2 $mg \bullet ml^{-1}$ FITC in DMF and stirred at room temperature for 4 h. The FITC–NH_2 nanoceria were washed once with acetone and twice with water and centrifuged at 10 000 rpm. The orange precipitate was diluted with water to reach a concentration of 22 $mg.ml^{-1}$ (FITC–NH_2-nanoceria).

3.2.2. Superparamagnetic iron oxide (SPION)

The reagents $FeCl_2.4H_2O$ (2 g) and $FeCl_3.6H_2O$ (3.25 g) were dissolved in 60 ml of acidic solution obtained with 10 ml of HCl 1 N and 50 ml of H_2O under vigorous stirring. The solution of iron salts was then added drop-wise under nitrogen flow to 100 ml of NaOH 1 M. The reaction mixture was left under stirring for 30 min. under nitrogen flow. The nanoparticles were washed 3 times with 20 ml of water and 3 times with 20 ml of ethanol using a magnet. The SPIONs synthesis was performed according to Yu and Chow.[1] The yield of the iron oxide nanoparticles was estimated in 53 % by assuming Fe_3O_4 as the average formula for the calculations. The obtained SPIONs concentration was 0.03 g per ml (SPIONs stock suspension).

3.3. Synthesis of sol-gel based film

3.3.1. Mesoporous Titania

Mesoporous titania sol was prepared using $TiCl_4$, EtOH, H_2O, and Pluronic F127, with the following molar ratios: $TiCl_4$:EtOH:F127:H_2O = 1:40:0.005:10. The precursor sol was obtained by addition of $TiCl_4$ into a mixture of EtOH and surfactant Pluronic F127 after 5 min. of stirring; water was then added dropwise at the precursor sol. Titania sol was deposited by dip-coating in a controlled chamber, with 25% relative humidity (RH) and a withdrawal rate of 15 cm.min.$^{-1}$. After deposition, the films were dried in an oven at 60 and 130 °C (24 h at each temperature). The samples were then calcined thermally treating them from 130 °C up to 350 °C with a heating rate of 1 °C min.$^{-1}$, with a final firing step of 2 h at 350 °C. Silicon wafers (Si-Mat) (100) cut, p-type boron doped, 350 μm thick, previously cleaned with water, acetone, and EtOH were used as substrates for film deposition.

3.3.2. Mesoporous Hafnia

Mesoporous hafnia films can be synthesised starting from chloride precursors as the Hf source. The precursors solution was prepared by the slow addition of $HfCl_4$ (6.33 g) to 46.13 ml of ethanol and 1.26 g of surfactant. Finally 3.6 ml of water was added to this sol under stirring. The molar ratios were: $HfCl_4$:EtOH:F127:H_2O = 1:40:0.005:10 The substrate was dip-coated in the fresh solution in a controlled chamber, with 25% relative humidity (RH) and a withdrawal rate of 15 cm**.**min.$^{-1}$. After deposition, the films were dried in an oven at 60 and 130 °C (24 h at each temperature). The samples were then calcined thermally treating them from 130 °C up to 350 °C with a heating rate of 1 °C min.$^{-1}$, with a final firing step of 2 h at 350 °C. Silicon wafers (Si-Mat) (100) cut, p-type boron doped, 350 μm thick, previously cleaned with water, acetone, and EtOH were used as substrates for film deposition.

3.3.3. Mesoporous Silica

Mesoporous silica films were prepared in two stages. In the first one a stock solution was prepared by mixing 21.7 ml of EtOH, 30 ml of TEOS and 2.55 ml of an acidic water solution (HCl $7.68.10^{-1}$M); the solution was stirred for 45 min. at 25°C in a closed vessel. In the second stage a solution containing the surfactant was prepared by dissolving 1.3 g of Pluronic F127 in 15 ml of EtOH and 1.5 ml of acidic water (HCl $5.7.10^{-2}$M). Finally the two solutions were mixed together and stirred for 15 min. at 25°C in a closed vessel. The final molar ratios of the mixture are the following: TEOS:EtOH:H2O:HCl: F127 = 1: 16.32: 5.42: $1.88.10^{-2}$: $5.08.10^{-3}$. Film was deposited on substrates by dip-coating deposition at a 15 cm**.**min.$^{-1}$withdrawal rate. The temperature in the deposition room was kept at 25°C and the relative humidity (RH) at 25%. The films, immediately after their deposition, were dried at 80°C for 18 hours in air, then at 150°C for 2 hours, and finally calcined in air at room pressure at 350°C for 3 hours. Silicon wafers (Si-Mat) (100) cut, p-type boron doped, 350 μm thick, previously cleaned with water, acetone, and EtOH were used as substrates for film deposition.

3.3.4. GPTMS hybrid films

The precursor sol was prepared by addition of GPTMS (10 ml) to a NaOH aqueous solution (4 ml, 1.85 M, pH 14) under stirring. The molar ratio of the components was set to GPTMS: H2O: NaOH = 1:5:0.167. Afterward the precursor sol was left in an open vessel at 25 °C and 40 % RH for 30 min. to avoid risk of overpressure due to vapors of methanol generated from the methoxyl groups hydrolysis. After this time, the sol was left under stirring for 12 h at 25°C in a closed vial and divided in two parts. One sol was used fresh (0d) and the other one was aged up to 6 days (6d) at 25°C without stirring. Both solutions were used for the deposition of hybrid films by spin-coating on silicon and silica substrates using a rotation speed of 5.000 rpm for 20 s. The substrates were cleaned with water, acetone and ethanol; after the deposition, the films were thermally treated at 100°C for 48 h.

3.4. Synthesis of nanocomposite films

3.4.1. Grafting of film surface with nanoparticles

The anchoring of nanoceria or SPION nanoparticles on the films was performed through a post grafting procedure via incubation with colloidal NP suspensions. Hybrid organic–inorganic films with an average surface area of 7.5 cm^2 were placed in Petri dishes (diameter = 60 mm) and then immersed for 48 h in a solution containing 0.04 g of NPs dispersed in 20.5 ml of ethanol. After incubation, the hybrid films were washed with ethanol and dried on the open air.

3.4.2. Nanoceria into the pores of thin film: DXRL approach

The titania, hafnia and silica mesoporous film have been prepared by following the procedure reported in the paragraph 3.3 for each types of film.

The ceria precursor sol was prepared by dissolving 2 g of urea, CTAB, or Pluronic F127 and 0.5 ml of HCl in 20 ml of 2-propanol and left under stirring for 5 min.; this solution was then added dropwise to the cerium nitrate solution which was previously prepared by dissolving 7 g of Ce $(NO_3)_3.6H_2O$ and 0.5 ml of HCl in 20 ml of 2-

propanol. The precursor sol was then deposited by spin coating on a titania mesoporous film using 400 rpm for 40 s. The as-prepared films were directly exposed to hard X-ray radiation using the deep X-ray lithography (DXRL) beamline at Elettra synchrotron facility (Trieste, Italy). The storage ring worked at 2 GeV. The sample was mounted on top of a water-cooled stainless steel plate (scanner), which was continuously rastering the sample in front of the beam to allow for a homogeneous exposure of areas larger than the beam size; the scanner rate was set to 20 mm s^{-1}. At the exposure plane (position of the sample) the beam size was 115.5 mm X 10.6 mm. The films were irradiated with different doses (energy per unit area at the sample surface) by changing the exposure time (61, 132, and 234 s). In fact, the energy per unit area is equal to the exposure time multiplied by the X-ray power per unit area, hitting the sample P = 2.472 W cm^{-2}. The films were exposed to doses corresponding to 163, 326, and 653 J cm^{-2}. A mask containing test patterns of different size, shape, and geometry (5−500 μm) was then used to produce patterns on the films that were exposed to the X-ray beam. The mask had a gold absorber 20 μm thick and a titanium transparent membrane with thickness of 2.2 μm. Mesoporous films were exposed, without mask, to the same X-ray doses of the patterned samples and then impregnated with a solution containing ethanol and Rh6G (5.10^{-3} M) to test the antioxidant properties. Afterward, the films were placed at a distance of around 5 mm from a UV lamp and exposed to UV radiations for increasing time. The lamp mounted a fluorescence tube for emission at λ = 365 nm with a nominal power density of 470 μW cm^{-2} at 15 cm. As a reference, Rh6G was deposited on silica slides and on pure mesoporous films, not containing ceria nanoparticles and not exposed to DXRL; the samples were then exposed to UV light following the above protocol.

3.5. Nanoparticles and films characterization

- *Nanoparticles*

X-ray diffraction (XRD) pattern of CeO_2 nanoparticles used in cell cultures was collected by a Bruker D8 "Discover" in grazing incidence geometry with a Cu Ka line (λ= 1.54056 Å); the X-ray generator worked at a power of 40 kV and 40 mA. The patterns were recorded in 2θ mode ranging from 20 to 80° with a step size of 0.02° and a scan speed of 0.5 s until an optimal signal-to-noise ratio was achieved. The average crystallite size D was calculated from the broadening of the X-ray line (1 1 1) using Scherrer's equation[2,3] and EVA program.

X-ray diffraction (XRD) patterns of CeO_2 nanoparticles grafted on hybrid films and patterns of mesoporous films loaded with CeO_2 nanoparticles were collected using a Bruker D8 discover instrument described above. The patterns in the first case were recorded in 2θ ranging from 25 to 75° and in the second case from 10 to 100° with a step size of 0.02° and a scan speed of 0.5 s by a repetition mode for 12 h until maximization of the signal-to-noise ratio. The patterns of SPIONs deposited on silicon substrates, and SPIONs grafted on hybrid films were recorded in 2θ ranging from 25° to 70° with a step size of 0.02° and a scan speed of 0.5. The XRD data were analyzed with the MAUD software according to the Rietveld method; average crystallite size and lattice strain were separated from the total broadening assuming a dependence of microstrain from the reflection order following an isotropic model.[4]

A Vertex 70 Bruker spectrophotometer in the 400–4000 cm^{-1} range, with a resolution of 4 cm^{-1} was used for Fourier transform infrared (FTIR) spectroscopy. Nanoceria, NH_2-nanoceria and FITC–NH_2-nanoceria solutions were casted onto a silicon wafer and then measured in transmission; bare silicon was used as a background reference. The FTIR spectra were analyzed in the 3700– 400 cm^{-1} region; the baseline was corrected using a concave rubberband function with OPUS 7 software. Transmission electron microscopy (TEM) images were obtained by using a Hitachi H-70000 microscope equipped with a tungsten cathode operating at 125 kV. For sample

measurements, few drops of nanoceria were cast on a carbon coated copper grid and dried for observations.

-Hybrid organic−inorganic films containing ceria and Spion nanoparticles

Fourier transform infrared (FTIR) measurements were performed using a Vertex 70 Bruker spectrophotometer in the 400−4000 cm^{-1} range with a resolution of 4 cm^{-1} on films deposited on a silicon wafer; silicon was used for the background reference. The FTIR spectra were analyzed in the 3750− 2750 cm^{-1} region correcting the baseline by subtracting a concave rubberband with OPUS 7 software. Optical properties have been measured by a Nicolet Evolution 300 UV−vis spectrophotometer working in intelliscan mode, silica glass has been used as background reference. An atomic force microscope (NT-MDT Ntegra) was used to analyze the topography of the samples. Surface was measured at 0.5−1 Hz scan speed in semicontact mode, using a silicon tip with nominal resonance frequency of 130 kHz, 4.4 $N.m^{-1}$ force constant, and 10 nm typical curvature radius. Measures of surface roughness were performed by using the WSxM 5.0 Develop 3.2 software.[5]

Transmission electron microscopy (TEM) images were obtained using a JEOL 200CX microscope equipped with a tungsten cathode operating at 200 kV. Prior to observation, a fragment of the sample was removed from the substrate and deposited on a carbon-coated copper grid after gentle grinding on an agate mortar.

A Bruker Senterra confocal Raman microscope working with a laser excitation wavelength of 532 nm at 50 mW of nominal power was used for ceria grafted on hybrid film Raman characterization. The 100X objective was selected and an array of 6 x 8 points was defined to cover an area of 15 x 20 μm with a step of 2.5 μm. Each spectrum of the map was obtained by averaging 5 acquisitions of 5 s. The Raman spectra were collected in a region of 5 μm^2 where ceria nanoparticles were previously identified by optical microscope. To monitor the ceria release, 3 points were measured in the selected region before and after immersion of the sample in the phosphate

buffer. The spectra were averaged in the 425−490 cm^{-1} range after rubberband baseline subtraction; OPUS 7 software was used for data manipulation. Every point of the release experiment was obtained by using different samples from the same batch; each sample was immersed for the selected delivery time. Before every release test the Raman reference spectra (time 0) were collected and compared to those ones after the test; finally the measured spectra have been normalized using the Raman spectra before the release test.

Optical properties have been measured by a Nicolet Evolution 300 UV–Vis spectrophotometer working in intelliscan mode; silica glass was used as background reference. For SPION grafted on hybrid film a Bruker Senterra confocal Raman microscope (100X objective) working with a laser excitation wavelength of 633 nm at 5 mW of nominal power was used for Raman characterization. Each spectrum of the map was obtained by averaging 6 acquisitions of 3 s. The Raman spectra were analyzed in the 800–150 cm^{-1} range for SPION and 490–430 cm^{-1} for ceria after rubberband baseline subtraction. The pattern of SPIONs grafted on the hybrid film was obtained using a 633 nm Raman laser at 20 mW. The corresponding laser spot size, s, was calculated using the following formula $s = 1.27\ \lambda/NA$, where λ is the laser wavelength and NA is the numerical aperture.[6] The patterned area was mapped with a 50 X objective, with a spot size of 1.6 μm, defining an array of 10 x 10 points to cover an area of 15 x 15 μm^2 with a step of 2.5 μm. Each spectrum of the map was obtained by averaging 5 acquisitions of 10 s. The Raman laser used for mapping was 633 nm at power of 2 mW.

SEM morphology analysis was performed by coating the samples with gold in an Edwards S150A Sputter Coater unit and examining them with a Zeiss EVOLS 10 environmental scanning electron microscopy (ESEM), in high vacuum modality with secondary electron detector.

An atomic force microscope (NT-MDT Ntegra) was used to analyze the topology and perform phase imaging on the hybrid organic–inorganic films. Surface was measured at 1 Hz scan speed in semicontact mode, using a silicon tip with nominal resonance frequency of 127 kHz, 4.4 N m^{-1} force constant, and 10 nm typical curvature radius.

Surface coverage of the nanoparticles on hybrid organic–inorganic films was evaluated using the ImageJ software.

- *Mesoporous films embedding ceria nanoparticles*

TEM images of titania, hafnia and silica embedding nanoceria were taken with a transmission electron microscope (TEM; JEM-2000FX, JEOL, Japan) operating at voltage of 200 kV. For observation, the films were scratched into fine powders and then dispersed in ethanol to form a slightly turbid suspension. A small drop of the resultant suspension was placed on a carbon-coated copper mesh grid and dried at room temperature. Pore and ceria nanoparticle sizes were estimated from line profile analysis performed on representative TEM images with the ImageJ program.[7]

A Wollam-α spectroscopic ellipsometer with fixed angle geometry was used for thickness measurements of thin films deposited on silicon substrates. The thickness was estimated by fitting the experimental data with a Cauchy model for transparent films on Si substrates. The fit showed an average mean square error (MSE) of about 12 for titania mesoporous films and 20 for titania mesoporous films loaded with ceria nanoparticles.

The mesostructure characterization of the titania, hafnia and silica films were performed using synchrotron radiation by small-angle X-ray scattering (SAXS) in grazing incidence (GISAXS) mode at the Austrian high-flux beamline of the electron storage ring ELETTRA (Trieste, Italy). The angle of incidence of the beam (λ = 1.54 Å) was set either to 90° (transmission mode) or slightly above the critical angle (grazing incidence mode or GISAXS). Two-dimensional patterns were recorded with a CCD detector (Photonic Science).

A Raman microscope was used to detect the formation of ceria nanoparticles inside the mesoporous films. A Bruker Senterra confocal Raman microscope working with a laser excitation wavelength of 532 nm at 12 mW of nominal power was used for optical microscopy (100X magnification) and Raman spectroscopy analysis; the spectra were recorded by averaging 30 acquisitions of 2 s. Raman imaging maps were

obtained by selecting the 100x objective, and an array of 10 x 10 points was defined to cover an area of 35 × 35 μm with a step of 3.5 μm. Each spectrum of the map was recorded by averaging five acquisitions of 5 s.

A Bruker M4 Tornado X-ray fluorescence spectrometer with a 10x objective was used to observe the Ce and Ti element content over an area of 1.8 x 1.8 mm of titania mesoporous films patterned with ceria nanoparticles. The samples were washed with fresh 2-propanol before measuring, to remove the unreacted ceria precursors from the unexposed regions. The maps were recorded under vacuum using an X-ray tube with Rh anode at 600 μA and 50 KV without any filter and with a spot size of 4 μm.

Absorption spectra of the Rh6G deposited on bare silica slides and CeNPs-loaded mesoporous titania films were measured in the 200− 900 nm wavelength range using a UV−vis Nicolet Evolution 300 spectrometer, at 500 nm**.**min.$^{-1}$ scan rate. Each acquisition was the average of three different scans collected with a bandwidth of 1.5 nm.

3.6. Incubation of nanoceria with cell cultures

3.6.1. Nerve Pheochromocytoma cells (PC12)

- *Cell culture and viability assay*

PC12 cells (ATCC CRL-1721), derived from a transplantable rat pheochromocytoma, are a valuable model for neuronal differentiation, mimicking any features of central dopaminergic neurons including dopamine production.[8] Cells were maintained at 37 °C in 60mm plastic culture plates in an atmosphere of 5% CO_2/95% humidified air. The formulation of the culture medium was prepared as follows: Dulbecco's modified Eagle's medium (DMEM) – F12 supplemented with 10% horse serum and 5% fetal bovine serum. For viability testing PC12 cells were exposed or not exposed (control) for 48 hours to different concentrations of ceria nanoparticles (5–5000 mg**.**ml^{-1}) in 24-well plates (10^5 cells per well). To evaluate ceria neuroprotective effect, PC12 cells were pre-treated for 24 h with 10, 20 and 50 mg ml^{-1} of ceria and then $MnCl_2$ and/or L-DOPA were added at the concentration of 750 mM and 20 mM respectively for

further 24 h. All experiments were done in triplicate. Cell viability was then assessed by the 3- (4, 5-dimethyl-thiazol-2-yl)-2, 5, diphenyltetrazolium bromide (MTT) assay. In this assay, viable cells convert the soluble dye MTT to insoluble (in aqueous media) blue formazan crystals. In details, 200 ml of MTT [5 mg ml^{-1} stock solution in phosphate buffered saline (PBS)] was added to 1 ml of medium and incubated at 37 °C for 4 h. The MTT was removed and the cells rinsed with PBS and centrifuged at 4000 rpm for 20 min. The resulting pellet was dissolved in 2 ml of isopropanol and centrifuged at 4000 rpm for 5 min. Finally the supernatant color was read at 600 nm using a Bauty Diagnostic Microplate Reader. A calibration standard curve was achieved before each experiment using different cells concentration.

- *PC12 apoptosis assessment*

PC12 cells were seeded in a 24-well plate, pre-treated for 24 h with 10, 20, 50 and 100 $mg.ml^{-1}$ of ceria, at concentration of $1.2.10^5$ cells per well and cultured overnight. Then $MnCl_2$ (750 mM) and/or L-DOPA (20 mM) were added to cells and incubated for further 24 h. After incubation the cells were washed with annexin binding buffer. Cell apoptosis was assessed using annexin V-fluorescein isothiocyanate (FITC) apoptosis detection kit (BD Biosciences, San Diego, USA). Cells were incubated with FITC-labelled annexin V and propidium iodide (PI) for 15 min. in dark at room temperature (20–25 °C). The cell percentage showing annexin V+/PI- and annexin V+/PI+ was used to evaluate apoptotic cells by a FACS Calibur with Cell Quest 6.0 software (BD Bioscience); 10 000 events were collected for each experiment.

- *Evaluation of ceria uptake into PC12 cells*

PC12 cells were exposed or not exposed (control) for 48 hours to different concentrations of FITC–NH_2-nanoceria (20–50–100 $mg.ml^{-1}$) in 24-well plates ($1.2.10^5$ cells per well). After incubation, the cells were washed 3 times with PBS and resuspended in Dulbecco's modified Eagle's medium containing 0.25% w/w of trypan blue. The uptake of FITC–NH_2-nanoceria into PC12 cells was evaluated by FACS

Calibur flow cytometer (Becton Dickinson, FACScalibur™, and USA) and Raman spectroscopy. The side scatter data obtained by flow cytometry were analyzed using CELL Quest 6.0 software (BD Bioscience).[9] For Raman analysis PC12 cells were seeded on gelatin (1 mg•ml^{-1} in sterile milliQ water) coated glass cover slips at 10^5 cells per ml and cultured overnight. Then cells were treated with ceria nanoparticles (40 mg•ml^{-1}) for another 24 h. After that, cells were rinsed two times with PBS and glass cover slips were placed and sealed on a microscope slide. The intracellular localization was detected by a Bruker Senterra confocal Raman microscope (50X magnification for optical images) working with a laser excitation wavelength of 532 nm at 12 mW of nominal power. Raman imaging maps were obtained by selecting the 50X objective, and defining an array of 598 points in order to cover an area of 25 x 22 mm with a step of 1.0 mm. Each spectrum of the map was recorded by averaging 10 acquisitions of 3 s.

For confocal microscopy analysis, PC12 cells were seeded on gelatin (1 mg**.**ml^{-1} in sterile milliQ water) coated glass cover slips at 10^5 cells per ml and cultured overnight. Then, the cells were treated with FITC–NH_2 nanoceria (10 or 20 mg**.**ml^{-1}) for another 24 h. Afterwards, the cells were rinsed two times with PBS and stained with DAPI (5 mg**.**ml^{-1} in PBS) for 15 min., protecting them from light. Cells were then rinsed one time with PBS and sealed on microscope slides. Samples were observed with a Leica Microscope, equipped with a Leica Confocal Laser System C2s. The images were analyses by Leica Application Suite Advance Fluorescence Lite (LAS AF) program.

- *Chromatographic analysis*

High performance liquid chromatography with electro-chemical detection (HPLC-EC) was used to quantify DA, dihydroxyphenylacetic acid (DOPAC), homovanillic acid (HVA), 3-methoxytyramine (3-MT) using an Alltech 426 HPLC pump equipped with a Rheodyne injector, column 15 cm 64.6 mm i.d. Alltech Adsorbsphere C18 5U, electrochemical detector Antec CU-04-AZ and Varian Star Chromatographic Workstation. Citric acid 0.5 M, Na acetate 1.0 M, EDTA 12.5 mM, MeOH 10% and

sodium octylsulphate 650 mg.ml^{-1} (pH 3.0) was the mobile phase; the flow rate was 1.3 ml min.$^{-1}$.[10]

- *Statistical analysis*

All *in vitro* data derive from at least three independent experiments and results are expressed as mean values with 95% confidence intervals. The statistical significance of differential findings between experimental and control groups was estimated by paired or unpaired t-test in Graph-Pad Prism 5.0 software (GraphPad Software, Inc, San Diego, CA, USA). These findings were considered significant if two-tailed P values were <0.05.

3.6.2. Cumulus-oocyte complex (COCs)

- *Oocyte collection and in vitro maturation*

Ovaries were collected from prepubertal lambs (Sarda breed; 30-40 days of age, body weight 6-10 kg) at a local abattoir and transported to the laboratory within 1–2 hr in Dulbecco phosphate buffered saline (PBS) with antibiotics. Collection of cumulus–oocyte complexes (COCs) was performed in sterile Petri dishes containing 20 mM Hepes buffered TCM 199 supplemented with 0.1% (w/v) polyvinyl alcohol (PVA) and antibiotics. Only COCs showing several intact cumulus cell layers and uniform cytoplasm with homogenously distributed lipid droplets were selected for *in vitro* maturation. *In vitro* maturation medium was TCM 199 supplemented with 10% heat-treated oestrus sheep serum (OSS), 0.1 IU/ml FSH, 0.1 IU/ml LH. COCs were evenly divided and cultured in maturation medium supplemented with CeO_2 NPs at concentration of 0 μg/ml, 44μg/ml, 88 μg/ml, 220 μg/ml. Thirty to thirty-five COCs were cultured for 24 hr in 5% CO_2 in air at 38.5°C in four-well Petri dishes (Nunclon; Nalge Nunc International, Roskilde, Denmark) with 600 ml of maturation medium, layered with 300 ml of mineral oil.

- Transmission Electron Microscopy for CeO_2 NPs uptake evaluation

To verify the potential internalization of the CeO_2 NPs, COCs were incubated for 2 hr (germinal vesicle oocytes – GV, n= 30) or for 24 hr (metaphase II oocytes - MII, n=30) with CeO_2 NPs (44μg/ml, 220 μg/ml, n=15 for each group) and analyzed by TEM. After incubation, GV and MII COCs were washed twice in cacodylate buffer (0.1 M, pH = 7.4), fixed in 2.5% glutaraldehyde and post-fixed in osmium tetroxide 2% in the same buffer. After centrifugation, the pellets were dehydrated in graded alcohol solutions and embedded in Embed-812 kit using a standard procedure. Ultrathin sections (60–70 nm) were counterstained with uranyl acetate and lead citrate before observation with an electron microscope Zeiss 109 EM Turbo (Carl Zeiss, Germany) at 80 kV.

- Immuno fluorescence labelling and analysis by confocal microscopy

Groups of oocytes matured *in vitro* in presence of CeO_2 NPs at increasing concentrations of 0μg/ml (n=30), 44 μg/ml (n=30), 88 μg/ml (n=30) and 220 μg/ml (n=30) were fixed and processed for microtubules, F-actin and DNA immunofluorescence as previously described.[11] Fixation was carried out for 45 min. at 38°C in a microtubule stabilizing buffer (100 mM PIPES, 5 mM $MgCl_2$, 2.5 mM EGTA, 2% formaldehyde, 0.1% Triton- X-100, 1 mM taxol, 10 U/ml of aprotinin, and 50% deuterium oxide). Oocytes were stored until use in a blocking solution comprising PBS supplemented with 2% bovine serum albumin, 2% skim milk powder, 2% normal goat serum, 100 mM glycine, 0.01% Triton-X-100, and 0.2% sodium azide. For immunostaining of microtubules and F-actin, oocytes were first incubated with mouse monoclonal anti–αβ-tubulin diluted 1:100 in blocking solution overnight at 4°C, followed by incubation for 1 hr at 37°C with donkey anti-mouse Alexa Fluor 488 secondary antibody (Invitrogen) at 1:100 final dilution combined with rhodamine phalloidin (1:150, Invitrogen). DNA was stained with Hoechst 33258 (1μg/ml in blocking solution) for 30 min. Oocytes were mounted under cover slips without compression in medium containing 50% glycerol and 25 mg/ml sodium azide. F-

Actin, microtubules and chromosomes were visualized on a confocal laser-scanning fluorescence microscope Leica TCS SP5, equipped with 543 nm HeNe, 488 nm Argon and 405 nm 405-diode laser. The images were acquired using an oil immersion 40x objective (NA=1, 25) and recorded in the host computer. Cortical F-actin images were recorded considering the sections corresponding to the equatorial plane of the cell by scanning the oocyte through the Z-axis.

- *Intracellular ROS measurement*

After IVM in medium supplemented with different concentrations of CeO_2 NPs (0 μg/ml, 44 μg/ml, 88 μg/ml, and 220 μg/ml) oocytes at the metaphase II (MII) stage were sampled for determination of intracellular ROS levels. Briefly, 2'7' dichlorodihydrofluorescein diacetate (H_2DCFDA) was used to detect intracellular ROS as green fluorescence. Thirty oocytes from each group were incubated in the dark for 30 min. in PBS-PVA containing 10 μM H_2DCFDA. After incubation, oocytes were washed 3 times in pre-warmed PBS-PVA and fixed overnight at 4°C with 2% paraformaldehyde solution in PBS. The oocytes were washed with PBS-PVA, placed in 20 μL droplets and then fluorescence was observed using an epifluorescence microscope (IX 70, Olympus, Italy) with 460 nm. Microscope adjustments and photomultiplier settings were kept constant for all experiments. Oocytes were positioned in the plane of focus, and the area of measurement was adapted to the size of the oocyte. The data of emission intensity/oocyte were reduced by compensation for the background fluorescence. Oocyte fluorescence intensities were analyzed using Image J software (version 1.40; National Institute of health, Bethesda, MD) and normalized to that of control oocytes.

- *In vitro fertilization and embryo culture*

After *in vitro* maturation, oocytes of the different experimental groups: 0 μg/ml (n=129), 44 μg/ml (n=127), 88 μg/ml (n=109) and 220 μg/ml (n=110) were fertilized *in vitro* (IVF) in SOF medium with 2% OSS for 22 hr at 38.5°C and 5% CO_2, 5% O_2 and 90% N_2 under mineral oil in four-well Petri dishes with frozen–thawed spermatozoa selected by swim-up technique (1.10^6 spermatozoa/ml). Zygotes were cultured for 7 days in groups in four-well Petri dishes in SOF essential and non-essential amino acids at oviductal concentration,[12] 0.4% BSA under mineral oil, in maximum humidified atmosphere with 5% CO_2, 5% O_2 and 90% N_2 at 38.5°C. The first cleavage was registered at 24 hr and 30 hr after the start of fertilization. Development to blastocyst stage was recorded on the 7th day of culture.

To differentially stain inner cell mass (ICM) and trophectoderm (TE) cell, blastocysts derived from the different maturation treatment groups were exposed to 1% Triton X-100 in 20mM Hepes buffered TCM 199 for 3–5 seconds, washed 3–5 times and incubated in the same medium containing 30 mg/ml propidium iodide (PI) for 30 seconds. The blastocysts were then transferred into ice-cold ethanol containing 10 mg/ml Hoechst 33342 for 5 min. The blastocysts were directly mounted into a small droplet of glycerol on a glass slide and examined under epifluorescent microscope (Olympus IX70, Italy). ICM nuclei appeared blue, caused by DNA labelling with Hoechst 33342, while TE cells appeared red due to staining of nuclear DNA with membrane impermeable PI.

- *Statistical analysis*

Statistical Analysis was performed using SPSS 15.0 (SPSS Inc., Chicago, USA). The data relative to the blastocyst number and ROS levels were normally distributed and were analysed with Univariate Analysis of Variance with Bonferroni's as post hoc test, using treatment as fixed factor. Data of nuclear maturation, embryo development, and chromatin and cytoskeleton morphology were analysed by Chi-square with Bonferroni's as post hoc test.

3.6.3. Spermatozoa

- *Experimental design*

Ram semen was collected and submitted to an initial assessment: only those ejaculates that scored at least 3 for mass motility and had a concentration of 3.10^9cells/ml were chosen for the experiment. After collection, each ejaculate was temporarily stored in a water bath at 30°C and processed by CASA (computer assisted sperm analysis). The ejaculates were pooled, diluted 1:5 in OVIXcell and analysed for the integrity of acrosomal and cytoplasm membranes (PI/PSA), kinematic parameters (CASA), oxidative stress (H_2DCFDA and Mitotracker) and DNA integrity (SCSA) in order to assess the initial conditions of the semen before the exposure to CeO_2 NPs (fresh control, 0h). The diluted samples were divided into 4 aliquots supplemented with increasing doses of CeO_2 NPs (0, 22, 44 and 220 μg/ml), allowed to gradually cool to 4°C for 2 h and stored at 4°C for up to 24h. Analysis on the interaction among sperm cells and nanoparticles, integrity of acrosome and cytoplasm membranes, kinematic parameters, oxidative stress and DNA integrity were carried out on the 4 treatment groups at 2 and 24 hours of exposure. The experiment was carried out in 6 replicates.

- *Animal management and semen collection*

For the present experiment ejaculates were collected from 5 healthy adults (2-6 years old) Sarda rams (Genetic Centre of AGRIS, Agenzia Regionale per la Ricerca in Agricoltura, Bonassai, Italy). The animals were of proven fertility and trained to service an artificial vagina. They were kept indoors and fed with concentrates (400 g/day) and hay *ad libitum*. Their sanitary status was assessed and a breeding soundness evaluation was carried out before selecting them for the experiment.

- *Transmission electron microscopy for the assessment of CeO_2 NPs uptake*

An aliquot of semen (50μL) from each group (fresh control and treated groups) was fixed in 4% glutaraldehyde in PBS. Samples were then post-fixed in 1% OsO_4

overnight, dehydrated, embedded in resin and sectioned for TEM. The sections (80 nm) were then observed at 80kV using a Zeiss 109 electron microscope (Carl Zeiss, Germany) in order to evaluate the interaction and potential uptake between nanoceria and spermatozoa.

- *Membrane integrity and acrosome status*

An aliquot of semen (10µL) from each group (fresh control and treated groups) was processed to assess membrane integrity and acrosome status by differential staining. Briefly, each aliquot was added to 290µL of PBS (phosphate buffer saline), 2.8µL PI (Propidium Iodide, 1mg/ml) and 4µL FITC-*PSA* (*Pisum Sativum* agglutinin conjugated with fluorescein isothiocyanate; 1mg/ml) and incubated in the dark for 15 min. at 37°C. Samples were then centrifuged at 4229 RPM for 3 min. and the supernatant was discarded. The pellets were re-suspended in 500µL PBS and centrifuged at 4229 RPM for 3min. This step was repeated once and the final pellet was re-suspended in 250µL PBS. A 10µL drop was placed on a warm slide with a cover slip and observed under fluorescence microscope (Olympus IX70, Olympus Optical Co. LTD, Japan). A total of 100 spermatozoa from each sample were analysed and classified into 4 categories: 1) viable (intact membrane, unstained, PI-/PSA-); 2) dead (altered membrane, red, PI+/PSA-); 3) viable reacted (acrosomal reaction, green, PI-/PSA+); 4) dead reacted (altered membrane and acrosomal reaction, red and green, PI+/PSA+).

- *Motility assessment by CASA*

Motility analysis was performed on fresh control and groups exposed to CeO_2NPs by CASA. Samples were analysed for total (TM) and progressive motility (PM) and specific kinematic parameters as smoothed path velocity (VAP), straight line velocity (VSL), track velocity (VCL), lateral head displacement (ALH), beat cross frequency (BCF), straightness (ratio VSL/VAP, STR), linearity (ratio VSL/VCL, LIN).

Morphology analysis and velocity distribution (rapid, medium, slow and static spermatozoa) were also evaluated.

- *Flow cytometer analyses*

Flow cytometry was performed using the BD FACSCanto™ platform and the data were analysed by BD FACS DIVA software (BD Biosciences, USA). A total of 20000 events per sample were acquired.

- *Sperm chromatin structure assay*

The labelling of fragmented DNA in fresh controls and in the samples incubated with CeO_2 NPs was carried out as previously described by Evenson et al.[13] The technique identifies spermatozoa with abnormal chromatin based on the metachromatic stain Acridine Orange that labels in red single strand DNA and in green the double strand DNA. Briefly, 50 µL of each sample was diluted in 150 µL TNE buffer (0.15M NaCl, 1mM EDTA, and 10mM Tris, pH 7.2) at 4°C, immediately plunged into liquid nitrogen and stored at -80°C until analysis. The frozen samples were thawed in crushed ice and 200 µL of the sperm/TNE suspension was mixed to 400 µL of Acid Detergent Solution (0.08 M HCl, 0.15 M NaCl, 0.1% Triton X-100, pH 1.4). After 30 sec, 1.2 ml of staining solution (0.15 M NaCl, 1 mM EDTA, 10 mM Tris, 0.2 M NA_2HPO_4, 0.1 M citric acid, pH 6) containing 6 µg/ml of Acridine Orange, was added to the mixture. Within 3 min. from the staining, the samples were run through the flow cytometer. The levels of DNA fragmentation were assessed calculating the DFI (DNA fragmentation index) as the ratio of red fluorescence and total fluorescence (green + red).

- *ROS production*

Reactive oxygen species production of samples incubated with CeO_2 NPs and controls were assessed by staining with 2',7'dichlorofluorescein diacetate (H_2DCFDA). Briefly, 25µL of each sample was diluted in 1ml PBS containing 10µM H_2DCFDA

and incubated in the dark for 30min. at 38°C. Following incubation, samples were centrifuged at 4229 RPM for 3 min., the supernatant was gently discarded, replaced by 500 µL 2% paraformaldehyde and left at 4°C for 1 h. After fixation, samples were centrifuged again at 4229 RPM for 3 min. and the supernatant removed and replaced by 300 µL PBS. Samples were stored in the dark at 4°C until flow cytometric analysis.

- *Mitochondrial activity*

Mitochondrial activity was labelled with Mitotracker Orange (Molecular Probes, Oregon, USA). An aliquot (25µL) from each group was diluted in 1ml PBS and incubated with Mitotracker Orange (100nM) in the dark for 30 min. at 38°C. Samples were then centrifuged (4229RPM x 3 min.), washed twice, and fixed following the steps described above for H_2DCFDA.

- *Statistical analysis*

Statistical Analysis was performed using SPSS 15.0 (SPSS Inc., Chicago, USA). The data were normally distributed and were analysed by Univariate Analysis of Variance with Bonferroni's as post hoc test, using time and treatment as fixed factors.

3.6.4. A peripheral blood mononuclear cells (PBMC)

Peripheral blood mononuclear cells (PBMC) derived from the blood bag buffy coat of healthy donor's blood transfusion center of Santissima Annunziata Hospital (Sassari). Buffy coat is a light stratum of blood between the plasma and the red blood cells after blood centrifugation, containing mostly white blood cells. Platelets are at the top of this coat; the other layers are lymphocyte, monocytes, granulocytes and adreticulocytes.

The PBMC cells have been isolated by using a modifying Boyum method.[14] Briefly, buffy coat has been resuspended in Hanks salts and then the blood has been sedimented on Ficoll Histopaque, which allows isolating lymphocytes from diluted whole blood. Then the cells have been counted and plated (2.10^6 per well) on the

titania, hafnia and silica films with and without embedded nanoceria, in RPMI (1640 with fetal calf serum) cell culture medium and incubated at 37°C in CO_2 5% for 24h. The incubated samples have been divided in two groups; one has been activated with Concanavalin A (10μg/ml of cell suspension) and the other one has been not treated.

- *PBMC apoptosis assessment*

After 24h incubation the cells were washed with annexin binding buffer. Cell apoptosis was assessed using annexin V-fluorescein isothiocyanate (FITC) apoptosis detection kit (BD Biosciences, San Diego, USA). Cells were incubated with FITC-labelled annexin V and propidium iodide (PI) for 15 min. in dark at room temperature (20–25 °C). The cell percentage showing annexin V+/PI- and annexin V+/PI+ was used to evaluate apoptotic cells by a FACS Calibur with Cell Quest 6.0 software (BD Bioscience); 10 000 events were collected for each experiment.

3.7. References

[1] Yu S., Chow G.M. J. Mater. Chem. **(2004)**, 14, 2781–2786.

[2] Athawale A.A., Bapat M.S., Desai P.A.J. Alloys Compd. **(2009)**, 484, 211–217.

[3] Samiee S., Goharshadi E.K. Mater. Res. Bull. **(2012)**, 47, 1089–1095.

[4] Lutterotti L., Gialanella S. Acta Mater. **(1998)**, 46, 101−10.

[5] Horcas I., Fernandez R., Gomez-Rodriguez J.M., Colchero J., Gomez-Herrero J., Baro A.M. Rev. Sci. Instrum. **(2007)**, 78, 013705− 013712.

[6] Lewis I.R., Edwards H.G.M. Handbook of Raman spectroscopy: from the research laboratory to the process line, vol 28., Practical spectroscopic series. CRC Press, NewYork, pp 149–153 ago **(2001)**.

[7] Schneider C.A., Rasband W.S., Eliceiri K.W. Nature Methods. **(2012)**, 9, 671−675.

[8] Ciofani G., Genchi G., Liakos I., Cappello V., Gemmi M.,. Athanassiou A, Mazzolai B., Mattoli V. Pharm. Res. **(2013)**, 30, 2133–2145.

[9] Suzuki H., Toyooka T., Ibuki Y. Environ. Sci. Technol. **(2007)**, 41, 3018–3024.

[10] Serra P.A., Rocchitta G., Esposito G.,. Delogu M.R, Migheli R., Miele E., Desole M.S., Miele M. Br. J. Pharmacol. **(2001)**, 134, 275–282.

[11] Simerly C., Navara C.S.,Wu G.J., Schatten G. Cytoskeletal organization and dynamics in mammalian oocytes during maturation and fertilization. In: Grudzinskas JG, Yovich JL, editors. Gametes - the oocyte. Cambridge: Cambridge University Press. 54–94, **(1995)**.

[12] Walker S.K., Hill J.L., Kleemann D.O., Nancarrow C.D. Biol. Reprod. **(1996)**. 55, 703-8.

[13] Evenson D., Jost L. Sperm chromatin structure assay for fertility assessment. Curr Protoc Cytom. **(2001)**, Chapter 7:Unit 7.13.

[14] Bøyum A. Scand. J. Immunol. **(1976)**, 5, 9-15.

4. Results and discussion

The main goal of this thesis is to test the potential of ceria nanoparticles as platform for biological applications, in particular as inorganic antioxidant, mimicking enzyme activity. This goal has been achieved through a careful selection of the nanoparticle synthesis, keeping in mind a fundamental requirement for the final application that is a nanoparticle dimension below 10 nm. As it is reported in Paragraph 1.2.6, the size is a critical parameter for determining the nanoceria reactivity, especially when radical scavenger property is required. This chapter is divided into two parts: the first part deals with the study of naked nanoceria and its interaction with the cellular environment while the second part is focused on the study of nanoceria in nanocomposite materials.

The first part reports on the nanoceria interactions with three types of cells: PC12, ovine oocytes and ram spermatozoa.

Nanoceria with controlled size have been studied as antioxidant agents for the *in vitro* protection of catecholaminergic cells (PC12) exposed to manganese, which is responsible for an occupational form of Parkinson-like disease. With the perspective to develop an innovative combined treatment, nanoceria has been tested either alone or in association with L-DOPA against the oxidative stress due to manganese chloride. Finally, the intracellular concentration of dopamine and its metabolites have been monitored as a function of the nanoceria dosing, in order to study the protective role of nanoceria on the metabolism of catecholamines.

As reported in Paragraphs 1.6.2, the *in vitro* maturation and fertilization of oocytes and spermatozoa are strongly affected by ROS, which can determine a defective development of the embryo. Therefore, we decide to investigate the capacity of nanoceria to neutralize ROS in both germinal cells. Prepubertal ovine oocytes have been cultured with different doses of ceria nanoparticles and then the study of embryonic development has been carried out. The nanoceria behaviour in TCM199 media and in water has been evaluated after 2, 4, 6, 8, 10 and 24 h of incubation

monitoring the nanoceria aggregation. The study of nanoceria in cumulus cells, both in the immature (GV stage) and mature (MII stage) oocytes, has been performed. The effects of different doses of nanoceria have been tested on chromatin and cytoskeleton morphology of the oocytes. The intracellular ROS productions have been also quantified.

The interaction and the short-term effects of increasing doses of ceria nanoparticles have been also investigated in ram spermatozoa, stored at 4°C for up to 24h. In particular we have studied the kinematic parameters, the membrane status and DNA fragmentation of spermatozoa. Then, we have also evaluated the nanoceria antioxidant properties against oxygen species (ROS) production and measured of mitochondrial activity.

The second part of the chapter is focused on the applications of nanoceria in films through the creation of multi-phase nanocomposite surfaces. This has been achieved with two different approaches: the anchoring of nanoceria on a hybrid organic-inorganic film with controlled surface chemistry (paragraphs 4.2.1 and 4.2.2) and the *in situ* nucleation of nanoceria by a combined top-down and bottom-up approach (Paragraphs 4.2.3 and 4.2.4).

Paragraphs 4.2.1 and 4.2.2 report on the study of the surface chemistry of a hybrid films with specific interaction with nanoceria and its controlled release in buffer solution. The controlled release of ceria nanoparticles from a hybrid organic-inorganic surface is expected to be used in the development of contact lenses based on a slow delivery of oxygen scavengers. A solventless synthesis, which used 3-glycidoxypropyltrimethoxysilane an organically modified alkoxide, of the hybrid films at high pH has been employed and the surface chemistry of the deposited films has been processed by controlling the aging time of the sol. The prepared hybrid film-ceria nanoparticles system has to fulfil the requirements of optical transparency and stability in buffer solutions which are necessary for contact lenses production.

Paragraphs 4.2.3 and 4.2.4 are focused on the nucleation and growth of nanoceria in mesoporous films through deep X-ray lithography and the toxicity evaluation of the obtained nanocomposites when they are used for cell culture. The nanocomposite films, which are made by mesoporous titania layers loaded with ceria nanoparticles, have been obtained by combining bottom-up self-assembly synthesis of a titania matrix with top-down hard X-ray lithography of nanocrystalline cerium oxide. At first the titania mesopores have been impregnated with the ceria precursor solution and then exposed to hard X-rays, which triggered the formation of crystalline cerium oxides within the pores inducing the in situ growth of nanoparticles with average size of 4 nm. Different types of coordinating agent have been used in the solution for nanoparticles formation. Diverse patterns have been also produced through deep X-ray lithography by spatially controlling the nanoparticle growth on the micrometer scale. The radical scavenging role of the nanocomposite films has been also tested using rhodamine 6G as a benchmark for UV photodegradation. Moreover the cellular toxicity of titania matrix with embedded nanoceria has been evaluated in PBMC cell culture and compare with another type of matrix, such as hafnia and silica.

4.1. Ceria nanoparticles for biomedical applications

The redox based regenerative anti-oxidant property of nanoceria and the capability of neutralizing and reducing ROS have generated deep interest among researchers as a potential tool for bio-medical applications. These properties are related to the presence of oxygen vacancies on the CeO_2 surface, which allows Ce ions to flip-flop between two oxidation states.[1] Since the antioxidant process is strictly correlated to the surface property, this effect becomes of extreme relevance when cerium oxide is used in form of nanosized particles.[2] When nanoceria is used in a biological environment, such as in cell cultures or animal models, the nanoparticles act as radical scavengers mimicking the role of superoxide dismutase and catalase. Compared to organic exogenous antioxidants, which are limited by chemical instability,[3] nanoceria shows the major

advantage of an auto-regenerative process.[4] In fact, the switching of cerium oxidation states allows restoring the radical scavenging properties without continuously dosing the drug, as in the case of organic exogenous antioxidants. In addition, antioxidant processes triggered by nanoceria provide an effective protection not only against ROS, but also towards other reactive molecules, such as nitrogen-based species (RNS)[5] enabling a simultaneous quenching of dangerous metabolic by-products. The applications of nanoceria in biomedical field include protection from radiation exposure, cancer therapy, neurodegenerative disease such as Parkinson and Alzheimer, cerebral ischemia and hypoxia, vision loss and eye disease, tissue regeneration and regenerative disease, endometriosis, etc.[6] However, the outcomes of ceria nanoparticles exposure can vary depending on the cell types.

4.1.1. Nanoceria characterization and functionalization

Nanoceria for incubation with PC12, oocyte and spermatozoa cells has been synthesized by a microwave treatment, a process that allows for a fast fabrication of well-dispersed nanoparticles in water without using thermal annealing.[7] The coordinating agent employed in this synthesis is urea, which is a biocompatible molecule. After synthesis, the nanoparticles (NPs) have been characterized by XRD and TEM to correlate their chemical–physical features with the functional properties. The XRD pattern in the 20°–80° 2θ angular range (Fig. 4.1) has been indexed according to the cubic fluorite structure of cerianite (JCPDS: 34-0394). The crystal size of nanoparticle, calculated by Scherer's equation, is 9 ±1 nm.

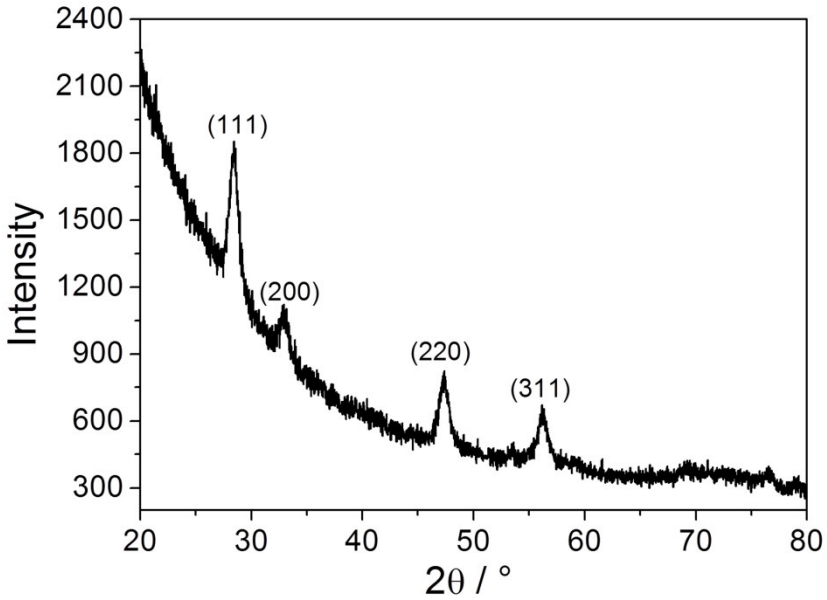

Fig.4.1 XRD pattern in the 20–80° 2θ range of ceria nanoparticles synthesized by microwave treatment. The peaks have been indexed according to the cerianite structure.

The size calculated by XRD is in accordance with nanoparticle diameter as measured by bright field TEM characterization (8.5 ± 1.3 nm) suggesting that the nanoparticles are formed by single crystals (Fig.4.2)

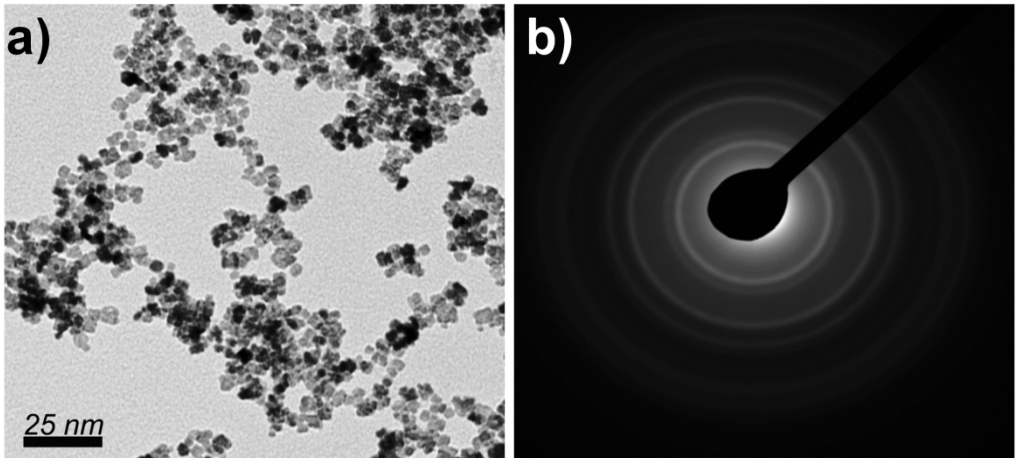

Fig.4.2 a) TEM image and b) electron diffraction pattern of ceria nanoparticles

Infrared spectroscopy has been used to characterize the functionalization of ceria NPs with the fluorophore FITC. Fig. 4.3a shows the spectrum of pure NPs in the 3700–400 cm^{-1} range; the broad band peaked at 3450 cm^{-1} is assigned to the symmetric stretching of the hydroxyl group on the nanoparticle surface[8] while the band at 1600 cm^{-1} is due to residual water. The bands below 1460 cm^{-1} (1465, 1319 and 1045 cm^{-1} respectively) have been attributed to the formation of CO_3^{2-} on the particle surface as a consequence of the interaction between CeO_2 and atmospheric CO_2.[9] Remarkably, the presence of these bands is strongly reduced if the particles are kept in solution.

Functionalization with FITC has been obtained through modification of the NPs surface with an organosilane linker (aminopropyl trimethoxysilane, APTES) containing a $–NH_2$ terminal group. Fig. 4.3b shows the change induced in the infrared spectra by the successful APTES modification. The broad band peaked at 3450 cm^{-1} decreases in absorbance, in accordance to the reduced amount of hydroxyls available on the NPs surface, while the introduction of aminosilane groups is confirmed by the appearance of three bands: the first one, at 1556 cm^{-1}, attributed to NH bending of the amide bond; the second one, peaked at 2966 cm^{-1}, due to CH_3 stretching mode and the third one, at 2932 cm^{-1}, related to CH_2 stretching. The broad band at 952 cm^{-1} has been assigned to the Ce–O–Si stretching vibration as a consequence of the covalent bond between APTES and nanoceria.[10] Fig.4.3d shows the spectrum of the NH_2 modified nanoceria after functionalization with FITC. By comparing the spectrum of the pure fluorophore, Fig. 4.3c, with that one of the FITC-functionalized nanoparticles, we observe the disappearance of the band relative to the isothiocyanate group N-C-S (at 2069 cm^{-1}) as a result of the coupling with the amine. A comparison between the spectra of Fig. 4.3d and c allows highlighting an increase of the CH_2 stretching band at 2930 cm^{-1} attributed to the fluorescent molecule linked to the ceria NPs.[10]

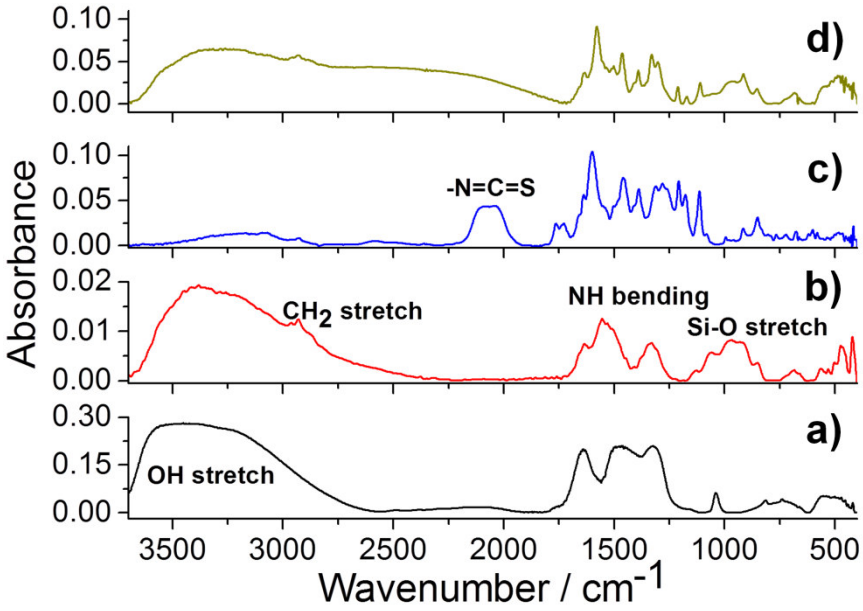

Fig.4.3 FTIR absorption spectra in the 3700–400 cm^{-1} range: (a) nanoceria (black line); (b) nanoceria functionalized with APTES (red line); (c) FITC (blue line) and (d) nanoceria functionalized with APTES and FITC (green line).

4.1.2. Nanoceria as a potential drug to treat Parkinson -like disease

Parkinson like disease (PLD) symptoms are produced by severe neurodegenerative processes caused by the interplay of a number of factors, such as environmental or genetic risk, age, mitochondrial dysfunction and other conditions leading to a reactive oxygen species (ROS) overproduction.[11] Among the different causes, oxidative stress has been widely believed to be an important pathogenetic mechanism of neuronal death in the disease, although it is still not clear whether it is an initial event causing cell death or a consequence of the disease. The causes of the oxidative stress can be found in a large variety of sources and, in some cases, the presence of PLD symptoms can be correlated with the exposure to transition metals such as Copper, Lead and Manganese.[12] In particular, chronic manganese intoxication in humans is responsible for early psychotic disorder that is later followed by permanent degenerative damage in the nigrostriatal system, resulting in a PLD. It is well known that manganese may stimulate dopamine (DA) autoxidation in the dopaminergic neuron, resulting in an

increase of the quinones levels. The generated quinones are thought to mediate toxicity by covalently binding to nucleophilic groups of biological macromolecules.[13] In virtue of the multiplicity of its oxidation states (commonly +2, +3, +4, +6 and +7), manganese shows a wide range of chemical interactions which becomes even more complex in a biological environment. This means that Mn can mimic other ions and enter into the brain through different carriers. As well as damage to the dopaminergic system, Mn induces mitochondrial dysfunction, impairment of cellular energy metabolism, glial activation, neuroinflammation and deep changes in synaptic transmission and astrocytes-neurons cross-talk;[14] all these factors contribute to the onset of the PLD. The administration of L-3,4-dihydroxyphenylalanine (L-DOPA), the natural precursor of dopamine in catecholaminergic neurons, is the most widely used treatment for PD-like syndrome; the alleviation of the symptoms related to the disease are due to a replenishment of DA in the surviving neurons. However, although many of the symptoms of PLD can be relieved, the therapy is not curative and dopaminergic cells continue dying in patients treated with L-DOPA. In fact, L-DOPA can undergo autoxidation and enzymatic oxidation, generating a variety of cytotoxic ROS, including superoxide, hydrogen peroxide, semiquinones, and quinones[15,16] which may further load the pre-existing condition of oxidative stress. Since L-DOPA induces oxidative stress-mediated apoptosis in cultured neuronal cells, the inappropriate L-DOPA-induced activation of apoptosis might have a role in neuronal death in PLD syndrome.[17] In this work, nanoceria has been tested as an adjuvant drug in the treatment of PLD syndrome which is an ideal model to test the nanoceria properties applied to neurodegenerative syndromes. The protective effects of nanoceria on manganese and L-DOPA-induced cytotoxicity have been evaluated in nerve pheochromocytoma cell line, PC12 cells. This cell line exhibits several physiological properties which are characteristic of dopaminergic neurons and therefore it is a good system for the study of oxidative stress in dopamine-containing cells.

- Effect of nanoceria concentration on the PC12 cells viability

To assess the toxicity of nanoceria, PC12 cells have been exposed to increasing concentrations of nanoparticles (from 0 to 5000 mg ml^{-1}) and their viability has been assessed by MTT assay. Fig. 4.4 shows that nanoceria has not affected on cells viability when administered in concentrations from 5 to 100 mg**.**ml^{-1} but starts becoming toxic at concentrations higher than 100 mg**.**ml^{-1}. This results in a statistically significant reduction ($p < 0.05$) of cell viability which gradually decreases in comparison with controls from 75%, at a concentration of 500 mg**.**ml^{-1}, down to 57% at a concentration of 4000 mg**.**ml^{-1}. MTT assay has allowed evaluating the maximum concentration of nanoparticles that does not induce cellular toxicity. According to these results, a range between 20 and 100 mg**.**ml^{-1} has been chosen to evaluate the NPs antioxidant effect by apoptosis assay on a cell culture previously exposed to an oxidative insult. $MnCl_2$ at a concentration of 750 mM has been selected as the oxidant agent to simulate the degenerative processes occurring in PDL syndrome caused by chronic manganese intoxication.

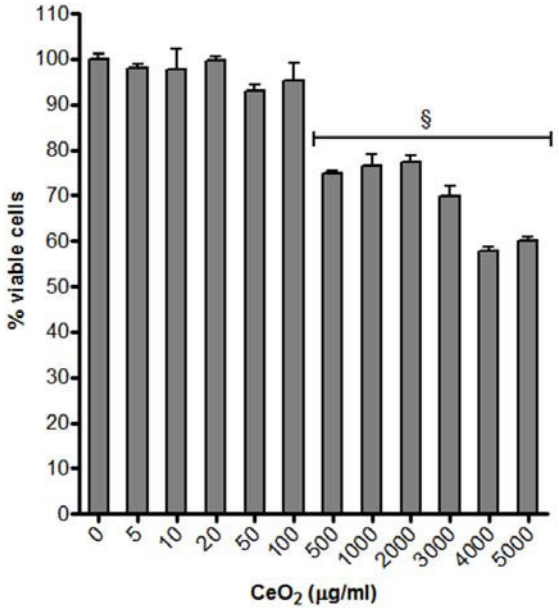

Fig.4.4 The effect of nanoceria (5–5000 mg ml^{-1}) on viability of PC12 for 48 h evaluated by MTT assay. § =p < 0.05 versus control group.

In Fig. 4.5 a representative flow cytometry profile PI/annexinV performed on cell cultures treated with CeO_2 and $MnCl_2$ have been shown. The oxidative insult causes a 27.7% cell apoptosis (Fig. 4.5b) with respect not-treated cells (Fig. 4.5a). However, if cells previously treated with 20 mg**.**ml^{-1} of nanoceria, the apoptotic cell percentage dramatically drops to 3.8% (Fig. 4.5d). Fig. 4.5c shows the effect of nanoceria administration compared to the control; the data show no significant variations in the cell apoptosis, in accordance to the MTT assay and previous studies.[18] The experiments have been reproduced in triplicate as a function of the NPs concentration and the averaged results have been reported in a bar plot (Fig. 4.5e). $MnCl_2$ causes 28 ±3.5% of apoptosis, while the injury decreases in the cells pre-treated with nanoceria; the PC12 cultures treated with 10, 20, 50 and 100 mg**.**ml^{-1} of CeO_2, in fact, show a percentage in apoptosis of 3% ±0.5, 4.5% ±0.5, 2.8% ±0.5 and 3% ±0.4, respectively.

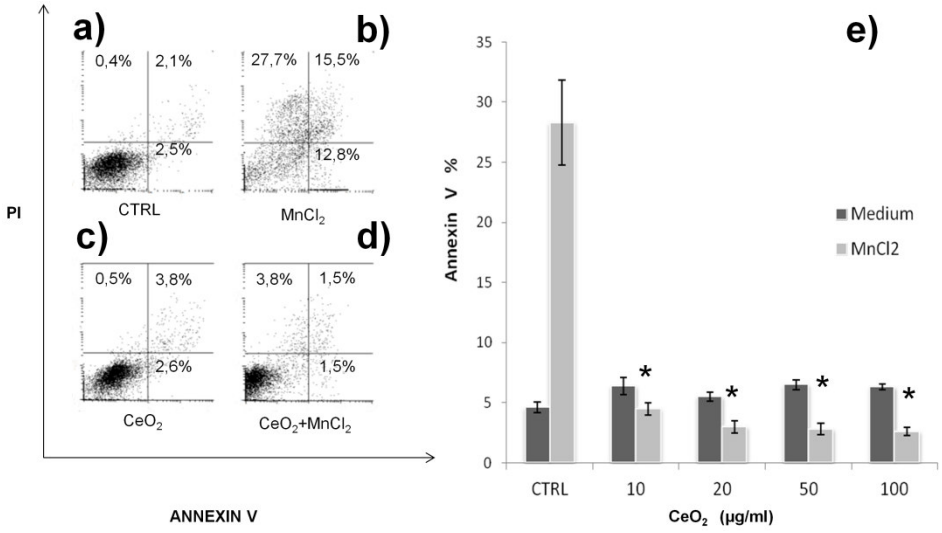

Fig.4.5 Flow cytometry profile PI/annexinV performed on PC12 cell culture. (a) PC12 control cells. (b) PC12 cells treated with $MnCl_2$. (c) PC12 cells treated with nanoceria in a concentration of 20 mg.ml^{-1} and with $MnCl_2$ insult. (d) PC12 cells treated with nanoceria. (e) Average results of apoptotic PC12 cells treated with different concentration of nanoceria and exposed to $MnCl_2$ insult. Asterisks indicate statistically significant differences between CeO_2-treated PC12 cells vs. $MnCl_2$ CTRL ($p < 0.01$).

- Monitoring nanoceria uptake into the PC12 cells

Flow cytometry with fluorescent nanoceria has been used to assess whether the CeO_2 antioxidant effect occurred indirectly, through ROS quenching in the extracellular environment, or directly, as a consequence of intracellular uptake. Fig. 4.6 shows the fluorescence intensity of the cells as a function of the nanoceria concentration; the median fluorescence intensity (MFI) increases from 9.97 to 137.16 a.u. with the increase of NPs concentration from 20 mg**.**ml^{-1} up to 100 mg**.**ml^{-1}. The cell cultures have been treated with trypan blue before cytometry, so that the fluorescence signal can be univocally attributed to NPs inside the cells. A higher nanoceria concentration causes an increase in the median fluorescence intensity of the cells; this indicates that there is an almost linear correlation between the amount of NPs incubated with the PC12 cultures and the number of nanoparticles up-taken by the cells.

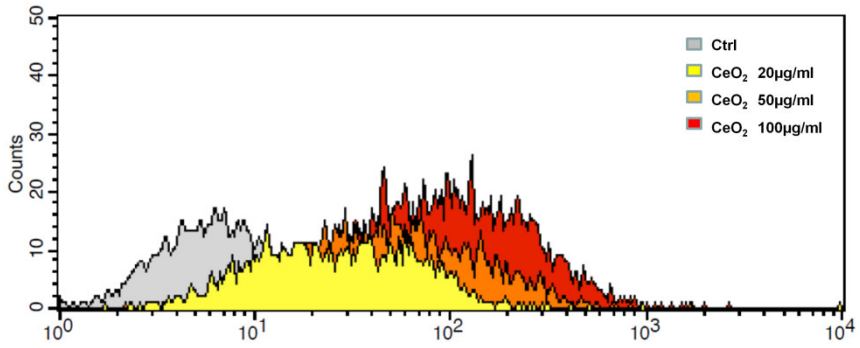

Fig.4.6 Median fluorescence intensity (MFI) histogram of the cells as a function of the nanoceria concentration.

To confirm the ceria uptake, PC12 cells fixed on a glass with a gelatin from bovine skin, have been analyzed by Raman imaging (Fig. 6a). The image in false color scale has been obtained by sampling the area shown in Fig. 6b with a Raman microscope and integrating the band peaked at 465 cm^{-1}, which is the main absorption band of nanoceria in water Fig. 6c.[19] Fig. 6d shows the difference in the Raman spectrum

when the microscope is sampling an area containing nanoceria (black line), in comparison with the extracellular area, where no particles are detected (red line).

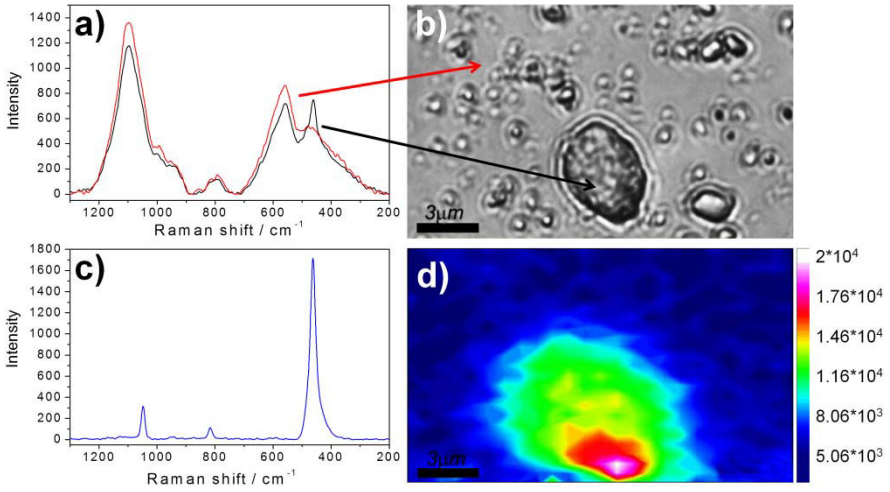

Fig.4.7 Raman imaging of PC12 cells incubated with nanoceria. (a) Raman spectra in the 1300–200 cm^{-1} range of extracellular environment (red line) and cellular environment (black line); (b) optical image of single PC12 cell; (c) Raman spectrum in the 1300–200 cm^{-1} of ceria NPs in water solution and (d) Raman image obtained by integrating the active mode of cerium oxide at 465 cm^{-1}. The integrated intensity is reported in false color scale.

The imaging clearly shows the presence of cerium oxide inside the cell due to nanoparticles uptake while no signals attributed to nanoceria are visible in the extracellular environment. Confocal microscopy has also confirmed the internalization of cerium oxide NPs into PC12 cells Fig. 4.8. After 24 h of incubation with 20 mg**.** ml^{-1} of FITC-nanoceria, the highly fluorescent green spots inside the cytoplasm cells prove the successful internalization. Z-stack and 3D rendering have confirmed that the NPs are effectively inside the cells and not on the cell surface while no evidence of NPs in the cell nuclei has been observed.

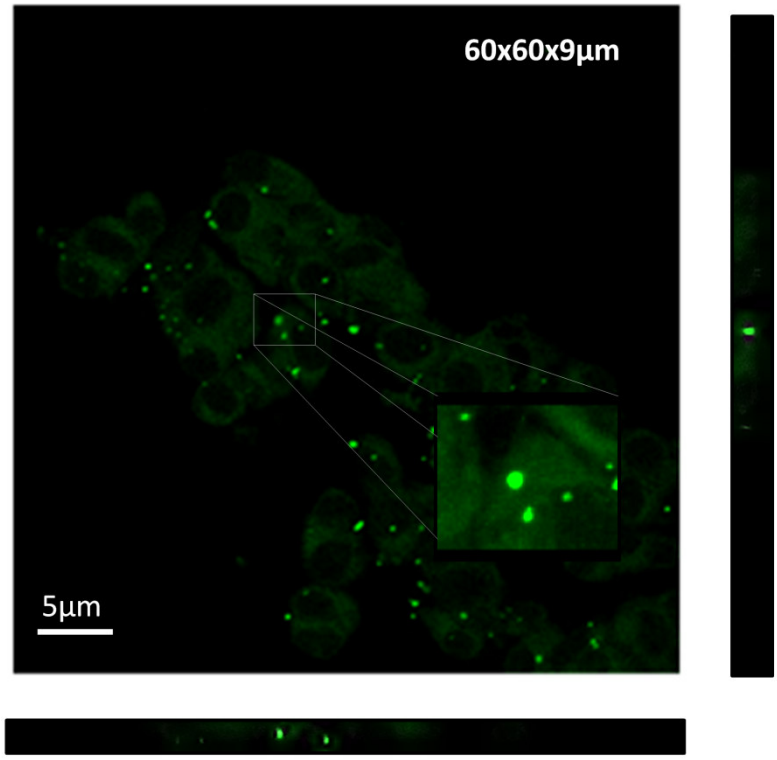

Fig.4.8 3D rendering through side projections of confocal Z-stack confirming ceria nanoparticles (green spots) internalization in PC12, as highlighted in the 4X zoom crop.

- Protective effect of nanoceria towards treatment of $MnCl_2$ and $MnCl_2$+ L-DOPA

The most common treatment of PLD syndromes is the administration of L-DOPA, which is the natural precursor of dopamine; however the auto- and enzymatic oxidation of this compound contributes to further increase of the oxidative stress in the cells. We have decided, therefore, to test the effect of administration of nanoceria on PC12 cells previously exposed to oxidative stress induced by $MnCl_2$ and potentiated by L-DOPA. The cell viability has been measured both by MTT and trypan blue assay to cross correlate the results obtained by the two techniques (Fig. 4.9). After the $MnCl_2$ insult, the viability is 55% and 65% compared to control, as shown by MTT and TB assays, respectively. The difference in these two values can be justified by

considering the different outputs of the techniques; MTT measures, in fact, the mitochondrial dehydrogenase activity while the TB assay allows direct staining of the dead cells. A live cell with reduced dehydrogenase activity, therefore, is accounted as "healthy cell" by TB assay although providing a lower contribution in the cell viability as assessed by MTT. When PC12 cells are pre-treated with increasing amounts of nanoceria, their viability after the $MnCl_2$ injury results enhanced. In particular, the cell viability raises of 15% with respect to the control after pre-treatment with 10 and 20 $mg{\cdot}ml^{-1}$ of cerium oxide NPs ($p < 0.05$). The simultaneous administration of $MnCl_2$ and L-DOPA shows a cell viability slightly lower but not statistically different from $MnCl_2$ alone (60% of control) while nanoceria pre-treatment gives a relative protection. However, the range of protective concentrations of ceria is lower during $MnCl_2$ exposure (10–20 $mg{\cdot}ml^{-1}$) than $MnCl_2$ + L-DOPA (20–50 $mg{\cdot}ml^{-1}$). Although the ceria-related increase in cell viability is around 10%, both the assays (MTT and TP) give a similar value, indicating that the both cell activity and viability are statistically enhanced ($p < 0.05$).

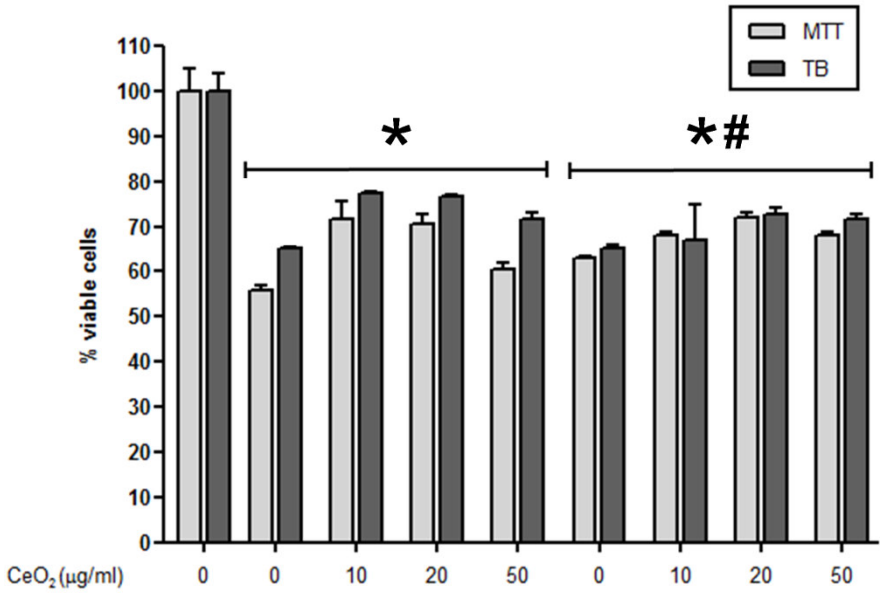

Fig.4.9 The effect of nanoceria on viability of cells treated with $MnCl_2$ (0.75 mM) and $MnCl_2$ + L-DOPA (0.75 mM + 0.02 mM) evaluated by MTT and trypan blue (TB) assays. Several concentrations of ceria nanoparticles have been used and the statistically significant relative protection has been calculated against $MnCl_2$ alone (* = $p < 0.05$) and $MnCl_2$ + L-DOPA (# = $p < 0.05$).

To evaluate the dopamine (DA) concentration in untreated and nanoceria-treated PC12 cells, we have measured its intracellular concentration and that of its metabolites dihydroxyphenylacetic acid (DOPAC), 3-methoxytyramine (3-MT) and homovanillic acid (HVA) by high performance liquid chromatography with electro-chemical detection. Fig. 4.10 shows the changes of the intracellular DA and metabolites content after treatments with nanoceria (20 mg.ml^{-1}), L-DOPA (0.02 mM), $MnCl_2$ (750 mM) and their combinations. Remarkably, the treatment with ceria does not cause any change in the intracellular amount of neurochemicals. On the contrary, the $MnCl_2$ insult causes a strong decrease of the neurochemical catabolities which is around 60%, 73% and 68% for DA, DOPAC and 3-MT, respectively. The HVA content appears almost constant, suggesting a strong resistance towards oxidation; an explanation of these responses can be provided considering the oxy-methylation reaction of the molecule. On the contrary, another oxy-methylated molecule (3-MT) showed a significant decrease after $MnCl_2$ exposure; this behavior could be in relationship with

the increased auto-oxidation of its metabolic precursor (DA). Similar decrease in DA, DOPAC and 3-MT concentrations has been also observed when $MnCl_2$ is used in association with L-DOPA. The co-treatment of $MnCl_2$ with nanoceria induces a significant protection on DA content, resulting in a 29% decrease with respect to the control value, while the DOPAC and 3-MT contents decrease. The protection of nanoceria against oxidation is still present but less pronounced when is used in association L-DOPA; in fact, the simultaneous treatment with $MnCl_2$ + nanoceria + L-DOPA causes a loss in DA, DOPAC and 3-MT content of 41%, 69% and 76%, respectively.

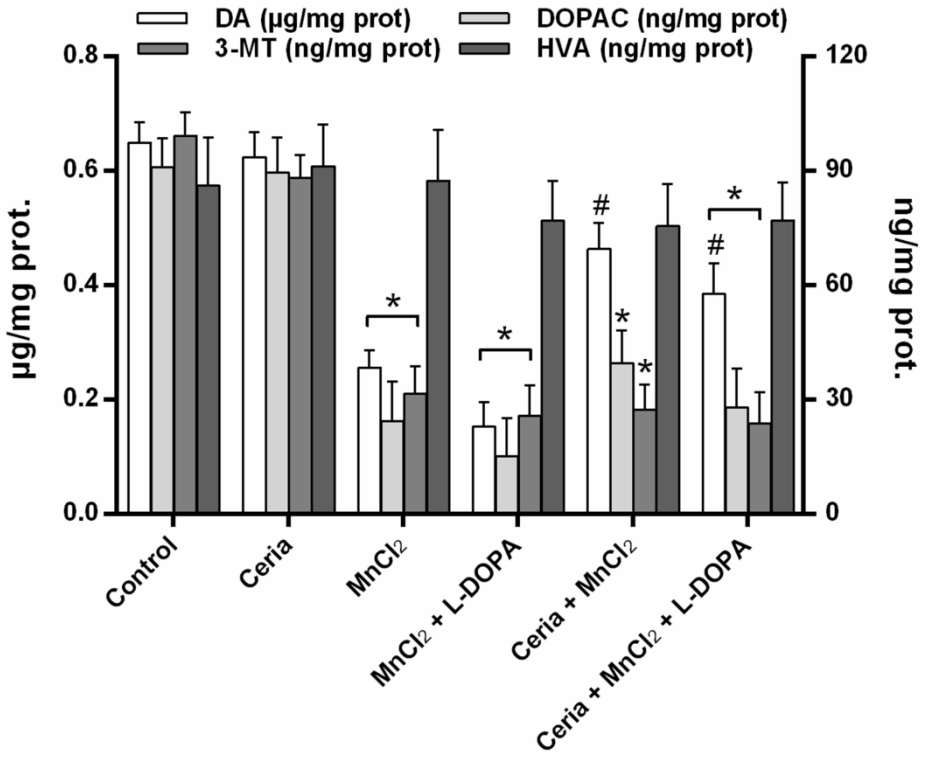

Fig.4.10 Effects of nanoceria on $MnCl_2$- and L-DOPA-induced changes in DA, 3-MT, HVA and DOPAC concentrations in PC12 tissue after 48 h exposure. Results are the means ± SEM of three experiments performed in triplicate. # p < 0.05 versus MnCl2 group, * p < 0.05 versus control group.

The results show that the use of nanoceria to neutralize ROS in PLD oxidative processes enhances the therapeutic effects of L-DOPA delaying neuronal cell degeneration. Although the antioxidant properties of nanoceria are not significantly influenced by the pH,[10] its role largely depends on the dimension and concentration. These parameters have to be carefully controlled to achieve protective effects. In fact, nanoceria at concentration of 20 $mg{\cdot}ml^{-1}$ has a high protective action towards oxidative stress caused by Mn^{2+} ions and auto-oxidation of L-DOPA, while, at concentration higher than 100 $mg{\cdot}ml^{-1}$, the cell viability is compromised. On the other hand, previous studies have shown the importance of controlling the nanoceria dimension; in fact, particles larger than 10 nm exhibit a lower antioxidant activity and enhanced photocatalytic properties.[20] This is the reason why we have carefully kept the nanoparticle dimension below this critical size. Understanding nanoceria uptake mechanism is also of paramount importance, for this reason we have used two different techniques to observe the nanoparticles within the cellular environment. At the optimized nanoceria concentration, the nanoparticles result efficiently internalized in the cytoplasm of PC12 cells. However no evidence of nanoparticles uptake in the cell nuclei has been observed, avoiding potential damaging of the DNA. Interestingly, the results of flow cytometry indicate that nanoceria itself is likely able of reducing the natural apoptosis ratio of the untreated cells; in fact the nanoceria pre-treated cells insulted by $MnCl_2$ show an even lower percentage apoptosis than the control. On the other hand, it is also remarkable that L-DOPA does not protect the cells against the same oxidative insult. This fact is not surprising, indeed in a previous study[13] has been observed that the L-DOPA enhances the prooxidative effect of manganese and an antioxidant (N-acetylcysteine) is only able to partially revert its negative effects on PC12 cells. A similar enhancement of the pro-oxidative process has been also observed *in vivo*, in particular in the striatum of freely-moving rats treated with manganese and L-DOPA.[21] This observation has important implications about the role of nanoceria during L-DOPA treatment; in fact, the protective effect of nanoceria on

$MnCl_2$ + L-DOPA-exposed cells confirms that the auto-oxidation of L-DOPA enhances the Mn-related oxidative stress.[13]

4.1.3. Role of nanoceria in Oocyte *in vitro* maturation

The oxidative stress, related to the increasing in ROS production, is responsible of the onset of defective in the embryo development. Several endogenous and exogenous factors can enhance the production of oxidative stress altering most type of cellular molecules and also inducing development block and retardation.[22] In a special way, the *in vitro* culture results in higher oxygen concentrations than *in vivo* environments. The role of ROS in IVM and its influence on later embryonic development have some relevance. ROS may participate in the meiotic arrest of the oocyte and they are a major cause of embryonic developmental arrest and cell death. Oxidative stress during meiotic maturation *in vitro* may induce chromosomal errors that prove undetectable in the living oocytes and whose developmental consequences may become manifest after fertilization.[23] The importance of protecting pre-implantation embryo from oxidative damage *in vitro* is being increasingly recognized. To optimise *in vitro* embryo production, oxidative stress must be controlled during the culture.

Among the large family of engineered nanoparticles, nanoceria is, recently, receiving particular attention for its potential applications in germ cells. Few studies have been focused on the influence of NPs on mammalian male[24,25] and female[26,27] germ cells. *In vivo* administration of CeO_2 NPs by intraperitoneal injection did not cause adverse consequences on the ovarian tissue and on the rate of oocyte maturation in the mouse.[28] Also, mice with experimentally induced endometriosis showed a significant reduction in pathological signs upon *in vivo* treatment with nanoceria; specifically, the treatment prevented or reduced the endometriosis-related adverse effects on the quality of oocytes.[29] Conversely, other studies indicated that, when mouse metaphase II (MII) oocytes are exposed to CeO_2 NPs, a genotoxicity effect is exerted on follicular cells and on the female gamete.[26] There are no reports, so far, about the effects of CeO_2 NPs

treatment on meiotic progression of the oocyte or on the consequences of this exposure on the preimplantation embryonic development. Most of the data have been provided from observations performed in the mouse. No experiments have been carried out in large animal models that, in human respects, could be more representative of events occurring during follicular growth and oocyte maturation. We have tried to evaluate the effect of CeO_2 NPs treatment during *in vitro* maturation of prepubertal ovine oocytes, which are characterized by a low developmental competence. In particular, the interaction and biological effects on the cumulus oocyte complexes and the assessment of their *in vitro* developmental competence up to embryonic preimplantation stage has been examined. To the best of our knowledge, this is the first study focused on the nanoceria interaction with the oocytes during *in vitro* maturation on subsequent preimplantation embryonic development.

- Evaluation of nanoceria uptake in oocyte germ cells

Before being used with the oocytes, the aggregation state and hydrodynamic radius of nanoceria have been evaluated by dynamic light scattering (DLS) in different media (TCM199 and water), as a function of concentration (44, 88, 220 μg/ml) and incubation time. A CeO_2 NPs concentration of 44 μg/ml in water allowed obtaining a suspension stable up to 8 hr, with an aggregate size distribution centred around 300 nm (Fig 4.11a). A higher incubation time caused a larger NPs aggregation; in fact, after 10 h, the size of CeO_2 aggregates significantly increased up to 1400 nm. Similar trend of the aggregate hydrodynamic radius, estimated from DLS analysis, has been observed in colloids containing increasing amounts of CeO_2 NPs dispersed in TCM 199 cell culture medium. In particular, after 6 h from dispersion in TCM 199, CeO_2 NPs form aggregates of 300 nm (Fig 4.11b). The aggregation state in water and in TCM 199 followed a similar trend when higher concentrations of CeO_2 NPs were suspended in water and TCM 199. Higher concentrations caused the formation of larger aggregates that showed a cyclic aggregation/disaggregation process (Fig. 4.12

and 4.13**)** both in water and in TCM199 medium. The size of the aggregates, however, did not cause sedimentation within a time scale of 2-3 h.

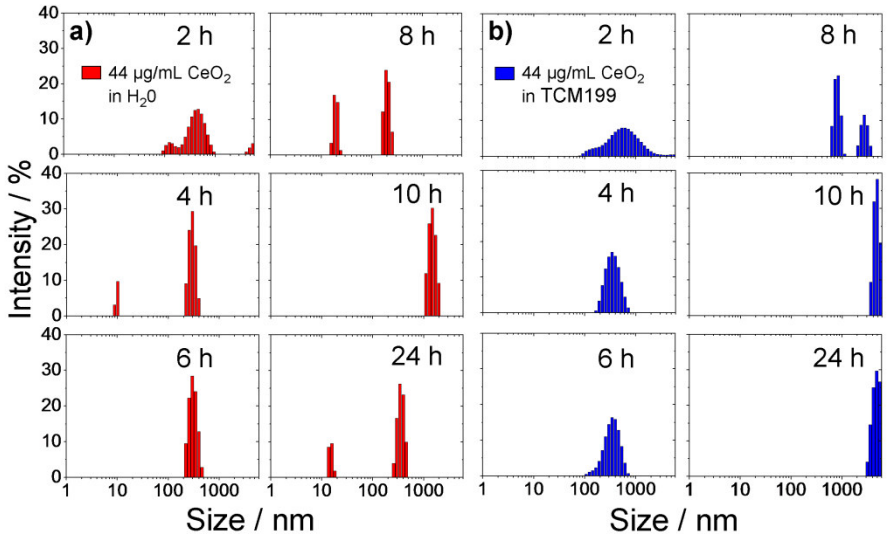

Fig.4.11 Size distribution of CeO_2 NPs in water and culture medium. Ceria NPs (44 µg/ml) size distribution in water (a, red bars) and in TCM 199 cell culture medium (b, blue bars) at increasing incubation times (2, 4, 6, 8, 10, 24 h) measured by DLS.

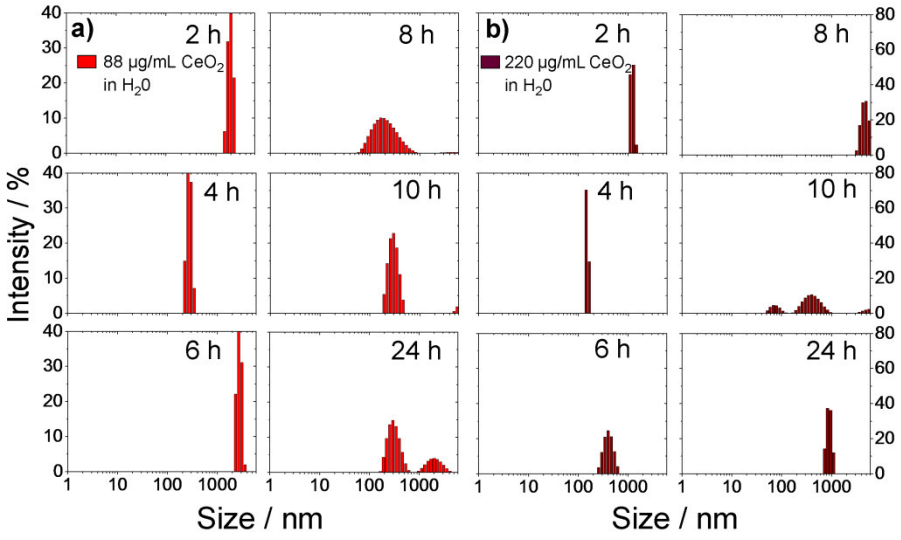

Fig.4.12 Ceria NPs size distribution in water at two different concentrations (a 88 µg/ml and b 220 µg/ml) measured by DLS at increasing incubation times (2, 4, 6, 8, 10, 24 h).

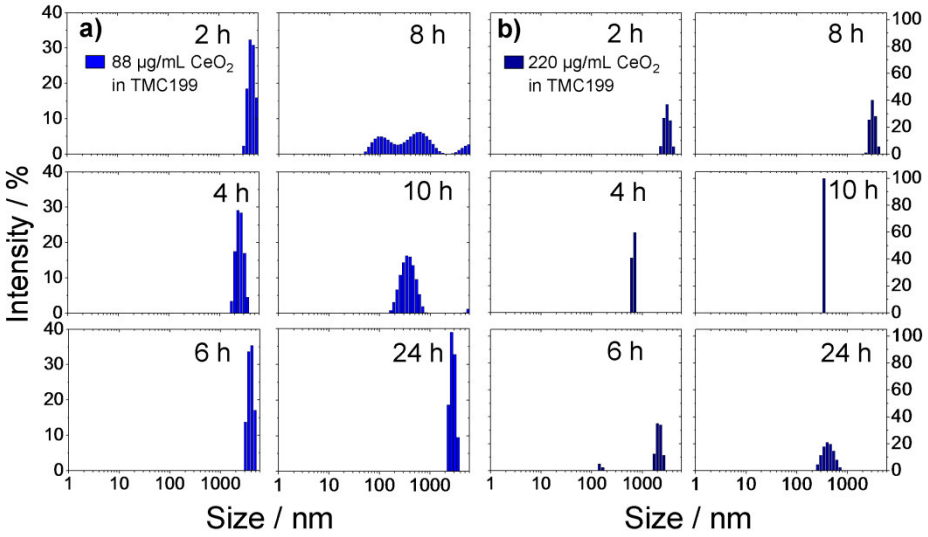

Fig.4.13 Ceria NPs size distribution in TCM199 medium at two different concentrations (a 88 µg/ml and b 220 µg/ml) measured by DLS at increasing incubation times (2, 4, 6, 8, 10, 24 h).

The nanoceria uptake onto the oocyte has been characterized by TEM measurements. We employed oocytes derived from prepubertal ovine animals as a model of oocytes with low developmental competence. The obtained data show the internalization of CeO_2 NPs by endocytosis in cumulus cells both in the immature (GV stage) and mature (MII stage) oocytes incubated for 2 h and 24 h (Fig 4.14); CeO_2 NPs aggregates have been observed only in the somatic cells but not inside the oocyte cytoplasm. The internalization in the cumulus cells was not homogenous and did not depend on the concentration of CeO_2 NPs but it has been correlated to the exposure time. Immature COCs internalized CeO_2 NPs (44 µg/ml or 220 µg/ml) following 2 h of incubation only in the somatic cells localized in the external layers of cumulus complex while endosomal trapping has been recorded in the somatic cell in contact with the zona pellucida after 24 h of incubation.

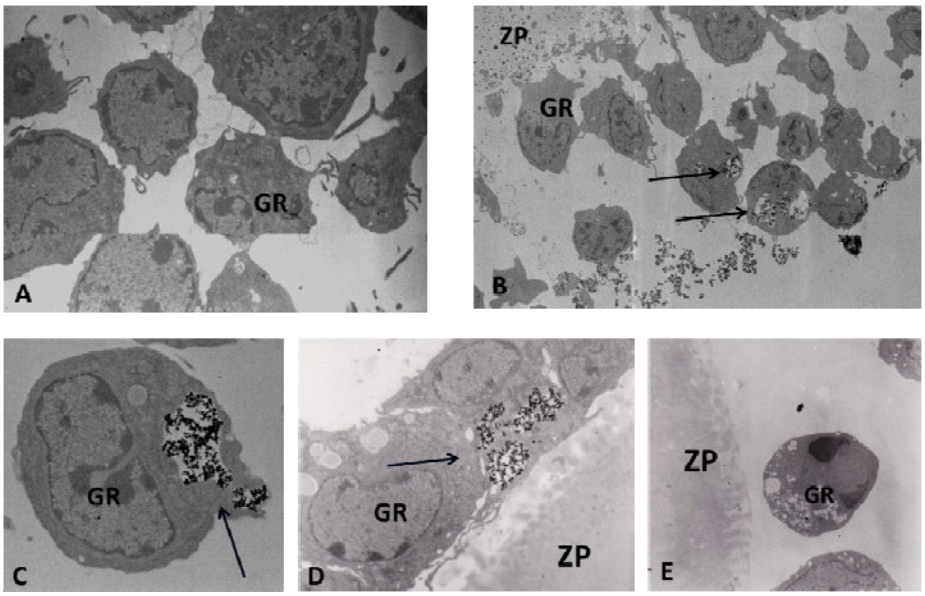

Fig. 4.14 Transmission electron microscopy images of cumulus cells and oocytes exposed to CeO_2 NPs. (A) Unexposed immature cumulus oocyte complex (COC); (B) COC exposed to 44 µg/ml of CeO_2 NPs for 2 h (immature oocyte); (C) Granulosa cell after exposition to 44 µg/ml of CeO_2 NPs for 2 h; (D) COC exposed to 44 µg/ml of CeO_2 NPs for 24 h (mature oocyte); (E) COC exposed to 220 µg/ml of CeO_2 NPs for 24 h (matured oocyte). Arrows indicate the internalization of nanoparticles, GR= cumulus cells; ZP= zona pellucida.

These experiments partially confirm the observations reported in a recent study carried out in mice[26], on short term *in vitro* exposure of MII oocytes to different concentrations of CeO_2 NPs. Ultrastructural analysis, in fact, showed that the endocytosis of CeO_2 NPs aggregates occurred in follicular cells surrounding the zona pellucida (ZP) but not in the oocyte. During *in vitro* maturation of prepubertal ovine oocytes, the internalization of nanoceria only occurred in the follicular cells of the cumulus- oocyte complex. Furthermore, we observed that the total absence of CeO_2 NPs in the oocyte was not dependent on either time of exposure or meiotic stage of the oocyte. Surprisingly, any internalization of CeO_2 NPs has been detected in the immature oocyte (germinal vesicle stage – GV), a stage when fully functional coupling is established between the somatic and oocyte compartment. In GV oocytes, cellular transport throughout the maturation stages occurs via the transzonal projections of adjacent granulosa cells, which penetrate the ZP and terminate at the

oocyte plasma membrane.[30,31] Moreover, internalization of CeO_2 NPs in the cumulus cells during 24 h of exposition progressively involved different layer of cumulus cells with a physical gradient. In fact, after incubation of GV oocytes to CeO_2 NPs for a short time, the internalization has been observed only in the external layers of cumulus cells, while, after 24 h, CeO_2 NPs were detected inside follicular cells surrounding the ZP. This different nanoceria uptake from the somatic cells may be not only time-dependent, but could be also related to the changes exerted on the cumulus cells by the gonadotropins during the *in vitro* maturation. In particular, follicle stimulating hormone (FSH) induces the process of mucification by the reduction of cell-to-cell interaction and thus may facilitate the internalization of the CeO_2 NPs in the granulosa cells adjacent to the ZP.[31] The distinct uptake of nanoparticles by the cells and their effects may also be related to several other factors including aggregation status, surface changes, different cell sensitivity and in particular chemical composition.[32,33,34,35] A selective uptake of different nanoparticles, for instance, has been reported in the somatic cells and oocyte during *in vitro* maturation of pig oocytes for 46 hr. Gold nanoparticles were easily internalized by oocytes, while silver and alloy particles accumulated mainly in the cumulus cell layer surrounding the oocyte.[36] This work also showed that neither any of the tested gold nanoparticles or gold-silver alloy particles with a silver molar fraction of up to 50% had any impact on oocyte maturation. Conversely, alloy nanoparticles with 80% silver molar fraction and pure silver nanoparticles inhibited oocyte maturation. The functional significance of the progressive internalization of the CeO_2 nanoceria in the cumulus cells during the oocyte *in vitro* maturation reported is not completely understood and will be better studied in future investigations.

- Effects of nanoceria during in vitro oocyte maturation

Three different nanoceria effects have been studied in oocytes culture: on chromatin and cytoskeleton morphology, on intracellular ROS and on *in vitro* maturation and embryo development.

- Effect of CeO_2 NPs on chromatin and cytoskeleton morphology of the oocytes.

The confocal microscope analysis listed in Fig. 4.15 show the effects of different concentrations of nanoceria (44, 88 and 220 µg/ml) on chromatin, spindle and cortical F-actin configuration in oocytes.

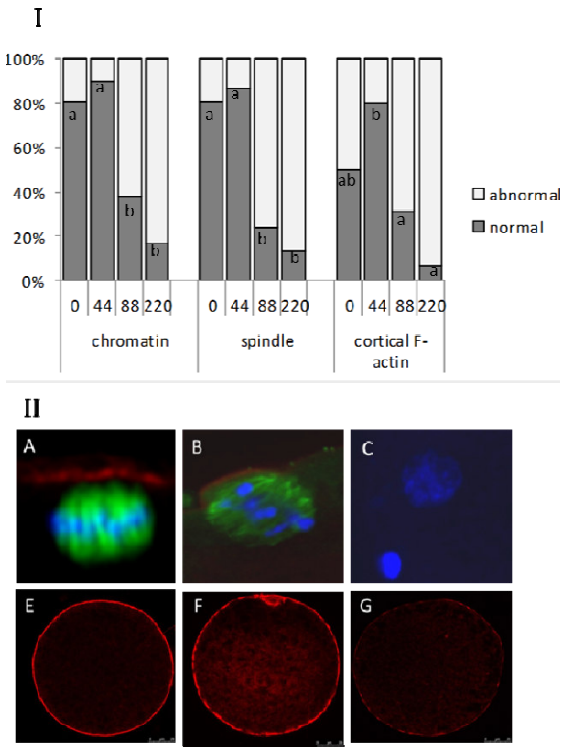

Fig. 4.15 Confocal analysis showing the effect of different concentrations of nanoceria during *in vitro* maturation on chromatin, spindle and cortical F-actin of prepubertal ovine oocytes. (I) Graph showing normal and abnormal configuration of chromatin, spindle and cortical actin after incubation with increasing doses of CeO_2 NPs (II) Immunostaining of chromatin (blue), microtubules (green) and F-actin (red): normal spindle and chromatin configuration (A); abnormal chromatin configuration and irregular spindle (B); activated chromatin and absence of spindle (C); normal homogeneous cortical F-actin network immediately beneath the plasma membrane (E) in contrast to an irregular and spotted (F) or discontinuous and reduced (G) pattern of distribution of microfilaments in the cortical area.

The obtained data showed that the oocytes, incubated with 44 μg/ml nanoceria have a percentage of normal pattern of chromatin, meiotic spindle and cortical F-actin assembly comparable to control oocytes and significantly higher than 88 μg/l, 220 μg/ml treated oocytes ($p<0.05$). Conversely, severe alterations of these components have been detected when oocytes were exposed to 88 and 220 μg/ml of CeO_2 NPs.

The damage to the microfilament network can affects the redistribution of cortical granule leading to the polyspermy.[37] Similar alterations of the cytoskeletal components and general reduction of developmental competence have been also reported in oocytes recovered from prepubertal ovine subjects that have a reduced developmental capacity compared with those collected from adult ewes.[38] Signs of their poor oocyte quality are cytoskeletal and chromatin abnormalities, a significant increase of polyspermy and low developmental rate up to the blastocyst stage.[39,40] The production of ROS specifically impacts on the cytoskeletal components of the oocyte affecting the meiotic maturation and subsequent embryonic development. The beneficial antioxidant effects of nanoceria on the cytoskeletal structures of the oocytes have been also confirmed by *in vivo* experiments performed in mice subjected to experimental endometriosis where pathology is characterized by a significant increase of oxidative radicals.[29]

- *Effect of nanoceria on intracellular ROS*

As it is reported in Fig. 4.15 II, by the epifluorescence analysis, the levels of ROS have been quantified and they resulted in no significantly different among the experimental groups (0 μg/ml:1.00±0.19; 44 μg/ml: 0.67±0.16; 88 μg/ml:1.17±0.19; 220 μg/ml:1.16±0.24 pixel/oocyte). However, in the oocytes matured in presence of 44 μg/ml CeO_2 NPs the amount of ROS tended to decrease while an increase has been observed in the groups of oocytes matured with 88 μg/ml e 220 μg/ml of CeO_2 NPs (Fig. 4.16 I). High doses of CeO_2 NPs (220 μg/ml) induced degenerative effects on the somatic cells of the cumulus-oocyte complexes.

The adverse effects generated from oxidative molecules, which inevitability occurs during *in vitro* culture, can be reduced by cumulus cells during oocyte maturation protecting the female gametes from oxidative stress.[41] An imbalance between the production of reactive oxygen species (ROS) and the intrinsic capacity of oocytes in detoxification causes damage to the cellular structures. A correlation between the antioxidant capacity of oocyte and subsequent *in vitro* embryonic development has been reported in several species. High content of molecules such as glutathione or superoxidismutase in the oocyte is associated to an increase of developmental competence in equine[42] and porcine oocytes.[43] A reduction of glutathione levels has been found in poor quality oocytes in goat[44]and in human oocytes derived from potential maternal ageing and post-ovulatory oocyte ageing.[45] A low concentration of glutathione has also been found in oocytes derived from patients with ovarian and uterine diseases[46] and in oocytes collected from prepubertal mice.[37] Oocytes recovered from prepubertal mice have a decreased ability to synthesize glutathione, leading to impaired potential to reduce ROS and form male pronuclei and blastocysts. The consequence of oxidative stress is a reduction of the intracellular Ca^{2+} store which impairs oocyte activation at fertilization. From our experiments we observed that nanoceria did not alter significantly the intracellular ROS levels in oocytes at the end of *in vitro* maturation. Possibly, the time and concentration of exposition is triggering changes that are more expressed during the preimplantation development. Moreover, the significance of slightly up and down level of ROS during oocyte maturation is still debated as their increase or decrease has been invariable considered to be related to the capability of the oocyte to develop up blastocyst stage.

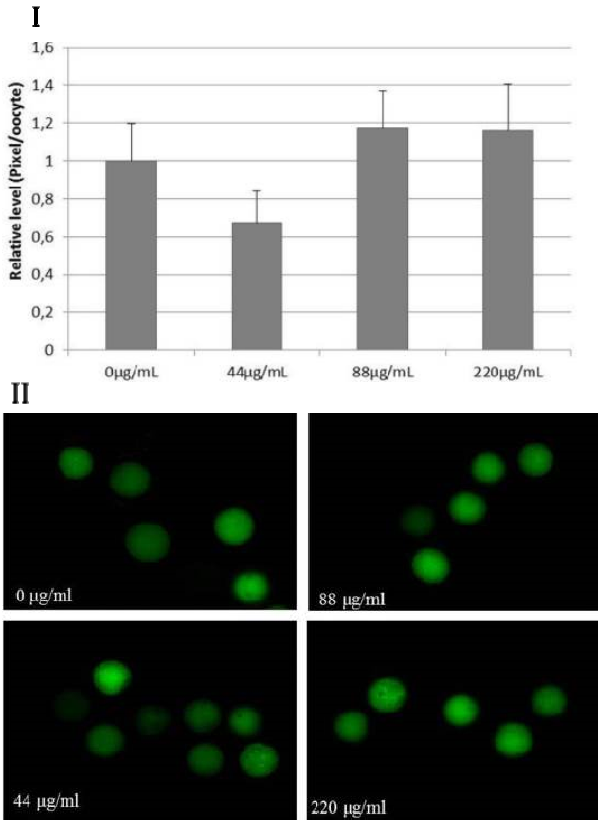

Fig.4.16 ROS levels in lamb oocytes exposed to increasing doses of CeO_2 NPs (I) Effects of different doses of CeO_2 NPs on intracellular ROS levels of lamb oocytes (II). Epifluorescence photomicrographs of lamb oocytes matured *in vitro* with 0, 44, 88, 220 µg/ml nanoceria after staining with 2',7'-dichlorodihydrofluorescein diacetate (H_2DCFDA) to detect ROS.

- Effect of nanoceria on oocyte in vitro maturation and embryo development

The treatment with CeO_2 NPs did not significantly affect the *in vitro* nuclear maturation of the oocytes irrespective to the concentration used (Tab.4.1). However, CeO_2 NPs at the low concentration (44 µg/ml) significantly increased the blastocyst yield, the total inner cell mass and trophectoderm cell numbers of the blastocysts compared to 0 µg/mL and 220 µg/mL groups as it has been shown in Tab.4.2.

CeO_2 NPs (μg/mL)	N° oocytes	N° MII (%)	N° cleaved embryos (%)		N° blastocysts (%)
			24 h	30h	
0	129	102 (79.0)	29 (28.4)	72 (70.6)[a]	9 (12.5)[a]
44	127	104 (81.1)	28 (26.9)	81 (77.8)[a]	29 (35.8)[b]
88	109	95 (87.1)	20 (21.0)	51 (53.7)[b]	7 (13.7)[a]
220	110	91 (82.7)	17 (18.7)	66 (72.5)[a]	6 (9.0)[a]

Tab.4.1 Effect of different doses of CeO_2 NPs on *in vitro* nuclear maturation, cleavage and embryo development of prepubertal ovine oocytes. a vs b P<0.05.

CeO_2 NPs (μg/mL)	N° Blastocysts	Embryo cell number (mean ± s.e.m.)		
		Total	ICM	TE
0	9	63.22±3.25	6.89±0.54[a]	56.33±2.78[a]
44	29	105.21±2.15	12.45±0.65[b]	92.76±2.13[b]
88	7	96.28±6.82	10.14±1.45[ab]	86.14±5.40[bc]
220	6	67±7.98	4.83±0.60[a]	62.17±7.64[ac]

Tab.4.2Total, Inner Cell Mass (ICM) and Trophectoderm cells (TE) number of blastocysts *in vitro* produced from prepubertal ovine oocyte matured in presence of different concentrations of CeO_2 NPs. a vs b vs c P<0.05

These results indicate that poor developmentally competent oocytes, matured in presence of low concentration of CeO_2 NPs, were able to develop up to blastocyst stage in a significant high percentage. The quality of blastocysts has been improved under these culture conditions as demonstrated by the increase of the total number of cells and the inner cell mass and trophectoderm cells. The lowest nanoceria concentration has not any obvious cytotoxic effect, even though the concentration used was significantly higher than those expected following environmental exposure. This may indicate that the impact of environmental exposure of nanoceria on the oocyte is low. Furthermore, we have not observed any internalization of CeO_2 NPs in the cytoplasm of oocytes at immature stage, a phase where there is a functional coupling between oocyte and somatic cells. All these data open the view for possible biomedical application of nanoceria during the *in vitro* maturation of the oocyte with a low competence. However, the hypothesis of a possible bioaccumulation in the ovary and genotoxic effect after longer exposure needs to be further investigated at the molecular level.

4.1.4. Spermatozoa germ cells-nanoceria interaction

Limited information has been reported about the cellular and tissue effects of NPs in the reproductive system. It has been demonstrated that they can cross the hemato-testicular barrier.[47,48] Recently, the effects of gold and silver NPs on spermatozoa have been evaluated, reporting that gold NPs do not have any effect and silver NPs are no detrimental for spermatozoa.[49] Similarly, gold and silver NPs do not affect vitality and motility parameters of human spermatozoa.[50] On the contrary, bovine spermatozoa incubated with gold NPs display alterations in the decondensation of chromatin[51] and exposure to silver led to cytotoxicity and genotoxicity of testicular cells in the mouse.[52]

Much less is known about the potential anti-oxidant effects of CeO_2 NPs in the reproductive system and gametes. In male rats, for example, nanoceria can trespass the hemato-testicular barrier and accumulate in the testis and epididymis,[53] and it has been

shown that the supplementation of CeO_2 NPs in the diet leads to an improvement in fertility through a reduction in oxidative stress.[54] The male gamete is highly susceptible to oxidative stress. Although physiological levels of ROS are required for key events such as capacitation and acrosome reaction, an over production can lead to an impairment of the fertilizing ability. In particular, ram spermatozoa are more sensitive to oxidative stress compared to other species[55] and a wide range of anti-oxidant substances have been tested to improve the quality of stored semen.[56] However, results are often controversial or show little improvement in semen quality. This paragraph focuses on the interaction and the short-term effects of increasing doses of nanoceria on ram spermatozoa, stored at 4°C for up to 24h, on the kinematic parameters, membrane status and DNA fragmentation. Moreover the antioxidant properties of these NPs on ROS production and mitochondrial activity have been also tested.

- *Study of nanoceria uptake in spermatozoa*

Before studying the nanoceria-spermatozoa interaction and then their up-take in germ cells, nanoparticles aggregation and hydrodynamic radius have been evaluated in OVIXcell medium as a function of concentration (22, 44, 220 μg/ml) and incubation time (0, 2 and 24h) by dynamic light scattering (DLS).

A CeO_2 concentration of 22 and 44μg/ml in medium allowed obtaining a suspension stable up to 24 h, with an aggregate size distribution centred around 180 nm (Fig4.17a and 4.17b). While the colloid with higher concentrations of CeO_2 (220 μg/ml) shows a formation of larger aggregates with a size of 250 nm (Fig.4.17c). The nanoceria suspension shows a monodisperse distribution in OVIXcell medium at all concentrations until 24h. The presence of protein in OVIXcell medium lead to the formation of protein corona[57] on a nanoceria surface which allowed to obtain a stable colloidal suspension until 24 h.

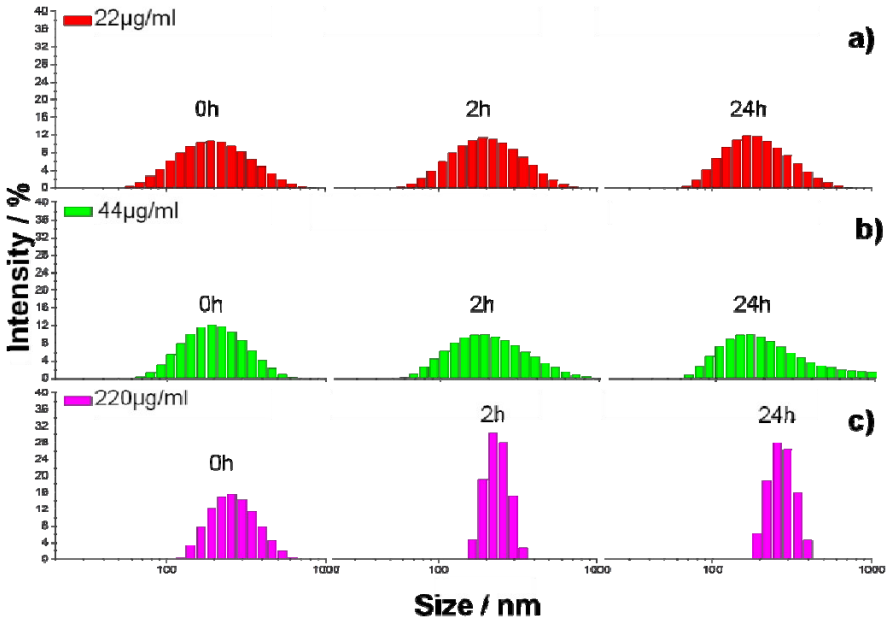

Fig.4.17 Ceria NPs size distribution in OVIXcell at concentration of a) 22 µg/ml b) 44 µg/ml and c) 220 µg/ml measured by DLS at increasing incubation times (from left to right 0, 2, 24 h).

To understand the fate of nanoceria during 24h in spermatozoa at 4°C, TEM analysis has been performed. Fig. 18 shows no intracellular CeO_2 NPs uptake by spermatozoa regardless of dose; only an occasional contact between nanoparticles and cells has been observed, mostly in the plasma membrane of sperm head (Fig.18a). All these findings indicate a high tolerance of ram semen to CeO_2 NPs. The concentrations chosen for the present experiment are similar to those used in previous studies exposing different types of somatic cells to CeO_2 NPs[58,59,60,61] and far above the levels commonly dispersed in the environment (in water 0.024 mg/l[62], in soil 1.12 mg/kg[63]). The present study is the first reporting the effects of increasing concentration of ceria nanoparticles on mammalian spermatozoa during 24h of exposure at 4°C.

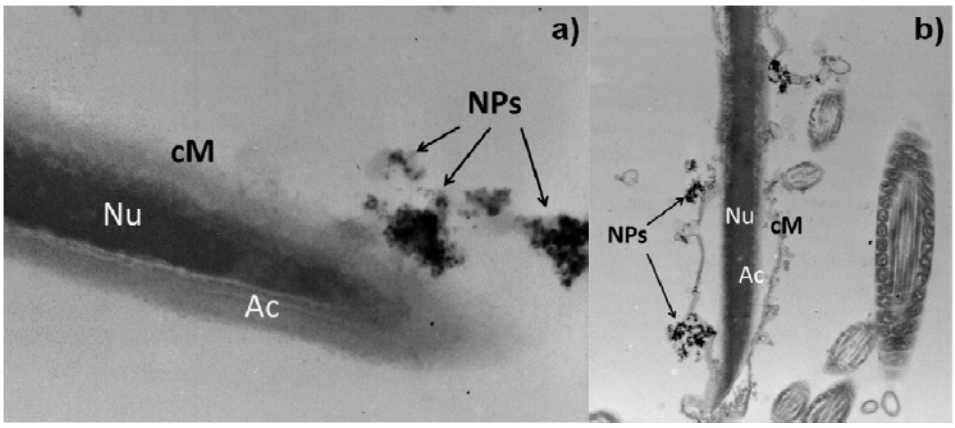

Fig.4.18 Transmission Electron Microscopy (TEM) images (a and b) showing occasional contacts between nanoceria (NPs) and the cytoplasmic membrane (cM) . No signs of evident uptake and absence of NPs in the nucleus (Nu) were seen. Ac: Acrosome.

The interaction between nanoparticles and spermatozoa has been mainly investigated to evaluate their potential use in the sperm-mediated gene transfer (SMGT) into the oocyte. Nanoparticles might improve the DNA internalization by the sperm allowing the introduction of the transgene to the future embryo[64,65] and optimize the transport of proteins by the sperm into the oocyte.[66] However, the intracellular uptake of nanoparticles by the spermatozoa seems to be strictly dependent on their nature (size, charge, and coating) and on the chemical composition, but it could also be related to the experimental species used. On this regard, internalization of gold nanoparticles (AuNPs) into the sperm head has been observed in human semen[50,67] while, in the bovine, only attachment of AuNPs to the cell membrane of spermatozoa has been reported, without any internalization of AuNPs.[68] Uptake of Fe_3O_4–PVA, Eu_2O_3, PVP–$Eu(OH)_3$ NP, PVA–$Eu(OH)_3$[66,69] and bio-conjugated CdSe/ZnS quantum dots[70] into spermatozoa has been described; conversely, silver and silver alloy nanoparticles are not internalized in bovine, porcine and human semen.[71] Among the different NPs, few reports are available about the interaction of CeO_2 NPs on female and male gametes. The results are in agreement with previous studies where the spermatozoa have been incubated with different types of nanoparticles.[71] The absence of uptake of

NPs by the spermatozoa could be explained by the lack in these cells of active mechanisms of endocytosis.

- *Nanoceria effects on the main kinematic spermatozoa parameters*

The spermatozoa kinematic parameters measured by CASA analysis, at different time points (0, 2 and 24 h), show that the incubation at 4°C with increasing doses of nanoceria has no effect on main motility parameters of ram semen and total progressive motility. In fact, as it is shown in Fig.4.19 a and b, no significant differences have been observed among groups for total (TM) and progressive motility (PM) respectively. Moreover the Fig.4.20 demonstrates that the secondary kinematic parameters such as VAP, VSL, VCL, ALH, BCF, STR and LIN, which are considered in the ram[72] and the bull[73] indicators of *in vivo* fertility, are not affected by co-incubation with CeO_2 NPs in the 24h.

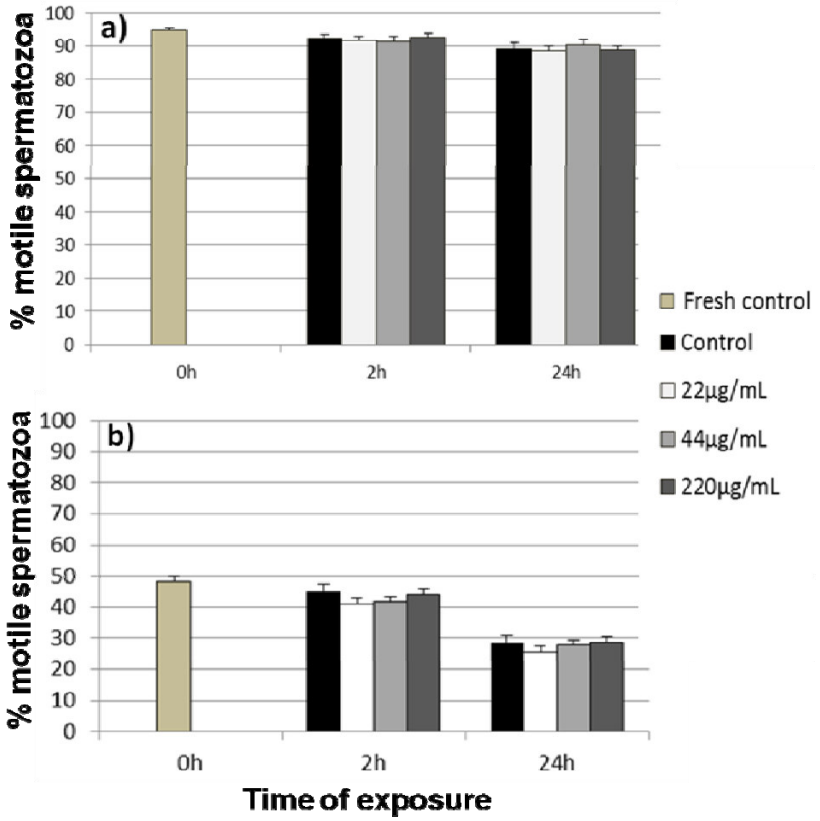

Fig.4.19 CASA analysis of a) Total and b) Progressive motility of ram semen exposed to increasing doses of nanoceria up to 24 h at 4°C. Results are shown as means ± SEM.

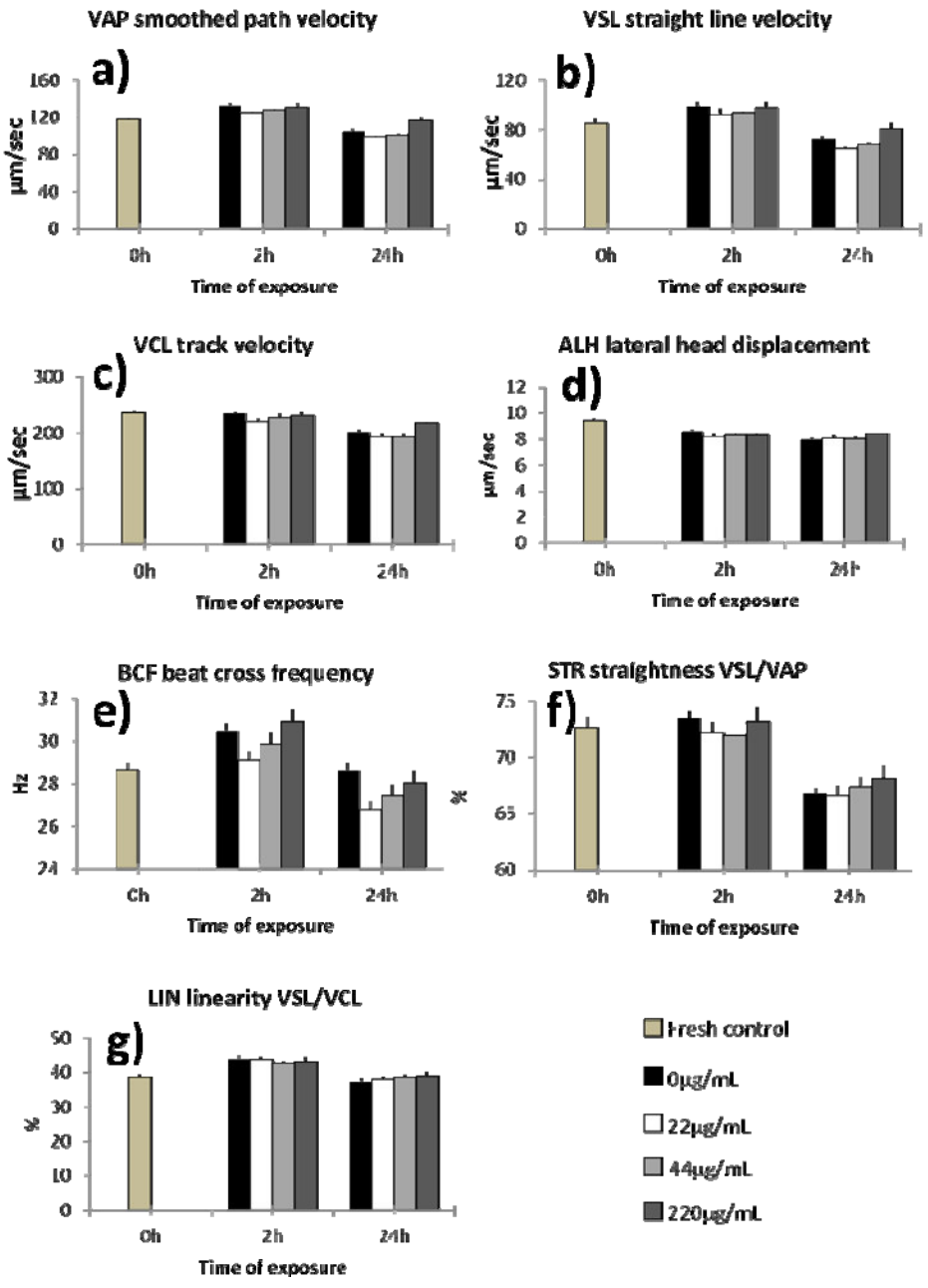

Fig.4.20 Secondary motility parameters of ram semen assessed by CASA after 0, 2 and 24 h of exposure at 4° C to different doses of nanoceria. Results are shown as means ± SEM.

The data relating to the velocity distribution and the morphology of the spermatozoa among groups are reported in details in Table 4.3. It is clear that there are no significant differences in morphology and in velocity between the spermatozoa treated and no treated with nanoceria at different concentration and time exposure.

Time of exposure (h)	CeO_2 NPs (µg/mL)	Morphology		Velocity Distribution			
		Elongation	Area	Rapid	Medium	Slow	Static
0	Fresh control	42.00±3.19	18.83±0.84	73.11±4.55	12.67±2.13	2.78±0.60	11.33±3.67
2	0	34.33±1.03	24.74±1.16	81.89±1.56	11.67±1.22	1.83±0.27	4.67±0.88
	22	34.33±1.03	27.52±1.76	74.59±2.86	16.50±1.81	2.78±0.62	6.06±1.01
	44	36.22±1.14	25.31±1.01	77.50±3.08	14.17±1.64	3.39±0.98	4.94±0.91
	220	38.56±2.30	23.33±0.77	78.94±2.68	13.22±1.43	3.33±0.54	4.67±0.87
24	0	33.72±1.14	23.99±0.51	62.50±3.24	22.56±1.36	4.72±0.88	10.17±1.71
	22	37.94±1.49	21.99±0.66	58.44±1.68	27.56±0.93	3.83±0.61	10.39±1.27
	44	34.33±1.67	24.24±0.86	58.17±2.30	28.11±1.52	4.11±0.75	9.89±1.37
	220	35.22±1.55	22.94±1.43	66.33±2.26	21.22±2.19	3.17±0.31	9.28±1.19

Tab.4.3 CASA analysis of morphology parameters and velocity distribution in ram semen exposed to increasing doses of CeO_2 NPs up to 24 h at 4°C. Results are shown as means ± SEM.

In reproductive biology the knowledge about the kinetics, transport and accumulation dynamics of nanoparticles in male and female gametes and their effects on the potential fertility is far away to be exhaustive and often controversial, as recently reviewed by Barkalina et al.[74] Sperm motility parameters represent an indirect predictor of male fertility, since they indicate the ability of moving progressively through the female genital tract and to fertilize the oocyte.[72] Impairment of motility in the male gamete leads unequivocally to the reduction of fertilizing ability. A decrease in spermatozoa motility has been reported in the bovine after exposure to europium oxide,[69] and to Au NPs.[75] Similar reduction of motility has been observed in human

fresh semen exposed to Au NPs[67] and to Ag NPs.[76] Conversely, motility and acrosome reaction of bovine sperm cells are not affected by exposure to magnetic iron oxide NPs (Fe_3O_4-NPs) coated with polyvinyl alcohol[69,77] or to europium hydroxide NPs ($EuOH_3$-NPs) conjugated with polyvinyl alcohol or polyvinylpyrrolidone.[69] In the rat, CeO_2 NPs supplemented with the diet, leads to a significant improvement of motility and viability of epididymal sperm.[54]

- Nanoceria effects on membrane , DNA and mitochondria

The assessment of the acrosome and plasma membranes, by PI and PSA staining, among the treated groups of ram semen exposed to increasing doses of nanoceria shows significant morphological changes in the membrane status (Fig.4.21). Usually, changes of these structures, as sperm capacitation and acrosome reaction, are involved in the fertilization, and any alteration or damage might compromise the functionality of the spermatozoa. These findings are in agreement with previous studies carried out on boar spermatozoa exposed to engineered nanoparticles. In fact, it has been reported that the co-incubation for a short time with nanoparticles of mesoporous silica,[74] gold and silver[36], cadmium selenide and zinc sulphide quantum dot[70] do induce any significant alteration of the integrity of sperm membranes showing that these nanoparticles do not exert any detrimental mechanical or chemical effects on the sperm cells.

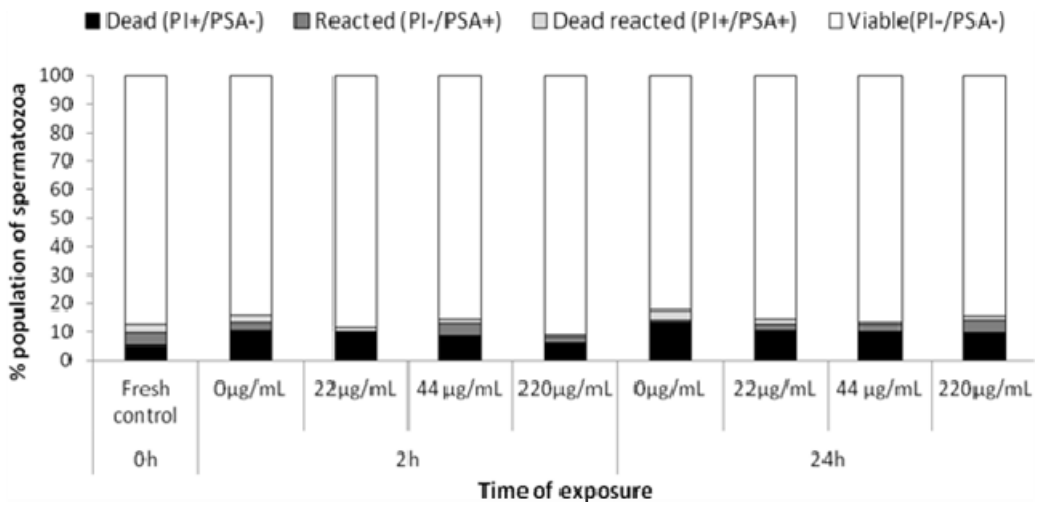

Fig.4.21 Membrane integrity and acrosome status in ram spermatozoa exposed to increasing doses of CeO_2 NPs assessed by PI and PSA staining. No significant differences in any of the classes of stained spermatozoa was observed (P>0.05).

The DNA fragmentation index (DFI) analysis has been performed to assess the effects of nanoceria on DNA in ram semen. Fig.4.22 shows that the exposure to increasing doses of nanoceria have no detrimental effects on the DNA of the spermatozoa while time had significant effects on it. Our findings clearly demonstrate that the exposure of ram spermatozoa to CeO_2 NPs up to 24 h does not increase the DNA fragmentation index even in presence of elevated concentrations of CeO_2 NPs indicating a high biocompatibility. It has been reported that the exposure of sperm cells to NPs causes genotoxic alteration with an increase of spermatozoa with fragmented DNA. Genotoxic effect on male germ cells has been observed in testicular cells of mouse after exposure to silver nanoparticles[52] and in bovine spermatozoa incubated with ultra-small gold nanoparticles.[51] Moreover, treatment of mouse epididymal sperm with gold nanoparticles (Au-NPs) results in inhibition of the chromatin decondensation process[78] and a dose-dependent induction of DNA damage has been observed in human spermatozoa exposed to TiO2-NPs and Zinc Oxide nanoparticles (ZnO-NPs).[79] The integrity of sperm DNA is correlated to the fertilizing ability.

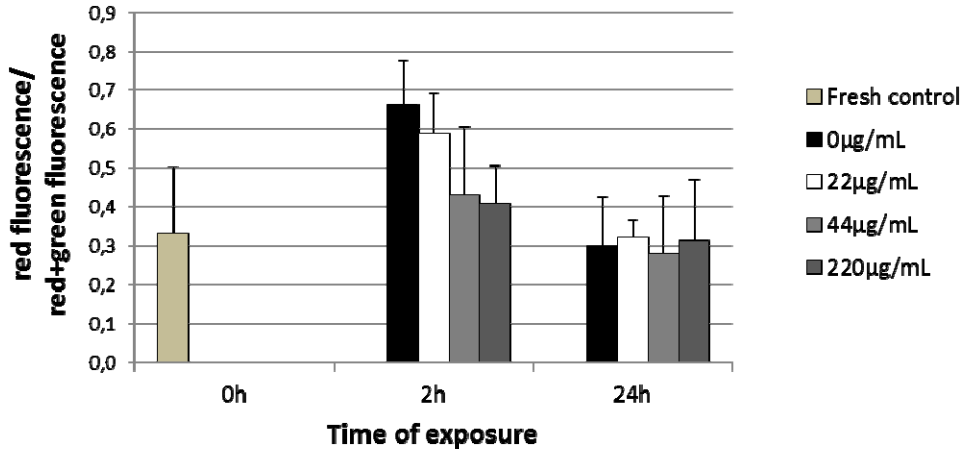

Fig.4.22 DNA fragmentation index in ram spermatozoa exposed to increasing doses of CeO_2 NPs for 24h at 4°C. No significant effects of the treatment on DNA integrity was observed (P>0.05).

The maintenance of morphological and functional parameters during semen storage is related to several factors such as temperature, energy supply, and production of ROS. Ram spermatozoa are very sensitive to oxidative stress and ROS production leads in the male gamete to the impairment of its fertilizing ability, compromising the integrity of the membranes and the activity of mitochondria. [80,81]

The ROS production and the mitochondrial activity of spermatozoa after exposure to nanoceria have been evaluated by using a fluorescent molecule 2',7' dichlorofluorescein diacetate (H_2DCFDA). Neither the time, nor the dose of nanoceria affects the oxidative status after 24 h of incubation. The levels of ROS in the treated groups are stable throughout the 24 hours of incubation at 4°C and do not differ from the untreated group, showing that the presence of nanoparticles does not exert either a pro or anti-oxidant activity (Fig.4.23a). This observation is supported by the analysis of mitochondrial activity (Fig. 4.23b) that is not affected by the presence of NPs. We can speculate that the anti-oxidant activity of CeO_2 NPs might be exerted in biological systems affected by strong oxidative stress. In fact in this study, spermatozoa have been submitted to a mild stressing source (the storage at 4°C), and after 24 hours the functional and morphological parameters of control and treated groups have been

highly satisfactory. This suggests the need for further investigations on the effects of these NPs on ram spermatozoa for different stressing conditions, such as for example, longer incubation times and lower temperatures. Moreover, the absence of effects of nanoceria on the redox system of ram semen could be also related to a species-specific sensitivity. Recently negative influences of CeO_2 NPs due to oxidative stress, genotoxic and mechanical effects have been reported in mouse sperm cells during *in vitro* fertilization.[82]

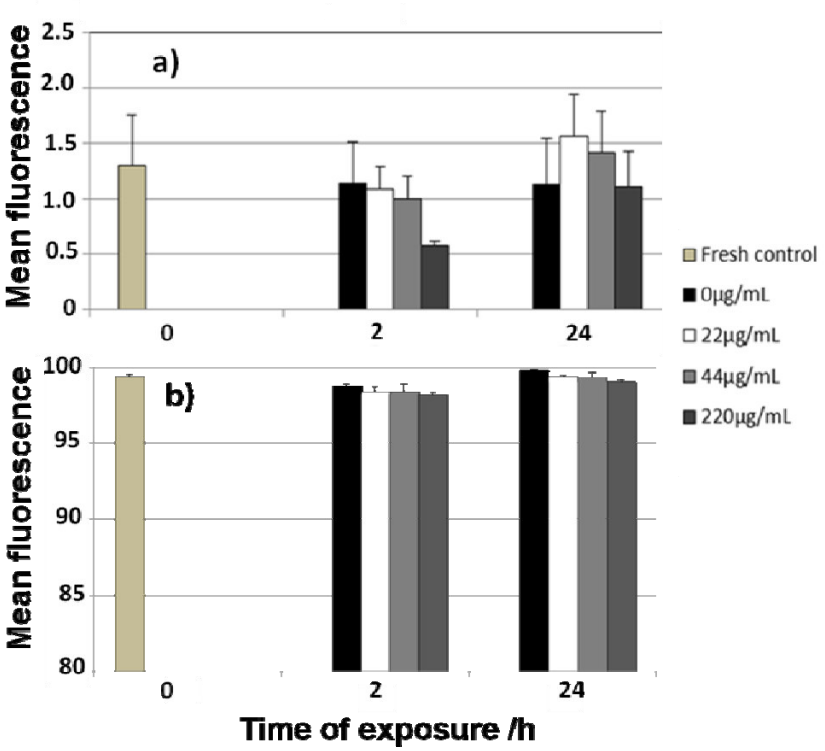

Fig.4.23 ROS production (a) and mitochondrial activity (b) by ram spermatozoa following 24h of exposure to increasing doses of nanoceria.

4.2. Ceria based nanocomposite coatings and their potential bio - applications

Development of new nanomaterials with oxide nanoparticles grafted or embedded with pores on hybrid organic-inorganic surfaces or on oxide matrices have gained much attention in material science because of the increasing applications of such nanocomposites in medical diagnostics, in biology, chemistry and etc.

Oxide nanoparticles, such as ceria, titania and superparamagnetic iron oxide nanoparticles (SPIONs), exhibit a number of remarkable functional properties, which make them the subject of an extensive research in several fields. Nanoparticles are usually dispersed in liquid phase to form a colloid and applied to a number of applications such as antibacterial treatment, contrast agent for magnetic resonance imaging,[83,84] ultrasensitive detection of biomolecules, etc. Interesting applications, however, could be revealed by the grafting of nanoparticles to flat surfaces for the development of functional coatings with a large tuning of the interface properties. Different applications can be envisaged for these systems, such as, for instance, the design of antibacterial coatings produced with low-cost materials[85] or the easy fabrication of superhydrophobic surfaces by tuning the roughness with grafted nanoparticles.[86] Up to now, only few pioneering studies have tried to develop this approach; Aboulaich et al. [87] have optimized a non-hydrolytic method for the synthesis of reactive anatase nanoparticles affording to a simple way to form nanoparticles monolayers. Despite the potential of such systems, the difficulty of obtaining a controlled nanoparticle grafting on different types of surfaces has represented until now a severe limitation for an extensive application of this approach. To strengthen the interactions between nanoparticles and surface, it is often applied a chemical modification of the nanoparticle surface using specific surfactant during the synthesis[88] or by post-functionalization with reactive groups such as amine, epoxide and vinyl. This method offers the advantage of increasing the nanoparticle solubility, avoiding the formation of aggregates and can also be exploited for selective binding of further molecules on the particle surface. Another possibility is the

chemical functionalization of the substrate, in order to obtain chemically bound nanoparticles. Although being effective, however, these routes are multistep and time-consuming processes that could lead to unwanted changes in the material properties due to the chemical modification at the NPs-coating interface. A direct grafting of nanoparticles onto films would overcome this drawback, although requiring changes of the surface properties without any chemical functionalization.[89] To obtain a thin layer of grafted nanoparticles on a suitable substrate, therefore, we have tried to deposit a thick film made of hybrid organic–inorganic material and then use it as a substrate. The advantage offered by this class of materials is the possibility of tuning the properties through small changes in the chemistry and processing. In particular, hybrids prepared employing 3-glycidoxypropyltrimethoxysilane (GPTMS) as a precursor offer several advantages because the structure and the surface can be designed through control of the epoxide opening and silica sol to gel reactions (Scheme 1). The epoxide reactivity has not only a strong influence on the material structure, but also affects the surface properties; in fact, when the epoxide groups are closed, the hybrid surface is relatively more hydrophobic, while with the growing number of hydroxyls moieties deriving from the epoxy opening reaction, the surface becomes increasingly hydrophilic. [90,91] The GPTMS hybrids on the other hand show also excellent optical properties and have been used to prepare different types of photonic devices, such as planar waveguides,[92] optical limiters,[93] and nonlinear optical materials.[94,95,96] The optical transparency and the antiscratch properties exhibited by GPTMS hybrids have also made this material a successful product in the market for optical contact lenses.[97,98,99]

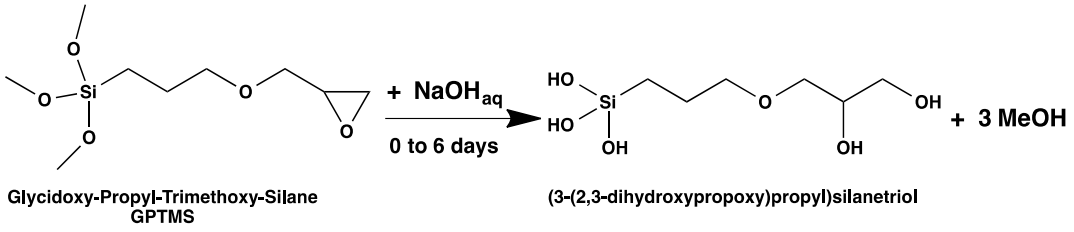

Scheme 4.1Reaction scheme of GPTMS with aqueous NaOH (pH 14)

It is, therefore, possible, to some extent, tuning the surface properties, which can be used for an oxide nanoparticle selective binding. In this thesis, we have then decided to test the orthogonal grafting of GPTMS films, by using two types of nanoparticles, nanoceria and SPIONs nanoparticles. The very basic idea in the case of nanoceria is to develop a new type of GPTMS material for potential application as functional contact lenses with advanced properties, which should be able not only to correct the vision problems of the eyes, but that could potentially play an active role on protecting them from degeneration processes. Topical delivery of ceria nanoparticles through eye drops, which is the simplest ophthalmic option, is not very efficient and in some cases some serious side effects[100,101] can arise. An alternative is the delivery through soft contact lenses which should slowly release the nanoparticles as an ophthalmic drug delivery system. We report in this work an example of GPTMS hybrid whose surface is covered with ceria nanoparticles that are able to be slowly released when immersed in a buffer solution.

While the use of SPIONs as a second type of nanoparticles, to test the orthogonal grafting of GPTMS films, is related to the fact that they are an highly attractive class of nanomaterials for the prospected applications in surface enhanced Raman scattering and as antibacterial surface in biology.[102,103,104] Despite SPIONs are one of the most studied class of functional nanomaterials, they are rarely used onto films surfaces because of the lack of reliable grafting methods. For example, self-assembly via Langmuir–Blodgett deposition requires the functionalization of nanoparticles and cannot be applied to any surface.[105] We have directly grafted SPIONs onto GPTMS films to produce functional layers, with no need of previous chemical functionalization, and the grafting obtained with SPIONs has been compared with that obtained with nanoceria as a function of the hybrid film processing.

4.2.1. Orthogonal grafting of oxide nanoparticles on hybrid film

Nanoceria has been synthesized using CTAB as coordinating agent and a microwave treatment. This synthesis has allowed obtaining a good control of dimension and size distribution of the particles. The XRD pattern in the angular range 25−75° of the CeO_2 NPs after the microwave treatment (Fig.4.24), shows diffraction peaks that correspond to the (111), (200), (220), (311), (222), and (400) planes for the cubic fluorite structure of CeO_2 cerianite (JCPDS: 34−0394). The patterns have been analyzed according to the Rietveld method,[106] using the program MAUD[107] running on a personal computer. The Rietveld fit gives 14.55 ± 2.3 nm for the crystallite size and 0.54 ± 0.37 nm for lattice parameter a, which is the same as the one reported for CeO_2 in the standard data (a = 0.5411 nm, space group Fm3m) (JCPDS: 34−0394).

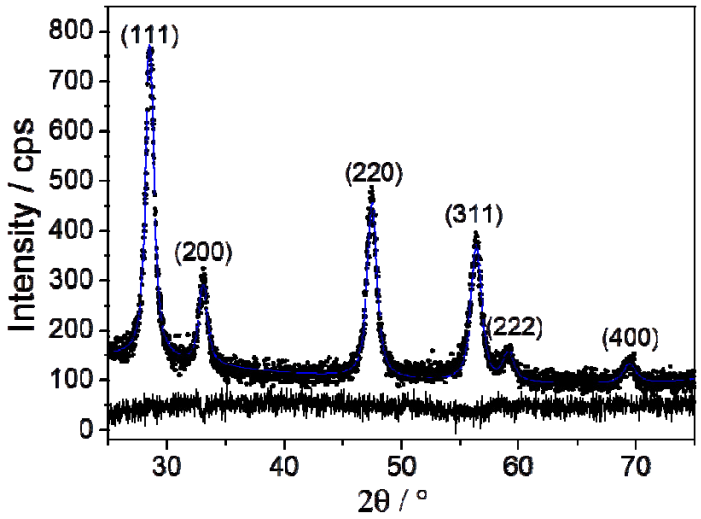

Fig.4.24 XRD pattern (black dots) of ceria nanoparticles after microwaves treatment; the Rietveld fit is shown with a continuous blue line. At the bottom of the figure is reported the curve of residuals Icalcs $^{1/2}$ − Iexp $^{1/2}$ (black line).

The aqueous dispersion of nanoceria has been also characterized by UV−vis spectroscopy; Figure 4.25 shows the UV−vis absorption spectrum in the 250 - 550 nm intervals, the concentration of ceria NPs is 80 mg ml^{-1}. The sample shows a strong

absorption with a well-defined absorbance peak at around 310 nm (4eV). The absorption in this region is due to the charge-transfer transitions from O 2p to Ce 4f, which overruns the f−f spin−orbit splitting of the Ce 4f state.[108,109] As reported in previous works, the broad absorption from 310 nm up to 500 nm is likely due to Rayleigh scattering of the nanoparticles in solution.[110]

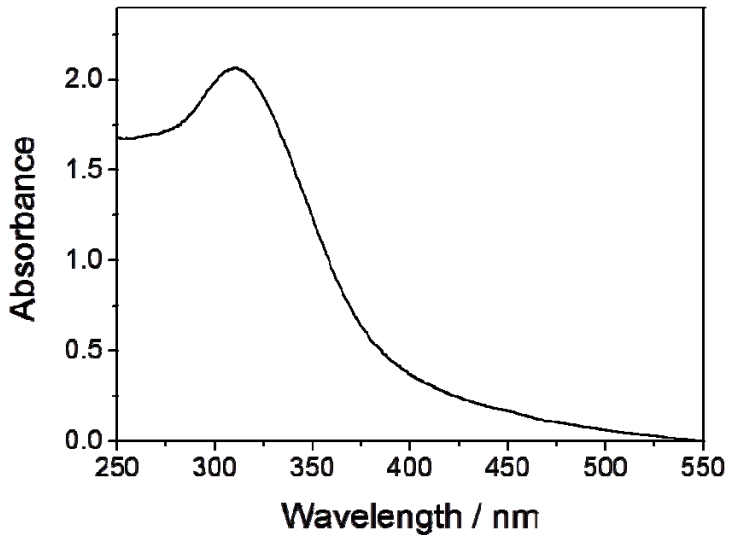

Fig.4.25 UV-Vis absorption spectrum in the 250 - 550 nm interval of an aqueous dispersion of nanoceria.

The synthesis of organic–inorganic films has been performed in highly basic conditions (pH 14) using GPTMS as precursor. This type of synthesis has the advantage to allow tuning the structure and surface of the hybrid films through aging of the precursor sol. In fact, the aging controls the extent of sol to gel reactions and affects the condensation degree of the inorganic silica network and at the same time the opening of the epoxides, which form organic chains into the hybrid. A high pH in the precursor sol promotes a very fast hydrolysis while it slows down the silica condensation and epoxide opening. This means that films deposited from a fresh sol will have a larger amount of unreacted epoxides, which will open and react with aging

of the sol.[111] FTIR spectroscopy has been used to study the structure and surface of the films in order to determine how these changes could affect the grafting of the SPIONs and nanoceria (Scheme 4.2).

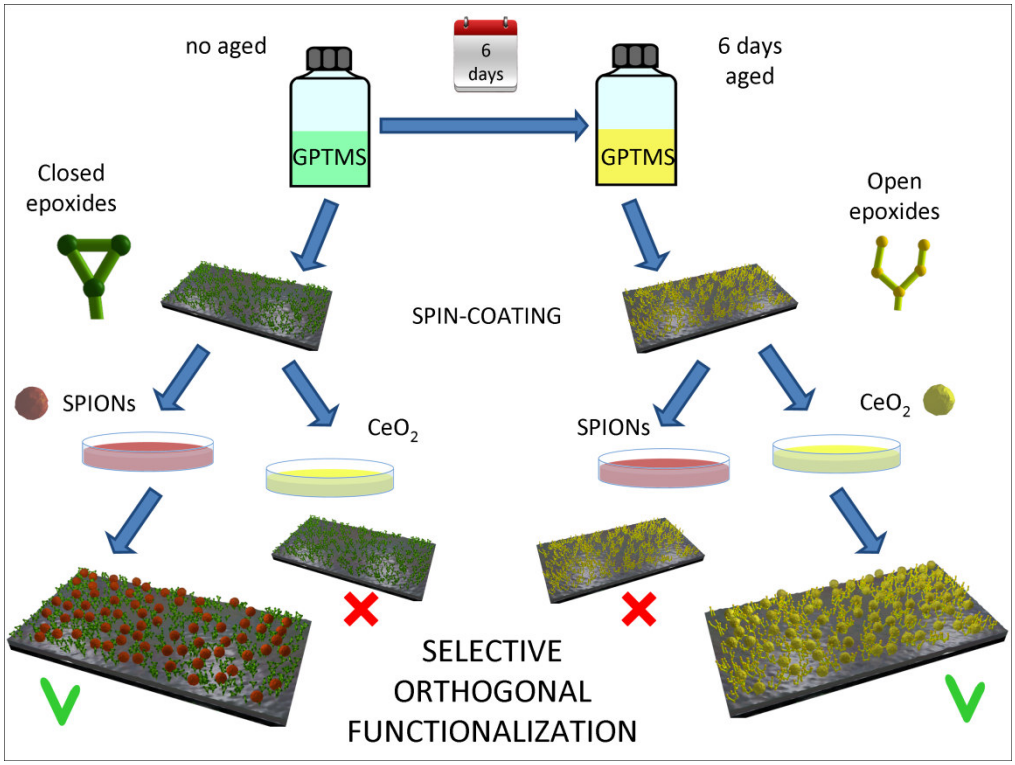

Scheme 4.2 Representation of the synthetic process involving the deposition of GPTMS films prepared by fresh and aged sol and subsequent grafting of SPIONs and ceria nanoparticles

Fig.4.26a shows the FTIR absorption spectra in the 3100−2750 cm^{-1} range of GPTMS films prepared from a fresh sol (black line) and 6 days aged sol (red line). This wavenumber interval corresponds to the CH_2 stretching region with the two main bands around 2920 and 2880 cm^{-1} which are assigned to CH_2 antisymmetric (CH_2, vasym) and CH_2 symmetric stretching (CH_2, vsym), respectively (spectra a and b in Fig. 4.26 have been normalized with respect to the band at 2850 cm^{-1}; baseline has been obtained using a rubberband function). These two main bands overlap with two absorption peaks, in particular at 3050 and 2955 cm^{-1}, which are attributed to

stretching modes of terminal CH_2 groups of the epoxides in GPTMS; another overlapped band at smaller wavenumbers around 2800 cm^{-1} is also assigned to epoxides.[112] These bands disappear in the aged sol sample, indicating that the epoxides full reacted upon aging; the same FTIR spectra in the region of Si−O−Si antisymmetric stretching mode[113] (1240− 950 cm^{-1} range, Fig.4.26b) indicate that the silica condensation is higher in the 6 days aged sol with respect to the fresh one. The wide intense band peaking around 1110 cm^{-1} (Si−O−Si, vasym), in fact, increases in intensity and the shoulder at 1150 cm^{-1} due to unreacted alkoxy groups disappears.[32] These changes clearly show that in films prepared from an aged sol the silica backbone is much more interconnected.

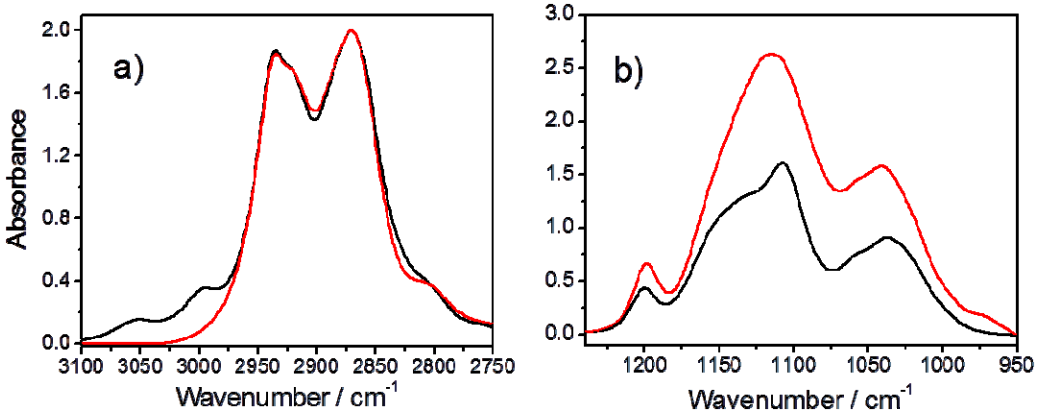

Fig.4.26 (a) FTIR absorption spectra in the 3100−2750 cm^{-1} and (b) in the 1240−950 cm^{-1} range of GPTMS films prepared from a fresh sol (black line) and 6 days aged sol (red line).

The extent of the condensation reactions affects also the hybrid film surface which becomes more and more hydrophilic in the samples prepared using a sol of longer aging times; the contact angle of the surface decreases from 55° in fresh sol films to around 32° in 6 days aged sol samples (Fig.4.27). A relative comparison of the contact angle change as a function of the amount of hydroxyls shows that there is a good correlation between the decrease in contact angle and the increase in hydroxyls content with sol aging.

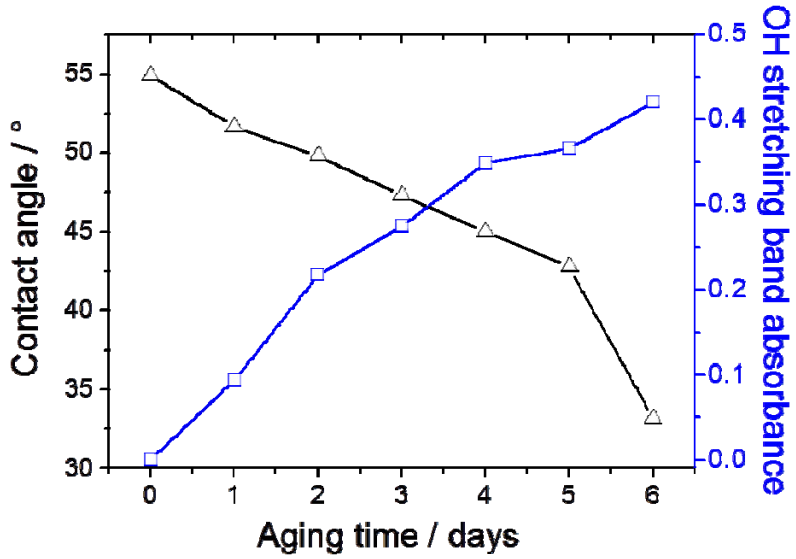

Fig.4.27Change of contact angle and OH stretching band absorbance (~3430 cm^{-1} band) in GPTMS films as a function of aging time. The lines are a guide for the eye.

The amount of hydroxyls has been evaluated on the ground of the OH stretching band[113] intensity around 3430 cm^{-1} from spectra normalized with respect to the band at 2850 cm^{-1} (Fig.4.28). The trend shown by the OH content is counterintuitive, because it should be expected that the amount of silanols decreases with the increase in aging time and the proceed of the polycondensation reactions. In this case, however, the presence of the epoxy groups which are hydrophobic changes the scenario; the epoxides at this high pH value (≈14) do not open all at the same time but slowly react with the aging time. When more and more epoxides react, they form a more hydrophilic environment, which is due to an increase of hydroxyl groups; this change also strongly affects the surface, which becomes more hydrophilic, as shown by the decrease in contact angle (Fig.4.27).

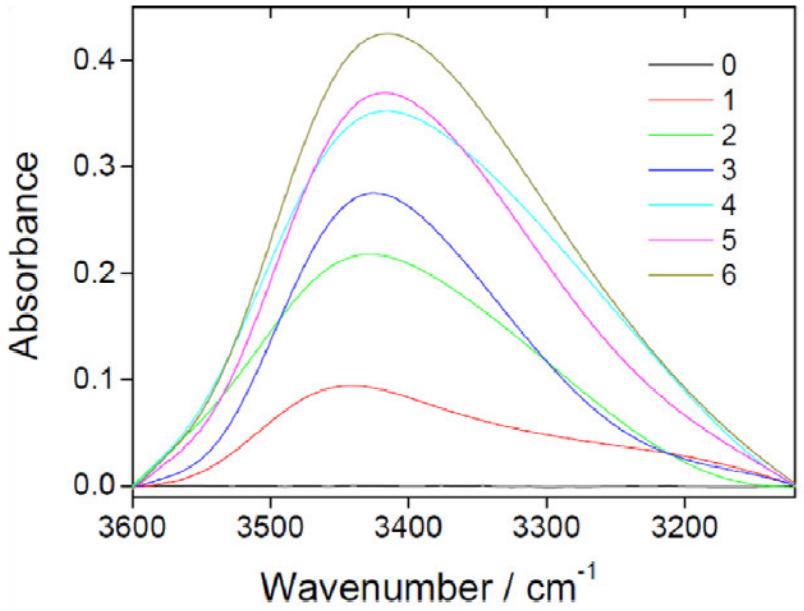

Fig.4.28 FTIR Absorption spectra in the range 3600-3120 cm^{-1} of GPTMS hybrid films as a function of the aging time. The legend is referred to the number of aging days.

- Post grafting functionalization of GPTMS film with ceria

The grafting of ceria nanoparticles on the surface of GPTMS films has been done considering that some peculiar properties are required. The surface of the film should allow an efficient and robust grafting of the NPS but, at the same time, the system should response when immersed in a buffer solution by slowly releasing the particles and maintaining an optical transparency of the film. The result of the grafting process has been tested by several techniques, UV−vis, XRD, TEM and AFM. Fig.4.29 shows the UV−vis absorption spectra in the 250−550 nm range of hybrid films with grafted CeO_2 NPs in the case of GPTMS with open epoxides (6 days aging, red line), and GPTMS with closed epoxides (fresh sol, blue line), GPTMS hybrid film spectrum obtained from 6 days aged sol is also reported as reference (black line). The spectra show that the grafting process is effective only in the case of GPTMS films which have been prepared from an aged sol and whose epoxides have been opened; the

UV−vis spectrum exhibits in fact the typical signature of the ceria NPs as can be estimated by comparing this spectrum with that one in Fig. 4.25 of pure ceria.

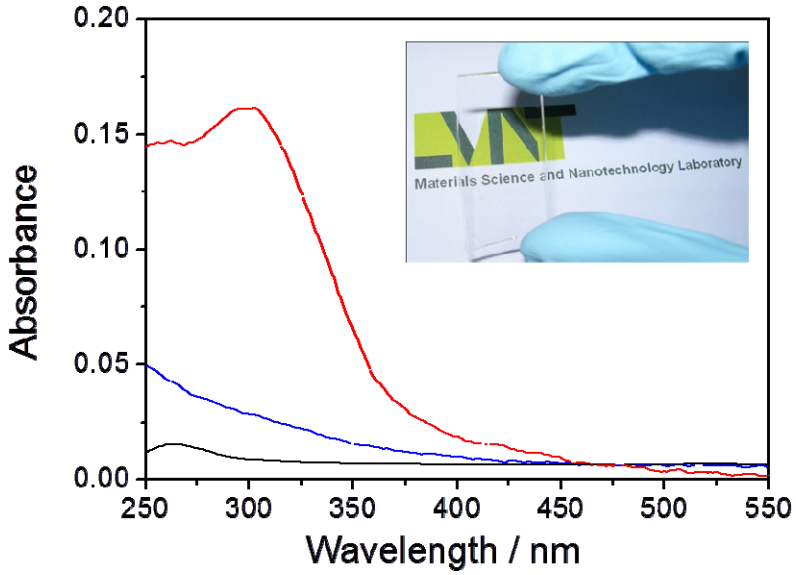

Fig.4.29 UV−vis absorption spectra in the 250−550 nm range of hybrid films; GPTMS with open epoxides (6 days aging, red line) grafted with CeO_2 NPs, GPTMS with closed epoxides (fresh sol, blue line) grafted with CeO_2 NPs, reference spectra of a GPTMS hybrid film (6 days aged, black line). The inset shows the optical image of the 6 days aged film with grafted ceria nanoparticles.

On the other hand, the hybrid reference film with open epoxides shows a high optical transparency while the sample with closed epoxides has only a not-structured small diffuse absorption from 350 to 250 nm, very likely due to a small amount of grafted particles. To confirm the successful grafting of ceria nanoparticles on the GPTMS hybrid film prepared from the aged sol, we have performed XRD analysis at grazing incidence on the coating. The sample shows a diffraction pattern which is assigned to cerianite NPs (Fig.4.30a), in accordance to XRD characterization of the ceria NPs in Fig.4.24; grafting the nanoparticles using the same protocol on the GPTMS fresh sol film does not work and no diffraction patterns have been recorded from this sample (Fig.4.30b). The XRD and UV−vis spectra are well in agreement each other and

indicate that grafting of ceria NPs is possible only on samples prepared from aged sols (open epoxide).

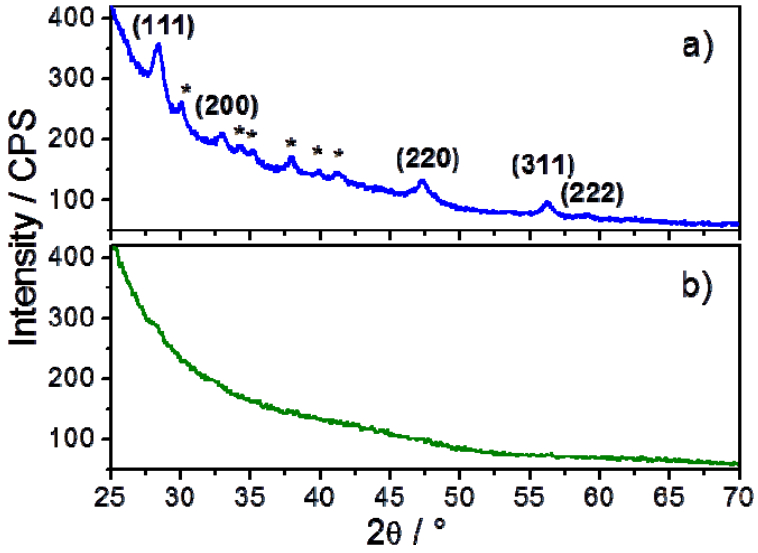

Fig.4.30 (a) XRD pattern of ceria nanoparticles grafted on the GPTMS hybrid film prepared from an aged sol (open epoxides) and (b) from a fresh sol (closed epoxides). The diffraction peaks from the silicon substrate are indicated by an asterisk.

We have also taken some fragments from the surface of the films to be analyzed by TEM; the bright and dark field images are shown in images a and b in Fig.4.31, respectively. The nanoceria appears well distributed within the sample and the dimension is in the range between 20 and 50 nm.

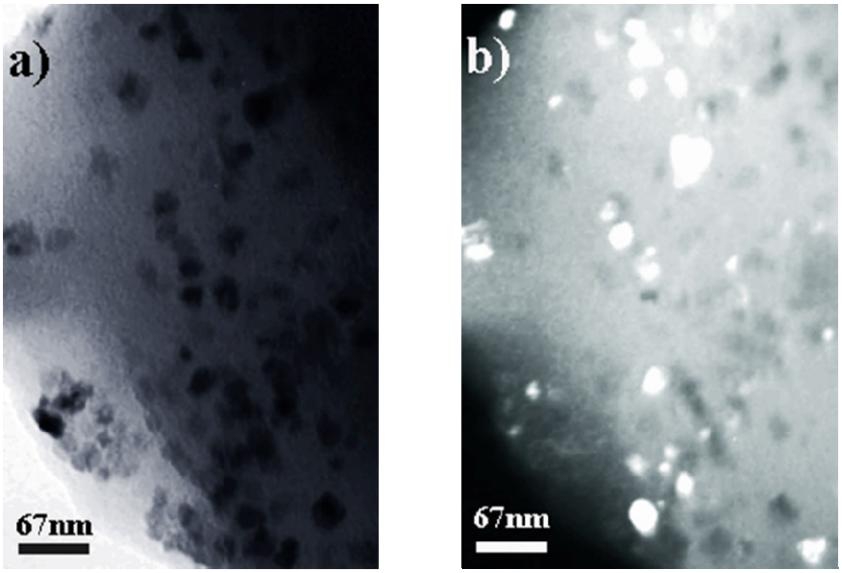

Fig.4.31 TEM images of a fragment taken from a GPTMS hybrid film with grafted nanoceria with open epoxides (prepared from the coating sol aged for 6 days). a) Bright and b) dark field image.

The samples surface has been analyzed by AFM, as shown Fig.4.32a and b respectively; the surface roughness topography of the GPTMS film before and after ceria grafting is also shown as inset in the same figures. The bare GPTMS surface appears smooth with a calculated root-mean-square (rms) of 0.73 nm, while after nanoparticles grafting the rms value increases to 22.31 nm. It is also interesting to observe that the topography of the film surface after particle grafting seems basically composed by a bimodal distribution which is given by two Gaussian components one centred around 50 nm and another one around 75 nm; this should indicate that the particles are distributed quite homogeneously on the film surface and some particles get closer to form small clusters, which increase the surface roughness.

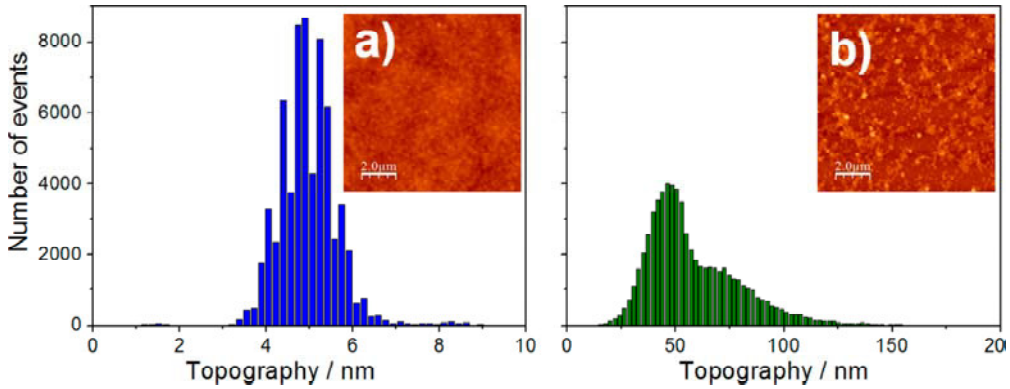

Fig.4.32 AFM images of the GPTMS film (a) before and (b) after ceria grafting. The surface roughness topography of the two images is reported as inset.

The previous data show that the GPTMS surface plays a primary role in the grafting process of the particles and that within some limits the surface itself can be used as a chemical switch with on-off response to nanoceria bonding. This property is directly correlated with the aging of the precursor sol which is used for the deposition, which means with the proceed of the polycondensation reactions of both the organic (epoxides) and the inorganic species (the silanols). Only when the epoxide has completely reacted (between 2 and 3 days of aging) the film will allow a successful grafting on the surface of the particles. The FTIR data show that with aging and opening of the epoxides more OH species are detected, they are the bonding sites which should favor the grafting between condensation reaction of OH species on the film and surface particles. The increase of hydrophilicity with aging also increases the surface wettability and the grafting efficiency. Hydrogen bonding also is likely to have an important role in binding the ceria NPs on the hybrid surface; in any case, the bonds should be strong enough to allow a robust grafting, but at the same time should allow a controlled releasing of the particles upon controlled conditions.

- Post grafting functionalization of GPTMS film with SPIONs

In order to prove the possibility to direct graft different types of nanoparticles on the hybrid surface without any post-synthetic functionalization step, we performed grafting experiment by using also superparamagnetic nanoparticles. The procedure and the hybrid film are the same used in nanoceria experiments. In the Fig.4.33a are shown the films prepared from a fresh sol without (pink line) and with SPIONs (blue line) while in Fig.4.33b are reported the film prepared from an aged sol without (green line) and with SPIONs (red line). There is no significant difference between the spectra of films before and after grafting of SPIONs, as they appear almost perfectly overlapped.

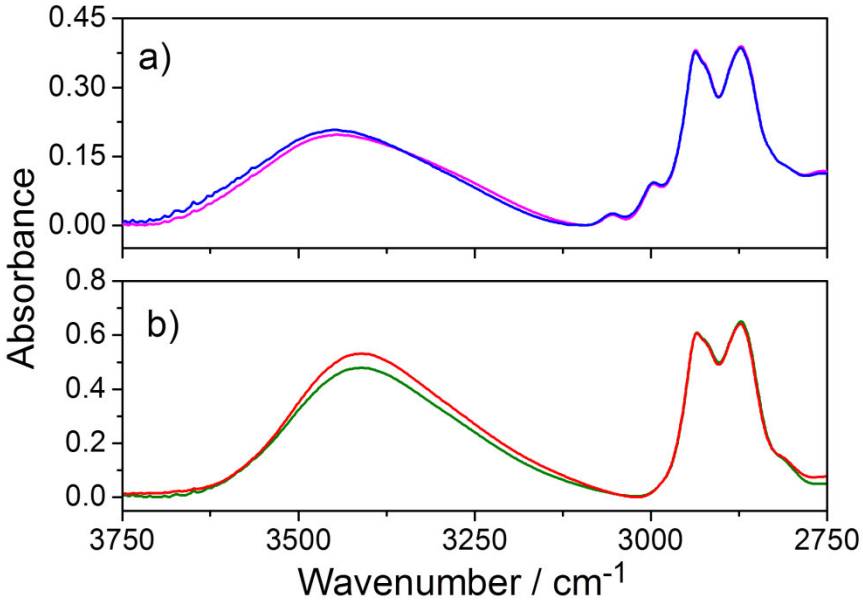

Fig.4.33 FTIR absorption spectra in the 3750–2750 cm^{-1} range of a GPTMS film prepared from a fresh sol without (pink line) and with (blue line) SPION; b GPTMS film prepared from an aged sol without (green line) and with SPION (red line).

The successful grafting of SPIONs on the hybrid film surface has been verified using grazing incidence X-ray diffraction and Raman spectroscopy. Fig. 4.34 shows the XRD patterns of SPION nanoparticles (bottom) and GPTMS film (top) prepared from a fresh (blue) or from an aged sol (red). The experimental data of SPION nanoparticles

are shown as black dots, while the Rietveld refinement is the orange line; the ticks show the diffraction peaks of the Fe_3O_4 magnetite crystalline phase (JSPDS 82-1533). The Rietveld analysis gives an average particle size of 8 nm, with a microstrain of 0.0015 and a cell parameter, a = 8.469 Å. It is important to underline that the diffraction patterns of the fresh and aged films show that SPIONs are observed only in the fresh samples, with a surface covered by a mixed presence of epoxides and silanols. These results have been also verified by Raman spectroscopy analysis, which has been performed on the same batch of samples; Fig. 4.35 shows the Raman spectra in the 800–150 cm^{-1} range of SPIONs (Fig. 4.35a).

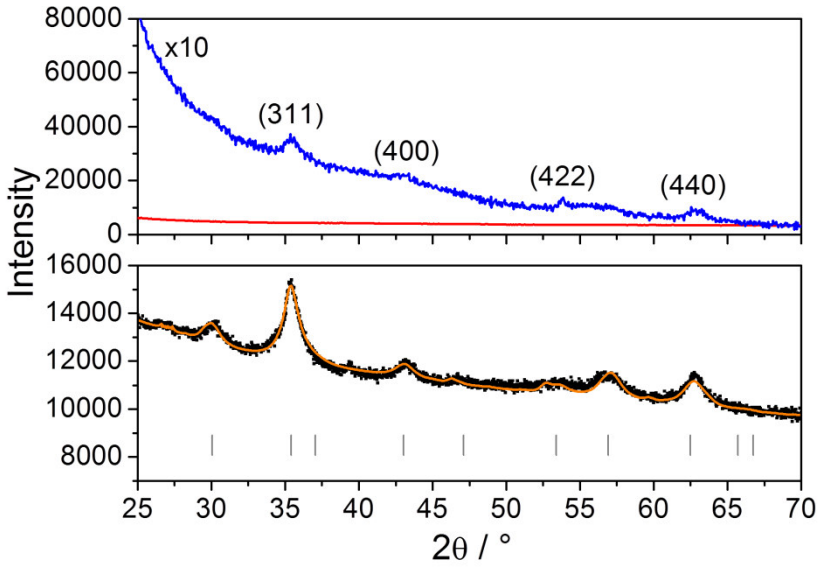

Fig.4.34 XRD patterns of SPION nanoparticles (bottom) and GPTMS film (top) prepared from a fresh (blue) or from an aged sol (red). The red and blue lines are both magnified by a factor 10. The experimental data of SPION nanoparticles are shown as black dots, while the Rietveld refinement is the orange line; the ticks show the diffraction peaks of the Fe_3O_4 magnetite crystalline phase.

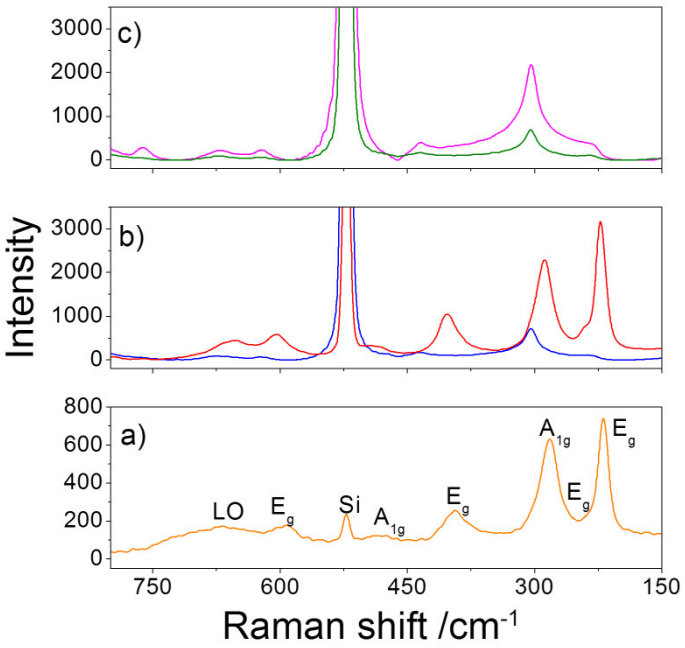

Fig.4.35 Raman spectra in the 800–150 cm^{-1} range of a SPION nanoparticles (orange line); b GPTMS film prepared from fresh sol with SPION (red line) and GPTMS film prepared from 6-day-aged sol with SPION (blue line); c GPTMS film prepared from fresh sol (green line) and 6-day-aged sol (pink line). The Raman mode of hematite are indicated in (a) on the corresponding bands.

GPTMS films prepared from fresh sol with SPIONs (red line) and GPTMS film prepared from 6-day-aged sol with SPION (blue line), (Fig. 4.35b) and GPTMS film prepared from fresh sol (green line) and 6-day-aged sol (pink line) (Fig. 4.35c). The Raman spectrum of the SPIONs in Fig. 4.35a shows scattering peaks which are typical of hematite,[114] α-Fe_2O_3, at 221 (A_{1g}), 289 (E_g), 391 (E_g), 486 (A_{1g}), 595 cm^{-1} (E_g) with a signal at 1.284 cm^{-1} which is due to the second order scattering of hematite; the peak at 500 cm^{-1} is generated by the silicon of the film substrate. The signal at 665 cm^{-1} which could be an indication of the presence of residual untransformed magnetite (A_{1g} mode),[115] is attributedto the Raman forbidden, infrared active longitudinal optical (LO) E_u mode of hematite which falls at the same value of Raman shift.[116,117] This mode is activated by disorder within the hematite crystal lattice, such as maghemite (γ-

Fe_2O_3)-like defects in the near surface regions.[117] The spectrum indicates, therefore, that exposure of SPIONs to the monochromatic laser light at λ= 633nm with a power of 5 mW induces a transformation of magnetite into hematite (Scheme 4.3). This has been well documented in literature and it has been also observed that the phase transition induced upon laser exposure depends on power intensity.[118] The transformation of magnetite into hematite occurs without formation of maghemite as intermediate phase, in accordance to the finding of Li et al.;[118] in powdered magnetite has been instead observed the formation of maghemite upon laser irradiation of fine powders, but not in coarse powders.[119] On the other hand, the exposure of magnetite nanoparticles on the film surface to a laser beam capable of inducing the change into hematite does not detach the particles and does not produce damage in the hybrid films.

Scheme 4.3Transformation of magnetite into hematite after exposure to laser beam at 633nm with a power of 5 mW.

The transformation from magnetite to hematite depends on the laser power intensity; in Fig.4.36 the Raman spectra in the 800–200 cm^{-1} range of GPTMS films whose surface has been modified with SPION nanoparticles and taken with different laser power intensity, from 0.2 to 20 mW, are shown. The sample illuminated with 0.2 mW of laser power shows a different spectrum, which is assigned to magnetite. The signals at 670 and 308 cm^{-1} are assigned to A_{1g} and T_{2g} modes, respectively, while the weak T_{2g} mode is overlapped by the substrate silicon signal and could not be detected.

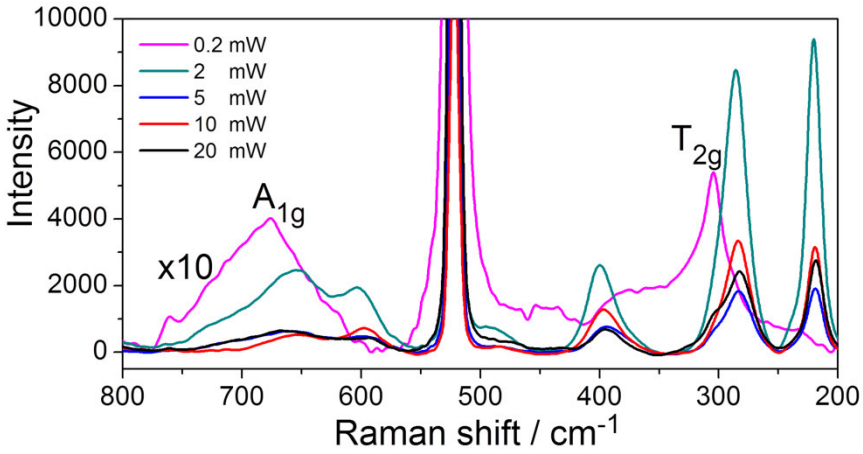

Fig.4.36 Raman spectra in the 800–200 cm^{-1} range of GPTMS films whose surface has been modified with SPION nanoparticles and taken with different laser power intensity, from 0.2 to 20 mW. The Raman mode of magnetite is indicated on the corresponding signals; magnetite is observed only at the lower laser intensity, in the other cases magnetite is transformed into hematite upon exposure to the laser light. The spectrum of 0.2 mW sample has been multiplied x10 to allow a better visualization of the data.

Magnetite is observed only at the lower laser intensity, in the other cases magnetite is transformed directly into hematite upon exposure to the laser light. The comparison of the Raman spectra (Fig. 4.35) has shown that iron oxide nanoparticles are bonded only on the surfaces containing epoxides (from fresh sol), supporting what has been observed by XRD analysis. The UV–Vis spectra of the films give a further support to this general finding; Fig.4.37a shows the absorption spectra of GPTMS film prepared from a fresh sol (red line) and GPTMS film whose surface has been modified with SPION (black line) in the 250–900 nm range; this sample shows an absorption band peaking at 370 nm which is the absorption signature of the iron oxide nanoparticles. In the films prepared from aged sols (Fig.4.37b), which therefore do not have closed epoxides, no absorption bands are detected.

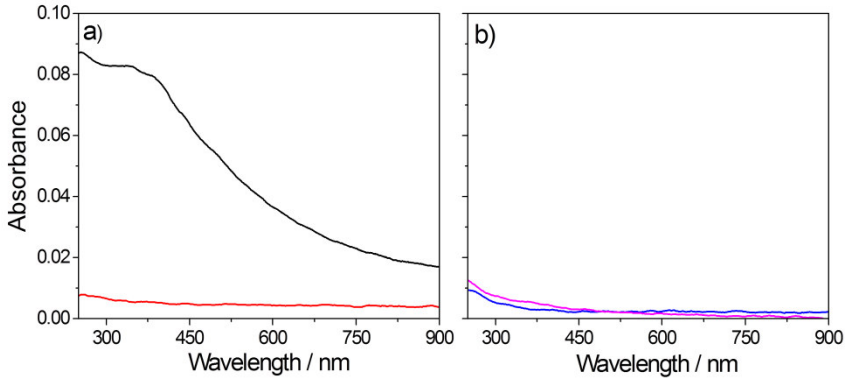

Fig.4.37UV–visible absorption spectra in the 250–900 nm range of a GPTMS film prepared from a fresh sol (red line) and GPTMS film whose surface has been modified with SPION (black line). b GPTMS films prepared from a 6-day-aged sol (blue line) and GPTMS film with SPION (pink line).

The changes induced by the laser beam on the structure of the SPIONs can be exploited for the fabrication of functional surfaces whose magnetic properties can be locally designed by inscribing them with a laser. We have demonstrated that it is possible to write patterns and circuits on the SPIONs layer by spotting the film surface with a laser. Fig. 4.38 shows the Raman imaging of a circular spot written using a laser intensity of 20 mW and 30 s of exposure. This power is enough to produce a selective phase transformation only in the illuminated area that changes to hematite while the not irradiated part remains magnetite.

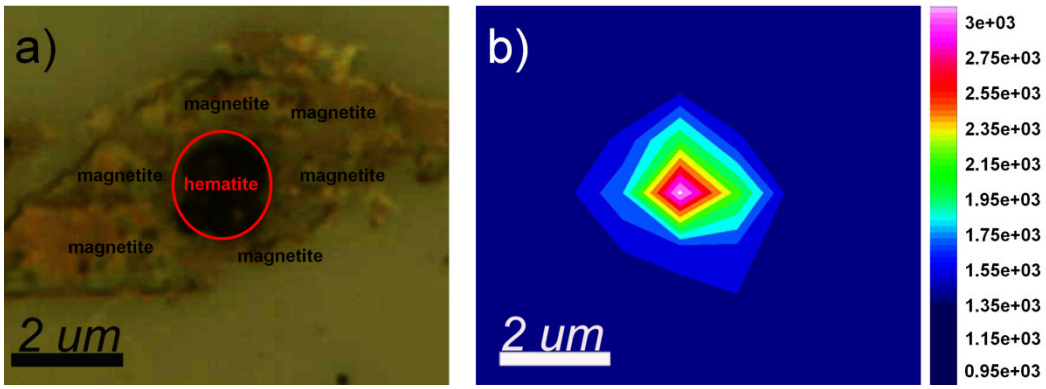

Fig.4.38 a) Optical image of SPION on GPTMS film pattern obtained using Raman laser at 366 nm at 20 mW. b) Raman mapping obtained from patterned SPION on GPTMS film using laser at 366 nm at 2 mW. The chemical image, reported in false colors scale, has been obtained by integration of the SPION hematite band at 219 cm^{-1}.

- Comparison between nanoceria and SPIONs grafted onto hybrid surface

In accordance to the previous results obtained with nanoceria, direct binding of SPIONs is achieved if the right balance between closed epoxide and hydroxyls groups is achieved on the hybrid film surface. The versatility of sol–gel chemistry allows for a wide range of modification of the hybrid film surface, and the content of hydroxyls and epoxides can be adjusted as a function of the processing parameters. In the case of SPIONs, chemical binding to the surface is achieved only in samples with epoxides, in other cases, such as nanoceria, we have observed an opposite response: films prepared from aged solutions are able to graft ceria nanoparticles on their surface. We have, therefore, made a comparison with grafting of ceria on GPTMS films prepared in the same conditions; Fig.4.39 shows XRD patterns of ceria nanoparticles (bottom) and GPTMS film (top) prepared from a fresh (blue) or from an aged sol (red). The XRD pattern in the angular range 25°–75° of the CeO_2 shows the (111), (200), (220), (311), (222), and (400) planes which indicate the formation of the cubic fluorite structure of CeO_2 cerianite (JCPDS: 34–0394) and whose average particle size was estimated in 14 nm. The ceria NPs are bonded only on GPTMS aged films where epoxides have completely reacted and only hydroxyls are present on the film surface.

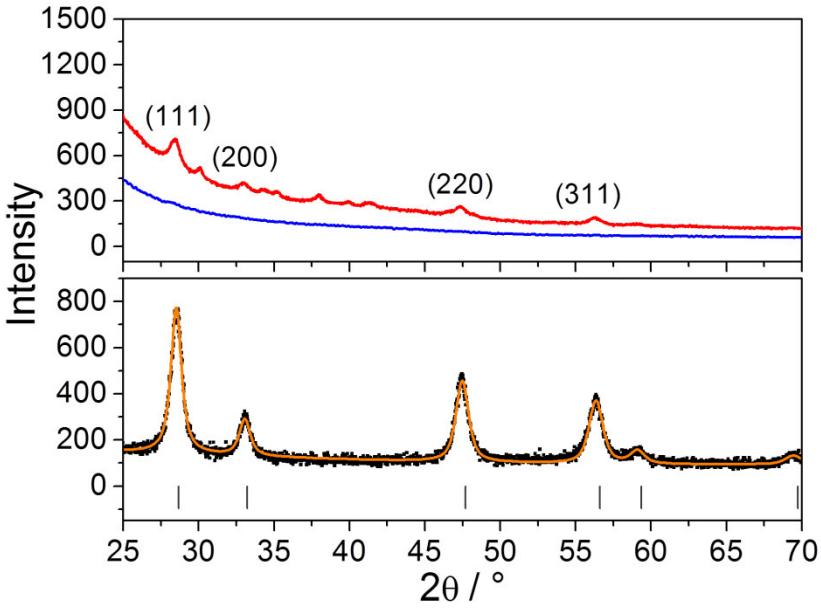

Fig.4.39 XRD patterns of Ceria nanoparticles (bottom) and GPTMS film (top) prepared from a fresh (blue) or from an aged sol (red).

This is confirmed by Raman spectra (Fig.4.40); at 465 cm^{-1} the Raman mode due to the symmetric breathing vibrations of the oxygen anions around the cerium cation,[120] which is a signature of crystalline ceria and is observed only in the aged sample without epoxides.

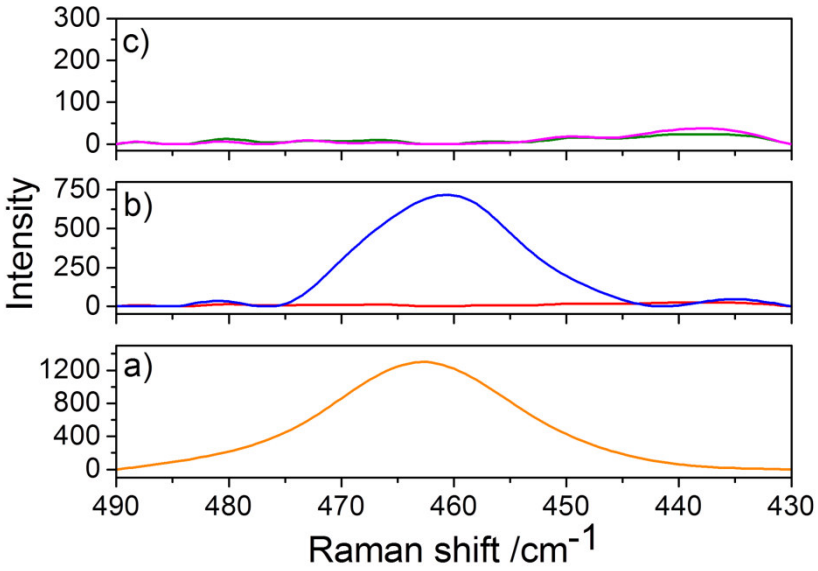

Fig.4.40Raman spectra in the 490–430 cm^{-1} range of a Ceria nanoparticles (orange line); b GPTMS film prepared from fresh sol with Ceria (red line) and GPTMS film prepared from 6-dayaged sol with Ceria (blue line); c GPTMS film prepared from fresh sol (green line) and 6-day-aged sol (pink line).

Fig.4.41 allows for a straight visual comparison of the orthogonal properties of the GPTMS films; 4 SEM images of the films, grafted with SPIONs and ceria nanoparticles respectively, after being deposited from sol aged 0 days (Fig.4.41a, c) and 6 days (Fig.4.41b, d), are reported. The Figure confirms that ceria nanoparticles are grafted only onto the 6d film whilst there is no presence of ceria on the 0d film. On the other hand, SPIONs are largely distributed on the 0d film surface and only scarcely on the 6d film.

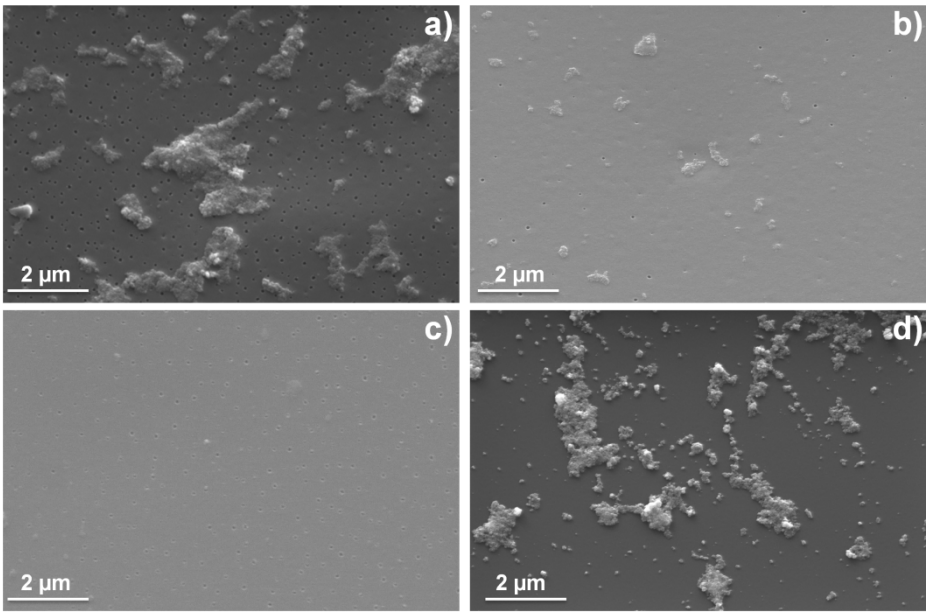

Fig.4.41SEM Images of GPTMS-SPIONs grafted onto 0d (a) and 6d (b) hybrid films; GPTMS-Ceria 0d (c) and 6d (d)

To have further insights on the surface coverage of the films due to the presence of nanoparticles, AFM analyses, both phase (Fig. 4.42) and topology imaging (Fig.4.43), have been performed on the samples confirming the results obtained by SEM imaging. More complete information about the nanoparticles distribution has been obtained by evaluating the surface coverage with imaging software on the phase imaging pictures. In fact, this analysis, by exploiting the phase image contrast related to the heterogeneity of the samples (nanoparticles vs hybrid films) has allowed determining the absence of ceria in the sample 0d and its presence in the 6d. Moreover, with regards to the SPIONs, the software analysis has revealed that the sample 0d has a surface coverage 20 times higher when compared to the 6d sample. Both SEM and AFM imaging confirm almost entirely what already evaluated by mean of Raman spectroscopy and XRD; the amount of SPIONs detected on the 6d film is almost negligible in comparison with that on 0d film.

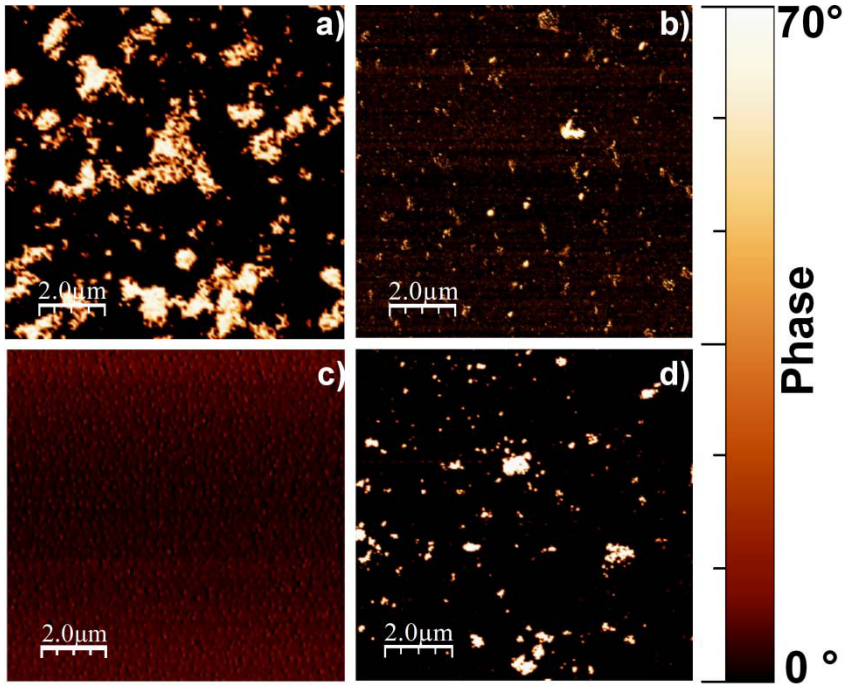

Fig.4.42 Phase Imaging of GPTMS-SPIONs by AFM: 0d (a) and 6d (b); GPTMS-nanoceria 0d (c) and 6 (d)

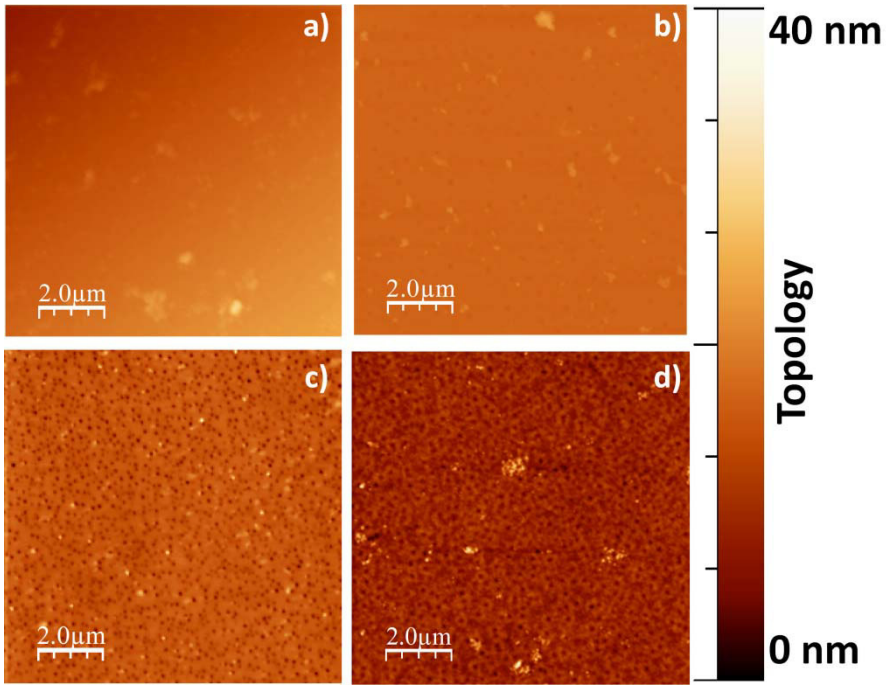

Fig.4.43 Topology imaging of GPTMS-SPIONs by AFM: 0d (a) and 6d (b); GPTMS-nanoceria 0d (c) and 6d(d).

The comparison between ceria and SPIONs shows that different types of nanoparticles could be bonded on the surface of the hybrid films if this is properly tuned; SPIONs are bonded when a mix of hydroxyls and epoxides are present on the surface, on turn, binding of ceria NPs is achieved only when epoxides are fully reacted. A drawing of this model is shown in Scheme 4.2. The tuning of the GPTMS surface chemistry allows a full compliance of the electrostatic requirements that are necessary for orthogonally binding one of the two types of NPs without using specific functionalization. However, unwanted residues of CTAB deriving from the ceria preparation could have been partially incorporated into the nanoparticles affecting their surface charge and therefore their ability in binding the film surface. It is also important to stress that the surface functionalization occurs both with nanoceria or SPIONs using the same solvent that is ethanol. Moreover, given the experimental evidences that we have achieved here and in our recent work performed on the

characterisation of hybrid organic–inorganic films,[121] we can hypothesise that the surface charge of GPTMS films changes as a function of the epoxide opening and therefore of the aging time of the GPTMS precursor sol. The surface charge of the films changes independently from the nanoparticles nature and therefore these should not affect their surface properties. This leads to the conclusion that the grafting procedure is controlled only by the nanoparticles properties and in particular by the different solvation environment which reflects their diverse chemical nature[122,123,124] In fact, the ethanol solvation sphere surrounding the nanoparticles provides the SPIONs with a more hydrophobic character, since the ethyl groups are directed on the outside shell, explaining therefore the binding capabilities to the more hydrophobic 0d films. On the other hand, the pristine hydrophobic nature of the nanoceria, due to the presence of CTAB residues on its surface, is reversed into hydrophilic by the solvation sphere of the ethanol molecules that direct their hydroxyls groups on the outer sphere, favouring therefore the binding onto the more hydrophilic 6d films. The surface tailoring of the film, therefore, is sufficient to ensure a solid electrostatic bond with a number of nano-object having remarkably different surface charge. In fact, despite its electrostatic nature, the bond appears to be strong enough to keep the nanoparticles grafted on the film surface even after three washing cycles with ethanol and this allows us to state that the particles are effectively bound to the surface and not just deposited onto it. The electrostatic interaction between NPs and GPTMS films enables the use of the NP layer as a functional material for a wide range of applications; in particular, the surface coating with naked SPIONs allows for micron-scale lithography of the magnetic properties through a local modification of the surfaces.

4.2.2. Release of nanoceria from hybrid film

To test the release of nanoceria from the films we have used Raman spectroscopy; we have also tried to apply the UV−vis spectroscopy by measuring the difference in absorbance before and after the release but, because of the small changes to be detected and the uncertainty in the baseline, we have not obtained reliable and reproducible results. We have used, therefore, Raman imaging which has two advantages, the crystalline ceria has only one Raman mode around 465 cm^{-1} due to the symmetric breathing vibrations of the oxygen anions around the cerium cation,[120] furthermore, it is possible collecting the spectra in a very specific area in imaging mode. This allows averaging the spectra to obtain a good signal-to-noise ratio of the Raman mode of ceria before and after the release. Fig.4.44a shows the Raman spectra in the 490−425 cm^{-1} range of ceria nanoparticles grafted on GPTMS film before (black line) and after a release test of 1 h (red line), 5 h (cyan) and 17 h (blue line) in phosphate buffer at pH 7.4.

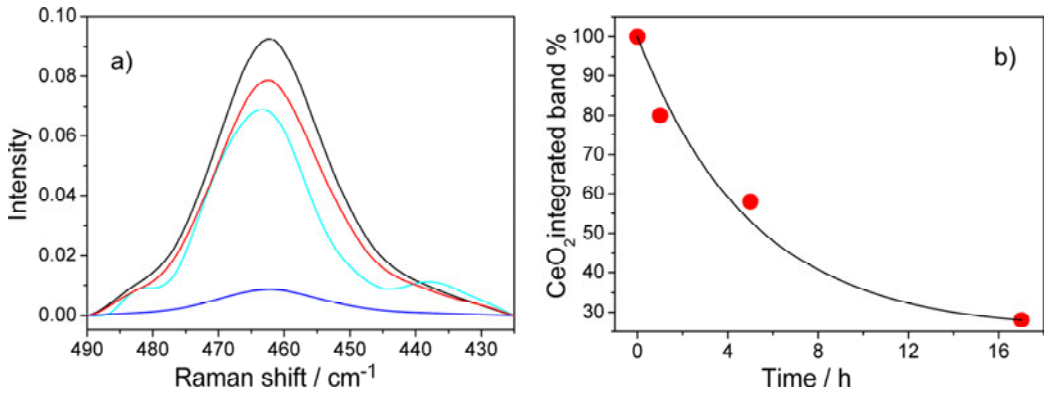

Fig.4.44 (a) Raman spectra in the 490−425 cm^{-1} range of ceria nanoparticles grafted on GPTMS film before (black line) and after a release test of 1 h (red line), 5 h (cyan) and 17 h (blue line) in phosphate buffer at pH 7.4. (b) Variation in ceria Raman integrated band area as a function of releasing test time (in hours); the black line is the exponential decay fit curve. The ceria nanoparticles concentration in water solution is 80 mg cm^{-3}.

The change of ceria Raman integrated band area as a function of releasing test time (in hours) is reported in Fig.4.44b; the data are well-fitted using an exponential decay

curve. This indicates that the particles are not released immediately after the immersion in the buffer, but it is a time dependent process that can be controlled. Within 17 h of immersion of the film with the grafted ceria nanoparticles around 70% of them are released in the buffer solution. This result shows that the system could be potentially developed for controlled release of ceria nanoparticles in materials such as contact lenses; the overall release process is illustrated in Fig.4.45.

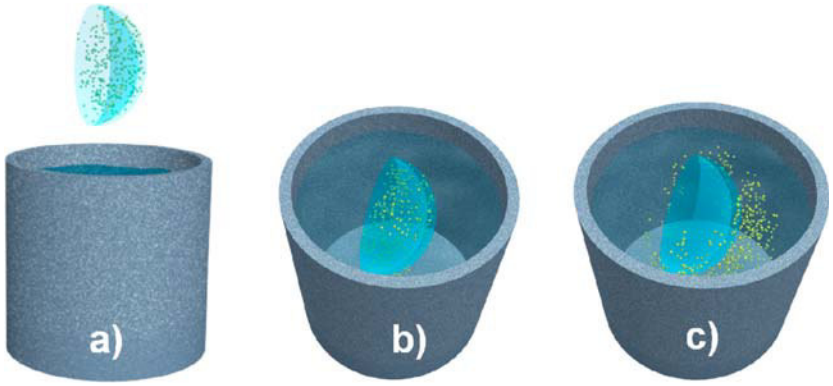

Fig.4.45 (a) Grafted ceria nanoparticles when the sample is (b) immersed in a buffer solution are (c) slowly released.

4.2.3. Top-down and bottom up routes to fabricate nanoceria into a porous matrix

The integration of bottom-up and top-down routes has recently become one of the main challenges for fabricating nanodevices with advanced functional properties. In particular, it has been shown that high-energy X-rays allow for direct patterning of soft matter and fabrication of devices by a fast and extremely versatile protocol.[125] The combination of hard X-ray and soft matter has several advantages; in fact, when a material is still in its "soft" state, it can be directly modified and patterned by hard X-rays. Sol−gel,[126,127] hybrid organic−inorganic materials,[128] mesoporous films,[129] metal−organic frameworks (MOFs),[130] and block copolymers[131] have shown to be suitable for integrating bottom-up and top-down fabrications. The combination of the

two methods turned out to be particularly effective when applied to functional mesoporous films; in fact, a mesoporous ordered film can be obtained via self-assembly through organization of supramolecular templates and the film lithography performed immediately after deposition allows for the densification of the wall structure and removal of the surfactant in one single step. Furthermore, when nanoparticle precursors are added to the material by one-pot synthesis or post impregnation of preformed films, X-ray exposure can be exploited to promote the growth of metal nanoparticles (NPs), such as gold[132] and silver,[133] within the porous matrix. The nanoparticles nucleate and grow in the film regions exposed to the X-ray beam, and this represents therefore a direct lithographic method for writing the material and producing devices for different applications such as nanoelectrodes[134] and surface-enhanced Raman spectroscopy (SERS) layers.[130] The functionalization of the porous matrix with oxide NPs would also be very interesting, but up to now, the achievement of a spatial control required for patterning a mesoporous film by controlled nucleation and growth of nano-objects is still a difficult task. In particular, crystalline nanoceria is of paramount importance because of its catalytic and radical scavenging properties.[135,136] The controlled formation of nanoparticles into a porous matrix would open the route to several important applications, especially in the field of nanobiotechnology. In fact, the design of smart nanocomposite surfaces could be applied for the fabrication of cell chambers and/or dishes for cell culture. The incorporation of functional properties at the interface between chambers and cells offers several advantages such as, for instance, a close interaction between biological species and the nanocomposite surface with no need of dispersing/capping agents or pH buffers to avoid particle aggregation in the cell media. For these reasons we have optimized a combination of bottom-up and top-down processing which allows producing ceria nanoparticles of controlled dimensions within a mesoporous ordered titania film. This matrix has been first selected to increase the hydrolytic stability of the nanocomposite. The overall material fabrication, however, has been designed to

minimize the crystallization of the titania matrix allowing at the same time the writing of selected areas with ceria nanoparticles having radical scavenging properties. Furthermore the best procedure obtained in a titania-ceria nanocomposite production has been chosen to fabricate materials based on hafnia and silica matrix with embedded nanoceria. The toxicity of the three nanocomposite has been tested in cell cultures employing peripheral blood mononuclear cell (PBMC).

The synthesis of titania mesoporous ordered films is based on self-assembly of a pore templating agent triggered by solvent evaporation; this is a well-established route, and several types of ordered titania films can be obtained using a variety of surfactants.[137] In the first step of the present synthesis we have prepared mesoporous ordered titania films by employing a triblock copolymer, Pluronic F127, as a template; the films result well ordered even after the thermal treatment at 350 °C used to remove the template.[138] The firing temperature has been selected to optimize the film properties; in fact, after thermal processing the organic template is fully removed, and the mesoporous titania films maintain the mesostructure.[139] Fig.4.46 shows the GISAXS pattern of a titania mesoporous film after thermal treatment at 130 °C for 24 h and 350 °C for another 2 h; the pattern is characteristic of an Im3m in the space group contracted along the [110] direction. The GISAXS pattern confirms that the mesostructure is retained after processing and the thermally induced uniaxial shrinkage[140] produces a small distortion of the pore structure.

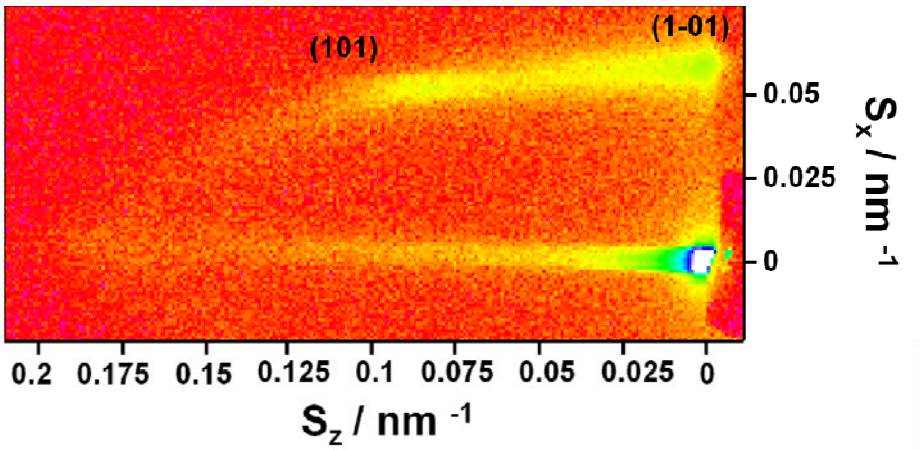

Fig.4.46 GISAXS pattern of a titania mesoporous film after thermal treatment at 130 °C for 24 h and 350 °C for another 2 h; the pattern is characteristic of an Im3m in the space group mesostructure contracted along the [110] direction.

In the second step of the preparation, the titania-ordered mesoporous films have been impregnated with the ceria precursor solution via spin coating that has shown to be the most effective route, while other methods (e.g., casting) have not given a homogeneous pore filling. The samples have been exposed to hard X-rays, generated by a synchrotron source, to induce the formation of ceria nanoparticles within the pores; the overall process is shown in Fig.4.47. The photons that have been used to irradiate the samples have energy between 2500 and 12 000 eV,[127] and they have been used in previous works as a lithographic tool for soft matter and in situ formation of metal nanoparticles in mesoporous films. As expected, the exposure to hard X-rays has induced the formation of ceria nanoparticles with selective control of the areas where these CeNPs grew up. Compared to other techniques, such as UV photo-assisted ceria synthesis,[141,142] a major advantage of the deep X-ray lithography is the penetration depth that can be reached;[143] this allows forming nanoparticles throughout the whole film thickness. Another advantage of DXRL is the loading that can be obtained; we have already tried to impregnate a mesoporous film with nanoparticles by using alternative approaches, such as post impregnation with colloidal nanoparticle solution or in situ formation of ceria nanoparticles. To the best of our knowledge, however,

these techniques do not allow a homogeneous loading of the inner part of the porous films. The mesoporous films have been therefore exposed to increasing doses of radiation, and the effect has been evaluated by electron microscopy, XRD, and Raman spectroscopy.

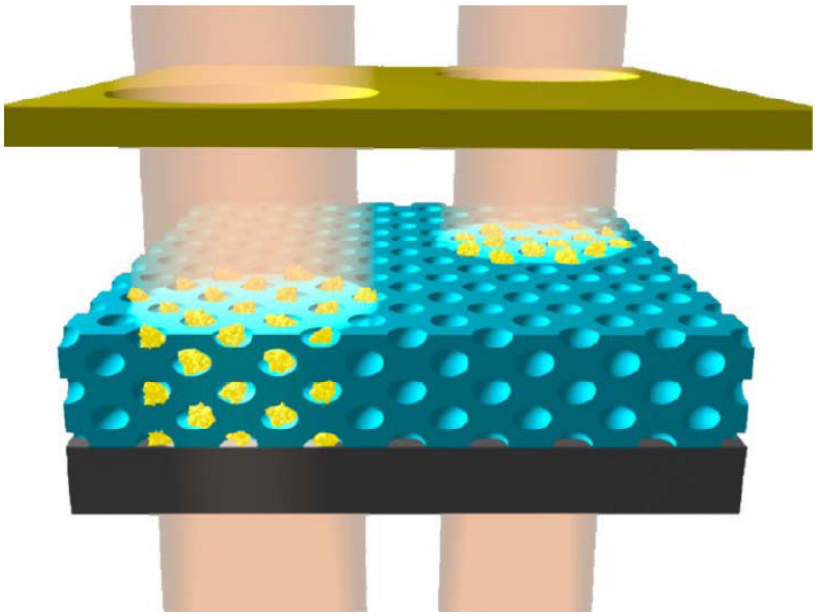

Fig.4.47 Drawing of the patterning process by in situ nucleation and growth of ceria nanoparticles.

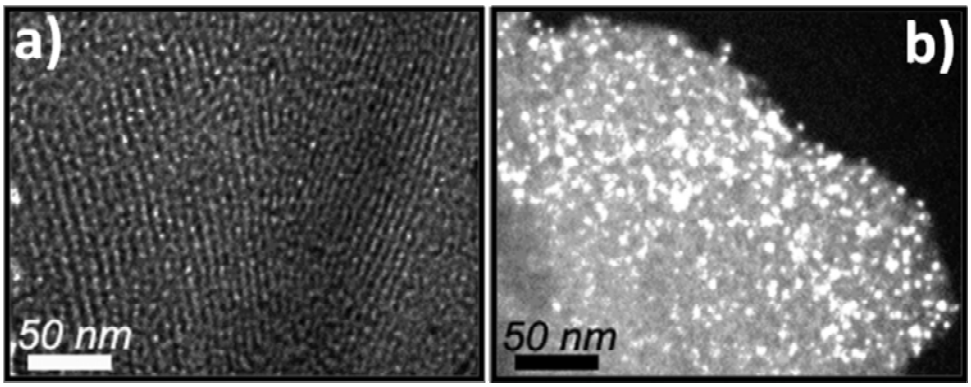

Fig.4.48 TEM images of (a) titania mesoporous film (bright field) and (b) titania mesoporous film with ceria nanoparticles (dark field) after X-ray exposure at the highest dose (653 J cm^{-2}).

TEM images of Fig.4.48 show representative bright (a) and dark (b) field images of the mesoporous film after X-ray exposure at the highest dose (653 J cm^{-2}). The samples retain the typical morphology of ordered porous films where pores in the mesoscale are stacked in a close cubic fashion. We have used a plot profile analysis of a large set of measurements to evaluate an average pore size of 5.4 ± 0.6 nm. This value, within the experimental error, is consistent with previous findings that also measured the surface area of the titania porous sample fired at 350 °C.[144] Following this reference, therefore, we have assumed a film surface of ≈ 595 m^{2}cm^{-3}. The dense and homogeneous distribution of the nanoparticles inside the porous matrix is clearly shown in the dark field images where the white spots are due to the cerium oxide nanocrystals; the average size of the nanoparticles has been estimated as 3.8 ± 0.9 nm. Spectroscopic ellipsometry has been used as a tool to evaluate differences in the film thickness before the X-ray exposure at 653 J cm^{-2}. The average thickness of all the samples is around 180 ± 20 nm, and we do not observe shrinkage after X-ray-induced nanoparticle formation. Fig.4.49 shows the XRD patterns in the angular range 20−100° of calcined titania mesoporous film whose pores have been filled with the urea−Ce solution (green line) and after exposure to 163 J cm^{-2} (black line), 326 J cm^{-2} (red line), and 653 J cm^{-2} (blue line) doses. After exposure to the lowest dose, the detection of a pattern with different sharp diffraction peaks indicates very likely the

fragmentation of the cerium nitrate induced by radiations. These peaks decrease in intensity and partially disappear after exposure to a higher dose, 326 J cm^{-2}, and are not detected any longer in the samples exposed to the highest radiation dose, 653 J cm^{-2}. On the other hand, with the increase of the dose, the films exhibit a diffraction pattern characterized by several broad and intense peaks which can be unambiguously assigned to crystalline cerium oxide. The diffraction peaks correspond to the (111), (200), (220), (311), (400), (331), (420), (422), and (511) planes of the cubic fluorite structure of CeO_2 cerianite.[145] It is also important to note that the thermal treatment at 350 °C and the exposure to X-rays do not induce further crystallization of titania, which is so little that it could not be detected by XRD. This point is particularly interesting because crystallites of anatase titania promote the formation of free radicals, while nanoparticles of ceria have the property of acting as a radical scavenger. The two effects could compete if titania crystallizes; nonetheless, in the present case, we have managed to find a method that allows producing nanocrystalline ceria within a solid mesoporous framework with a minimum amount of crystallinity.

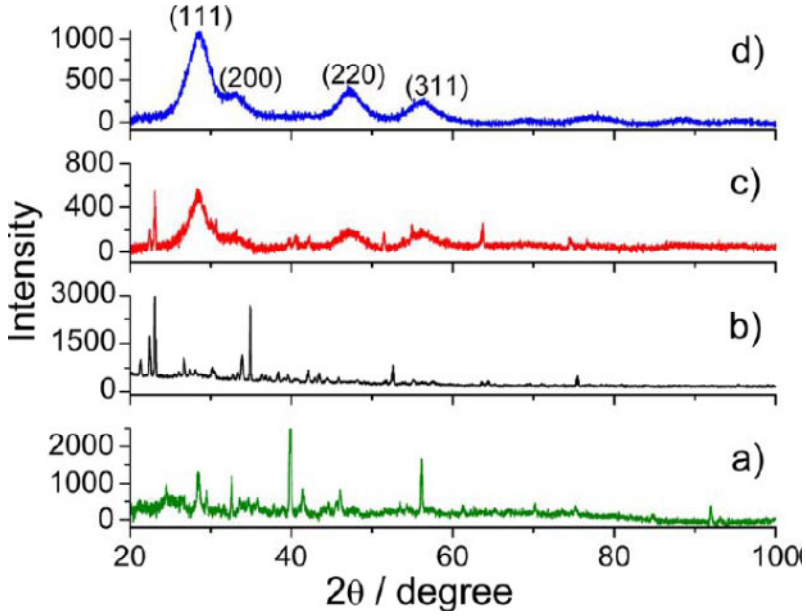

Fig.4.49 XRD patterns of titania mesoporous films at different processing steps: (a) as-prepared mesoporous titania film after filling the pores with urea−ceria solution (green line); (b) after exposure to a dose of 163 J cm^{-2} (black line); (c) after exposure to a dose of 326 J cm^{-2} (red line), and (d) after exposure to a dose of 653 J cm^{-2} (blue line).

On the other hand, mesoporous titania has the advantage to be highly hydrolytically stable in comparison to silica-based mesoporous materials and is more suitable to develop applications when chemical durability in water environment is requested.[146] We have characterized the nanoceria from XRD patterns using the Rietveld method; the fit (Fig.4.50) gives 4.05 nm for the crystallite size and 0.545 nm for lattice parameter a, which is the same value reported for CeO_2 in the standard data (a = 0.541 nm, space group Fm3m),[107] and the microstrain is 0.0029. At the highest exposure dose the films result in being composed of mesoporous titania whose pores contain nanoceria with an average dimension of 4 nm, in accordance with TEM analysis. Raman spectroscopy has been performed on the irradiated samples to detect the formation of cerium oxide; in detail, it has followed the evolution of the 465 cm^{-1} Raman active mode of cerium oxide, which is due to the symmetric breathing vibrations of the oxygen anions around the cerium cation.

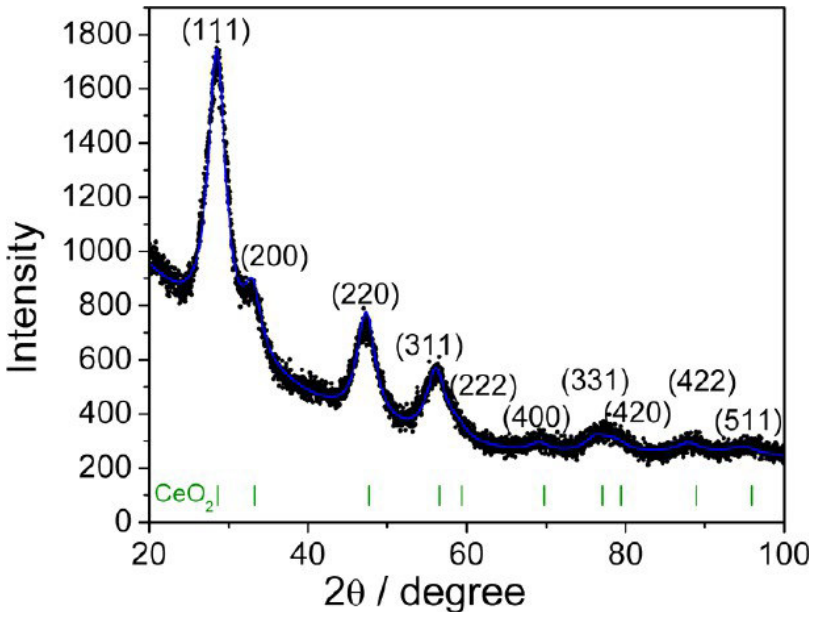

Fig.4.50 XRD pattern (black dots) of ceria nanoparticles after hard X-ray exposure (653 J cm^{-2}). The Rietveld fit is reported as a continuous blue line.

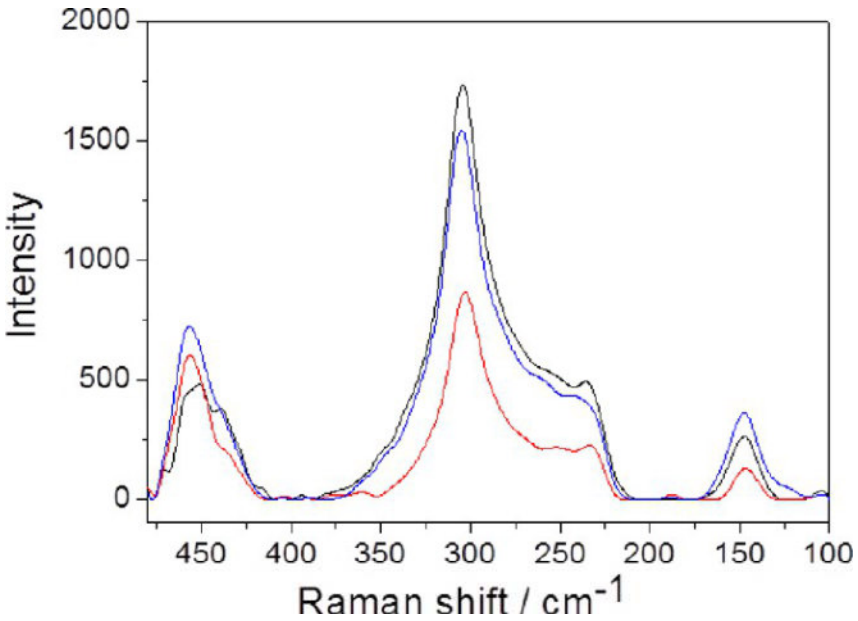

Fig.4.51 Raman spectra in the 475−410 cm^{-1} range of mesoporous films whose pores have been filled by cerium nitrate and urea solution after exposure to a dose of 163 J cm^{-2} (black line), 326 J cm^{-2} (red line), and 653 J cm^{-2} (blue line).

Fig.4.51 shows the Raman spectra in the 480−100 cm^{-1} range of urea-Ce titania mesoporous films upon exposure to different doses: 163 J cm^{-2} (black line), 326 J cm^{-2} (red line), and 653 J cm^{-2} (blue line). The Raman mode of ceria is clearly observed in the samples exposed to 326 and 653 J cm^{-2}, while around 143 and 450 cm^{-1}, there are two bands which are attributed to anatase and rutile phases, which are formed in the mesoporous structure as a consequence of the thermal treatment.[147] The crystalline fraction of the films and the size of the crystalline domains, however, are very small since the XRD patterns (vide infra) do not show diffraction peaks attributed to titania phases. We have also tested two other precursor solutions of ceria, which have been used to impregnate the mesopores of titania films through an identical protocol. Fig.4.52 and Fig.4.53 show the XRD patterns of the mesoporous films whose pores have been impregnated by a precursor solution containing cerium nitrate and,

respectively, Pluronic F127 and CTAB. After impregnation, similarly to the urea−ceria samples, the films have been exposed to increasing doses of hard X-rays.

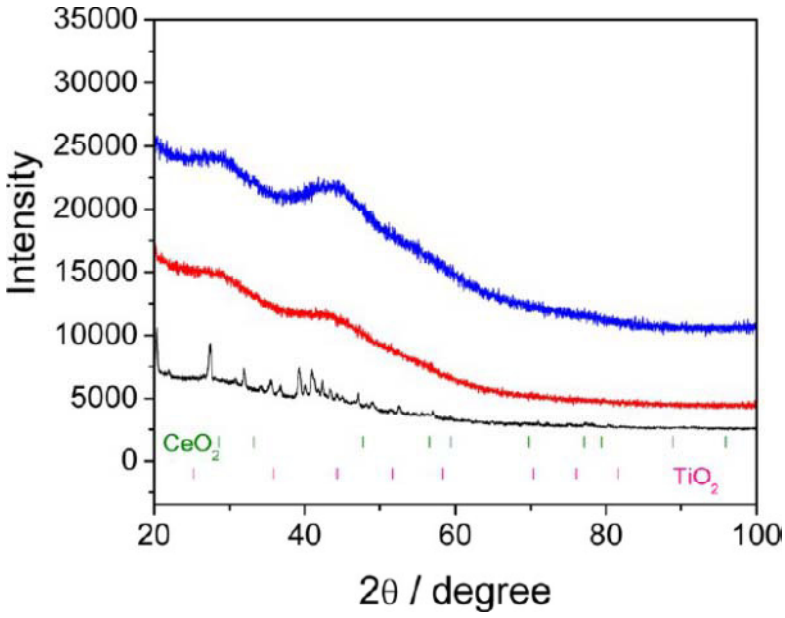

Fig.4.52 XRD patterns of titania mesoporous films whose pores have been filled by using a cerium nitrate and Pluronic F127 solution after exposure to a dose of 163 J cm^{-2} (black line), 326 J cm^{-2} (red line), and 653 J cm^{-2} (blue line).

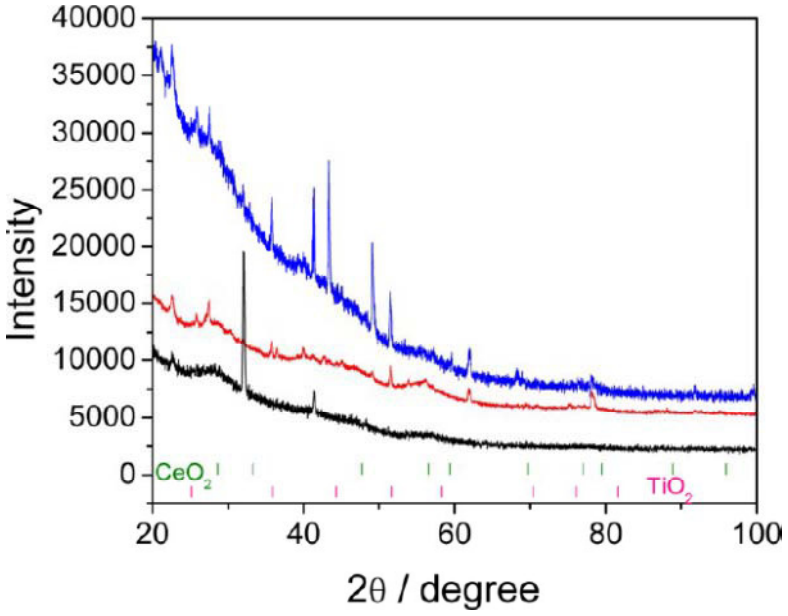

Fig.4.53 XRD patterns of titania mesoporous films whose pores have been filled by using a cerium nitrate and CTAB solution after exposure to a dose of 163 J cm^{-2} (black line), 326 J cm^{-2} (red line), and 653 J cm^{-2} (blue line).

The comparison among the different preparation methods shows that the results are considerably different and the type of surfactant appears therefore to play a fundamental role in the formation of ceria nanoparticles upon exposure to hard X-rays. In the case of Pluronic-F127 samples (Fig.4.52), nanoceria is formed, but the XRD peaks attributed to cerium oxide are less intense and wider, indicating the formation of nanoparticles with smaller dimension. In the case of sample prepared with CTAB as surfactant, only a very weak and wide signal assigned to ceria could be observed (Fig.4.53), indicating that CTAB does not allow an efficient formation of CeO_2-NPs. The sharp peaks are assigned to fragmentation of precipitates from the precursor sol produced by the X-ray exposure. A comparison of the different results obtained employing a block copolymer (Pluronic F127), an ionic surfactant (CTAB), and a coordinating agent (urea) gives some indications about the formation of the ceria nanoparticles by DXRL. We have seen that the dose plays an important role; only when some threshold value is reached, the ceria nanoparticles form. The first effect is

the fragmentation of the compounds that crystallize after solvent evaporation of the precursor solution inside the mesoporous films. The second one is the production of free radicals $OH^{\bullet}$ that induce the oxidation of Ce^{3+} to Ce^{4+}. The overall effect, however, depends on the dispersing/ coordinating agent that has been used in the solution of ceria precursors to impregnate the films; in fact the formation of nanoceria is effective with urea and, to some extent, with Pluronic but does not work with CTAB. The amines in urea play, most likely, a primary role by favoring the nucleation process of ceria nanocrystals via coordination of Ce^{4+} ions,[148] and a similar mechanism should be activated in the presence of triblock copolymers. On the other hand the CTAB, characterized by a cationic moiety, is not able to coordinate the Ce^{4+} because of the charge repulsion that disfavors the nucleation process. Nanoceria is of paramount importance because of its catalytic and radical scavenging properties, and the controlled formation into a porous matrix should enable the fabrication of antioxidant substrates for cell cultures. We have performed a simple test to verify the antioxidant effect by measuring the photodegradation of a dye, Rh6G, when deposited on a silica slide, bare mesoporous titania films, or mesoporous titania films loaded with ceria nanoparticles. The three samples have been then exposed to UV light at 365 nm monitoring the photodegradation of Rh6G as a function of time by UV−visible spectroscopy (Fig.4.54a, b, and c respectively).

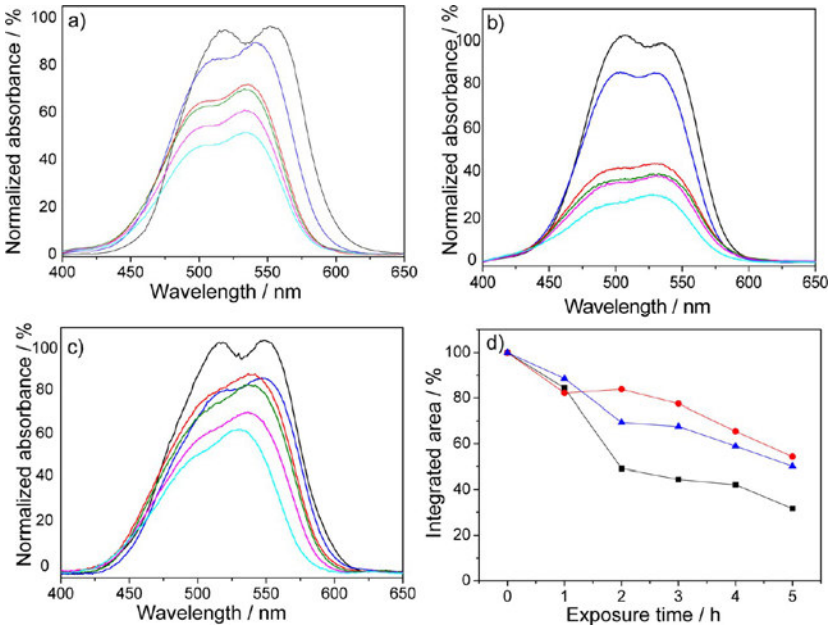

Fig.4.54 UV−vis absorption spectra in the 400−650 nm range of Rh6G on silica (a), Rh6G on bare mesoporous titania films (b), and nanoceria-loaded mesoporous titania films (c) exposed to UV light for increasing times: 0 (black line), 1 h (blue line), 2 h (red line), 3 h (green line), 4 h (pink line), and 5 h (light blue line). (d) Photodegradation of Rh6G, percentage decrease of the integrated band in the 400−650 nm range as a function of the UV exposure time: the blue triangles are referred to Rh6G on silica, the black squares to Rh6G on bare film, and the red spots to Rh6G on nanoceria-loaded film. The solid lines are guides for the eyes.

Before exposure, the absorption spectrum of the films in the 400−600 nm range is mainly due to the typical absorption bands of Rh6G in the form of monomers and dimers. Rh6G dimers, in fact, have two distinct absorption maxima, at higher (J-type dimers) and lower (H-type dimers) wavelengths with respect to the absorption peak of the monomer band (≈530 nm).[149] After 1 h of exposure, the decrease of absorbance percentage, in the films without nanoceria, is higher compared to pure Rh6G on silica, indicating a weak photocatalytic effect of the porous matrix. On the contrary, the absorbance of the nanoceria-loaded film shows a slower and less sharp decrease if compared to the photodegradation of the pure dye on silica. Fig.4.54d shows the value of the integrated absorbance in the range between 400 and 600 nm as a function of the UV exposure time. The bleaching effect due to Rh6G photodegradation is clearly visible both in the dye on silica and in the film without CeO_2-NPs, where the

absorbance decreases roughly 70% after 5 h of exposure. The degradation of the dye not deposited on mesoporous films may be considered somehow surprising since it should not absorb the UV light in the 365 nm range.[150] However, this effect is easily explained if we consider that the UV lamp is not completely monochromatic and the photodegradation can be triggered by the formation of radical species from the residual solvent among the dye molecules or by the environmental moisture (water) which can be absorbed during the exposure. The dye degradation upon UV exposure is sensitively reduced in the films loaded with nanoceria, despite the weak photocatalytic effect of the substrate; after 5 h the absorbance decreases less than 50%. This effect is due to the free radical scavenging of ceria nanoparticles, which protects the organic molecules from the degradation induced by the radicals produced by UV light. According to previous results, in fact, the size of the ceria nanocrystals, grown within the porous matrix, has been tuned to maximize the radical scavenging properties of the oxide and limit its photocatalytic activity that becomes dominant for particles of larger dimensions.[151] The antioxidant property shown by the material is of extreme interest for all those applications where it is necessary to avoid or delay the degradation of organic molecules directly induced by free radicals or indirectly caused by exposure to sources that give rise to the formation of free radicals. The XRD and Raman data show that the exposure to high energy photons induces the formation of ceria nanoparticles; this process has the advantage to be used for patterning the mesoporous films. DXRL, in fact, allows the controlled formation of the particles only in selected areas of the films by using proper masks; the nanoceria is formed in the pars of the film which are directly exposed to the flux of photons, while in the masked side, no particles are able to grow up. Fig.4.55 shows the optical image of a mesoporous titania film impregnated with a urea−ceria precursor solution which has been patterned by DXRL using a dose of 653 J cm^{-2}.

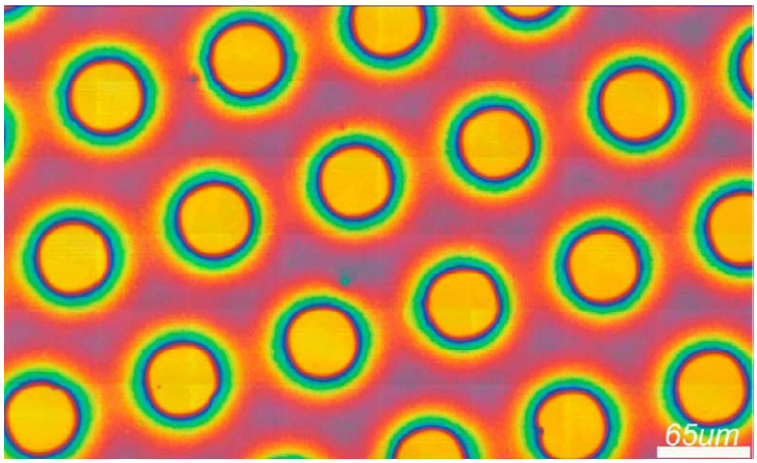

Fig.4.55 Optical microscope image of patterned titania mesoporous film with ceria nanoparticles. The exposure dose is 653 J cm^{-2}.

The areas which appear yellow have not been irradiated, while the exposed region has a dark red color. The Raman image taken on a circular spot, which represents the unexposed part where the nanooceria should not be present, is shown in Fig.4.56; the image is obtained by integrating the band of the Raman active mode of cerium oxide (see Fig.4.49), and the intensity is reported in false color scale. The area of the circular spot appears in blue, which indicates, following the intensity scale, that ceria is not present in the unexposed region.

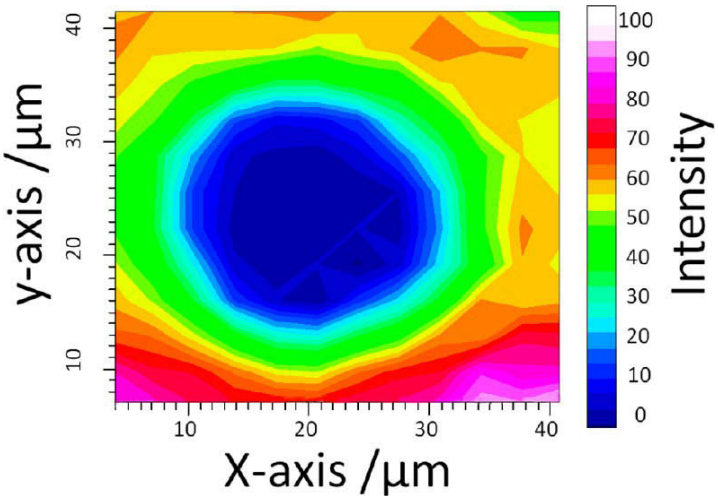

Fig.4.56 Raman image obtained by integrating the band of the Raman active mode of cerium oxide; the intensity is reported in false color scale. The sample has been obtained by X-ray exposure with a 653 J cm^{-2} exposure dose.

The X-ray fluorescence mapping performed on a sample, obtained by DXRL using 653 J cm^{-2} exposure dose and an urea−ceria precursor sol, gives also some interesting information as shown in Fig.4.57. Three different elemental maps are shown in the figure: Si (red) left side, Ti (violet) center, and Ce (yellow) right side. The Ce map well reproduces the pattern of the mask, and cerium appears to be present only in the exposed areas (the circular regions in dark correspond to the unexposed areas). Cerium partially absorbs the fluorescence from the Silicon substrate, and this explains the darker color of the patterns of the Silicon areas.[152] The signal of Titanium is instead well homogeneously distributed, indicating the homogeneity of the sample.

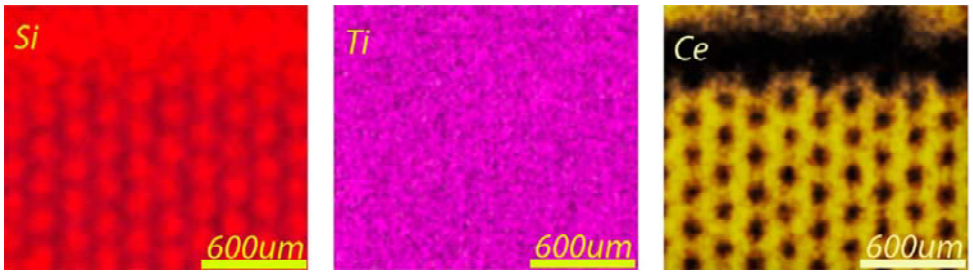

Fig.4.57 X-ray fluorescence map of patterned titania mesoporous film with ceria nanoparticles. Three different images are shown obtained by Si (red) left side; Ti (purple) center; and Ce (yellow) right side. The sample has been obtained by X-ray exposure with a 653 J cm^{-2} exposure dose.

- Evaluation of ceria-nanocomposite toxicity in cell culture

In the previous paragraph we have shown that the use of urea as a coordinating agent is highly effective for the production for nanoceria-titania nanocomposites. The same method has been adopted to design other nanocomposites with different matrix based on hafnium and silicon oxides. It has been already proved that titania, silica and hafnia are biocompatible,[153,154] however they show different physicochemical properties such as hydrolytic stability, reflective index and photocatalytic activity. Titania is hydrolytically stable, it has a high refractive index and it have a photocatalytic activity specially when it is crystalline, hafnia has the same properties of titania, but it is not photocatalytic and the silica is not hydrolytically stable, it has a low refractive index and it does not have photocatalytic activity. These properties play an important role for the material design selection. The refractive index of the supported materials affects the phase contrast in microscopy characterization for *in vivo* cells observation.[155] The hydrolysis of the matrix affects the potential release of nanoceria in cell cultures and therefore is a potential cause of toxicity. The presence of photocatalytic activity of the substrate is related to the radicals production, which can influence antioxidant properties of nanoceria embedded in the porous matrix. Besides the physicochemical properties, the possibility to transfer the nanocomposite films on plastic Petri dishes

with a perspective of improving the cell culture environment has been also taken into account.

The synthesis of hafnia and silica mesoporous ordered films is based on self-assembly of a pore templating agent, Pluronic F127, triggered by solvent evaporation as it has been reported for titania in the section 4.2.3. The Fig.4.58a shows the typical GISAXS pattern of hafnia mesoporous film; the pattern is characteristic of an Fm3m in the space group contracted along the [111] direction. The Fig.458b shows silica mesoporous pattern which can be indexed as 2d-hexagonal p6mm.

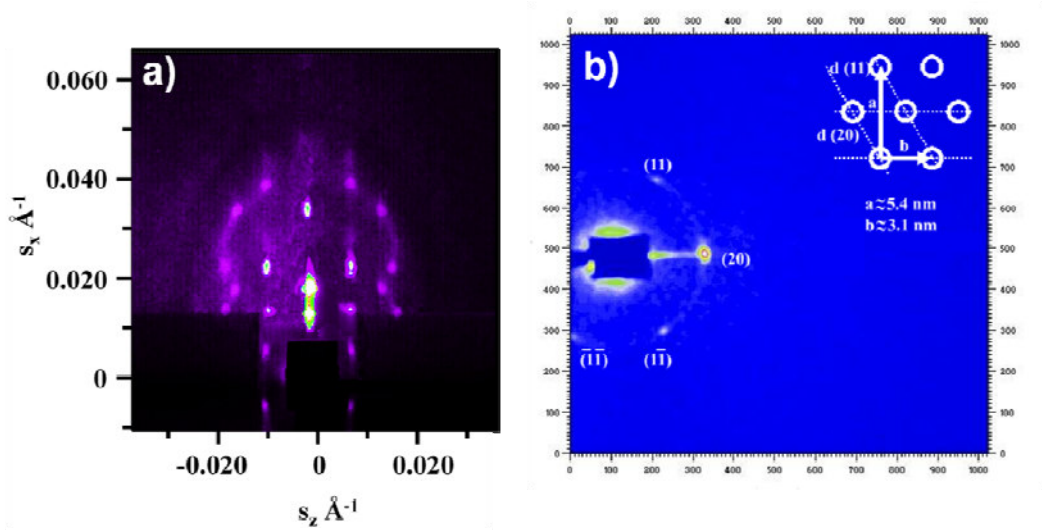

Fig.4.58 GISAXS pattern of a) hafnia and b) silica mesoporous film after thermal treatment; the pattern of hafnia mesoporous film is characteristic of an Fm3m in the space group mesostructure contracted along the [111] direction. The silica mesoporous film pattern can be indexed as 2d-hexagonal p6mm.

The hafnia and silica mesoporous films already prepared have been impregnated with the ceria precursor solution following the procedure used for titania matrix. Then samples have been exposed to hard X-rays, generated by a synchrotron source, to induce the formation of ceria nanoparticles within the pores. As it has been obtained

for the titania, the exposure to hard X-rays induces a spatially-controlled formation of nanoceria within the mesopores.

Fig.4.59 α and β show the XRD patterns in the 2θ angular range of calcined hafnia and silica mesoporous film whose pores have been filled with the urea−Ce solution and exposed at increasing X-ray doses. After exposure to the lowest dose, the detection of a pattern with different sharp diffraction peaks indicates very likely the fragmentation of the cerium nitrate induced by radiations, in agreement to the previous experiments on the titania films impregnated with nanoceria precursor sol.

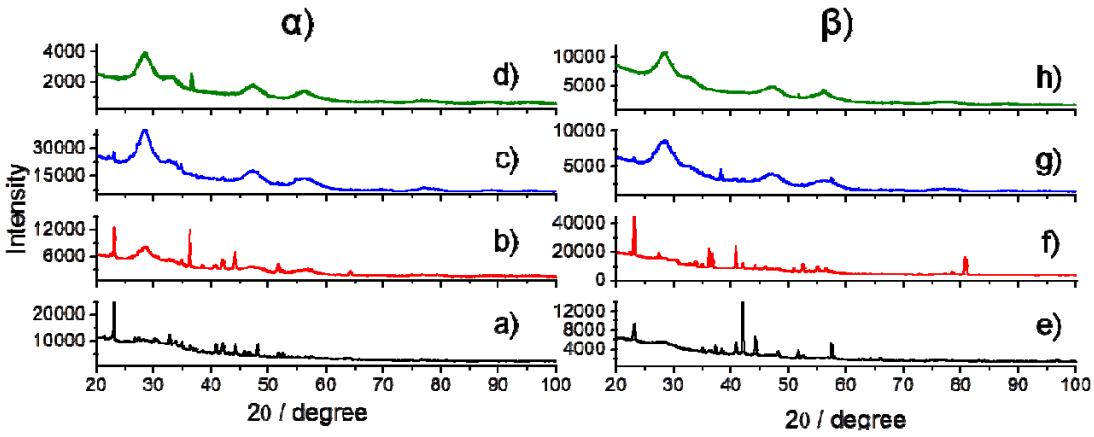

Fig.4.59 XRD patterns of α)hafnia and β)silica mesoporous films at different processing steps: (a) as-prepared mesoporous film after filling the pores with urea−ceria solution (black line); (b) after exposure to a dose of 163 J cm^{-2} (red line); (c) after exposure to a dose of 326 J cm^{-2} (blue line), and (d) after exposure to a dose of 653 J cm^{-2} (green line).

These peaks decrease in intensity and partially disappear after exposure to a higher dose, 326 J cm^{-2}, and are not detected any longer in the samples exposed to the highest radiation dose, 653 J cm^{-2}. On the other hand, with the increase of the dose, the peaks related to crystalline cerium oxide become more intense. These diffraction peaks correspond to the cubic fluorite structure of CeO_2 cerianite.

We have then characterized the nanoceria, obtained at the highest exposure dose, by XRD using the Rietveld method for both hafnia and silica films. These results have

compared with those of titania film. The fit obtained by the Rietveld method (Fig.4.60a, b and c) allow estimating a nanocrystalline size of 3.3, 3.8 and 4 nm for silica, titania and hafnia matrix. The pores sizes of the three matrices have been measured by TEM and analysed using an Image J program (Figure 4.61a, b and c). The nanoceria size nucleated by lithography are compatible with the pores dimensions of the tree systems, that are 4.5, 5.5 and 7.2 nm for mesoporous silica, titania and hafnia, respectively. This results and TEM characterization indicate that the nanoparticles can really growth inside the pores.

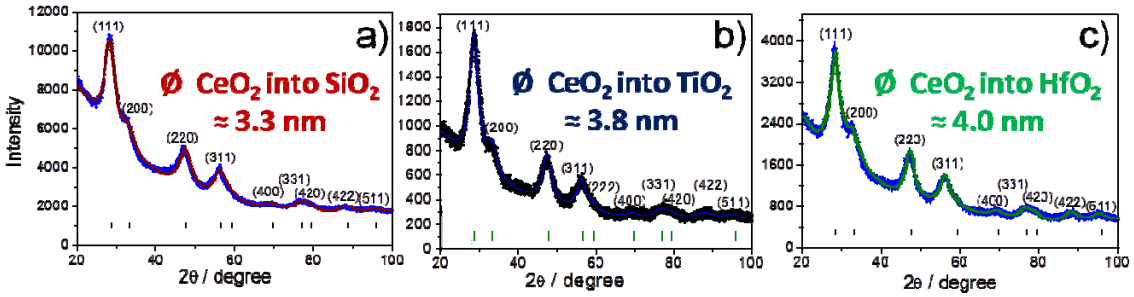

Fig.4.60 XRD pattern (dots) of ceria nanoparticles after hard X-ray exposure (653 J cm^{-2}). The Rietveld fit is reported as a continuous a)red, b)blue and c)green line for nanoceria embedded in silica, titania and hafnia mesoporous films.

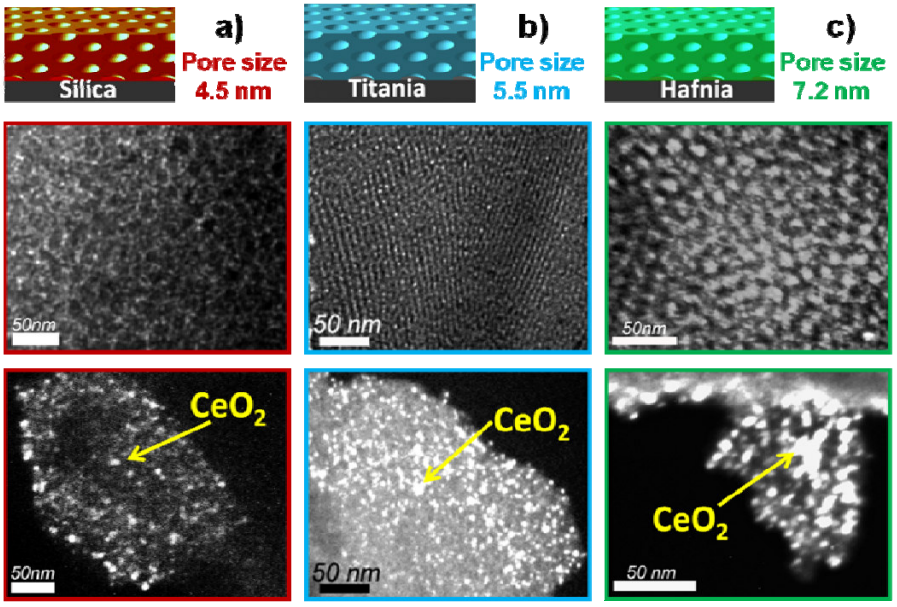

Fig.4.61 TEM images of (a) silica, (b) titania and (c) hafnia mesoporous film with ceria nanoparticles after X-ray exposure at the highest dose (653 J cm^{-2}).

To assess the toxicity of the matrix and the ceria-based nanocomposites, the materials have been placed in close contact with a PBMC cells culture for 24h. After this period, the apoptotic cells have been measured by flow cytometry. Fig.4.62 shows the percentage of total apoptotic cells for the bare mesoporous matrix (group a "CeO_2 not treated"), the nanocomposite systems (group b "CeO_2 treated") and the control (red bar). Among the three matrices, titania and hafnia are detrimental for the cell culture causing and increase in the cell death of respect to the control, which has a value ≈ 15%. On the other hand, silica matrix (yellow bar) is positively affecting the PBC cells since it is slightly capable to reduce the cells death compared to the control.

When PBMC cells are incubated with the nanoceria-composites the results are completely different from those obtained with the bare matrices. In fact, the cells death is reduced for the nanoceria-loaded nanocomposites made by titania. Moreover, positive effects can also be observed in hafnia-ceria nanocomposite, if compared with the results obatined from bare hafnia matrix. On the contrary, the nanocomposites

based on silica-nanoceria show increase the cell death with respect to the silica matrix. This is probably due to the hydrolytic instability of silica matrix that causes the release of nanoceria and therefore an increase of nanoceria in the cellular environment.

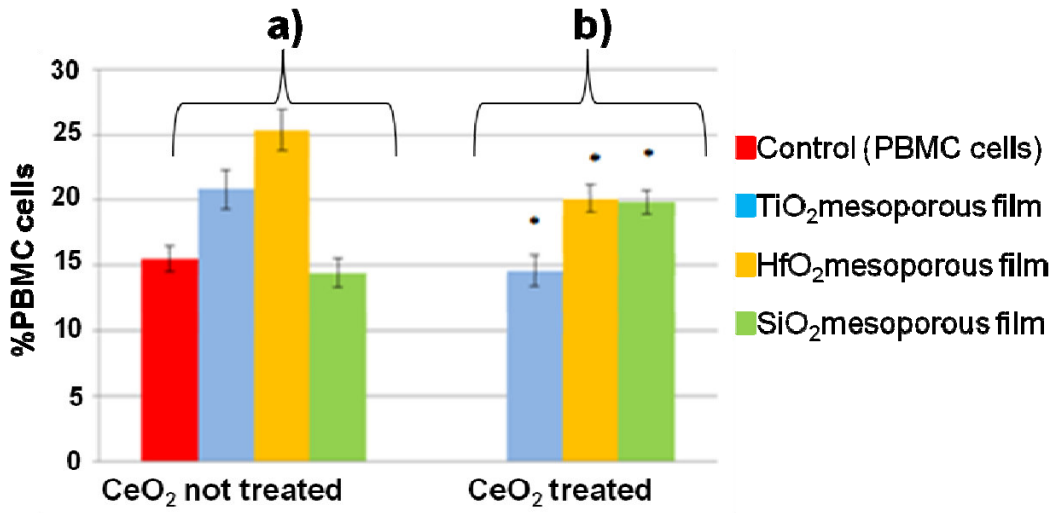

Fig.4.62 Average results from flow cytometry profile PI/annexinV of apoptotic PBMC cells treated with bare mesoporous films (a) or nanoceria-loaded nanocomposites (b). Asterisks indicate statistically significant differences between mesoporous film-treated PBC cells vs. nanocomposite-treated PBC cells ($p < 0.008$ Titania< Titania-Ceria, $p<0.007$ Hafnia<Hafnia-Ceria and $p<0.004$ Silica<Silica-Ceria).

4.3. References

[1] Reddy B.M., Khan A. Catal. Surv. Asia. **(2005)**, 9, 155–171.

[2] Esch F., Fabris S., Zhou L., Montini T., Africh C., Fornasiero P., Comelli G., Rosei R. Science. **(2005)**, 309, 752–755.

[3] Stevanovìc M., Savìc J., Jordovìc Br., Uskokovìc D. Colloids Surf. B. **(2007)**, 59, 215–223.

[4]Yang L., Sundaresan G., Sun M., Jose P., Hoffman D., McDonagh P.R., Lamichhane N., Cutler C.S., Perezc J.M., Zweit J. J. Mater. Chem. B. **(2013)**, 1, 1421–1431.

[5] Dowding J.M., Dosani T., Kumar A., Seal S., Self W.T. Chem. Commun. **(2012)**, 48, 4896–4898.

[6] Das S., Dowding J.M., Klump K.E., McGinnis J.F., Self W., Seal S. Nanomedicine. **(2013)**, 8, 1483–1508.

[7] Samiee S., Goharshadi E.K. Mater. Res. Bull. **(2012)**, 47, 1089–1095.

[8]Lord M.S., Jung M.S., Teoh W.Y., Gunawan C., Vassie J.A., Amal R., Whitelock J.M. Biomaterials. **(2012)**, 33, 7915– 7924.

[9] Zaki M.I., Hussein G.A.M., Mansour S.A.A., El- Ammawy H.A. J. Mol. Catal. **(1989)**, 51, 209–220.

[10] Zhang Z., Yu L., Liu W., Song Z. Appl. Surf. Sci. **(2010)**, 256, 3856–3861.

[11] Antony P.M.A., Diederich N.J., Kruger R., Balling R. FEBS J. **(2013)**, 280, 5981–5993.

[12]Willis A.W., Evanoff B.A., Lian M., Galarza A., Wegrzyn A., Schootman M., Racette B.A. Am. J. Epidemiol. **(2010)**, 172, 1357–1363.

[13] Migheli R., Godani C., Sciola L., Delogu M.R., Serra P.A., Zangani D., De Natale G., Miele E.M., Desole S. J. Neurochem. **(1999)**, 73, 1155–1163.

[14] Aschner M., Erikson K.M., Herrero Hernàndez E., Tjalkens R. Neuro Mol. Med. **(2009)**, 11, 252–266.

[15] Lee J.J., Kim Y.M., Yin S.Y., Park H.D., Kang M.H., Hong J.T., Lee M.K. Biochem. Pharmacol. **(2003)**, 66, 1787–1795.

[16] Basma A.N., Morris E.J., Nicklas W.J., Geller H.M. J. Neurochem. **(1995)**, 64, 825–832.

[17] Lee M.Y., Choi E. J., Lee M.K., Lee J. J. Nutr. Res. Pract. **(2013)**, 7, 249–255.

[18] Chen S., Hou Y., Cheng G., Zhang C., Wang S., Zhang J. Biol. Trace Elem. Res. **(2013)**, 154, 156–166.

[19] Wang G., Mu Q., Chen T., Wang Y.J. J. Alloys Compd. **(2010)**, 493, 202–207.

[20]Singh N., Cohen C.A., Rzigalinski B.A. Ann. N. Y. Acad. Sci. **(2007)**, 1122, 219–230.

[21] Serra P.A., Esposito G., Enrico P., Mura M. A., Migheli R., Delogu M. R., Miele M., Desole M. S., Grella G., Miele E. Br. J. Pharmacol. **(2000)**, 130, 937–945.

[22] Guerin P. El Mouatassim S. Menezo Y. Hum. Reprod. update. **(2001)**, 7, 175-189.

[23] Cetica P.D., Pintos L.N., Dalvit G.C., Beconi M.T. IUBMB Life. **(2001)**, 51, 57–64.

[24] Taylor U., Barchanski A., Kues W., Barcikowski S., Rath D. Reprod. Dom. Anim. **(2012),** 47, 359–368.

[25] Baki M.E., Miresmaili S.M., Pourentezari M., Amraii E., Yousefi V., Spenani H.R., Talebi A.R., Anvari M., Fazilati M., Fallah A.A., Mangoli E. *Iran J. Reprod. Med*. **(2014)**, 12, 139- 44.

[26] Courbiere B., Auffan M., Rollais R., Tassistro V., Bonnefoy A., Botta A., Rose J., Orsiere T., Perrin J. Int. J. Mol. Sci. **(2013)**, 14, 21613-21628.

[27] Spivak N.Y., Shepel E.A., Zholobak N.M., Shcherbakov A.B., Antonovitch G.V., Yanchiy R.I., Ivanov V.K., Tretyakov Y.D. Nano. Biomed. Eng. **(2012)**, 4, 188-194.

[28] Chaudhury K., Babu N.K., Singh A.K., Das S., Kumar A., Seal S. Nanomed. Nanotechnol. **(2013)**, 9, 439-48.

[29] Lacham-Kaplan O., Trounson A. Reprod. Biol. Endocrinology. **(2008)**, 6, 58.

[30] Li R., Albertini D.F. Nat. Rev. Mol. Cell. Biol. **(2013)**, 14, 141-152.

[31] Eppig J.J. Biol. Reprod. **(1980)**, 23, 545-552.

[32] Ould-Moussa N., Safi M., Guedeau-Boudeville M.A., Montero D., Conjeaud H., Berret J.F. Nanotoxicology. **(2014)**, 8, 799-811.

[33] Kim I.S., Baek M., Choi S.J. J. Nanosci. Nanotechnol. **(2010)**, 10, 3453-3458.

[34] Safi M., Sarrouj H., Sandre O., Mignet N., Berret,J.F. Nanotechnology. **(2010)**, 21,145103.

[35] Asati A., Santra S., Kaittanis C., Perez J.M. ACS Nano. **(2010)**, 4, 5321-31.

[36] Tiedemann D., Taylor U., Rehbock C., Jakobi J., Klein S., Kues W.A., Barcikowski S., Rath D. Analyst. **(2014)**, 139, 931–942.

[37] Jiao G.Z., Cao X.Y., Cui W., Lian H.Y., Mao Y.L., Wu X.F., Ying D.H., Tan J.H. PLoS ONE. **(2013)**, 8, 58018.

[38] Leoni G.G., Bebbere D., Succu S., Berlinguer F., Mossa F., Galioto M., Bogliolo L., Ledda S., Naitana S. Mol. Reprod. Dev. **(2007)**, 74, 249-57.

[39] Ledda S., Bogliolo L., Leoni G., Naitana. S. Biol. Reprod. **(2001)**, 65, 247-52.

[40] Ptak G., Matsukawa K., Palmieri C., Della Salda L., Scapolo P.A., Loi P. Hum. Reprod. **(2006)**, 21, 2228-2237.

[41] Cobelles C. BioMed. Online. **(2009)**, 18, 864-880.

[42] Luciano A.M., Goudet G., Perazzoli F., Lahuec C., Gerard N. Mol. Repro. Dev. **(2006)**, 73, 658–666.

[43] Maedomari N., Kikuchi K., Ozawa M., Noguchi J., Kaneko H., Ohnuma K., Nakai M., Shino M., Nagai T., Kashiwazaki N. Theriogenology. **(2007)**, 67, 983–993.

[44] Abazari-Kia A.H., Mohammadi-Sangcheshmeh A., Dehghani-Mohammadabadi M., Adegani F., Veshkini A., Zhandi M., Cinar M.U., Salehi M. J. Assist. Reprod. Genet. **(2014)**, 31, 313-21.

[45] Tarín J.J. Mol. Hum. Reprod. **(1996)**, 2, 717-724.

[46] Saito H., Seino T., Kaneko T., Nakahara K., Toya M., Kurachi H. Gynecol. Obstet. Invest. **(2002)**, 53, 46-51.

[47] De Jong W.H., Hagens W.I., Krystek P., Burger M.C., Sips A.J., Geertsma R.E. Biomaterials. **(2008)**, 29, 1912-9.

[48] Lan Z., Yang W.X. Nanomedicine. **(2012)**, 7, 579-96.

[49] Tiedemann D., Taylor U., Rehbock C., Jakobi J., Klein S., Kues W.A., Barcikowski S., Rath D. Analyst. (2014), 139, 931-42.

[50] Moretti E., Terzuoli G., Renieri T., Iacoponi F., Castellini C., Giordano C., Collodel G. Andrologia. **(2013)**, 45, 392-6.

[51] Zakhidov S.T., Pavlyuchenkova S.M., Samoylov A.V., Mudzhiri N.M., Marshak T.L., RudoyV.M., Dement'eva O.V., Zelenina I.A., Skuridin S.G., Yevdokimov Yu. M. Biology Bulletin. **(2013),** 40, 493-9.

[52] Asare N., Instanes C., Sandberg W.J., Refsnes M., Schwarze P., Kruszewski M., Brunborg G. Toxicology. **(2012)**, 291, 65-72.

[53] Geraets L., Oomen A.G., Krystek P., Jacobsen N.R., Wallin H., Laurentie M., Verharen H.W., Brandon E.F., de Jong W.H. Part Fibre Toxicol. **(2014)**, 11, 30.

[54] Kobyliak N.M., Falalyeyeva T.M., Kuryk O.G., Beregova T.V., Bodnar P.M., Zholobak N.M., Shcherbakov O.B., Bubnov R.V., Spivak M.Y. EPMA J. **(2015)**, 6, 12.

[55] Muiño-Blanco T., Pérez-Pé R., Cebrián-Pérez J.A. Reprod. Domest. Anim. **(2008)**, 43, 18-31.

[56] Bansal A.K., Bilaspuri G.S. Vet. Med. Int. **(2010)**, 686137, 1-7.

[57] Kumar A., Das S., Munusamy P., Self W., Baer D.R., Saylee D.C., Seal S. Environ. Sci. Nano. **(2014)**, 1, 516.

[58] Das M., Patil S., Bhargava N., Kang J.F., Riedel L.M., Seal S., Hickman J.J. Biomaterials. **(2007)**, 28, 1918-25.

[59] Chigurupati S., Mughal M.R., Okun E., Das S., Kumar A., McCaffery M., Seal S., Mattson M.P. Biomaterials. **(2013)**, 34, 2194-201.

[60] Kumari M., Singh S.P., Chinde S., Rahman M.F., Mahboob M., Grover P. Int. J. Toxicol. **(2014)**, 33, 86-97.

[61] Zhou X., Wang B., Chen Y., Mao Z., Gao C. J. Nanosci. Nanotechnol. **(2013)**, 13, 204-15.

[62] O'Brien N., Cummins E. J. Environ. Sci. Health A Tox Hazard Subst Environ Eng. **(2010)**, 45, 992-1007.

[63] Park B., Donaldson K., Duffin R., Tran L., Kelly F., Mudway I., Morin J.P., Guest R., Jenkinson P., Samaras Z., Giannouli M., Kouridis H., Martin P. Inhal. Toxicol. **(2008)**, 20, 547-66.

[64] Campos V.F., Komninou E.R., Urtiaga G., de Leon P.M., Seixas F.K., Dellagostin O.A., Deschamps J.C., Collares T. Theriogenology. **(2011)**, 75, 1476-81.

[65] Kim T.S., Lee S.H., Gang G.T., Lee Y.S., Kim S.U., Koo D.B., Shin M.Y., Park C.K., Lee D.S. Reprod. Domest. Anim. **(2010),** 45, e201-6.

[66] Makhluf S.B.D., Abu-Mukh R., Rubinstein S., Breitbart H., Gedanken A. Small. **(2008)**, 4, 1453-8.

[67] Wiwanitkit V., Sereemaspun A., Rojanathanes R. Fertil Steril. **(2009)**, 91, e7-8.

[68]Taylor U., Barchanski A., Petersen S., Kues W.A., Baulain U., Gamrad L., Sajti L., Barcikowski S., Rath D. Nanotoxicology. **(2014)**, 8, 118-27.

[69] Makhluf S.B.D., Arnon R., Patra C.R., Mukhopadhyay D., Gedanken A., Mukherjee P., Gedanken A., Mukherjee P., Breitbart H. J. Phys. Chem. C. **(2008)**, 112, 12801-7.

[70] Feugang J.M., Youngblood R.C., Greene J.M., Fahad A.S., Monroe W.A., Willard S.T., Peter L.R. J. Nanobiotechnology. **(2012)**, 10, 45.

[71] Taylor U., Tiedemann D., Rehbock C., Kues W.A., Barcikowski S., Rath D. Beilstein J. Nanotechnol. **(2015)**, 6, 651-64.

[72] Robayo I., Montenegro V., Valdés C., Cox J.F. Reprod. Domest. Anim. **(2008)**, 43:393-9.

[73] Kathiravan P., Kalatharan J., Edwin M.J., Veerapandian C. Anim. Reprod. Sci. **(2008)**, 104, 9-17.

[74] Barkalina N., Charalambous C., Jones C., Coward K. Nanomedicine. **(2014)**,10, 921-38.

[75] Taylor U., Barchanski A., Garrels W., Klein S., Kues W., Barcikowski S., et al. In: Zahavy E., Ordentlich A., Yitzhaki S., Shafferman A., editors. Nano-Biotechnology for Biomedical and Diagnostic Research: Springer Netherlands. **(2012)**, 125-33.

[76] Terzuoli G., Iacoponi F., Moretti E., Renieri T., Baldi G., Collodel G. I. J. Siena Acad. Sciences. **(2012)**, 3, 1.

[77] Makhluf S.B.D., Qasem R., Rubinstein S., Gedanken A., Breitbart H. Langmuir. **(2006)**, 22, 9480-2.

[78] Zakhidov S.T., Marshak T.L., Malolina E.A., Kulibin A.Y., Zelenina I.A., Pavluchenkova S.M., Rudoi V.M., Dement'eva O.V., Skuridin S.G.,. Yu M.E. Biochemistry (Moscow) Supplement Series A: Membrane and Cell Biology. **(2010)**, 4, 293-6.

[79] Gopalan R.C., Osman I.F., Amani A., De Matas M., Anderson D. Nanotoxicology. **(2009)**, 3, 33-9.

[80] Kasimanickam R., Pelzer K.D., Kasimanickam V., Swecker W.S., Thatcher C.D. Theriogenology. **(2006)**, 65, 1407-21.

[81] Martinez-Pastor F., Johannisson A., Gil J., Kaabi M., Anel L., Paz P., Rodriguez-Martinez H. Anim Reprod Sci. **(2004)**, 84, 121-33.

[82] Preaubert L., Courbiere B., Achard V., Tassistro V., Greco F., Orsiere T., OrsiereT., Botter J.Y., Rose J., Auffan M., Perrin J, Nanotoxicology. **(2015)**, 1-7.

[83] Tran N., Mir A., Mallik D., Sinha A., Nayar S., Webster T. In. J. Nanomed. **(2010)**, 5, 277–283.

[84] Tartaj P., del Puerto M.M., Veintemillas-Verdaguer S., Gonzàlez- Carrenõ T., Serna C.J. J Phys D**(2003)** , 36, R182–R197.

[85] Ahliah I.W., Zainal A.A., Puteh R. J. Nano. Mater. **(2013)**, 2013, 1–6.

[86]Xu Q.F., Wang J.N. Front. Mater. Sci. China. **(2010)**, 4, 180–188.

[87] Aboulaich A., Boury B., Mutin P.H. Chem. Mater. **(2010)**, 22, 4519–4521.

[88] Aboulaich A., Lorret O., Boury B., Mutin P.H. Chem. Mater. **(2009),** 21, 2577–2579.

[89] Pichon B.P., Buchwalter P., Carcel C., Cattoën X., Wong Chi Man M., Begin-Colin S. Open Surf. Sci. J. **(2012)**, 4, 35–41.

[90] Takahashi M., Figus C., Kidchob T., Enzo S., Casula M., Valentini M., Innocenzi P. Adv. Mater. **(2009)**, 21, 9146–9152.

[91] Carboni D., Pinna A., Malfatti L., Innocenzi P. New. J. Chem. **(2014)**, 38, 1635–1640.

[92] Innocenzi P., Martucci A., Guglielmi M., Armelao L., Battaglin G., Pelli, S., Righini G. C. J. Non-Cryst. Solids. **(1999)**, 259, 182−90.

[93] Innocenzi P., Brusatin G., Guglielmi M., Signorini R., Meneghetti M., Bozio R., Maggini M., Scorrano G., Prato, M. J. Sol-Gel Sci. Technol. **(2000)**, 19, 263−66.

[94] Innocenzi P., Miorin E., Brusatin G., Abbotto A., Beverina L., Pagani G.A., Casalboni M., Sarcinelli F., Pizzoferrato M. Chem. Mater. **(2002)**, 14, 3758−66.

[95] Brusatin G., Abbotto A., Beverina L., Pagani G.A., Casalboni M., Sarcinelli F., Innocenzi P. Adv. Funct. Mater. **(2004)**, 14, 1160−66.

[96] Brusatin G., Innocenzi P., Beverina L., Pagani G.A., Abbotto A., Sarcinelli F., Casalboni M.J. Non-Cryst. Solids. **(2004)**, 345, 575−79.

[97] Philipp G., Schmidt H. J. Non-Cryst. Solids. **(1984)**, 63, 283−92.

[98] Kasemann R., Schmidt H., Wintrich E. Mater. Res. Soc. Symp. Proc. **(1994)**, 346, 915−21.

[99] Sanchez C., Belleville P., Popall M., Nicole L. Chem. Soc. Rev. **(2011)**, 40, 696−53.

[100] Nagarsenker M.S., Londhe V.Y., Nadkarni G. D. Int. J. Pharm. **(1990)**, 190, 63−71.

[101] Bourlais C.L., Acar L., Zia H., Sado P.A., Needham T., Leverge R. Prog. Retin. Eye Res. **(1998)**, 17, 33−58.

[102] Aronniemi M., Saino J., Lahtinen J. Thin Solid Films. **(2008)**, 516, 6110–6115.

[103] Guo L., Huang Q., Li X., Yang S. Phys. Chem. Chem. Phys. **(2001)**, 3, 1661–1665.

[104] Colombo M., Carregal-Romero S., Casula M.F., Gutierrez L., Morales M.P., Böhm I.B., Heverhagen J.T., Prosperi D., Parak W.J. Chem. Soc. Rev. **(2012)**, 41, 4306–4334.

[105] Kanga Y.S., Lee D.K., Stroeve P. Thin Solid Films. **(1998)**, 327–329, 541–544.

[106] Young R.A., Ed. The Rietveld Method, Oxford University Press: Oxford, U.K., **(1993)**.

[107] Lutterotti L., Gialanella S. Acta Mater. **(1998)**, 46, 101−10.

[108] Marabelli F., Wachter P., Phys. Rev. B. **(1987)**, 36, 1238−43.

[109] Patsalas P., Logothetidis S. Phys. Rev. B. **(2003)**, 68, 035104.

[110] Goharshadi E.K., Samiee S., Nancarrow P.J. Colloid. Interface. Sci. **(2011)**, 356, 473−80.

[111] Innocenzi P., Figus C., Kidchob T., Valentini M., Alonso B., Takahashi M. Dalton. Trans. **(2009)**, 42, 9146–9152.

[112] Alonso B., Massiot D., Valentini M., Kidchob T., Innocenzi P. J. Non-Cryst. Solids. **(2008)**, 354, 1615−26.

[113] Innocenzi P. J. Non-Cryst. Solids. **(2003)**, 316, 309−19.

[114] de Faria D.L.A., Venancio Silva S., de Oliveira M.T. J. Raman Spectrosc. **(1997)**, 28, 873–878.

[115] Shebanova O.N., Lazor P. J. Solid State Chem. **(2003)**, 174, 424–430.

[116] Jubb A.M., Allen H.C. ACS Appl. Mater. Interfaces. **(2010)**, 2, 2804–2812.

[117] Chernyshova I.V., Hochella M.F.Jr., Madden A.S. Phys. Chem. Chem. Phys. **(2007)**, 9, 1736–1750.

[118] Li Y.S., Church J.S., Woodhead A.L. J. Magn. Magn. Mater. **(2012)**, 324, 1543–1550.

[119] Shebanova O.N., Lazor P. J Solid State Chem. **(2003)**, 174, 424–430.

[120] McBride J.R., Hass K.C., Poindexter B.D., Weber W.H. J Appl Phys. **(1994)**. 76:2435–2441.

[121] Carboni D., Pinna A., Malfatti L., Innocenzi P. New. J. Chem. **(2014)**, 38, 1635–1640.

[122] Laurent S., Forge D., Port M., Roch A., Robic C., Vander Elst L., Muller R.N. Chem. Rev. **(2008)**, 108, 2064–2110.

[123] Noguera C.J., Goniakowski J.Chem. Rev. **(2013),** 113, 4073–4105.

[124] Xu Q.F., Wang J.N. Front. Mater. Sci. China. **(2010)**, 4, 180–188.

[125] Innocenzi P., Malfatti L., Falcaro P. Soft Matter. **(2012)**, 8, 3722−3729.

[126] Falcaro P., Malfatti L., Vaccari L., Amenitsch H., Marmiroli B., Grenci G., Innocenzi P. Adv. Mater. **(2009)**, 21, 4932−4936.

[127] Innocenzi P., Malfatti L., Kidchob T., Costacurta S., Falcaro P., Marmiroli B., Cacho-Nerin F., Amenitsch H. J. Synchrotron Radiat. **(2011)**, 18, 280−286.

[128] Falcaro P., Costacurta S., Malfatti L., Buso D., Patelli A., Schiavuta P., Piccinini M., Grenci G., Marmiroli B., Amenitsch H., Innocenzi P. ACS Appl. Mater. Interfaces **(2011)**, 3, 245−251.

[129] Falcaro P., Costacurta S., Malfatti L., Takahashi M., Kidchob T., Casula M.F., Piccinini M., Marcelli A., Marmiroli B., Amenitsch H., Schiavuta P., Innocenzi P. Adv. Mater. **(2008)**, 20, 1864−1869.

[130] Dimitrakakis C., Marmiroli B., Amenitsch H., Malfatti L., Innocenzi P., Grenci G., Vaccari L., Hill A.J., Ladewig B.P., Hill M.R., Falcaro P. Chem. Commun. **(2012)**, 48, 7483−7485.

[131] Innocenzi P., Kidchob T., Costacurta S., Falcaro P., Marmiroli B., Cacho-Nerin F., Amenitsch H. Soft Matter. **(2010)**, 6, 3172−3176.

[132] Malfatti L., Marongiu D., Costacurta S., Falcaro P., Amenitsch H., Marmiroli B., Grenci G., Casula M.F., Innocenzi P. Chem. Mater. **(2010)**, 22, 2132−2137.

[133] Malfatti L., Falcaro P., Marmiroli B., Amenitsch H., Piccinini M., Falqui A., Innocenzi P. Nanoscale. **(2011)**, 3, 3760−3766.

[134] Faustini M., Marmiroli B., Malfatti L., Benjamin L., Krins N., Falcaro P., Grenci G., Laberty-Robert C., Amenitsch H., Innocenzi P., Grosso D.J. Mater. Chem. **(2011)**, 21, 3597−3603.

[135] Rzigalinski B.A., Danelisen I., Strawn E.T., Cohen C.A., Liang C. Nanoparticles for Cell Engineering − A Radical Concept; Nanotechnologies for the Life Sciences; Wiley: New York, **(2007)**.

[136] Karakoti A.S., Monteiro Riviere N.A., Aggarwal R., Davis J.P., Narayan R.J., Self W.T., McGinnis J., Seal S. JOM. **(2008)**, 60, 33−37.

[137] Crepaldi E.L., Soler-Illia G.J.A.A., Grosso D., Cagnol F., Ribot F., Sanchez C.J. Am. Chem. Soc. **(2003)**, 125, 9770−9786.

[138] Malfatti L., Falcaro P., Amenitsch H., Caramori S., Argazzi R., Bignozzi C.A., Enzo S., Maggini M., Innocenzi P. Microporous Mesoporous Mater. **(2006)**, 88, 304−311.

[139] Innocenzi P., Malfatti L., Kidchob T., Enzo S., Della Ventura G., Schade U., Marcelli A. J. Phys. Chem. C. **(2010)**, 114, 22385−22391.

[140] Innocenzi P., Malfatti L., Kidchob T., Falcaro P., Costacurta S., Guglielmi M., Mattei G., Bello V., Amenitsch H. J. Synchrotron Radiat. **(2005)**, 12, 734−738.

[141] Takamura H., Takahashi N. Solid State Ionics. **(2010)**, 181, 100−103.

[142] Kamada K., Horiguchi K., Hyodo T., Shimizu Y. Cryst. Growth Des. **(2011)**, 11, 1202−1207.

[143] Munnik F., Benninger F., Mikhailov S., Bertsch A., Renaud P., Lorenz H., Gmür M. Microelectron. Eng. **(2003)**, 67−68, 96−103.

[144] Oveisi H., Rahighi S., Jiang X., Nemoto Y., Beitollahi A., Wakatsuki S., Yamauchi Y. Chem. Asian J. **(2010)**, 5, 1978−1983.

[145] Joint Committee on Powder Diffraction Standards (JCPDS) database: 34-0394.

[146] Bass J.D., Grosso D., Boissiere C., Belamie E., Coradin T., Sanchez C. Chem. Mater. **(2007)**, 19, 4349−4356.

[147] Bersani D., Antonioli G., Lottici P.P., Lopez T.J. Non-Cryst. Solid. **(1998)**, 232−234, 175−181.

[148] Zhang Q.C., Yu Z.H., Li G., Ye Q.M., Lin J.H. J. Alloys Compd. **(2009)**, 84, 477−481.

[149] Malfatti L., Kidchob T., Aiello D., Aiello R., Testa F., Innocenzi P. J. Phys. Chem. C. **(2008)**, 112, 16225−16230.

[150] Ghazzal M.N., Kebaili H., Joseph M., Debecker D.P., Eloy P., De Coninck J., Gaigneaux E.M. Appl. Catal. B. **(2012)**, 115− 116, 276−284.

[151] Zholobak N.M., Ivanov V.K., Shcherbakov A.B., Shaporev A.S., Polezhaeva O.S., Baranchikov A.Ye., Spivak N.Ya., Tretyakov Y.D.J. Photochem. Photobiol. B. **(2011)**, 102, 32−38.

[152] X-Ray mass attenuation and mass energy-absorption coefficients of Cerium, Silicon and Titanium elements can be found at the following link: http://www.nist.gov/pml/data/xraycoef/index.cfm.

[153] Matsuno H., Yokoyama A., Watari F., Uo M., Kawasaki T. Biomaterials. **(2001)**, 22, 1253 - 1262.

[154] Asefa T., Tao Z. Chem. Res. Toxicol. **(2012)**, 25, 2265−2284.

[155] Hart S.J., Leski T.A. NRL/MR/6110-06-8967.

5. Conclusion and future outlooks

The experimental work developed for this doctoral thesis has explored the antioxidant property of cerium oxide nanoparticles on different type of cell culture. In particular, we have developed the possibility of using nanoceria in several combinations, not only as naked nanoparticles dispersed in solution, but also in combination with inorganic and hybrid matrices. Nanoceria has actually proved to be a multifunctional material, capable to show its anti-oxidant or pro-oxidant properties depending on its size and concentration.

Nanoceria is effective for the treatment of neurodegenerative Parkinson-like diseases induced by chronic manganese intoxication. The antioxidant capability of nanoceria in PC12 cells has been tested by using $MnCl_2$ instead of H_2O_2. Nanoceria concentration of 20 $mg{\cdot}ml^{-1}$ provides the highest antioxidant effect on cell cultures pre-treated with $MnCl_2$, however to reach the maximum antioxidant effect in PC12 cells the nanoceria dimension and the concentration should be kept under 10 nm and 100 $mg{\cdot}ml^{-1}$, respectively. Nanoceria is also able to reduce the oxidative stress caused by auto-oxidation in a simultaneous treatment with L-DOPA, envisaging an innovative therapeutic application. Further studies are ongoing for a better understanding of the CeO_2 antioxidant biochemical mechanisms in the intracellular environment and a further in vivo investigation is necessary for exploring the potential role of these nanoparticles in the treatment of Parkinson like diseases.

The effect of nanoceria has also been studied in the germ cells, to reduce their oxidative damaging for the subsequent embryo development. The results show a different behaviour of nanoceria in both oocyte and spermatozoa.

During the *in vitro* maturation nanoceria produces positive effects on the oocyte with a low competence. In fact, the obtained results indicate that poor developmentally competent oocytes, matured in presence of low concentration of CeO_2-NPs, are able to develop up to blastocyst stage in a significant high percentage. The quality of blastocysts is improved under these culture conditions as it has been demonstrated. The lowest nanoceria concentration has not any obvious cytotoxic effect, even though the

concentration used has been significantly higher than those expected following the environmental exposure. This may indicate that the impact of environmental exposure of CeO_2 NPs on the oocyte is low. Despite the positive effects on oocyte maturation, further investigations at the molecular level are needed.

Regarding to the other germinal cells, ram spermatozoa, nanoceria at higher used concentrations and low temperature (4°C) seem to be well tolerating, but without significant effects on specific morphological and functional spermatozoa characteristics, in particular ROS production and mitochondrial activity. Further experiments are needed to assess the free radical scavenger activity of nanoceria on ram sperm and the potential consequences of *in vivo* and *in vitro* fertilising ability.

The versatility of nanoceria as a "functional platform" for biological systems has been also proved in nanocomposite materials. Nanoceria has been used in combination with different kind of matrix with the final goal of engineering controlled antioxidant properties.

Hybrid matrix based on glycidoxypropyltrimethoxysilane has been demonstrated to be very successfully as a matrix that anchor nanoceria without any previous functionalization. In fact, by changing the aging time of the precursor sol it is possible to obtain a smart surface, which increases its hydrophilicity with aging and grafts not only nanoceria, but also another type of nanoparticles, such as SPION.

The nanoceria-loaded films slowly release the CeO_2-NPs upon immersion in a buffer solution, showing that this system is a potential candidate to develop new types of medical devices, such as contact lenses, for controlled release of free radical scavenger nanoparticles in degenerative ocular diseases.

Mesoporous ceramic matrix loaded with nanoceria have also allowed to successfully prepared nanocomposite films with functional properties. The nanoparticles have been nucleated and grown within the pores upon exposure to an intense source of X-rays. The formation of ceria nanoparticles induced by hard X-rays depends on the X-ray dose and the chemical nature of the compounds used to disperse the ceria precursor. It has been observed that urea is an effective agent to promote nucleation and growth of

ceria, this being due to the presence of amine groups, which favour the coordination of Ce^{4+} ions.

Between the hafnia, titania and silica matrix, titania embedded nanoceria shows to be the best nanocomposite material with radical scavenging property. Its antioxidant property has been demonstrated *in vitro* by the photodegradation experiment using Rh6G dye, since upon exposure to UV light the material containing the ceria nanoparticles protects the dye from photodegradation and also in cell culture where the titania-ceria based nanocomposite is able to reduce the PBMC cell apoptosis. These results confirm the possibility to transfer the nanocomposite in plastic Petri dishes in order to develop a system capable to increase mechanical property leading to a better cell culture. However, more studies in the future are needed to achieve this goal.

Some of the results obtained during my doctoral work have been published in international journals and they are very promising to develop a new antioxidant product with high biocompatibility and versatility.

6. Acknowledgements

Dedico questo lavoro alla mia famiglia, babbo, mamma e mio fratello, per avermi sostenuta in questi anni, soprattutto nei momenti piu difficili, facendomi capire che non bisogna mai mollare.

Per questo lavoro di tesi ringrazio in primo luogo il mio relatore Dr. Luca Malfatti e il mio correlatore Prof. Plinio Innocenzi, per avermi dato l'opportunità di svolgere e concludere questo percorso di dottorato. Li ringrazio per aver creduto in me e avermi fornito gli strumenti necessari alla mia formazione di ricercatrice: dalle conferenze, alle collaborazioni internazionali fino alle numerose pubblicazioni del mio lavoro in riviste scientifiche. Per avermi aperto ad un mondo come quello della ricerca, a me prima sconosciuto; mondo che ho imparato ad amare fino a farlo diventare il mio lavoro.

Ringrazio i miei colleghi del laboratorio LMNT, Dr. Davide Carboni per disponibilità e la pazienza mostrata sia in campo scientifico che personale, per gli scontri costruttivi e per le correzioni "of my bad english". Barbara Lasio per il prezioso supporto durante tutti questi anni, per i nostri viaggi SS-Porto Conte arricchiti da lunghe chiacchierate nano e non. Kazumasa Suzuki per i "funny moments" e i discorsi in mille lingue, inglese, italiano, giapponese e spagnolo.

Vorrei ringraziare il Dr. Paolo Falcaro che durante il mio periodo in Australia mi ha dato la possibilità di poter esprimere le mie capacità e le mie idee anche su nuovi argomenti, per il supporto e l'umanità che lo contradistingue.

Desidero inoltre ringraziare il Prof. Masahide Takahashi per essere stato disponibile e di supporto durante il mio primo colloquio internazionale, il Prof. Stefano Enzo per i preziosi consigli di cristallografia a raggi X.

Ringrazio il gruppo SAXS e DXRL, il Dr. Luca Malfatti, il Dr. Davide Carboni, la Dr.Benedetta Marmiroli ed il Prof. Heinz Amenitsch per aver condiviso notti insonni e di alta scienza al Sincrotrone di Trieste (Elettra) incluse le mangiate e bevute in Slovenia con "il Colibrì".

Vorrei ringraziare tutte le persone con cui ho collaborato durante questi anni, il Prof. Sergio Ledda, la Dr. Grazia Galleri e la Dr. Rossana Migheli con i loro rispettivi gruppi di ricerca, per avermi accolta nei loro laboratori dandomi la possibilità di sviluppare quella parte della ricerca che mi coinvolge in maniera particolare: la nano-biomedicina.

Ringrazio le mie amiche, soprattutto Maria Laura, ValentinaM., Giuliana e Valentina S. che non hanno mai smesso di credere in me, sostenedomi soprattutto in un periodo difficile all'inizio del mio dottorato.

Ringrazio il consorzio INSTM per aver contribuito al finanziamento della borsa di dottorato.

Ringrazio inoltre tutte le persone che ho incontrato lungo questo cammino che nel bene e nel male hanno contribuito a farmi crescere come persona.

7. Appendix

- Publications related to doctorate

[1] Ariu F., Bogliolo L., Pinna A., Malfatti L., Innocenzi P., Falchi L., Ledda S. Cerium oxide nanoparticles (CeO_2 NPs) improve the developmental competence of *in vitro* matured prepubertal ovine oocytes. Reprod. Fertil. Dev. **(2015)**. Submitted.

[2] Falchi L., Bogliolo L., Galleri G., Ariu F., Zedda M.T., Pinna A., Malfatti L., Innocenzi P., Ledda S. Cerium dioxide nanoparticles did not alter the functional and morphological characteristics of ram sperm during short term exposure. Theriogenology. **(2015)**. Submitted.

[3] Pinna A., Malfatti L., Galleri G., Manetti R., Cossu S., Rocchitta G., Migheli R., Serra P.A., Innocenzi P. Ceria nanoparticles for the treatment of Parkinson-like diseases induced by chronic manganese intoxication. RSC Advances. **(2015)**, 5, 20432.

[4] Falchi L., Bogliolo L., Galleri G., Vlachopoulou G., Murrone O., Epifani G., Pinna A., Innocenzi P., Ledda S. 266 Biocompatibility of nanoceria in Ram sperm during 24hours of incubation. Reprod. Fert. Develop. **(2014)**, 27, 222-222.

[5] Pinna A., Lasio B., Carboni D., Marceddu S., Malfatti L., Innocenzi P. Engineering the surface of hybrid organicinorganic films with orthogonal grafting of oxide nanoparticles. J. Nanopart. Res. **(2014)**, 6, 2463.

[6] Pinna A., Lasio B., Piccinini M., Marmiroli B., Amenitsch H., Falcaro P., Tokudome Y., Malfatti L., Innocenzi P. Combining Top-Down and Bottom-Up Routes for Fabrication of Mesoporous Titania Films Containing Ceria Nanoparticles for Free Radical Scavenging. ACS Appl. Mater. Interfaces. **(2013)**, 5, 3168−3175.

[7] Pinna A, Figus C, Lasio B, Piccinini M, Malfatti L, Innocenzi P. Release of Ceria Nanoparticles Grafted on Hybrid Organic−Inorganic Films for Biomedical application Application. ACS Appl. Mater. Interfaces. **(2012)**, 4, 3916−3922.

- Other publications

[8] Jiang Y., Carboni D., Pinna A., Marmiroli B., Malfatti L., Innocenzi P. Hard X-rays for processing of hybrid organic-inorganic thick films. J. Synchrotron Radiat. In press.

[9] Carboni D., Pinna A., Amenitsch H., Casula M.F., Loche D., Malfatti L., Innocenzi P. Getting order in mesostructured thin films, from pore organization to

crystalline walls, the case of 3-glycidoxypropyltrimethoxysilane. Phys. Chem. Chem. Phys. **(2015)**, 17, 10679-10686.

[10] Vacca A., Mascia M., Mais L., Delogu F., Palmas S., Pinna A. Electrodeposition of Zirconium from 1-butyl-1-methylpyrrolidinium-bis(trifluoromethylsulfonyl)imide: Electrochemical Behaviour and Reduction Pathway. Mater. Manuf. Process. **(2015)**, 31, 74-80.

[11] Malfatti L., Pinna A., Enzo S., Falcaro P., Marmiroli B., Innocenzi P. Tuning the phase transition of ZnO thin films through lithography: an integrated bottom-up and top-down processing. J. Synchrotron Radiat. **(2015)**, 22, 165–171.

[12] Innocenzi P., Malfatti L., Lasio B., Pinna A., Loche D., Casula M.F., Alzari V., Mariani A. Sol-gel chemistry for graphene-silica nanocomposite films. New J. Chem. **(2014)**, 38, 3777-3782.

[13] Carboni D., Malfatti L., Marongiu D., Rassu P., Pinna A., Amenitsch H., Casula M.F., Innocenzi P. Enhanced Photocatalytic Activity in Low-Temperature Processed Titania Mesoporous Films. J. Mater. Chem.A. **(2014)**. 118, 12000−12009.

[14] Carboni D., Pinna A., Malfatti L., Innocenzi P. Smart tailoring of the surface chemistry in GPTMS hybrid organic-inorganic films. New J. Chem. **(2014)**. 38, 1635-1640.

[15] Falcaro P., Trinchi A., Doherty C., Buso D., Costacurta S., Hill A.J., Patelli A., Scopece P., Marmiroli B., Amenistch H., Lasio B., Pinna A., Innocenzi P., Malfatti L. 3D Spatially Controlled Chemical Functionalization on Alumina Membranes. Sci. Adv. Mater. **(2014)**, 6, 1520.

[16] Malfatti L., Falcaro P., Pinna A., Lasio B., Casula M.F., Loche D., Falqui A., Marmiroli B., Amenitsch H., Sanna R., Mariani A., Innocenzi P. Exfoliated Graphene into Highly Ordered Mesoporous Titania Films: Highly Performing Nanocomposites from Integrated Processing. ACS Appl. Mater. Interfaces. **(2013)**, 6, 795−802.

[17] Carboni D., Malfatti L., Pinna A., Lasio B., Tokudome Y., Takahashi M., Innocenzi P. Molecularly imprinted La-doped mesoporous titania films with hydrolytic properties toward organophosphate pesticides. New J. Chem. **(2013)**, 37, 2995-3002.

[18] Pinna A., Malfatti L., Piccinini M., Falcaro P., Innocenzi P. Hybrid materials with an increased resistance to hard X-rays using fullerenes as radical sponges. J. Synchrotron Radiat. **(2012),** 19, 586–590.